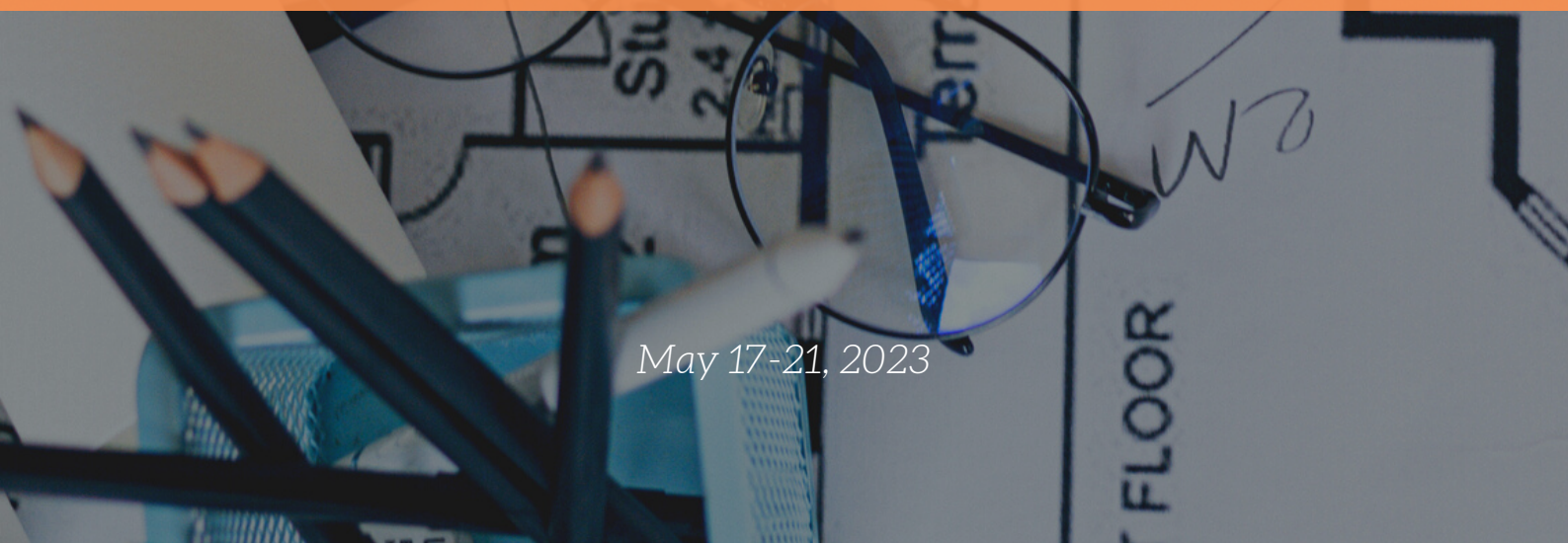


www.icens.eu

ICENS

9TH INTERNATIONAL CONFERENCE ON
ENGINEERING AND NATURAL
SCIENCES

BOOK OF PROCEEDINGS



May 17-21, 2023

Organized by



CSUN



Partners

CNR GROUP



**9th INTERNATIONAL CONFERENCE ON ENGINEERING AND NATURAL
SCIENCES (ICENS)**

ISBN 978-605-81426-1-9

ISSN 2687-2447

**PROCEEDINGS OF THE
9th INTERNATIONAL CONFERENCE ON ENGINEERING AND NATURAL
SCIENCES (ICENS)
MAY 17 TO 21, 2023 IN SARAJEVO, BOSNIA AND HERZEGOVINA**

Edited by

Prof. Dr. Özer Çınar

© CNR Group, 2023

Published by:

**info@icens.eu
www.icens.eu
www.cnrgroup.eu**

CNR Group Laboratuvar ve Arge Hizmetleri Sanayi Ticaret Limited Şirketi Çifte Havuzlar Mah., Eski Londra Asfaltı Cad., Kuluçka Mrk., A1 Blok, 151/1C, İç Kapı No:1 B-20, Esenler / İstanbul, 34220

This work is subject to copyright. All rights are reserved, whether the whole or part of the material is concerned. Nothing from this publication may be translated, reproduced, stored in a computerized system or published in any form or in any manner, including, but not limited to electronic, mechanical, reprographic or photographic, without prior written permission from the publisher. The individual contributions in this publication and any liabilities arising from them remain the responsibility of the authors. The publisher is not responsible for possible damages, which could be a result of content derived from this publication.

ISBN 978-605-81426-1-9

ISSN 2687-2447

SCIENTIFIC COMMITTEE

1. Prof. Dr. Adisa Parić - University of Sarajevo - Bosnia and Herzegovina
2. Prof. Dr. Aleksandar Dimitrov - Ss. Cyril and Methodius University - North Macedonia
3. Prof. Dr. Alexander Golub - National University of Kyiv-Mohyla Academy - Ukraine
4. Prof. Dr. Alexander Litvinenko - National University of Food Technologies (Kyiv) - Ukraine
5. Prof. Dr. Alit Ibraimi - University of Tetova - North Macedonia
6. Prof. Dr. Anita Grozdanov - Ss. Cyril and Methodius University - North Macedonia
7. Prof. Dr. Asif Šabanović – International University of Sarajevo - Bosnia and Herzegovina
8. Prof. Dr. Bekir Erol Ak - Harran University - Turkey
9. Prof. Dr. Cem Şensöğüt - Dumlupınar University - Turkey
10. Prof. Dr. Christos Douligeris - University of Erlangen-Nurnberg - Germany
11. Prof. Dr. Dragutin T. Mihailović - University of Novi Sad - Serbia
12. Prof. Dr. Evgeniy Shtefan - National University of Food Technologies (Kyiv) - Ukraine
13. Prof. Dr. Falko Dressler - University of Paderborn - Germany
14. Prof. Dr. Houssam Toutanji – Western Michigan University - USA
15. Prof. Dr. Ian F. Akyıldız – Georgia Institute of Technology - USA
16. Prof. Dr. İsmail Usta - Marmara University - Turkey
17. Prof. Dr. Kateryna Derevska - National University of Kyiv-Mohyla Academy - Ukraine
18. Prof. Dr. Liljana Gavrilovska - Ss Cyril and Methodius University - Macedonia
19. Prof. Dr. Lukman Thalib - Qatar University - Qatar
20. Prof. Dr. M. Asghar Fazel – University of Environment - Iran
21. Prof. Dr. Mikhailov Volodymyr - Taras Shevchenko National University of Kyiv - Ukraine
22. Prof. Dr. Mykola Glybovets - National University of Kyiv-Mohyla Academy - Ukraine
23. Prof. Dr. Muammer Koç - Hamad bin Khalifa University - Qatar
24. Prof. Dr. Nadia Bilko - National University of Kyiv-Mohyla Academy - Ukraine
25. Prof. Dr. Özer Çınar – Yıldız Technical University - Turkey
26. Prof. Dr. Perica Paunovic - Ss. Cyril and Methodius University - Macedonia
27. Prof. Dr. Rifat Škrijelj – University of Sarajevo - Bosnia and Herzegovina
28. Prof. Dr. Samir Đug - University of Sarajevo - Bosnia and Herzegovina
29. Prof. Dr. Tanju Karanfil – Clemson University - USA
30. Prof. Dr. Ümit Alver – Karadeniz Technical University - Turkey
31. Prof. Dr. Wolfgang Gerstaecker - University of Erlangen-Nurnberg - Germany
32. Prof. Dr. Vladyslav Sukhenko - National University of Life and Environmental Sciences of Ukraine (Kyiv) - Ukraine
33. Prof. Dr. Vullnet Ameti - University of Tetova - North Macedonia
34. Prof. Dr. Yılmaz Yıldırım - Bülent Ecevit University - Turkey
35. Prof. Dr. Yousef Haik - Hamad bin Khalifa University - Qatar
36. Assist. Prof. Dr. Abdelwahab Tahsin - Egyptian Russian University - Egypt
37. Assist. Prof. Dr. Agon Memeti - University of Tetova - North Macedonia
38. Assoc. Prof. Dr. Alaa Al Hawari - Qatar University - Qatar
39. Assist. Prof. Dr. Arianit Reka - University of Tetova - North Macedonia
40. Assoc. Prof. Dr. Fatih Ungan - Cumhuriyet University - Turkey
41. Assoc. Prof. Dr. Izudin Dzafic - International University of Sarajevo - Bosnia and Herzegovina
42. Assoc. Prof. Dr. Kateryna Syera - National University of Life and Environmental Sciences of Ukraine (Kyiv) - Ukraine
43. Assist. Prof. Dr. Muhamed Hadziabdic - International University of Sarajevo - Bosnia and Herzegovina
44. Assoc. Prof. Dr. Nusret Drešković - University of Sarajevo - Bosnia and Herzegovina
45. Assoc. Prof. Dr. Polina Vakuliuk - National University of Kyiv-Mohyla Academy - Ukraine
46. Assoc. Prof. Dr. Senija Tahirovic - International University of Sarajevo - Bosnia and Herzegovina
47. Assoc. Prof. Dr. Victor Karamushka - National University of Kyiv-Mohyla Academy - Ukraine
48. Assoc. Prof. Dr. Victoria Konovalova - National University of Kyiv-Mohyla Academy - Ukraine
49. Assoc. Prof. Dr. Yuriy Kravchenko - National University of Life and Environmental Sciences of Ukraine (Kyiv) - Ukraine
50. Assist. Prof. Dr. Fatih Taktak - Uşak University - Turkey
51. Assist. Prof. Dr. Fouzi Tabet - German Biomass Research Center - Germany
52. Assist. Prof. Dr. Haris Gavranovic - International University of Sarajevo - Bosnia and Herzegovina
53. Assist. Prof. Dr. Hüseyin Pehlivan - Gebze Technical University - Turkey
54. Assist. Prof. Dr. Sasan Rabieh - Shahid Beheshti University - Iran
55. Assist. Prof. Dr. Ševkija Okerić - University of Sarajevo - Bosnia and Herzegovina
56. Assist. Prof. Dr. J. Amudhavel - VIT Bhopal University - India
57. Dr. Zsolt Hetesi - National University of Public Service, Budapest - Hungary
58. Dr. Zsolt T. Németh - National University of Public Service, Budapest - Hungary

ORGANIZATION COMMITTEE

Chairman of the Conference

Prof. Dr. Özer Çınar – Yıldız Technical University

Members of the Committee

Prof. Dr. Ümit Alver (Co-Chairman) - Karadeniz Technical University - Turkey

Assist. Prof. Dr. Sasan Rabieh - Shahid Beheshti University - Iran

Alma Ligata - Zenith Group - Bosnia and Herzegovina

Ismet Uzun - Zenith Group - Bosnia and Herzegovina

Musa Kose - Zenith Group - Bosnia and Herzegovina

WELCOME TO ICENS 2023

On behalf of the organizing committee, we are pleased to announce that the 9th International Conference on Engineering and Natural Sciences (ICENS 2023) held from May 17 to 21, 2023 in Sarajevo, Bosnia and Herzegovina, Turkey. ICENS provides an ideal academic platform for researchers to present the latest research findings and describe emerging technologies, and directions in Engineering and Natural Sciences issues. The conference seeks to contribute to presenting novel research results in all aspects of Engineering and Natural Sciences. The conference aims to bring together leading academic scientists, researchers and research scholars to exchange and share their experiences and research results about all aspects of Engineering and Natural Sciences. It also provides the premier interdisciplinary forum for scientists, engineers, and practitioners to present their latest research results, ideas, developments, and applications in all areas of Engineering and Natural Sciences. The conference will bring together leading academic scientists, researchers and scholars in the domain of interest from around the world. The scientific program will focus on current advances in the research, production and use of Engineering and Natural Sciences with particular focus on their role in maintaining academic level in Engineering and Applied Sciences and elevating the science level. The conference's goal will to provide a scientific forum for all international prestige scholars around the world and enable the interactive exchange of state-of-the-art knowledge. The conference will focus on evidence-based benefits proven in clinical trials and scientific experiments.

*Best regards,
Prof. Dr. Özer ÇINAR*

CONTENT	Country	Page
Approaches Developed to Solve Fractional Differential Equations	Macedonia	1
Revised stratigraphy of Jurassic sediments from Kosrelik and Kosrelikizigi Areas (N Ankara)	Turkey	10
Comparison of Support Systems Used in Underground Mining	Turkey	18
Effect of air-entraining admixture usage rate on dynamic yield stress and viscosity in Portland cement systems containing urea	Turkey	23
Benthic Foraminiferal Fossils: Indicators and Tracers of Climate Change	Turkey	31
A General Evaluation of The Usage of Fly Ash in Concrete Mixtures	Turkey	36
Effect of Boron Waste on Mechanical and Durability Properties of Concrete	Turkey	39
Investigation of Thermal Performance of a Ground Coupled Carbonated Soft Drink Cooling System with an Underground Thermal Energy Storage Tank	Turkey	50
Land Cover And Land Use Classification Of Patch-Based Denoised Sar Images	Turkey	60
Analysis Of Y-Balance Test Data Used In Sports Sciences With Machine Learning Methods	Turkey	66
Fire Risk Assessment in High-Rise Buildings with Combustible Aluminum Composite Panels	Sudan	72
Analysis of Multi-Level Parabolic Leaf Spring Systems Designed by using Different Materials	Turkey	83
Wind Turbine Power Estimation Based on ANFIS Under Changing Air Density And Wind Speed Conditions	Turkey	88
Investigation of the Electrochemical Behavior of a Pillar[5]arene Derivative on the Glassy Carbon Electrode Surface	Turkey	97
Forest Fire Detection Using Unmanned Aerial Vehicle Images and Deep Learning	Turkey	104
Performance analysis comparison for a ground source heat pump with and without using solar collectors	Iraq	111



The comparative petiole anatomy of some <i>Hedysarum</i> species (Fabaceae) in Turkey	Turkey	122
A Preliminary Study on Potentiodynamic Polarisation Behaviour of UNS S32760 Duplex Stainless Steel	Turkey	128
Analysis of the Combined Usage of Plasticizer and Accelerator Effects on Microstructure for Mortar	Turkey	133
Utilization of PVC Wastes on Concrete Bicycle Roads	Turkey	143
Determining the Structural Performance of the Concrete Ventilation Shaft of a Historic Waterway	Turkey	149
Analyzing Seismic Performance of a Timber Structure: Modeling and Analysis Considerations	Turkey	158
Seismic Performance Assessment of a Masonry Building with Timber and Reinforced Concrete Slab	Turkey	166
Nonlinear FEA Analysis for Seismic Performance Assessment of an RC Shear Wall-Frame Building	Turkey	175
Evaluating the Effectiveness of Jacketing and CFRP Strengthening for an RC building through Seismic Performance Analysis	Turkey	182
Seismic Performance of a Masonry Building through Finite Element Analysis and Kinematic Limit Analysis	Turkey	191

Approaches Developed to Solve Fractional Differential Equations

*Flamure Sadiki*¹, *Krutan Rasimi*², *Alit Ibraimi*³, *Ylldrita Salih*⁴, *Miranda Xhaferi*⁵

Abstract

Fractional calculus is not a new topic, in reality it has almost the same history as that of classical calculus. In this paper, new approaches are developed to solve a class of nonlinear fractional differential initial value problems with fractional derivative defined in Caputo sense. Two numerical methods have been presented, Fractional Adams-Bashforth-Moulton Method (FABMM) and Fractional Differential Transformation Method (FDTM) compared with Adomian Decomposition Method (ADM), used for very specific type of problems. The methods are used on two different nonlinear fractional differential equations of the form, $D^\alpha y(t) = f(y(t))$, with and without exact solution for the same initial condition $y(0) = 0$. We present new results that deal with the Adomian Decomposition Method (ADM), suitable to handle fractional calculus applications. The results are obtained with comparisons made between FDTM, FABMM and the exact solutions at each integration point, given, both graphically and tabularly, for different fractional orders $0 < \alpha \leq 1$, constant step-size $h = 0.01$ and small time interval $t \in [0, 0.5]$. Our work, with using symbolic software packages as Wolfram Mathematica, can be considered as an alternative to existing techniques, and will have wide applications in science and engineering fields.

Keywords: Adomian Decomposition Method, Exact solution, Fractional Adams-Bashforth-Moulton method, Fractional differential problem, Fractional Differential Transform Method.

1. BASIC DEFINITIONS

For many years fractional calculus has been a topic studied by many researches. Like an ongoing process can recognize that within this study, new techniques and mechanisms shown up, which in turn make it possible, to find important challenging insights and unknown correlations between many areas of physics [1,4].

As most fractional differential equations do not have analytic solutions, we have to use different methods to convert such differential equations to more accurate equations for which we can then use various numerical techniques. We introduce two numerical methods, Adams-Bashforth-Moulton Method (FABMM) and Fractional Differential Transformation Method (FDTM) compared with Adomian Decomposition Method

¹ Corresponding author: University of Tetova, Department of Mathematics, Tetovo, North Macedonia. flamure.sadiki@unite.edu.mk

² University of Tetova, Department of Mathematics, Tetovo, North Macedonia, krutan.rasimi@unite.edu.mk

³ University of Tetova, Department of Mathematics, Tetovo, North Macedonia, alit.ibraimi@unite.edu.mk

⁴ University of Tetova, Department of Mathematics, Tetovo, North Macedonia, yldrita.salih@unite.edu.mk

⁵ University of Tetova, Department of Mathematics, Tetovo, North Macedonia, miranda.xhaferi@unite.edu.mk

(ADM), used for very specific type of nonlinear problems with fractional derivative defined in Caputo sense [3,9].

Examples are illustrated to be approximately solved by the well known FABMM, with the prediction step which calculates a rough approximation of the desired solution and the corrector step which refines the initial approximation using another means compared with FFDTM an semi-numerical method, that exploits the power series representation of the solution [6,9].

Definition 1.1. [1,5] The Riemann-Liouville fractional integral operator of order $0 < \alpha \leq 1$ of a function $f(t)$ is defined as:

$${}_0 I_t^\alpha f(t) = D_t^{-\alpha} = \frac{1}{\Gamma(-\alpha)} \int_0^t (t-\tau)^{-\alpha-1} f(\tau) d\tau \tag{1.1}$$

Definition 1.2. [1,3,4] The Riemann-Liouville fractional derivative of a function $f(t)$, of order $0 < \alpha \leq 1$ is defined by:

$$D_t^\alpha f(t) = \frac{1}{\Gamma(n-\alpha)} \frac{d^n}{dt^n} \int_0^t (t-\tau)^{-\alpha+n-1} f(\tau) d\tau \tag{1.2}$$

Definition 1.3. [1,4] The Caputo fractional derivative of a function $f(t)$, of order $0 < \alpha \leq 1$ is defined by:

$$D_t^\alpha f(t) = \frac{1}{\Gamma(n-\alpha)} \int_0^t (t-\tau)^{\alpha-1} f^{(n)}(\tau) d\tau \tag{1.3}$$

Is chosen to use Caputo fractional derivative, because it allows initial and boundary conditions to be included in the formulation of the problem. Two main advantages of this definition are: fractional derivative of a constant is zero, and, fractional differential equation of Caputo type has initial conditions of classical non-integer derivative type, in contrast to fractional differential equation of Riemann-Liouville type, where initial conditions are of fractional type.

Definition 1.4. [4,5] The problem:

$$D_t^\alpha y(t) = f(t, y(t)), \quad y(0) = y_0, \quad 0 < \alpha \leq 1 \tag{1.4}$$

we will construct the methods, assuming that a solution of (1.4) is sought on some time interval $[0, T]$ arbitrary $0 < \alpha \leq 1$ and $f : [0, T] \times D \rightarrow \mathbb{R}$, $D \subseteq \mathbb{R}$. The interval $[0, T]$ is divided into l subintervals. Consider an equi-spaced grid with step length h , $t_j = jh$, $j = 0, 1, \dots$. Let y_j denote the approximated solution at t_j and $y(t_j)$ denote the exact solution of the initial value problem (1.4).

2. NUMERICAL METHODS

2.1. Adams- Bashforth- Moulton Method

If $\left[D_t^{-\alpha} f(t, y(t)) \right]_{t=t_{n+1}}$ is approximated by the fractional trapezoidal formula, the following fractional trapezoidal rule is derived:

$$y_{n+1} = \sum_{j=0}^{m-1} \frac{t_{n+1}^j}{j!} y_0^{(j)} + \sum_{j=0}^{n+1} a_{j,n+1} f(t_j, y_j) \quad (2.1)$$

$$\text{where } a_{j,n+1} = \frac{\Delta t^\alpha}{\Gamma(\alpha+2)} \begin{cases} n^{\alpha+1} - (n-\alpha)(n+1)^\alpha, & j=0 \\ (n-j+2)^{\alpha+1} - 2(n-j+1)^{\alpha+1} + (n-j)^{\alpha+1}, & 1 \leq j \leq n \\ 1, & j=n+1 \end{cases}$$

If $\left[D_t^{-\alpha} f(t, y(t)) \right]_{t=t_{n+1}}$ is approximated by the left fractional rectangular formula:

$$y_{n+1} = \sum_{j=0}^{m-1} \frac{t_{n+1}^j}{j!} y_0^{(j)} + \Delta t^\alpha \sum_{j=0}^{n+1} b_{j,n+1} f(t_j, y_j) \quad (2.2)$$

$$\text{where } b_{j,n+1} = \frac{1}{\Gamma(\alpha+1)} \left[(n-j+1)^\alpha - (n-j)^\alpha \right]$$

The predictor-corrector method, we first use (2.2) to get y_{n+1}^p (predictor), then we use (2.1) to get y_{n+1} (corrector) by replacing y_{n+1} with y_{n+1}^p on the right-hand side of (2.1), which leads to the fractional FABMM [6,8,9].

2.2. Fractional Differential Transformation Method

The differential transform method is derived from the Taylor series expansion. The DTM does not require a symbolic evaluation of derivatives. Instead, relative derivatives are computed iteratively. The k -th differential transform of a function $y(t)$ is defined as follows:

$$F(k) = \frac{1}{k!} \left. \frac{d^k y(t)}{dt^k} \right|_{t=t_0} \quad (2.3)$$

for $k = 1, 2, 3, \dots$. The differential inverse transform is defined as:

$$y(t) = \sum_{k=0}^{\infty} F(k) (t-t_0)^k \quad (2.4)$$

Differential transforms of basic linear and nonlinear functions were presented in many studies, along with numerous examples of FDTM application for solving integer-order ordinary differential equations [6,7,9].

2.3. Adomian Decomposition Method

In ADM solution of equation (1.4) is expressed in the form of infinite series:

$$u = \sum_{n=0}^{\infty} u_n \tag{2.5}$$

with $u_0 = y(t)$. Further it is assumed that the nonlinear term $N(u)$ can be expressed as $\sum_{n=0}^{\infty} A_n$, where A_n are Adomian polynomials [4]. The (2.5) becomes

$$\sum_{n=0}^{\infty} u_n = y(t) + L \left[\sum_{n=0}^{\infty} u_n \right] + \sum_{n=0}^{\infty} A_n = y(t) + \sum_{n=0}^{\infty} L[u_n] + \sum_{n=0}^{\infty} A_n \tag{2.6}$$

Where the Adomian polynomials A_n are given by expression:

$$A_n = \frac{1}{n!} \left[\frac{d^k}{d\lambda^k} N \left(\sum_{k=0}^n u_k(t) \lambda^k \right) \right]_{\lambda=0} \tag{2.7}$$

The solution to (1.4) is always given in the form of k -term approximate solution [5] $u = \sum_{n=0}^{k-1} u_n$.

3. APPLICATIONS

Example 1. Let us solve the fractional differential equation

$$D^\alpha y(t) = 1 + y^2(t), \quad 0 < \alpha \leq 1 \tag{3.1}$$

with $y_0 = 0$, using ADM, FMDTM and FABMM.

Solution. To solve this problem with ADM, firstly, we apply the LTM:

$$L[D^\alpha y(t)] = L[1] + L[y^2], \quad L[y(t)] = Y$$

$$L[D^\alpha y(t)] = s^\alpha Y - s^{\alpha-1} y(0) = s^\alpha Y, \quad Y = \frac{1}{s^{\alpha+1}} + \frac{1}{s^\alpha} L[y^2]$$

For the decomposition $y(t) = \sum_{n=0}^{\infty} y_n(t)$ we obtain $Y = \sum_{n=0}^{\infty} Y_n$, $y^2 = \sum_{n=0}^{\infty} A_n$ where A_n are the Adomian polynomials [5]:



$$A_0 = y_0^2, A_1 = 2y_0y_1, A_2 = y_1^2 + 2y_0y_2, A_3 = 2y_1y_2 + 2y_0y_3, \dots$$

$$\sum_{n=0}^{\infty} Y_n = \frac{1}{s^{\alpha+1}} + \frac{1}{s^{\alpha}} \sum_{n=0}^{\infty} A_n,$$

$$Y_0 = \frac{1}{s^{\alpha+1}} \square y_0 = \frac{t^{\alpha}}{\Gamma[\alpha+1]} \square A_0 = y_0^2 = \frac{t^{2\alpha}}{\Gamma^2[\alpha+1]}$$

$$Y_1 = \frac{1}{s^{\alpha}} L[A_0] \square Y_1 = \frac{1}{s^{\alpha}} L\left[\frac{t^{2\alpha}}{\Gamma^2[\alpha+1]}\right] = \frac{1}{s^{3\alpha+1}} \frac{\Gamma[2\alpha+1]}{\Gamma^2[\alpha+1]}$$

$$y_1 = L^{-1}Y_1 \square y_1 = \frac{\Gamma[2\alpha+1]}{\Gamma^2[\alpha+1]} \frac{t^{3\alpha}}{\Gamma[3\alpha+1]}, A_1 = 2y_0y_1$$

$$Y_0 = \frac{1}{s^{\alpha+1}} \square y_0 = \frac{t^{\alpha}}{\Gamma[\alpha+1]} \square A_0 = y_0^2 = \frac{t^{2\alpha}}{\Gamma^2[\alpha+1]}$$

$$Y_1 = \frac{1}{s^{\alpha}} L[A_0] \square Y_1 = \frac{1}{s^{\alpha}} L\left[\frac{t^{2\alpha}}{\Gamma^2[\alpha+1]}\right] = \frac{1}{s^{3\alpha+1}} \frac{\Gamma[2\alpha+1]}{\Gamma^2[\alpha+1]}$$

$$y_1 = L^{-1}Y_1 \square y_1 = \frac{\Gamma[2\alpha+1]}{\Gamma^2[\alpha+1]} \frac{t^{3\alpha}}{\Gamma[3\alpha+1]}, A_1 = 2y_0y_1$$

By using properties of DTM method [7] transforms to:

$$Y(k+\alpha\beta) = \frac{\Gamma\left[1+\frac{k}{\beta}\right]}{\Gamma\left[1+\alpha+\frac{k}{\beta}\right]} \left[\sum_{l=0}^k Y[l]Y[k-l] + \delta[k] \right] \quad (3.2)$$

$Y[k] = 0, k = 0, 1, 2, \dots, \alpha\beta - 1$ where $Y(k)$ is obtained for different values of α and then using (3.1) is evaluated by dividing the $[0, T]$ into M subintervals to assume solution of (3.1).

The problem is solved with a constant step-size $h = 0.01$ and the results are given in a) for the ADM and b) for approximated values obtained by FDTM and FABMM. For $\alpha = 1$ and $y_0 = 0$ the exact solution of (3.1) is $y(t) = \tan(t)$.

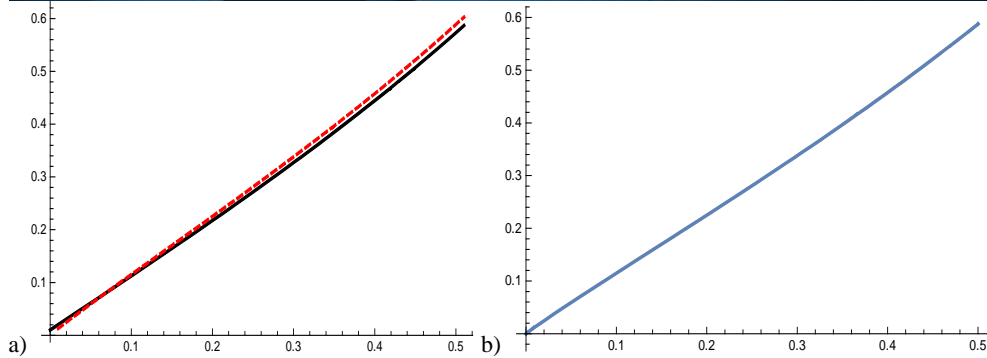


Figure 1. Partial data values of the time-series $y(t)$ for increasing t of the numerical approximation values

a) $y(t)$ time-series of equation (3.1) with $\alpha = 0.95$, $y_0 = 0$, $h = 0.01$ and $t \in [0, 0.5]$, FMDTM (black solid line), FABMM (red dashed line); b) ADM (blue solid line).

Table 1. Exact and approximated solutions $y(t)$ of equation (3.1) obtained by ADM, FDTM, FABMM

t	$\alpha = 0.95$			$\alpha = 1$		
	t_{ADM}	t_{FDTM}	t_{FABM}	t_{exact}	t_{FDTM}	t_{FABM}
0.01	0.0128485	0.0102057	0.0128488	0.0100003	0.0100003	0.0100005
0.05	0.0593467	0.0510713	0.059348	0.0500417	0.0500417	0.0500425
0.1	0.115048	0.10241	0.11505	0.100335	0.100335	0.100336
0.15	0.170045	0.15429	0.170049	0.151135	0.151135	0.151138
0.2	0.225182	0.206995	0.225188	0.20271	0.20271	0.202713
0.25	0.281032	0.260826	0.281045	0.255342	0.255342	0.255346
0.3	0.338082	0.316112	0.338116	0.309336	0.309336	0.309341
0.35	0.396798	0.37321	0.396886	0.365028	0.365028	0.365033
0.4	0.457651	0.432535	0.45786	0.422793	0.422793	0.422798
0.45	0.521131	0.494538	0.521593	0.483055	0.483055	0.48306
0.5	0.58776	0.559755	0.588711	0.546302	0.546302	0.546307

Example 2. Let us solve the fractional differential equation

$$D^\alpha y(t) = 1 + 2y(t) + y^2(t), \quad 0 < \alpha \leq 1 \tag{3.2}$$

with $y_0 = 0$, using FDTM and FABM [6].

Solution. Exact solution for equation (3.2) is $y(t) = \frac{t^\alpha}{\alpha - t^\alpha}$ for $\alpha = 0.99$ closer to 1, initial value $y_0 = 0$ and time interval $[0, 0.5]$. Transformed function using FDTM is

$$Y(k+\alpha\beta) = \frac{\Gamma\left[1+\frac{k}{\beta}\right]}{\Gamma\left[1+\alpha+\frac{k}{\beta}\right]} \left[\sum_{l=0}^k Y[l]Y[k-l] + 2Y[k] + \delta[k] \right]$$

$$Y[k] = 0, k = 0, 1, 2, \dots, \alpha\beta - 1$$

Results are shown for the exact solution and approximated ones taken by FDTM, FABM algorithms, shown in Figure 2.

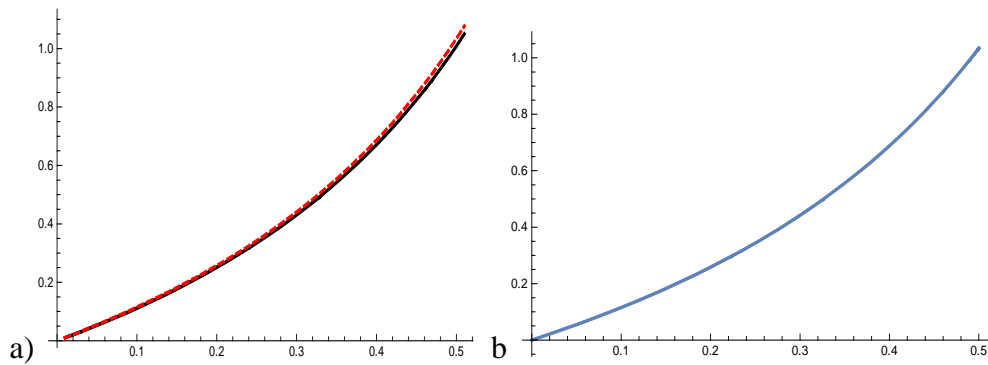


Figure 2. . Partial data values of the time-series $y(t)$ for increasing t of the numerical approximation values; a) $y(t)$ time-series of equation (3.2) with $\alpha = 0.99$, $y_0 = 0$, $h = 0.01$ and $t \in [0, 0.5]$, FMDTM (black solid line), FABMM (red dashed line); b) $y(t)$ exact solution (blue solid line);

Table 2. Approximated values obtained by each algorithm, comparing with exact solutions. Exact and approximated solutions $y(t)$ of equation (3.2) of Exact, FDTM, FABMM for $\alpha = 0.99$

t	t_{exact}	t_{FDTM}	t_{FABM}
0.01	0.0106901	0.0101444	0.010627
0.05	0.0548979	0.0528674	0.0545857
0.1	0.115278	0.111637	0.114653
0.15	0.182616	0.177356	0.181679
0.2	0.258333	0.251333	0.257098
0.25	0.344177	0.335231	0.342671
0.3	0.442379	0.431187	0.440657
0.35	0.555855	0.542004	0.554014
0.4	0.688504	0.671424	0.686708
0.45	0.845664	0.824559	0.844189
0.5	1.03485	1.00859	1.03416

For $\alpha = 0.99$, $\alpha = 0.8$ and $\alpha = 0.7$, the method rapidly diverges from the exact solution. The situation is more noted for the investigated fractional order $\alpha = 0.7$.

There we can see the divergence of the method FABM, if fractional order decrease gradually from $\alpha = 0.9$, $\alpha = 0.8$ and $\alpha = 0.7$, the method rapidly diverge from the exact solution. The situation is more noted for the investigated fractional order $\alpha = 0.7$.

The following tables illustrate the concluded results by computing fractional derivatives of order $0 < \alpha \leq 1$ for $f(t)$ at specific points of t .

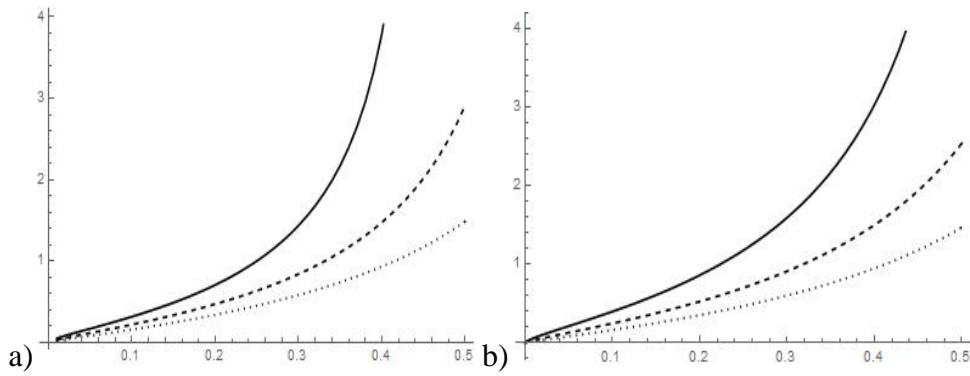


Figure 3. Partial data values of the time-series $y(t)$ for increasing t of the numerical approximation values a) $y(t)$ exact solution of equation (3.2) b) $y(t)$ time-series of equation (3.2). $\alpha = 0.9$ (black solid line); $\alpha = 0.8$ (black dashed line) and $\alpha = 0.7$ (black dotted line), $y_0 = 0$, $h = 0.01$ and $t \in [0, 0.5]$ using FABM

Table 3. Exact and approximated solutions $y(t)$ of equation (3.2) obtained by t_{exact} and t_{exact} obtained by FABM, for $\alpha = 0.9$, $\alpha = 0.8$ and $\alpha = 0.7$.

t	$\alpha = 0.7$		$\alpha = 0.8$		$\alpha = 0.9$	
	t_{exact}	t_{FABM}	t_{exact}	c	t_{exact}	t_{FABM}
0.01	0.060302	0.0461214	0.0324164	0.0277885	0.0179256	0.0167672
0.05	0.212799	0.164678	0.128395	0.110817	0.0810345	0.0760084
0.1	0.398675	0.312037	0.247056	0.21473	0.162629	0.153016
0.15	0.609236	0.484542	0.377449	0.330872	0.252322	0.238258
0.2	0.862353	0.702439	0.52656	0.466662	0.353228	0.334972
0.25	1.1802	0.997493	0.701682	0.630881	0.468608	0.446716
0.3	1.59751	1.4338	0.912402	0.836408	0.602517	0.578097
0.35	2.17554	2.17272	1.17257	1.10422	0.760363	0.735505
0.4	3.03581	3.79517	1.50352	1.47191	0.949669	0.928247
0.45	4.46048	11.5867	1.94034	2.01518	1.18132	1.17055
0.5	7.29111	$1.2228 \cdot 10^2$	2.5453	2.91482	1.47176	1.48542

4. CONCLUSIONS

The numerical techniques were tested on two nonlinear problems. The results obtained show that the techniques can be applied to solve these types of equations efficiently obtaining the exact solution, they are in good agreement with those obtained by using the ADM and exact one (if it exist). The study emphasized our belief that the methods are in a reliable technique to handle fractional differential equations with advantages in terms of their straightforward applicability, their computational effectiveness and their accuracy. The superiority of each numerical method over the other methods depends on the particular equation under investigation: in the first case (Example 1), FABMM and ADM were shown to be a better approximations than FABM and FMDTM, according to the taken fractional order $\alpha = 0.95$, FMDTM like a best approximation for $\alpha = 1$ compared to the exact solution of the nonlinear problem, in the second case (Example 2) the situation is the same, there we can see an good agreement between FABM and FABMM.

REFERENCES

- [1]. B. Ross, *A brief history and exposition of the fundamental theory of fractional calculus*, Fractional Calculus and its Applications, Springer Lecture Notes in Mathematics, vol. 57, pp. 1-36, 1975.
- [2]. Ch. Li, F. Zhang, *A survey on the stability of fractional differential equations*, The European Physical Journal Special Topics, 193(1), pp. 27-47, 2011.
- [3]. V. Daftardar-Gejji, H. Jafari, *Analysis of a system of non autonomous fractional differential equations involving Caputo derivatives*, J. Math. Anal. Appl., 328, pp. 1026–1033, 2007.
- [4]. Y. Zhou, J.R. Wang, L. Zhang, *Basic Theory of Fractional Differential Equations*, World Scientific Publishing Co. Pte. Ltd., Singapore, 2016.
- [5]. S. K. Miller, B. Ross, *An introduction to the fractional calculus and fractional differential equations*, John Wiley and Sons, Inc., Canada, 1993.
- [6]. Y. Seferi, G. Markoski and A. Gjurchinovski, *Numerical solution and chaotic dynamic of fractional-order Lorenz and Chen system*, Journal of Natural Sciences and Mathematics of UT, vol. 4, pp. 223-229, 2019.
- [7]. C. Bervillier, *Status of the differential transformation method*, Applied Mathematics and Computation, vol. 20, pp. 10158-10170, 2012.
- [8]. Ch. Li, Ch. Tao, *On the fractional Adams method*, Computers and Mathematics with Applications, vol. 58, pp. 1573–1588, 2009.
- [9]. Ch. Li, F. Zeng, *Numerical Methods for Fractional Calculus*, CRC Press Taylor and Francis Group, New York, 2015.

Biography

Ylldrita Brief curriculum vitae should also be provided for the presenting author at the end of the paper.

Revised stratigraphy of Jurassic sediments from Kosrelik and Kosrelikkizigi Areas (N Ankara)

Kubra Yayan¹, Hakan Ozkeles², Muhittin Gormus²

Abstract

Transgressive and widespread sediments of the Jurassic Period and various geological units from north Ankara provide paleontological and sedimentologic data to interpret the past geological history. In the study, we made a proper stratigraphical revision for the Jura sediments from the Kosrelik and Kosrelikkizigi areas in northern Ankara. For the revised stratigraphy, the obtained field and laboratory work results and the literature information were used. A Total of 47 samples were collected from the Jurassic-aged units. Two stratigraphical sections were measured. In the area, the Bayirkoy Formation, more than 600 meters in thickness and early Jurassic in age comprise the following members from the bottom to top: Corakliktepe, Kosrelik, Hacikavagi, Beytepe and Turnacesme members. It starts with transgressive basal conglomerates and continues with arkosic quartzitic sandstones, rhythmic marl and mudstone sediments and ends with sandstones. Foraminiferal findings support the Jurassic age. Lithological and faunal contents of the Jurassic sediments show open marine deeper paleoenvironment.

Keywords: Mesozoic, stratigraphy, Kosrelik, Kosrelikkizigi, Ankara

1. INTRODUCTION

Foraminifera are unicellular marine organisms with shells that have been widely utilized as biostratigraphic and paleoenvironmental indicators due to their abundance, diversity, and rapid evolutionary characteristics. The Mesozoic era played a crucial role in the evolutionary history of foraminifera, making the study of Mesozoic foraminifera vital for comprehending their evolution.

However, research performed on foraminifera from the Kosrelik district in Ankara (Figure 1) has yielded conflicting results concerning the correspondences between formation and fossil ages [1; 5; 6; 7; 9; 10; 11; 12; 14]. The objective of this study is to address these disparities by providing a comprehensive analysis of the systematics, numerical data, and environmental interpretations of grain foraminifera found in Triassic-Jurassic sediments within the region.

To accomplish this objective, a new field study was performed, during which new sampling locations were identified, and measured stratigraphic sections (MSS) were obtained. This study focuses primarily on investigating Mesozoic grain foraminifera discovered in the Kosrelik region of Ankara. The present paper emphasizes the initial phase of the study, which involves fieldwork for sample collection from various locations within the region.

¹ Eskisehir Osmangazi University, Department of Geological Engineering, Eskisehir kokur@ogu.edu.tr

² Ankara University, Department of Geological Engineering, Ankara



Fig.1: Field study area

2. LITERATURE

Numerous studies have been carried out on various fossil assemblages from Mesozoic outcrops in Ankara. This section presents the investigations performed in the Kosrelik and Kosrelikkizigi areas. Stratigraphic [14], sedimentological [4; 8; 9], and paleontological [10; 12; 13] analyses have been performed in the Kosrelik and Kosrelikkizigi areas, located north of Ankara. The principal findings of these studies are presented below. The stratigraphy of the region has been investigated by [2; 10; 14], and particularly in the Ammonitico Rosso facies. [4], [7], and [9] have studied the region's formation, while [12] and [13] have conducted paleontological studies, examining bivalves, gastropods, annelids, and foraminifera in the area.

Studies on the Ammonitico Rosso facies are numerous. [14] investigated the Ammonitico Rosso facies in the Ankara Jurassic sequence and found that it bears paleontological and sedimentological similarities with the red nodular limestones of the Northern and Southern Alps. They identified the stack as conglomerates, sandstones, Ammonitico Rosso-type sediments from bottom to top, nodular limestones within these, and sandstones towards the top, and revealed that a slightly metamorphosed rock unit tectonically covers them. [2] examined Jurassic ammonites in Ankara and Kelkit areas and identified Upper Sinemurian-Middle Lower Carixian-aged ammonites. They stated that the correlation of some species is challenging because they are endemic. [11] presented foraminiferal findings in the Kosrelik Kizigi, Kosrelik, Tahar, and Alacatli environments, identifying Sinemurian-Pliensbachian and Toarcian-aged foraminifera in the Jurassic outcrops, which exhibit a transgressive stack feature. Due to the deep-water environments in this region, typical Tethys forms were not encountered. [10] described the ostracod findings in the early Jurassic Ammonitico Rosso facies, which are included in the Kosrelik Member and Turnacesme Member around Kosrelik Kizigi, and revealed their ages in his study. The Kosrelik Member is said to be located in the shallow part of the Neotetis Ocean during the early Jurassic period.

When examining formation studies, it is evident that [4] and [8] presented the lithostratigraphy of the region as follows, from bottom to top: the Karakaya Complex, Bayirkoy Formation, Cakirlardere Formation, Sogukcam Formation, Uzuncarsidere Formation, Orhaniye Formation, Tekke Volcanites, Dodurga 6 Formation, and Alluvium. Furthermore, they subdivided the Bayirkoy Formation into four members: Corakliktepe, Uzundere, Beytepe, and Turnacesme, with the Beytepe Member identified as Early Toarcian in age. The authors determined that the environment was a very shallow marine setting, supported by the presence of fossils and microbial valleys found in Triassic-aged rocks. By incorporating isotope geology and geochemistry analyses into their fossil research, they obtained a substantial dataset for environmental interpretation. In a comparative analysis, [9] observed different facies in the stacks around Beytepe and Kosrelik based on sedimentological characteristics.

In a literature review focused on bivalves, gastropods, and annelids, [12] conducted a study on these organisms within the Early Jurassic Ammonitico Rosso facies in the Kosrelik Region. They categorized the Ammonitico Rosso facies into two types of deposits: carbonate submarine hills and turbiditic deposits with high clay content.

Several species were identified, including *Glomerula gordialis*, an annelid species, as well as various mussel and gastropod species.

Regarding foraminifera, [13] conducted a recent study involving foraminiferal identifications on thin sections prepared from outcrops in the Kosrelik and Tuluntas Regions. The author highlighted a contradiction in the literature by identifying different fossil ages than those previously reported.

3. METHODOLOGY

This study includes detailed fieldwork primarily performed in Kosrelik, Kosrelikkizigi, and their surrounding areas. The fieldwork was carried out in November 2022, during which geological maps of the region from previous studies were examined, and these maps were compared with topographic maps on Google Earth images. In the study area, 47 samples were collected from Mesozoic-aged outcrops, and stratigraphic sections were measured at two locations that were deemed important. The coordinates of the measured stratigraphic sections are provided in Table 1.

Table 1: Measured Section Coordinates

Region		Coordinates	Height
Kosrelik Area	Kosrelik Section		
	Startup	36T 0488963E, 4435985 N	1155 m
	Finish	36T 0488955E, 4435994 N	1155 m
Kosrelikkizigi Area	KosrelikKizigi Section		
	Startup	36T 0490483E, 4439464 N	1054 m
	Finish	36T 0490479E, 4439479 N	1060 m

During the fieldwork, detailed observations were made on geological features, including lithologies of formations, existing stratigraphy, folded structures, faults, and overlaps. Notes were taken, and stratigraphic sections were measured at each sampling site. The collected rock samples will undergo washing, thin section preparation, and isotope analysis.

To determine the age and depositional environment of the collected samples, various laboratory analyses will be conducted. Thin sections of the rock samples will be studied to identify microfossils such as foraminifera and conodonts. Isotope analyses will be performed to determine the ages of the rock samples and to obtain information about the depositional environment. Specifically, oxygen and carbon isotope analyses will be conducted on selected samples of carbonate rocks, and strontium isotope analyses will be carried out on the samples of clastic rocks.

Overall, the combination of detailed fieldwork and laboratory analyses will provide a comprehensive understanding of the geological characteristics and evolution of the study area.

4. STRATIGRAPHY

Around Ankara (Fig. 2) the Karakaya Complex is mainly represented by Triassic aged slightly metamorphosed sedimentary rocks. Karakaya Complex overlies Jurassic sediments with reverse faulted relationships around Kosrelik and Kosrelikkizigi (Fig. 3). Jurassic Bayirkoy Formation starts with basal conglomerates. The Jurassic sediments starting with conglomerates and sandstones continue with quartzites and variegated unit towards the top. In previous studies, the Bayirkoy Formation was divided into Corakliktepe Member, Uzundere Member, Beytepe Member, Kosrelik Member, and Turnacesme Member from bottom to top [10, 13].

Bayirkoy Formation Bayirkoy Formation, initially named as "Bayirkoy sandstone" in 1960, is a sedimentary unit located in the Bilecik region. It was later defined as the Bayirkoy Formation in [3]. The formation is composed of five members and consists of conglomerate, sandstone, and limestone of various colors. It is estimated to be at most 300 meters thick and is believed to be older than the Jurassic period. Fossil groups such as Ammonite, Belemnite, Brachiopoda, Pelecypoda, Gastropoda, and Crinoid have been commonly found in the formation. The lower parts of the formation represent a terrestrial environment while the upper parts represent a coastal-shallow marine environment.

Corakliktepe Member: The Corakliktepe Member is a sedimentary unit located in the southeast of Ankara, consisting of green-brown, grained conglomerates in thick layers. The conglomerates contain phyllite, chert, igneous rocks, and rock fragments, and vary in size from a few centimeters to 20 centimeters. The member is estimated to be 2-20 meters thick and is believed to be relatively Sinemurian in age. It is suggested that the unit was deposited in a fan delta environment in the vicinity of Alacaatli and reflects a very shallow marine-land transition environment. The basal conglomerates of the member are laterally transitioned with the Kosrelik sandstone member and Beytepe member.

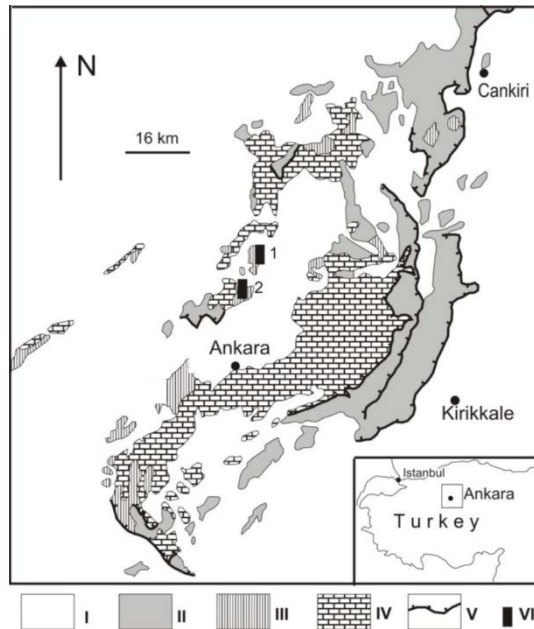


Fig. 2: Simplified geological map of the Ankara region and location of the study sections [11]. I, Upper Campanian and younger sediments. II, Cenozoic ophiolite melange. III, Jurassic-Lower Cretaceous. IV, Carboniferous-Triassic Karakaya Complex. V, Overlaps. VI, Cross sections (1, Kosrelikkizigi, 2, Kosrelik)

Uzundere Member: The Uzundere Member, located in the Kosrelik area near Alacaatli, is a thin to medium layered limestone formation that varies in thickness from 2-5 meters. It is conformably overlaid by the Corakliktepe Member and is laterally transitional with other members. The member is known to contain numerous ammonite fossils and has been dated to the Sinemurian-Carixian age. According to previous studies, the red-colored limestone found in the member was deposited on the shallow shelf as bioclastic sand dunes due to the influx of material from the land.

Beytepe Member: The Beytepe Member was named by [7] and is part of the Bayirkoy Formation. It is widespread and observed in different areas such as Alacaatli and Kosrelik. The member consists of pinkish colored thick-bedded nodular limestone, pink colored brachiopod cocinae limestone, red colored mudstone and limestone. It starts with red colored hardground type limestone at the base and continues with mudstones with abundant ammonoids, red colored marl with ammonoids, brachiopod limestone and red colored nodular limestone. The thickness of the member varies between 2-5 meters. The Beytepe Member is laterally transgressive with the Seyhlertepe Member and conformable with the Turnacesme Member. Its age is Lower Toarsian, and it was deposited on a shallow Pelagic Carbonate Platform.

Kosrelik Member: The Kosrelik Member is a separate member of the Bayirkoy Formation, consisting of quartz sandstones located on the conglomerates belonging to the Corakliktepe Member and sometimes present lenticular appearances within the Beytepe Member. It was previously named Bileystone but it would be more appropriate to name it Kosrelik Member. The sediments belonging to this member outcrop in certain thicknesses just east of Kosrelik Village, at the beginning of Hacikavagi stream, and southeast of Kosrelik Pond. The greenish colored fine-medium grained sandstones are composed of quartz grains and some laminated appearances are also present.

Coraklitepe Member: The Kosrelik Member is a sedimentary layer with a thickness ranging from 1 cm to 20 meters, and it is located at the base of the Coraklitepe Member. Although it is mostly found within the Beytepe Member, it is thought to be a separate member due to its unique characteristics. No macro or micro fossils were found in the quartz sandstones, but its stratigraphic position and lithologic features suggest that it was formed as shallow marine, deltaic sediments in the Lower Jurassic period.

Turnacesme Member: The Turnacesme Member, named by [6], is a greenish-colored unit consisting of mudstones and sandstones that outcrops in the northern parts of Kosrelik village and western parts of Hacettepe University Beytepe Campus. It starts with thin-bedded or laminated mudstone-sandstone succession at the base, followed by grain-supported conglomerate in the middle parts, and dark colored, thick and cross-bedded sandstones at the top. The thickness of the member ranges between 26-180 meters and it is thought to be relatively Upper Toarsian (?) -Batonian in age based on its stratigraphic relationships. The member was deposited relatively deep at the base and under the storm wave base towards the upper parts southwest of Ankara.

5. RESULTS AND DISCUSSION

Two measured stratigraphic sections from the study area were transferred to the computer (Fig. 4).

Kosrelik Section

Coordinates of the angular section, initial: X: 36T 0488963D, 4435985K and the end coordinates are Y: 36T 0488955D, 4435994K. The units forming the section are generally siltstones and sandstones. Details such as observed differences and thickness information are as seen on the section.

Kosrelikkizigi Section

Coordinates of the Kosrelikkizigi cross section, initial: X: 36T 0490483 D, 4439464 N and the end coordinates are Y: 36T 0490479 D, 4439479 N. The units forming the section are generally lumpy limestones. Details such as observed differences and thickness information are as seen in the section.

The field studies carried out in Kosrelik and Kosrelikkizigi and their surroundings revealed important information about the Mesozoic aged units in the study area. The geological maps prepared in previous studies were updated and the units in the field were examined in detail. The lithologies, stratigraphy, folded structures, faults, and overlaps were observed and necessary notes were taken during the fieldwork.

The results obtained from this study provide important data for understanding the geological history of the study area and contribute to the literature on the Mesozoic aged units in Ankara. Further studies, including sedimentological, paleontological, and geochemical analyses, are needed to fully understand the depositional environments and the tectonic evolution of the region.

6. CONCLUSION

Based on the detailed fieldwork conducted in the Mesozoic-aged outcrops of Kosrelik and Kosrelikkizigi areas in Ankara, Turkey, this study aims to provide a better understanding of the geological evolution of the study area. Using geological and topographic maps, a total of 47 rock samples were collected, and stratigraphic sections were measured to thoroughly investigate the study area and observe the geological features of the formations. The collected rock samples will undergo further analysis to obtain a comprehensive understanding of the Mesozoic-aged units in the study area. The study results will not only contribute to understanding the geological evolution of the Kosrelik and Kosrelikkizigi areas but also provide valuable information for future paleontological and paleoenvironmental studies in the region



SYSTEM	CRETA.	UPPER		MIDDLE	LOWER	MEMBER	THICKNESS	LITHOLOGY	
SERIES									
AGE		UPPER CYNOMURIAN-LOWER PLEURIAN							
FORMATION		BAKIRKOY FORMATION							
PERMIAN TRIASSIC							500 m		Limestone blocky metasediments
						Çoraklık Tepe Member	150 m		Arkosic quartz sandstone
						Kösrelilik Member	20 m		Red marl with brachiopod fragments
						Hacıkaşağı Member	50 m		Nodular limestone
						BEYTEPE MEMBER TURNAÇEŞME	100 m		Turbiditic sediments
							100 m		
							275 m		Red marl Limestone
							75 m		Pelagic limestone

Fig. 3: Stratigraphic section of the region (modified from [15])

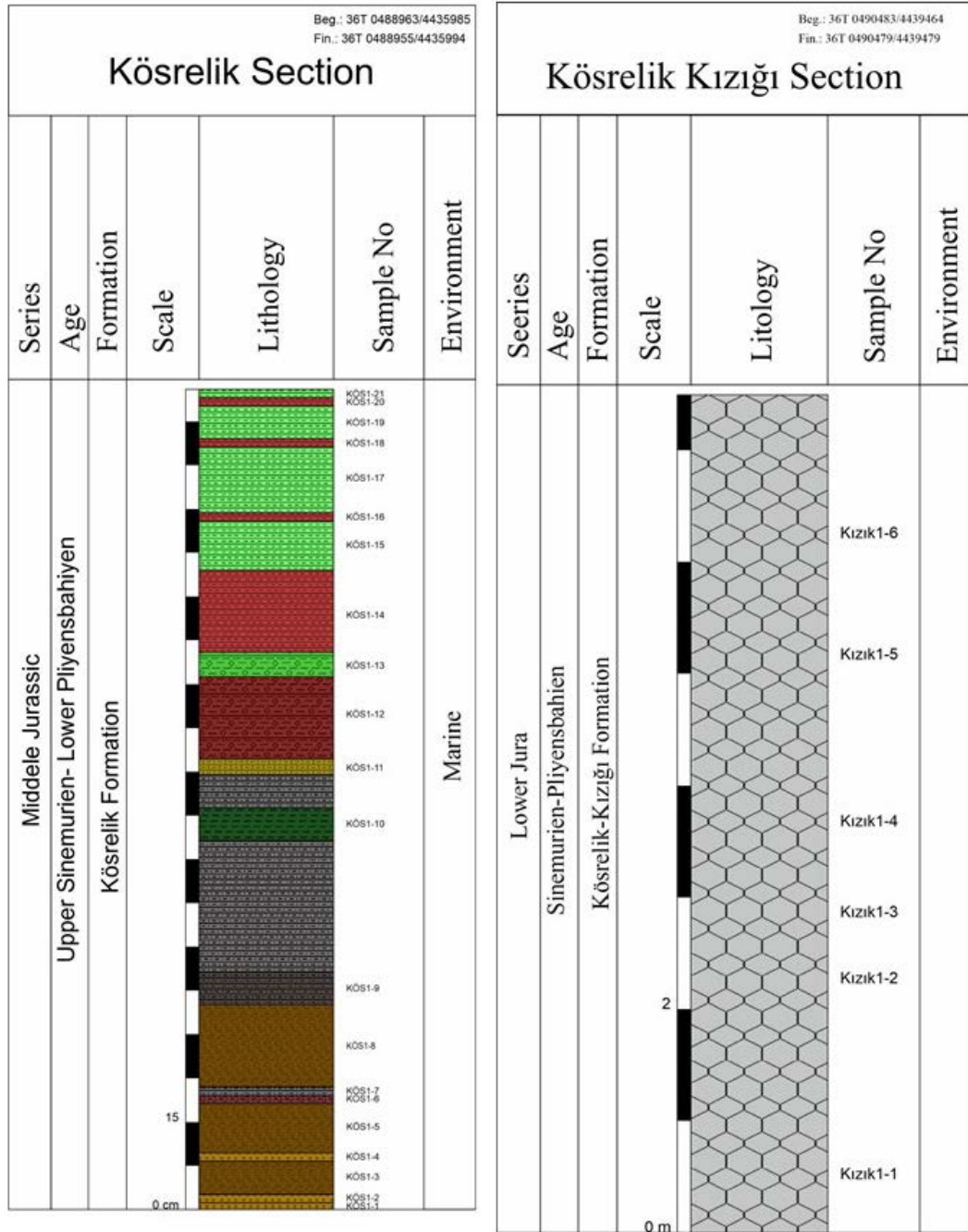


Fig. 4: Two measured stratigraphic sections measured in the study area: Kosrelük Section and Kosrelük Kızığı Section

ACKNOWLEDGMENT

We would like to express our gratitude to Merdan Atayev and Merve Cakmak for their valuable contributions to this study. Their diligent efforts and hard work during the fieldwork have significantly contributed to the success of this research.

REFERENCES

- [1] B. Akyurek, M. Duru, Y.F. Sutcu, I. Papak, F. Saroglu, N. Pehlivan, O. Gonenc, S. Granit, T. Yasar (1997). 1/100 000 ölçekli acinsama nitelikli Türkiye jeoloji haritaları, Ankara I29 paftası, MTA Jeoloji Etudleri Dairesi, Ankara, 35 s, 1997.
- [2] F. Alkaya, C. Meister, Liassic ammonites from the central and eastern Pontides (Ankara and Kelkit areas, Turkey), *Revue de Paléobiologie*, 14(1); 125-193. 1995.
- [3] G.E. Altinli, Inegol havzasinin jeolojisi ve hidrojeolojik incelemesi, *G.U. Fen Fak. Mecmuasi*, B, 28(3-4); 173-199, 1965.
- [4] N. Atasagun, Kosrelik-Kosrelik Kizigi-Memlik (KD Ankara) Bolgesi Jura-Kretase Yasli Cokellerin Sedimantolojisi , S.U. Fen Bilimleri Fakultesi, Konya, 2014.
- [5] A. Deli, Beytepe Koyu- Alacaatli-Etimesgut (GB Ankara) yoresinde Jura-Kretase cokellerin sedimantolojik ozellikleri, Selcuk Univ. Fen Bil. Enst. Doktora Tezi, Konya, 226, 2005.
- [6] A. Deli, H. Orhan, Alacaatli-Beytepe koyu (GB Ankara) bolgesinde yuzeyleyen Jura- Kretase yasli cokellerin stratigrafisi, *S.U. Muh.-Mim. Fak. Derg.*, 22(4); 61-80, 2007.
- [7] A. Delikan, N. Atasagun, Stratigraphic and Sedimentological Characteristics of Jurassic–Lower Cretaceous Sediments at Kosrelik–Kosrelikizigi (North of Ankara, Turkey), 2014.
- [8] A.Delikan, N. Atasagun, Facies characteristics of Jurassic–Lower Cretaceous successions at Kosrelik–Kosrelikizigi (North of Ankara, Turkey), *Carbonates Evaporites*, 33: 375–402, 2018.
- [9] A.Delikan, H. Orhan, Sedimentology of Jurassic pelagic carbonate platforms in the Ankara region (Central Anatolia-Turkey), *Facies*, 66: 1-21, 2020.
- [10] B.Korkmaz, Kosrelikizigi (Baglum/Ankara) Cevresinde Gozlenen Pliyensbahiye Yasli “Ammonitiko Rosso Fasiyesi” Ostrakoda Topluluğu, Hacettepe Universitesi, Fen Bilimleri Enstitusu Yuksek Lisans Tezi, 90s. 2018.
- [11] K.I. Kuznetsova, N.Y. Bragin, U.K. Tekin, A.I. Voznesensky, Jurassic foraminiferal assemblages from Ankara Region, Turkey an initial report 4th International Symposium an Eastern Mediterranean Geology, Isparta, Turkey, Proceedings, 123-138, 2001.
- [12] Y. Okan, I. Hosgor, Kosrelik (Ankara) Civarinda Ammonitiko Rosso Fasiyesinin Gec Sinemuriyen-Erken Pliyensbahiye Bivalvia, Gastropoda Faunasi ve Turkiye’de ilk kez Saptanan Annelid Turunun Varligi Paleocografik ve Paleoekolojik Ozellikleri, *MTA Dergisi*, 135: 19-29, 2007.
- [13] H. Ozkeles, Alacaatli-Beytepe ve Kosrelik (Ankara) cevresindeki mesozoyik yasli cokellerin stratigrafik ve paleontolojik verilerinin karsilastirmasi, (Master’s thesis, Fen Bilimleri Enstitusu), 2021.
- [14] B. Varol, E. Gokten, The facies properties and depositional environments of nodular limestones and red marly limestones (Ammonitico Rosso) in the Ankara Jurassic sequence central Turkey, *Terra Research*, 6: 64-71. 1994.

Comparison of Support Systems Used in Underground Mining

Kenan Ciftci¹, Zehra Funda Akbulut², Soner Guler,³

Abstract

The consolidation process to prevent the collapse of a hole opened in the mineral deposit is called support. In underground mining operations, underground galleries are opened due to works such as reaching the ore, determining the boundaries of the ore, and ore excavation. These galleries opened for production and preparation in underground mines, must maintain stability throughout production. For this purpose, temporary or long-term support systems are used. In recent years, with the development of equipment and materials, support systems with faster and simpler installation procedures, such as rock bolts, steel mesh, shotcrete, and cemented rock fill, have been used to manage more complex and more difficult underground excavations and control ground instability. These support systems are used in single or mixed form when the rock is weak or strong. In this study, a general evaluation of the advantages and disadvantages of underground support systems used in underground mining has been made.

Keywords: Underground mining, support systems, rock bolts, shotcrete, steel mesh

1. INTRODUCTION

The consolidation process to prevent the collapse of a hole opened in the mineral deposit is called fortification. Spaces such as galleries and wells are opened to carry out production in the mine. Support applications are carried out using materials such as wood, concrete, and steel to prevent loss of life and property in these gaps. Stress-induced rock breakage and collapse may occur in the gaps opened during underground mining works. To ensure the continuity of production in mining works, the instability of the underground spaces must be controlled. However, it is difficult to predict the formation of these soil behavior types that may occur due to stress in underground works, and special support systems have been developed to control them. When deciding on the soil support system in underground excavations, many parameters such as soil conditions, rock mass parameters, stress state, and the size and geometry of the underground excavation need to be evaluated. Because, in real field conditions, the ground and the acting forces can change. Therefore, it is not theoretically possible to design a complete support [1-4]. Accurate estimation of rock mass conditions is a major focus of the underground construction industry and tunneling efforts. However, most underground rock mass conditions are poorly known before construction. Therefore, analysis of rock mass conditions is mostly considered for the worst-case scenario.

In addition, if the uncertainties in rock mass conditions are well modeled and analyzed before construction begins, project costs and risks in excavation support selection can be significantly reduced.

In addition, the cost of the support element and the advantages and disadvantages of the support elements relative to each other are very important factors in the decision of the support element. Rock mass classification systems are used to select support in underground openings. Rock mass classification system; It emerges as a result of the statistical evaluation of measurements made on the rock mass, field data, and engineering experiences. The rock mass class must be known to determine which support system to choose in the

¹ Author: Van Yuzuncu University, Department of Geophysics Engineering, Tusba/Van, Turkey. muh.ciftickenan@gmail.com

² Corresponding author: Van Yuzuncu University, Department of Mining Engineering, Tusba/Van, Turkey. fundaakbulut@yyu.edu.tr

³ Author: Van Yuzuncu University, Department of Civil Engineering, Tusba/Van, Turkey. gulersoner@yyu.edu.tr

underground opening. In this way, the strength and deformation properties of the rocks in the environment can be compared [5-7].

2. UNDERGROUND SUPPORT SYSTEMS

2.1. Rock Bolts

Rock bolts are widely used in the civil and mining engineering industries to reinforce the rock mass around underground excavations. In underground excavations, rock studs connect the loose blocks that may fall from the ceiling and mirror walls to the solid ground. Rock studs are usually made of corrosion-resistant steel rods or cables [8]. Rock bolts must be strong to support the dead weight of loose and unstable rock blocks. Rock bolts can be used in both shallow and deep excavations. However, rock bolts used in shallow excavations are insufficient, as stress-induced rock failures such as rock explosion and rock compression occur more in deep excavations. Therefore, new rock bolts are required to deal with stress-induced instability problems at greater depths. Rock bolts can be classified into 3 groups according to their performance: strong, ductile, or energy-absorbing. Generally, rather short rock studs can be used in enterprises where solid rock units dominate or where relatively stable rock mass conditions are present [9].

Rock bolts are widely used in rock reinforcement design for their many advantages, such as versatility, flexibility, efficiency, cost, and ease of installation. Conventional rock studs can be exemplified in three categories: injected rock studs, inflatable rock studs, and expansion shell bolts. The structure of the stone is also very important in determining factors such as rock stud type, length, and mounting model in the selection of rock stud design [10].

Figure 1. Rock bolt application

2.2. Shotcrete

Shotcrete is widely used in engineering projects such as mines, railway tunnels, and subways to control the surrounding rock. Two methods are used for shotcrete, dry and wet. The high dust concentration produced in dry shotcrete application poses a great threat to workers' physical and mental health in the working environment. Wet spraying is a viable method of solving the dust problem. However, one of the disadvantages of this method is that it only affects the construction efficiency due to the rebound in the shotcrete process and causes a lot of material wastage [11-13].

Shotcrete is made after the shell cleaning process is carried out on the mirrors whose transportation has been completed. The purpose of this application is to prevent small pieces that may come from the mirror walls and to prevent the emergence of deterioration that will affect the strength depending on time by cutting the connection of the solid rock with the air. It is especially used in shotcrete pavements with dense rock studs in compacted soil conditions [14-16].



Figure 2. Shotcrete applications

2.3. Steel mesh

The increase in casualties due to accidents in our country in recent years has brought forward the importance of choosing suitable support systems according to the rock load by determining the optimum properties of steel fortifications that make up the footpaths and galleries in the mining sector of our country. The use of steel fortification systems such as steel mesh and steel arches as support elements has increased in recent years. It has increased the use of steel support systems in soil conditions where compression and swelling are problematic and when deep excavation is required [17], [18].

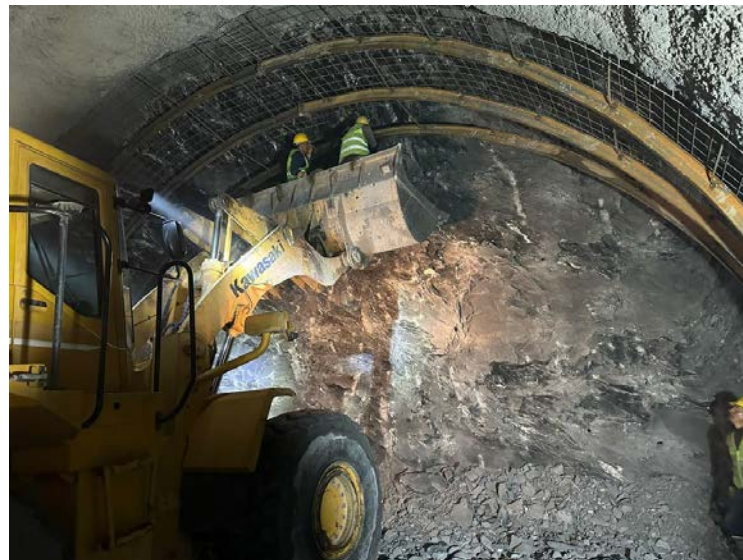


Figure 3. Wire mesh application

2.4. Cemented Rock Fill

The cemented rock fill method is another method used to support the galleries whose mining production has been completed. If production is to be carried out on a lower floor of the gallery whose production has been completed, the completed gallery is filled with a filler containing 8% cement. If the gallery's lower floor has been previously worked and filled with filler, this gallery is filled with filler containing 6% cement. The filling material is prepared above ground in the concrete plant, and the filling material prepared in the automatic mixer is sent underground by trucks. The filling is done by compressing the material with a construction machine.

One or more support systems can be used together to support the underground opening in an underground mine. For example, while shotcrete application is used alone in production galleries, reinforcement types such as steel mesh, rock stud, and shotcrete can be used together in wide openings and junctions. Especially since mines such as coal excavated in soft rock are subject to great deformation, combined support systems such as steel mesh, rock bolt, and shotcrete are used [19],[20].

CONCLUSION

This study compares methods used to support underground cavities, such as shotcrete, rock studs, steel mesh, and cement fill. The study shows that rock studs, steel mesh, and shotcrete applications are used together to support the cavities opened in underground excavations, depending on whether the rock is strong or weak. In addition, it has been determined that issues such as working environment safety and cost are extremely important in selecting these methods.

ACKNOWLEDGMENT

This study is supported by the Department of Scientific Research Projects of the University of Van Yuzuncu Yil, Van, Turkey, with the project ID: FYL 2023-10640.

REFERENCES

- [1]. I. Kilerci, A. Bassullu, B. Onder, & I.P.E.K. Onur, (2019). Trapez Kesitli Rijit Celik Tahkimatlarda Kullanilan Celik Profillerin Yuke Uygun Sekilde Seciminin Sonlu Elemanlar Metodu Destekli Olarak Incelenmesi. *Scientific Mining Journal*, vol. 58(3), 229-238.
- [2]. M. Ghorbani, K. Shahriar, M. Sharifzadeh, & R. Masoudi, (2020). A critical review on the developments of rock support systems in high stress ground conditions. *International Journal of Mining Science and Technology*, 30(5), 555-572.
- [3]. L. Chen, P. Li, G. Liu, W. Cheng, & Z. Liu, (2018). Development of cement dust suppression technology during shotcrete in mine of China-A review. *Journal of Loss Prevention in the Process Industries*, 55, 232-242.
- [4]. L. Malmgren, & E. Nordlund, (2008). Interaction of shotcrete with rock and rock bolts—a numerical study. *International Journal of Rock Mechanics and Mining Sciences*, 45(4), 538-553.
- [5]. M. Kanik, & Z. Gurocak, (2018). Kazi Derinliginin Puskurtme Beton Dayanimi Uzerindeki Etkisi: Sayisal Bir Yaklasim. *Gumushane Universitesi Fen Bilimleri Dergisi*, 8(1), 63-74.
- [6]. C. Agan, & S. Erturk, (2017). Turkiye'nin uzun sulama tuneli Suruc Tunesinde geoteknik ve tahkimat tasarimlari. *Teknik Dergi*, 28(3), 7897-7926.
- [7]. E. Hoek, & D. Wood, (1989). Rock support. *World Tunnelling and Subsurface Excavation*, 2(2).
- [8]. O. Aydan, (2019). Dynamic response of support systems during excavation of underground openings. *Journal of Rock Mechanics and Geotechnical Engineering*, 11(5), 954-964.
- [9]. S. Wu, H. Chen, H.L. Ramadi, P. Hagan, B. Hebblewhite, A. Crosky, S. Saydam, Investigation of cable bolts for stress corrosion cracking failure. *Construction and Building Materials* 2018;187:1224e31
- [10]. A. Lisjak, T. Young-Schultz, B. Li, L. He, B.S.A. Tatone, & O.K. Mahabadi, (2020). A novel rockbolt formulation for a GPU-accelerated, finite-discrete element method code and its application to underground excavations. *International Journal of Rock Mechanics and Mining Sciences*, 134, 104410.
- [11]. L. Chen, Z. Sun, G. Liu, G. Ma, & X. Liu, (2022). Spraying characteristics of mining wet shotcrete. *Construction and Building Materials*, 316, 125888.
- [12]. I. Galan, A. Baldermann, W. Kusterle, M. Dietzel, F. Mittermayr, Durability of shotcrete for underground support-Review and update, *Constr. Build. Mater.* 202 (2019) 465–493, <https://doi.org/10.1016/j.conbuildmat.2018.12.151>.
- [13]. J.Armengaud,G.Casaux-Ginestet,M.Cyr,B.Husson,M.Jolin,Characterizationof fresh dry-mix shotcrete and correlation to rebound, *Constr. Build. Mater.* 135 (2017) 225–232, <https://doi.org/10.1016/j.conbuildmat.2016.12.220>.
- [14]. Y. LIU, Y. GUO, H. LI, et al., Experimental study on effect of recycled aggregate from construction waste on conveying performance of mine filling paste, *Journal of Shandong University of Science and Technology (Natural Science)* 3 (2020) 59–65.

- [15]. I. Galan, A. Baldermann, W. Kusterle, M. Dietzel, & F. Mittermayr, (2019). Durability of shotcrete for underground support–Review and update. *Construction and Building Materials*, 202, 465-493.
- [16]. A.H. Thomas, & R.H. Dimmock, (2018, June). The design philosophy for permanent sprayed concrete linings. In *Proceedings of the International Symposium on Sprayed Concrete*, Trondheim, Norway (pp. 11-14).
- [17]. E. Komurlu, & A. Kesimal, (2013). Gecmisten gunumuze tunelcilik ve tahkimat malzemeleri. *Madencilik*, 52, 33-47.
- [18]. V.M. de Alencar Monteiro, & F. de Andrade Silva, (2021). On the design of the fiber reinforced shotcrete applied as primary rock support in the Cuiabá underground mining excavations: A case study. *Case Studies in Construction Materials*, 15, e00784.
- [19]. H. Jiang, M. Fall, Y. Li, & J. Han, (2019). An experimental study on compressive behaviour of cemented rockfill. *Construction and Building Materials*, 213, 10-19.
- [20]. B.A. Sainsbury, S. Gharehdash, & D. Sainsbury,(2021). Large-scale characterisation of cemented rock fill performance for exposure stability analysis. *Construction and Building Materials*, 308, 124995.

Effect of air-entraining admixture usage rate on dynamic yield stress and viscosity in Portland cement systems containing urea

Oznur Biricik¹, Neslihan Caparoglu², Ali Mardani³

Abstract

Air-entraining admixtures added to cementitious systems in order to increase freeze-thaw resistance also affect the fresh state properties of the mixture. In this study, the effect of the use of air-entraining admixtures on the rheological properties of urea-containing Portland cement systems was investigated. For this purpose, 3 different paste mixtures were prepared by adding 0.15% and 0.30% air-entraining admixtures to the control mixture containing 3% urea instead of cement. The dynamic yield stress and viscosity values of the prepared mixtures were determined in accordance with the Herschel Bulkley model. It was determined that the dynamic yield stress values of the paste mixtures increased and the viscosity values decreased with the use of air-entraining admixtures. It was understood that this behavior became more evident with the increase in the use of admixtures.

Keywords: Viscosity, flowability, loop test, thixotropy, air entraining admixture

1. INTRODUCTION

Concrete exposed to many environmental influences such as freeze-thaw [1], impact [2], abrasion and cavitation [3], high temperature [4], alkali silica effect [5], sulfate effect [6], corrosion [7], acid effect [8] and alkali-carbonate reaction [9]. In order for the concrete to serve for many years, it must be protected from these effects. Destructions occur in concrete structures exposed to the freeze-thaw cycle. The reason for this destruction is that the water leaking into the various voids in the concrete structure turns into ice at low temperature, while the volume expands by 9% [10]. One of the measures to be taken to reduce the freeze-thaw effect is to ensure impermeability and the other measure is to increase the freeze-thaw resistance of concrete by using air-entraining chemical admixtures (AEA) [11,12]. As a result of using AEA, air bubbles varying between 10 μm and 1 mm are formed [13]. These air bubbles both prevent capillary water absorption and prevent the pressure exerted on the walls by the ice mass formed by the freezing water [14]. The effect of the use of air-entraining admixtures on the fluidity properties, strength and durability performance of concrete was investigated by various researchers.

In a study conducted by Yalcinkaya and Yazici [15], it was stated that the fluidity of the concrete mixture increased, but the compressive strength decreased with the use of air-entraining admixtures. In another study by Atas [16], it was reported that the use of inorganic-based air-entraining admixtures increased the compressive and flexural strength of the mortar mixture by 5% and 8%, respectively. It was emphasized that this is due to the fact that the admixture in question entrains less air and improves the flow performance of the mixture, preventing the formation of irregular air spaces. However, it was declared that the strength performance of the mixture is seriously adversely affected due to the addition of fatty alcohol and ammonium salt-based air-entraining admixtures and the greater amount of air entrainment.

In a study by Guleryuz et al. [17], the effect of adding 0.5% AEA to a mortar mixture containing 30% fly ash (FA) and 10% silica fume (SF) instead of cement on the freeze-thaw resistance, water absorption and compressive strength of the mixture was investigated. It was emphasized that the consistency, workability, permeability

¹ Department of Civil Engineering, Faculty of Engineering, Bursa Uludag University, Bursa, Turkey, oznurbiricik@uludag.edu.tr, 0000-0003-4884-7350

² Department of Civil Engineering, Faculty of Engineering, Bursa Uludag University, Bursa, Turkey, neslihanaparoglu@gmail.com, 0009-0009-9467-616X

³ Corresponding author: Department of Civil Engineering, Faculty of Engineering, Bursa Uludag University, Bursa, Turkey, ali.mardani16@gmail.com/alimardani@uludag.edu.tr, 0000-0003-0326-5015

properties and resistance to freeze-thaw of the mixture were positively affected by the addition of air-entraining admixtures. In the study conducted by Kodak [18], it was reported that the compressive strength of the self-compacting concrete mixture decreased with the addition of 0.1% air-entraining admixture, but the flow performance increased. In the study carried out by Ozerkan [19], the effects of air-entraining admixtures (0%, 0.15%, 0.3%) and fly ash (15%, 30% and 45%) on the flow performance and freeze-thaw resistance of self-compacting concrete mix were investigated. In the study, a software was developed by basing the air gap parameters of the concrete on the image analysis of the concrete surface. With the developed method, it was used to determine the air void parameters of self compacting concrete and to determine the strength effect of these parameters in freeze-thaw cycles. At the end of the study, it was stated that if the void factor value used in the evaluation of freeze-thaw resistance is less than 0.4, the void factor should not be limited to 0.2, since it can maintain its resistance to freeze-thaw. It was reported that the lowest freeze-thaw resistance was measured in the mixture without air entrainment and with the maximum fly ash content (45%). It has been declared that the highest freeze-thaw resistance is observed in the mixture that does not contain air-entraining and contains 30% fly ash, and mixtures containing 0.15% air-entraining and 45% fly ash. It was determined that the fluidity of the mixture increased with the use of air-entraining admixtures and this effect decreased with the increase in the use of fly ash. In the study by Sahin [20], effect of the use of air-entraining admixtures with 6 different chemical properties (neutralized vinsol resin, neutralized colophon resin, fatty alcohol and ammonium salt, fatty alcohol derivative, sodium salts mixture, synthetic) on the freeze-thaw damage of concrete mixtures under experimental conditions with different freezing rates was investigated. In non-air-entrained concretes, mixtures with an W/C ratio of 0.55 suffered flaking damage under all test conditions. On the other hand, the mixture with low W/C (0.40) ratio was damaged under standard freezing cycle and long freezing time conditions. It was determined that the flaking value remained below the damage criterion in fast freezing speed and slow freezing speed conditions. Air-entrained concretes, on the other hand, indicated that they provided sufficient performance under all test conditions. With the decrease of plastic viscosity values of concrete mixtures, the amount of air obtained decreased. In mixtures where the viscosity of the concretes increased over time, the amount of air decreased over time, regardless of the chemical basis of the air-entraining admixture.

As it is understood from the literature, it is very important to investigate the effect of air-entraining admixtures added to increase the freeze-thaw resistance in cementitious systems on fluidity. It was reported by Mardani-Aghabaglou [21] that the flow performance of mixtures can be directly determined by rheological parameters such as shear stress and viscosity.

In the literature, there are some studies stating that the freeze-thaw resistance of mixtures increases with the use of urea, which is an industrial product [22]. In a study conducted by Demirboga [22], the compressive strength of mixtures prepared with urea was examined by exposing them to temperatures of -5, -10, -15 and -20 °C. As a result of the study, it was reported that the use of urea increased the compressive strength of the concrete mixture at -5 °C, but had no effect at lower temperatures. In another study, the effect of the use of antifreeze admixtures on the mechanical properties of concrete mixtures containing urea and calcium nitrate, exposed to cold weather conditions while fresh, was investigated by Polat [23]. Decreases were observed in the compressive strength of mixtures containing urea. It is understood from the literature that studies on the effect of urea use on the mechanical and durability performance of mixtures were conducted [22,23]. However, no study has been found on the effect of using urea and air-entraining admixture together on the rheological properties of cementitious mixtures. In this study, the effect of air-entraining admixture usage rate on dynamic yield stress and viscosity values of urea-containing portland cement systems was investigated. For this purpose, paste mixtures were prepared by adding different dosages of air-entraining admixture to the control mixture containing 3% urea instead of cement. The rheological properties of the mixtures were measured in accordance with the Hershel Bulkley model.

2. MATERIAL and METHOD

2.1. Materials

Within the scope of the study, CEM I 42.5R type cement (PC) produced by Bursa Cement was used. The chemical component, physical and mechanical properties of the cement supplied by the manufacturer are summarized in Table 1. Some properties of the urea and air-entraining admixture supplied by the manufacturer are presented in Table 2.

Table 1. Chemical composition and physical properties of cement

Oxide	(%)	Mechanical and physical properties		
SiO ₂	18.74	Compressive strength (MPa)	1-Day	2.43
Al ₂ O ₃	5.37		28-Day	39.3
Fe ₂ O ₃	3.04	Setting Time (min)	Initial	201
CaO	64.11		Final	321
MgO	1.21	Fineness	Blaine specific surface (cm²/g)	3600
Na ₂ O	0.34		Residual on 0.090 mm sieve (%)	0.4
K ₂ O	0.62		Residual on 0.045 mm sieve (%)	7.4
SO ₃	2.68		specific gravity	3.15
Cl	0.038	Volume expansion (mm)		<1

Table 2. Some properties of urea and air-entraining admixture

Admixture	Density (g/cm ³)	pH	Colour	Physical Condition	Melting point (°C)	Solids Ratio (%)
(CO(NH ₂) ₂)	1.32	9	White	Solid	133	-
AEA*	1.01	4.66	Transparent	Liquid	-	3.91

* Air entraining admixture

2.2. Mixture proportion

Within the scope of the study, control paste mixes with a water/cement ratio of 0.36 and containing urea at a rate of 3% by weight of cement were produced. By adding 0.15% and 0.30% of the total weight air-entraining admixture to the control mixture, 2 more batches of paste mixture were prepared. The denotation of the mixtures was made according to the use of air-entraining admixtures. For example, the control mixture without air-entraining admixtures is shown as PC-0%. The paste mixture containing 0.15% of the total weight of air-entraining admixtures was denoted PC-0.15%.

After urea and water were mixed at 62 rpm for 30 seconds, cement was added and mixed at the same speed for another 30 seconds. Then, air-entraining admixture was added and mixed at 62 rpm for 30 seconds. The parts of the mixture adhering to the bowl were cleaned with the help of a spatula and homogeneous mixing was ensured. Then, the mixture was taken into a rheometer measuring cup by mixing at 125 rpm for 120 seconds.

2.3. Test methods

The method followed in determining the dynamic yield stress and viscosity values of paste mixtures prepared within the scope of the study is explained in detail in Figure 1. In addition, the shear stress-shear rate and viscosity-shear rate graphs of the control mixture are shown in Figure 1 as an example.

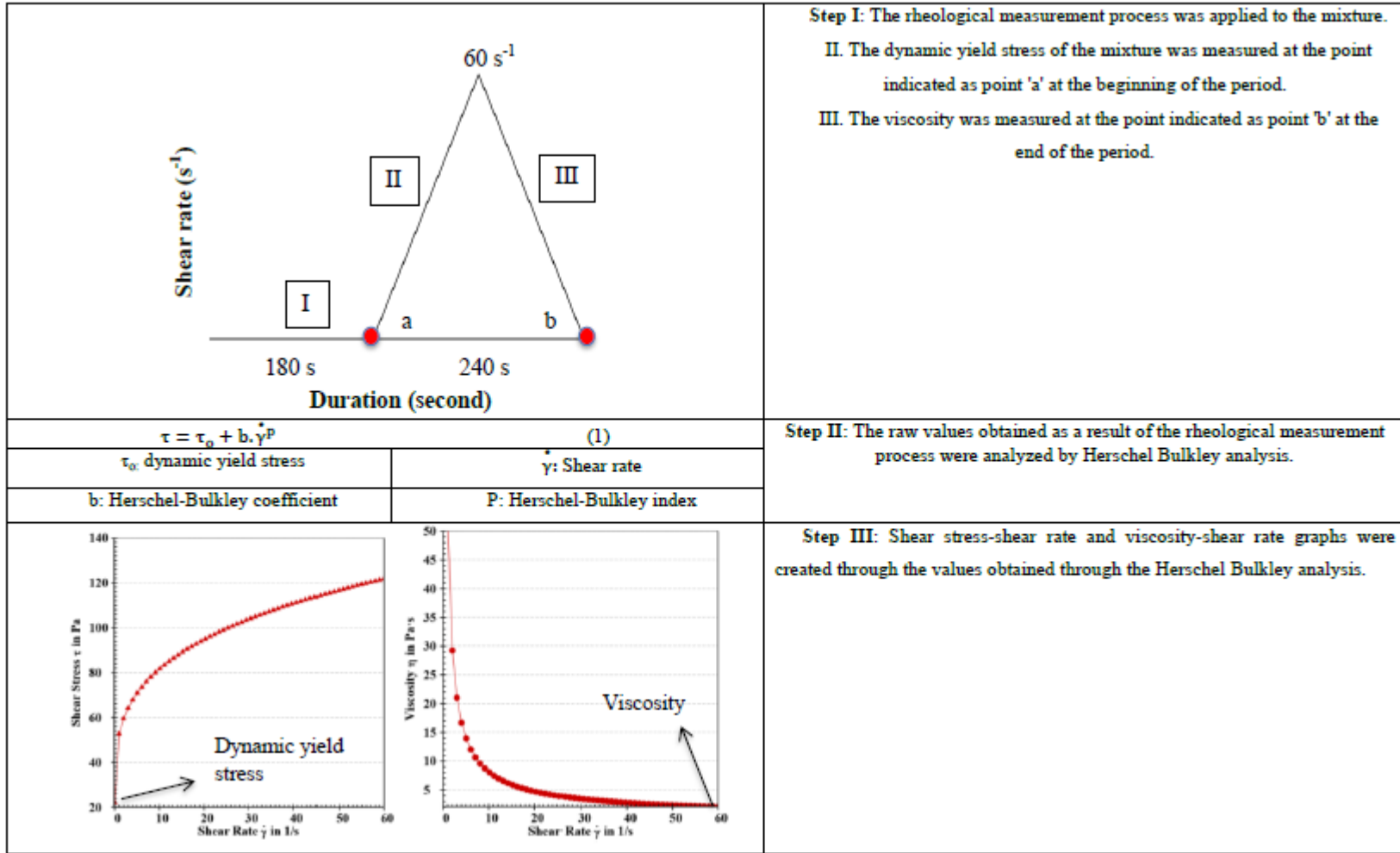


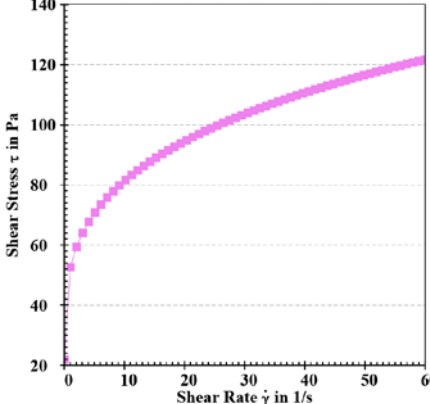
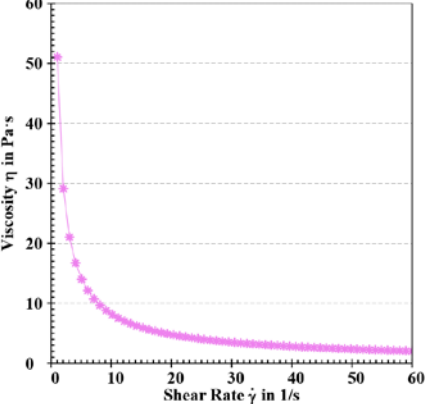
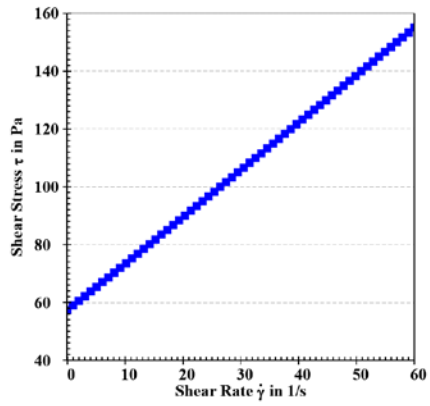
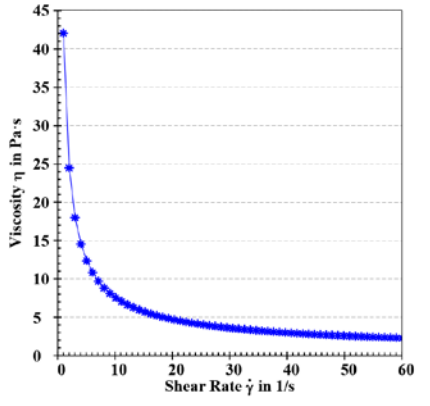
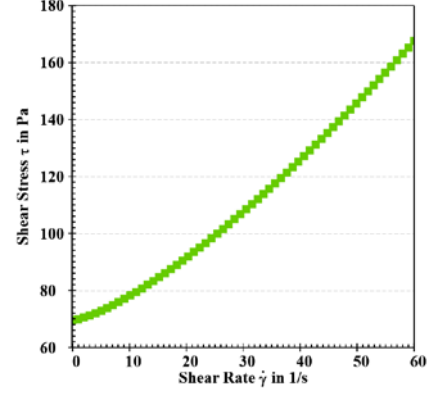
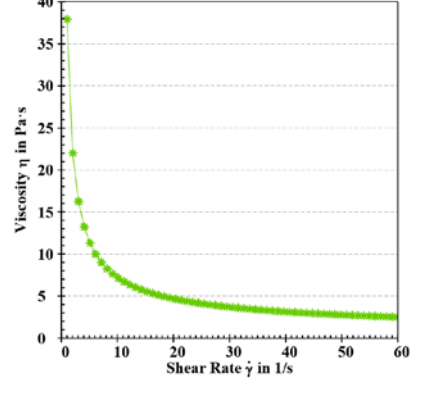
Fig. 1. Determination of dynamic yield stress and viscosity values of paste mixes

3. DISCUSSION AND CONCLUSION

The dynamic yield stress and viscosity values of the mixtures are given in Table 3. As seen in Table 3, a 1.6-fold increase in dynamic yield stress value was observed with the addition of 0.15% air-entraining admixture in cement paste mixtures containing urea. In the case of 0.30% air-entraining admixture use, the dynamic yield stress value increased by 215% and 21%, respectively, compared to the mixtures using 0% and 0.15% air-entraining admixtures. Similar results were reported by other researchers for urea-free mixtures [24-27]. Huang et al. [27], the effect of the combined use of polycarboxylate-based water-reducing admixture, rosin resin-type air-entraining admixture and powder viscosity-regulating admixture on the rheological properties of self-compacting concrete mixture was investigated. It was stated that the addition of air-entraining admixture causes an increase in the yield stress of the mixture and a decrease in the plastic viscosity, while weakening the shear-thickening behavior due to the high air content. It was emphasized that when the air content reaches 8.7%, shear thickening behavior completely disappears and shear thinning behavior occurs.

As can be seen from Table 3, an 18% decrease in viscosity value was measured by adding 0.15% air-entraining admixture to cement paste mixtures containing urea. In the case of 0.30% air-entraining admixture use, the viscosity value decreased by 26% and 10%, respectively, compared to mixtures using 0% and 0.15% air-entraining admixtures. Similar results for urea-free mixtures were reported by other researchers [28-32], it was reported that the plastic viscosity values of concrete mixtures containing recycled concrete aggregate using air-entraining admixtures decreased.

Table 3. Rheological measurement results of paste mixtures

Mixture	Dynamic Yield Stress (Pa)	Viscosity (Pa.s)
PC-0%	 <p>22.1</p>	 <p>51.1</p>
PC-0.15%	 <p>57.5</p>	 <p>42.0</p>
PC-0.30%	 <p>69.6</p>	 <p>37.9</p>

4. CONCLUSION

The results obtained in line with the materials used and the methods applied within the scope of the study are presented below.

- In cement paste mixtures containing urea, the dynamic yield stress values increased with the use of air-entraining admixtures and the increase in the usage rate.
- In cement paste mixtures containing urea, the viscosity values decreased with the use of air-entraining admixtures and the increase in the usage rate.

Data Availability Statement

All data, models, and code generated or used during the study appear in the submitted article.

Funding

This research did not receive any specific grant from funding agencies in the public, commercial, or not-for-profit sectors.

Conflicts of Interest/Competing Interests

The authors declare that they have no known competing financial interests or personal relationships that could have appeared to influence the work reported in this paper.

Acknowledgments

The authors appreciate contributions of the Bursa Uludag University Science and Technology Centre (BAP) under grant numbers FHIZ- 2022-1165. In addition, the authors would like to acknowledge Bursa Cement Factory, Polisan A.S. for their kind assistance in providing the cements, air entraining admixture as well as determining the technical properties of these products.

REFERENCES

- [1]. Akcaozoglu, K., & Guldur, S. E. (2017). The Investigation of the Effect of Micronized Calcite and Fly Ash Addition on the Concrete Properties. *Afyon Kocatepe University Journal of Science and Engineering Sciences*, 17(2), 658-668. (In Turkish).
- [2]. Alkayis, M. H., & Basyigit, C. (2021). Effect of Fiber Additive on Concrete Impact Strength *European Journal of Science and Technology*, (24), 455-462.
- [3]. Baradan, B., and Aydin, S. (2013). Betonun Durabilitesi, *Hazir Beton Kasim-Aralik 2013 Makale Article*.
- [4]. Topcu I.B. ve Demir. A., 2007, Yuksek Sicaklik Uygulama Suresinin Harc Ozelliklerine Etkisi, *Ulusal Beton Kongresi, Sakarya Insaat Muhendisleri Odasi*.
- [5]. Ramyar. K., (2013). Betonda Alkali-Silis Reaksiyonu, *Hazir Beton Kasim-Aralik 2013 Article Makale*.
- [6]. Ilica. T., (2008). Farkli Cimentolarla Uretilen Betonlarda Sulfat Etkisi ve Klorur Gecirirmliligi, *Istanbul Teknik Universitesi Fen Bilimleri Enstitusu Insaat Muhendisligi Bolumu Yapı Anabilim Dalı Yuksek Lisans Tezi, Istanbul*.
- [7]. Yavuz. R., Gunaydin. O. ve Gucluer. K., (2019). Donatili Betonda Korozyon ve Aderansin Arastirilmesi, *KSU Muhendislik Bilimleri Dergisi*, 22, Ozel Sayi, 2019 *KSU J Eng Sci*, 22, Special Issue, 2019 *Uluslararası İleri Muhendislik Teknolojileri Sempozyumu (ISADET)*.
- [8]. Yurt. U., Dundar B. ve Cinar. E., (2020). Jeopolimer Betonlarda Sulfurik Asit Etkisinin Arastirilmesi, *Duzce Universitesi Bilim ve Teknoloji Dergisi Arastirma Makalesi*.
- [9]. Mather, B., (2004). *Concrete Durability. Cement and Concrete Composites*, 26: 3-4
- [10]. Baradan, B., Turkel. S., Yazici. H., Un. H., Yigiter. H., Felekoglu. B., Tosun. K., Aydin. S., Yardimci. Y.M., Topal. A., Ozturk AU. (2012). *Beton. Izmir, Turkiye, Dokuz Eylul Universitesi Muhendislik Fakultesi Yayinlari*.
- [11]. Snyder. KA., (1998). "A numerical test of air void spacing equations". *Advanced Cement Based Materials*, 8, 28-44.

- [12]. Sahin H.G., Mardani, A., Ozen S. & Emin, A., (2022). Utilization of high-range water reducing admixture having air-entraining agents in cementitious systems. *Journal of Building Engineering*, 105565.
- [13]. Erzengin. G., (2010). Kimyasal Katkilarin Cimento Bazli Malzemelerin Dayanimina, Reolojisine ve Mikro Yapısına Etkileri, Ankara Universitesi Fen Bilimleri Enstitusu Kimya Muhendisligi Anabilim Dalı Doktora Tezi, Ankara.
- [14]. Neville AM., (1997). *Properties of Concrete*. London, England, John Wiley & Sons Inc.
- [15]. Yalcinkaya. C. ve Yazici., H., (2009). Hava Surukleyici Katkinin Kendiliginden Yerlesen Celik Lifli Betonun Islenebilirliğine ve Basinc Dayanimina Etkisi
- [16]. Atas, Z. (2013). Investigation of Mechanical Behavior of Cement Mortars Containing Air Entraining Agent and Fibers Under Freeze-thaw Effect, Gumushane University Institute of Science and Technology (Master Thesis) (In Turkish).
- [17]. Guleryuz. E., Ozen. S. ve Aghabaglou. A.M., (2020). Mineral Katki Kullaniminin Hava Surukleyici Katkili Cimentolu Harclarin Taze ve Sertlesmis Hal Ozeliklerine Etkisi, Pamukkale Universitesi Muhendislik Bilimleri Dergisi.
- [18]. Kodak. I., (2019). Hava Surukleyici ve Ucucu Kul Katkilarinin Kendiliginden Yerlesen Betonun Islenebilirliğine ve Basinc Dayanimina Etkisi, Kutahya Dumlupinar Universitesi Fen Bilimleri Enstitusu Yuksek Lisans Tezi.
- [19]. Ozerkan. N., (2009). Evaluation of Air Void Parameters of Fly Ash Incorporated Self Consolidating Concrete by Image Processing, Middle East Technical University in Partial Fulfillment of The Requirements for The Degree of Doctor of Philosophy in Civil Engineering.
- [20]. Sahin. Y., (2013). Characterization of Air Entraining Admixture and Effect of Test Conditions on Freezing-Thawing Damage of Concrete, Istanbul Technical University Institute of Science and Technology Thesis (PhD).
- [21]. Mardani-Aghabaglou. A., (2016). Portland Cimentosu ve Superakiskanlastirici Katki Uyumunun Incelenmesi, Ege Universitesi Fen Bilimleri Enstitusu Insaat Muhendisligi Anabilim Dalı Doktora Tezi, Izmir.
- [22]. Demirboga. R., Karagol. F., Polat. R. and Kaygusuz. M.A., (2014). The effects of urea on strength gaining of fresh concrete under the cold weather conditions, *Construction and Building Materials*, 64(2014)114-120
- [23]. Polat. R., (2016). The effect of antifreeze additives on fresh concrete subjected to freezing and thawing cycles, *Cold Regions Science and Technology*, 127 (2016) 10–17
- [24]. Rahman, M. A., & Nehdi, M., (2003). Effect of geometry, gap, and surface friction of test accessory on measured rheological properties of cement paste. *Materials Journal*, 100(4), 331-339.
- [25]. Struble, L. J., & Jiang, Q., (2004). Effects of air entrainment on rheology. *Materials Journal*, 101(6), 448-456.
- [26]. Łażniewska-Piekarczyk. B., (2013). The influence of chemical admixtures on cement hydration and mixture properties of very high performance self-compacting concrete. *Construction and building materials*, 49, 643-662.
- [27]. Huang. F., Li. H., Yi. Z., Wang. Z., & Xie. Y., (2018). The rheological properties of self-compacting concrete containing superplasticizer and air-entraining agent. *Construction and Building Materials*, 166, 833-838.
- [28]. Szwabowski, J., & Łażniewska-Piekarczyk, B., (2008). The increase of air content in SCC mixes under the influence of carboxylate superplasticizer. *Cement Wapno Beton*, 4, 205-215.
- [29]. Tattersall G. H., Banfill P. F., (1983). *The rheology of fresh concrete*.
- [30]. K.-K. Yun, S.-Y. Choi, J.H. Yeon., (2015). Effects of admixtures on the rheological properties of high-performance wet-mix shotcrete mixtures, *Constr. Build. Mater.* 78 (2015) 194–202
- [31]. X. Zhang, H. Zhang, H. Gao, Y. He, M. Jiang, (2019). Effect of bubble feature parameters on rheological properties of fresh concrete, *Constr. Build. Mater.* 196 (2019) 245–255.
- [32]. Bizinotto. M.B., Faleschini. F., Fernández. C.G.J., Hernández. D.F.A., (2017). Effects of chemical admixtures on the rheology of fresh recycled aggregate concretes, *Construction and Building Materials*, 151 (2017) 353–362

Benthic Foraminiferal Fossils: Indicators and Tracers of Climate Change

*Kubra Yayan*¹

Abstract

*Climate change is one of the most pressing environmental issues of our time, and its effects on the Earth's ecosystems are of great concern to scientists and policymakers alike. Benthic foraminiferal fossils are increasingly recognized as important tools for studying the impact of climate change on the marine environment. As sessile organisms, benthic foraminifera are highly sensitive to changes in their environment, and their fossilized remains provide a record of past environmental conditions. In this study, we review the current state of knowledge regarding the use of benthic foraminiferal fossils as indicators and tracers of climate change. We discuss the various factors that affect the abundance and diversity of benthic foraminiferal communities, including changes in water temperature, salinity, and oxygen levels. We also examine the role of benthic foraminiferal fossils in reconstructing past sea level changes, ocean circulation patterns, and sedimentary environments. Fossilized foraminifera have been used as important indicators of environmental change in the Paleogene and Neogene periods. Alveolinids, such as *Alveolinella quoyi* and *Alveolinella hanai*, are indicative of warm, shallow water environments, while *Nummulites*, particularly the species *Nummulites fichteli*, are associated with high-energy, shallow water environments. *Orbitolites*, including *Orbitolites complanatus* and *Orbitolites media*, are commonly found in reef and lagoon settings and are also indicative of warm, shallow water environments. These fossilized foraminifera provide valuable information about past environmental conditions and can be used to better understand the impact of climate change on marine ecosystems. Finally, we highlight the potential of benthic foraminiferal fossils as tools for predicting future climate change impacts on marine ecosystems. Our study underscores the importance of benthic foraminiferal fossils in understanding the impact of climate change on the marine environment, and provides a foundation for further research in this field.*

Keywords: Benthic Foraminiferas, climate change, fossils, paleoecology

1. INTRODUCTION

Benthic foraminifera are marine single-celled organisms that live on the seafloor (Fig. 1), and their fossil records have been extensively used as a tool to study the paleoenvironmental changes over the geological timescale. Their fossil shells provide valuable information on various aspects of paleoceanography such as temperature, salinity, oxygen levels, and water depth ([5], [9]). In recent decades, global climate change has become a major topic of concern, and benthic foraminifera fossils have been increasingly used to study the past and present climate changes and their impacts on the marine ecosystems (e.g. [3]).

The potential of benthic foraminifera as indicators and proxies of climate change lies in their sensitivity to environmental parameters, which is reflected in their morphological, ecological, and geochemical characteristics ([3], [9]). For example, the assemblage composition and diversity of benthic foraminifera can reflect changes in water depth, substrate, and productivity (e.g. [5]). The oxygen isotopic composition of their shells is used to reconstruct past changes in seawater temperature and salinity (e.g. [3], [9]), while the carbon isotopic composition can provide information on the carbon cycle and productivity. In addition, the trace element and heavy metal contents of foraminiferal shells have been used as indicators of environmental pollution (e.g. [3]).

¹ Corresponding author: Eskisehir Osmangazi University, Department of Geological Engineering, 26048, Meselik/Eskisehir, Turkey. kokur@ogu.edu.tr

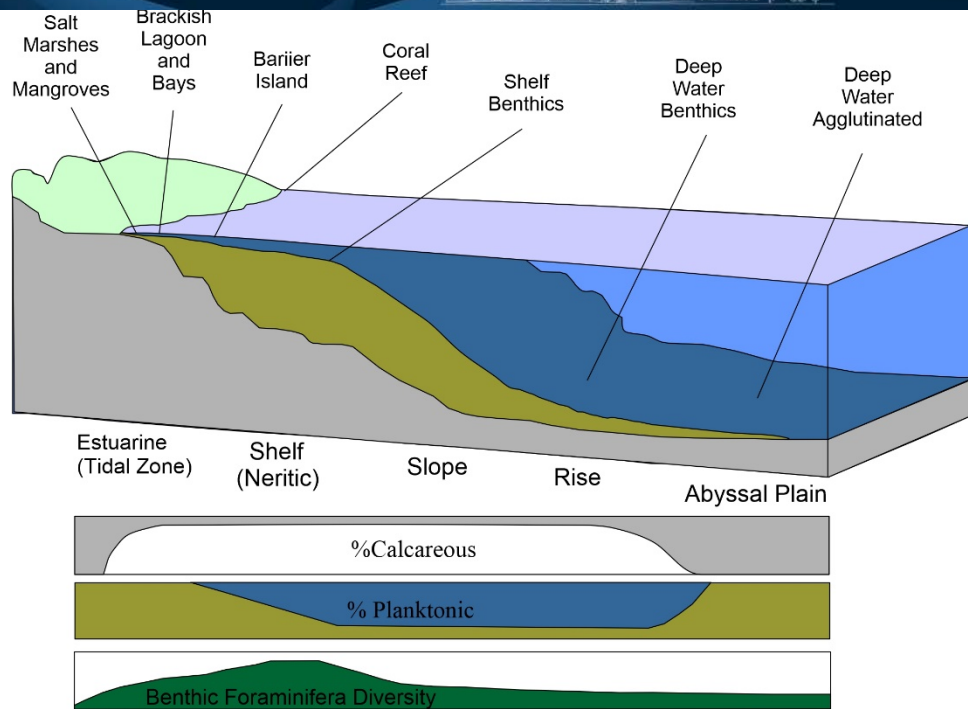


Fig. 1: Paleoenvironmental reconstruction of modern Foraminifer assemblages (Modified by [4])

Therefore, benthic foraminifera fossils hold a great potential as a tool to understand the past and present climate changes and their effects on the marine ecosystems. This review aims to provide an overview of the current state of research on the use of benthic foraminifera fossils as climate proxies, and to highlight their potential and limitations as indicators of environmental change. By synthesizing the existing literature, we aim to provide a comprehensive and critical evaluation of the methods and applications of benthic foraminifera in paleoenvironmental reconstructions.

2. LITERATURE REVIEW

Foraminifera are single-celled eukaryotic organisms that are abundant in marine environments and are important paleoenvironmental proxies due to their sensitivity to environmental changes. The use of foraminifera as proxies for paleoenvironmental reconstruction has a long history, dating back to the 19th century. Among foraminifera, benthic foraminifera are particularly useful for paleoenvironmental reconstruction because they inhabit the benthic zone and are sensitive to environmental changes such as temperature, salinity, and water depth ([15]).

Benthic foraminifera have been used to reconstruct past climate change for several decades, including in the North Atlantic, Mediterranean Sea ([11]), and the Southern Ocean ([7]). Studies have shown that changes in benthic foraminifera assemblages can be linked to changes in sea level, ocean circulation, temperature, and food supply ([5]).

Recent advances in microfossil analysis techniques, such as scanning electron microscopy and X-ray computed tomography, have allowed for more detailed analysis of benthic foraminifera fossils and have led to new

insights into past climate change ([2]). In addition, molecular approaches have been used to investigate the genetic diversity of benthic foraminifera and their responses to environmental changes.

Overall, benthic foraminifera fossils have proven to be valuable paleoenvironmental proxies for studying past climate change, and continued research in this field holds promise for improving our understanding of how the Earth's climate system operates over long timescales.

3. THE IMPORTANCE OF BENTHIC FORAMINIFERA IN UNDERSTANDING CLIMATE CHANGE

Benthic foraminifera are single-celled organisms that live on the ocean floor and are widely used as bioindicators for paleoenvironmental (Fig. 2) reconstructions. The abundance, diversity, and morphology of benthic foraminifera are closely related to environmental conditions, especially water temperature, salinity, and substrate composition. Therefore, the study of benthic foraminifera provides a unique opportunity to reconstruct past climate changes and to predict future climate scenarios.

Benthic foraminifera have been widely used in paleoenvironmental studies, particularly in reconstructing the history of the Earth's climate over the past few million years. The oxygen isotopic composition of benthic foraminifera shells, for example, has been used to reconstruct past changes in sea surface temperature and global ice volume. The stable isotopic composition of benthic foraminifera can also provide information on changes in seawater chemistry, such as changes in the carbonate ion concentration, which is important for understanding ocean acidification ([3]).

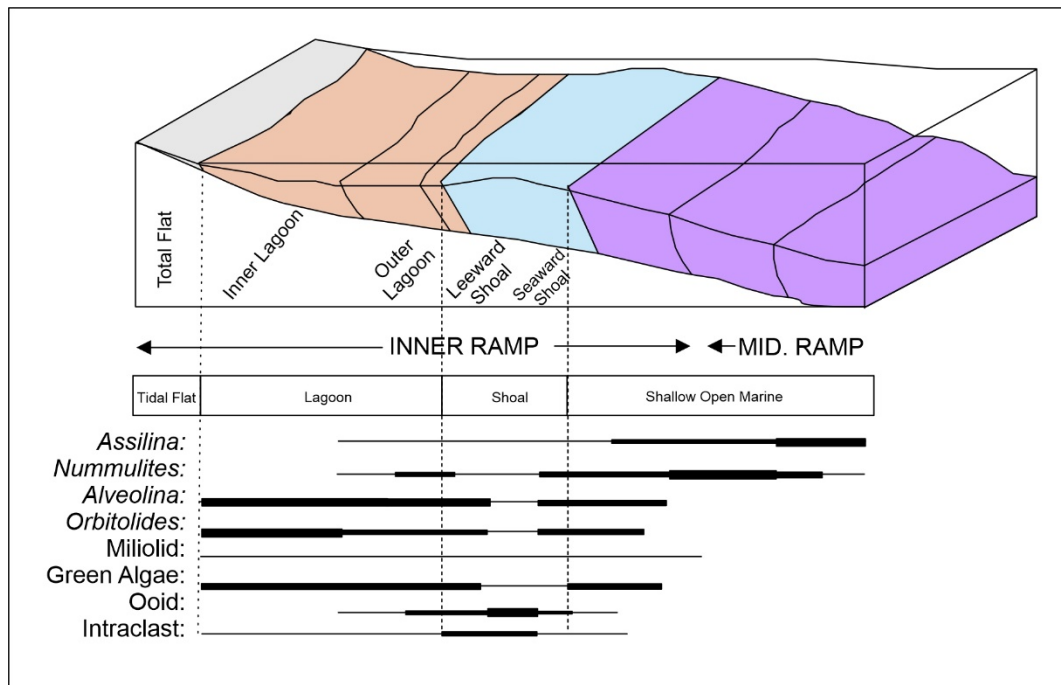


Fig. 2: Seafloor habitats of different foraminifera genera (Modified from [1])

Benthic foraminifera are also used to reconstruct past changes in ocean currents and circulation patterns. For example, the abundance of certain species of benthic foraminifera is related to the strength of the Atlantic Meridional Overturning Circulation (AMOC), which plays a key role in the global climate system ([6]). Changes in ocean circulation can have significant impacts on the Earth's climate, including changes in regional temperature, precipitation, and the distribution of heat and moisture. Furthermore, benthic foraminifera can also provide information on changes in sedimentation rates, substrate composition, and environmental conditions,

such as changes in nutrient availability and oxygenation ([5]). These factors can have important implications for understanding past climate changes and the impact of human activities on the environment.

In summary, benthic foraminifera are a valuable tool for understanding past climate changes and predicting future climate scenarios. The use of benthic foraminifera in paleoenvironmental studies has provided important insights into the Earth's climate history, including changes in temperature, ice volume, ocean circulation, and seawater chemistry. As our understanding of the Earth's climate system continues to evolve, benthic foraminifera will remain a key tool for understanding the impacts of climate change on the environment.

4. FUTURE PROSPECTS FOR BENTHIC FORAMINIFERA AS CLIMATE INDICATORS

Benthic foraminifera are currently important indicators of climate change, but the potential for other indicators in the future is an exciting area of research. One promising area of investigation is the use of DNA in benthic foraminifera to infer past environmental conditions, as changes in DNA can be linked to changes in climate variables. Recent studies have shown that DNA in benthic foraminifera can be used to reconstruct past sea surface temperatures (SSTs) and even infer past ocean circulation patterns ([8]). Additionally, studies have shown that the stable isotopes of carbon and nitrogen found in benthic foraminifera can be used as proxies for past nutrient levels, ocean acidity, and productivity ([3]).

Another promising approach is the use of machine learning algorithms to identify patterns in benthic foraminifera morphology that are associated with environmental conditions. This has the potential to greatly expand the range of environmental variables that can be inferred from benthic foraminifera fossils ([10]). Additionally, emerging technologies such as high-resolution X-ray computed tomography (CT) scanning can provide detailed 3D images of benthic foraminifera shells, allowing for more precise measurements of shell characteristics ([2]).

In conclusion, while benthic foraminifera are currently the most widely used indicators of past climate conditions, the potential for other indicators is vast. DNA analysis, stable isotope analysis, machine learning, and emerging technologies such as high-resolution CT scanning all show great promise for expanding our understanding of past climate variability.

5. RESULTS AND DISCUSSION

The analysis of benthic foraminiferal fossils in sediment cores from various regions has revealed valuable information about past climate change. The assemblages of different species of foraminifera in the sediment cores reflect the varying environmental conditions that existed during their formation. By analyzing the ratios of stable isotopes of oxygen and carbon in the foraminifera, we can reconstruct past changes in temperature and carbon cycle dynamics. Our research confirms the utility of benthic foraminiferal fossils as sensitive indicators of past climate change.

Our study suggests that benthic foraminiferal fossils have the potential to be used as indicators of future climate change. In addition to stable isotope analysis, new techniques such as DNA sequencing and lipid biomarker analysis may offer further insights into the environmental conditions that affected the growth and distribution of foraminifera. Furthermore, the incorporation of machine learning and artificial intelligence algorithms can aid in identifying patterns in the vast datasets generated by these methods. By combining these techniques, we can develop a more comprehensive understanding of past and future climate change, and the role of benthic foraminifera in this process.

6. CONCLUSION

Benthic foraminiferal fossils have proven to be valuable indicators and tracers of past climate change. Through analysis of their morphology, isotopic composition, and geochemistry, we have been able to reconstruct past environmental conditions with high accuracy. Moreover, recent studies have shown that benthic foraminifera can also serve as proxies for assessing the impacts of human-induced climate change on marine ecosystems.

While there are still some limitations to the use of benthic foraminifera as climate proxies, ongoing research efforts are addressing these issues and refining our understanding of their potential. Given the sensitivity of benthic foraminifera to environmental changes, they hold great promise for use in future climate research.

7. FUTURE WORK

The potential of benthic foraminifera as climate proxies has yet to be fully realized. Future research should focus on expanding our understanding of the relationship between benthic foraminiferal assemblages and environmental variables, such as temperature, salinity, and dissolved oxygen. Furthermore, more research is needed to explore the use of benthic foraminifera as indicators of anthropogenic pollution and other human impacts on marine ecosystems.

Additionally, advances in technology, such as micro-computed tomography and high-throughput DNA sequencing, hold promise for further improving our understanding of benthic foraminiferal ecology and their use as climate proxies. Finally, long-term monitoring of benthic foraminiferal populations and assemblages will be crucial for detecting and predicting future environmental changes and their impacts on marine ecosystems.

REFERENCES

- [1] M. H. Adabi, A. Zohdi, A. Ghabeshavi, ve H. Amiri-Bakhtiyar, "Applications of nummulitids and other larger benthic foraminifera in depositional environment and sequence stratigraphy: an example from the Eocene deposits in Zagros Basin, SW Iran," *Facies*, cilt 54, no. 4, ss. 499-512, 2008.
- [2] A. Golreihan, C. Steuwe, L. Woelders, A. Deprez, Y. Fujita, J. Vellekoop, ... & M. B. Roeffaers, "Improving preservation state assessment of carbonate microfossils in paleontological research using label-free stimulated Raman imaging." *PLoS One*, 13(7), e0199695, (2018).
- [3] S. C. Doney, V. J. Fabry, R. A. Feely, & J. A. Kleypas, "Ocean acidification: The other CO₂ problem," *Annual Review of Marine Science*, 1, 169-192, 2009.
- [4] C. Haller, "Application of Modern Foraminiferal Assemblages to Paleoenvironmental Reconstruction: Case Studies from Coastal and Shelf Environments" (Doctoral dissertation, University of South Florida), 2018.
- [5] Meric, E., Avsar, N., Yokes, M. B., & Dincer, F. "Atlas of recent benthic foraminifera from Turkey." *Micropaleontology*, 60(3-4), 211-398, 2014.
- [6] Depuydt, P., Mojtahid, M., Barras, C., Bouhdayad, F. Z., & Toucanne, S. "Intermediate ocean circulation and cryosphere dynamics in the northeast Atlantic during Heinrich Stadials: benthic foraminiferal assemblage response." *Journal of Quaternary Science*, 37(7), 1207-1221, 2022.
- [7] Seidenkrantz, M. S., Kouwenhoven, T. J., Jorissen, F. J., Shackleton, N. J., & Van der Zwaan, G. J. "Benthic foraminifera as indicators of changing Mediterranean–Atlantic water exchange in the late Miocene." *Marine geology*, 163(1-4), 387-407, 2000.
- [8] Ertan, K. T., Hemleben, V., & Hemleben, C. "Molecular evolution of some selected benthic foraminifera as inferred from sequences of the small subunit ribosomal DNA." *Marine Micropaleontology*, 53(3-4), 367-388, 2004.
- [9] Pearson, P. N. "Oxygen isotopes in foraminifera: Overview and historical review." *The Paleontological Society Papers*, 18, 1-38, 2012.
- [10] Aagaard-Sørensen, S., Haugland Johansen, T., & Junttila, J. "First-order machine learning based detection and classification of foraminifera in marine sediments from Arctic environments." In *EGU General Assembly Conference Abstracts* (p. 7606), 2020.
- [11] Majewski, W., Holzmann, M., Gooday, A. J., Majda, A., Mamos, T., & Pawlowski, J. "Cenozoic climatic changes drive evolution and dispersal of coastal benthic foraminifera in the Southern Ocean." *Scientific Reports*, 11(1), 19869, 2021.

A General Evaluation of The Usage of Fly Ash in Concrete Mixtures

Zehra Funda Akbulut¹, Soner Guler²

Abstract

Concrete is a building material that uses cement, fine and coarse aggregates, water, and different chemical additives. In their mixtures, Portland cement (PC) or cement with additives is used as binding material. The release of a high amount of carbon dioxide (CO₂) gas into the environment during cement production causes significant environmental problems. To reduce the damage caused by cement production to the environment, it is important for sustainability to replace cement with pozzolanic materials in concrete mixtures. The most important pozzolanic materials obtained from various industrial activities in our country are blast furnace slag, silica fume, and fly ash (FA). FAs are obtained from thermal power plants that produce electricity. FA is stored in dust catchers called electro filters or cyclones at the top of the chimney while burning very low-calorie coals, which are not generally used in industrial facilities, by grinding them into fine grain size and burning them in the thermal power plant furnace. Although it does not show a binding feature on its own, it provides a significant advantage in terms of cost by being used to replace cement. This study is to make a general evaluation of the potential of the FA in our country and its use in concrete mixtures.

Keywords: Concrete, fly ash, sustainability, physical and mechanical properties

1. INTRODUCTION

The use of binders in the concrete industry dates back to ancient times. The ancient Egyptians used gypsum mortars as binding material, while the ancient Greeks and Romans used lime mortars. Recently, it has been observed that the use of quality binders such as water lime and Portland cement (PC) as binding materials has developed rapidly with the developing technology [1-3]. Apart from these, it is seen that PC and special cement types develop according to their usage purposes. Also, hydration products, hydration heat, compressive strength, setting time, hardening, volume expansion, shrinkage, and creep can be developed using FA in concrete mixtures. These developments have been followed using binders such as fly ash (FA), silica fume, blast furnace slag, and metakaolin in concrete mixes [4-10]. FA emerges as a waste by-product in coal-fired thermal power plants [11-13]. It can be used in FA concrete mixes by replacing the cement binder in certain proportions. It is a pozzolanic mineral admixture type that can be used as filler in concrete mixes [14-16]. According to the source they are obtained from, FA has a finer grain structure than PC [17-18]. FA is a useful additive for the concrete industry, potentially improving its fresh and hardened properties and economic advantages [19-22]. With the development of the industry, many waste materials and by-products are released as a result of the production in the industrial field. Very few of them are reused, and most of them are stored. This causes environmental pollution [23-25]. To prevent this, the use of these waste materials in the concrete sector should be expanded. Thus, the use of limited natural resources is reduced, and the damages that may occur in nature are minimized. In addition, to reduce the emission of high carbon dioxide (CO₂) and greenhouse gases originating from PC production to the atmosphere and to prevent damage to nature, the use of pozzolanic materials such as FA by replacing cement in the concrete sector has become mandatory in terms of sustainability [26-30]. PC production worldwide was approximately 4 billion tons in 2015, while it was 75 million tons in Turkey. In producing one ton of Portland cement, 0.8 tons of carbon dioxide (CO₂) emissions occur. During the production of 75 million tons of Portland cement in Turkey, an average of 60 million tons of carbon dioxide (CO₂) gas is released into the atmosphere annually [31]. The FA are mostly used as secondary binders in mortar

¹ Corresponding author: Van Yuzuncu Yil University, Department of Mining Engineering, 65080, Tusba/Van, Turkey. fundaakbulut@yyu.edu.tr

² Author: Van Yuzuncu Yil University, Department of Civil Engineering, 65080, Tusba/Van, Turkey. gulersoner@yyu.edu.tr

and concrete production. FA is used as additive cement instead of a part of PC in weight percent. They affect the workability and water requirement of fresh concrete and its properties, such as transpiration, weathering, air entrainment, the heat of hydration, and plastic shrinkage. By reacting with the lime formed from cement hydration, they form an additional binder gel, fill the voids in the cement paste, increase the compactness, decrease the permeability, and provide the concrete with higher durability properties [32-34]. In addition, they ensure that the hardened concrete samples have better mechanical properties [35-37]. Concrete compressive strength, strength gain rates, high modulus of elasticity, and time-dependent deformations such as creep and shrinkage are affected by using mineral additives such as the FA. In addition, mineral additives also affect durability properties such as impermeability, resistance to acids and sulfates, alkali-aggregate reaction, resistance to freeze-thaw repetitions, and reinforcement corrosion. The effect of FA on these properties generally depends on the type of FA, characteristics of coal and burning method, amount of use, method of use, and physical, chemical, and pozzolanic properties [38-41]. FA is an artificial pozzolan consisting of glassy, spherical granular particles used as a mineral-based additive in concrete. Although they do not have binding properties, they form a hydration reaction with slaked lime and harden in water [42-44].

2. CONCLUSION

The use of concrete, the most widely used building material in the world, in the construction sector, continues to increase. Its most important advantages are its high compressive strength, ease of application, easy shaping, easy availability, and cheapness compared to other materials. However, Portland cement is widely used as a binding material in concrete production today. The high amount of CO₂ gas released into the air during cement production poses a significant environmental threat. In addition, it increases the cost of concrete as an important expense item of cement. In light of these developments, studies have been carried out in recent years to reduce the amount of cement without disturbing the concrete properties required in the standards to produce both environmentally friendly and less costly concrete. Today, the increasing energy need with rapid industrialization and the fossil fuels used to meet this need bring along important environmental problems. On the one hand, ensuring sustainable development, on the other hand, increasing the quality of life of people by reducing environmental pollution can be achieved by using such waste materials in different areas. In addition, due to the use of pozzolanic creams such as FA in place of cement, the emission of CO₂ gas originating from cement production to the atmosphere will be significantly reduced. In this context, using coal-derived fly ash, which causes important environmental problems, in the construction industry, especially in concrete production, by replacing cement with pozzolan is extremely important in terms of sustainability. In addition, the use of this material in the production of high-performance concrete will be inevitable shortly since FA improves the durability properties of concrete and its durability properties.

REFERENCES

- [1]. W.H. Gourdin, & W. D. Kingery, (1975). The beginnings of pyrotechnology: Neolithic and Egyptian lime plaster. *Journal of Field Archaeology*, 2(1-2), 133-150.
- [2]. M. A. Sakr, M. A., Shahin, & Y. M. Metwally, (2009). Utilization of lime for stabilizing soft clay soil of high organic content. *Geotechnical and Geological Engineering*, 27, 105-113.
- [3]. N. Y. Mostafa, S. A. S., El-Hemaly, E. I., Al-Wakeel, S. A., El-Korashy, & P. W. Brown, (2001). Characterization and evaluation of the pozzolanic activity of Egyptian industrial by-products: I: Silica fume and dealuminated kaolin. *Cement and Concrete Research*, 31(3), 467-474.
- [4]. S. A. Khedr, & M. N. Abou-Zeid, (1994). Characteristics of silica-fume concrete. *Journal of Materials in Civil Engineering*, 6(3), 357-375.
- [5]. T. Nochaiya, W., Wongkeo, & A. Chaipanich, (2010). Utilization of fly ash with silica fume and properties of Portland cement-fly ash-silica fume concrete. *Fuel*, 89(3), 768-774.
- [6]. N. M. Al-Akhras, (2006). Durability of metakaolin concrete to sulfate attack. *Cement and concrete research*, 36(9), 1727-1734.
- [7]. M. I. Khan, & R. Siddique, (2011). Utilization of silica fume in concrete: Review of durability properties. *Resources, Conservation and Recycling*, 57, 30-35.
- [8]. E. Badogiannis, & S. Tsivilis, (2009). Exploitation of poor Greek kaolins: Durability of metakaolin concrete. *Cement and Concrete Composites*, 31(2), 128-133.
- [9]. R. Siddique, & J. Klaus, (2009). Influence of metakaolin on the properties of mortar and concrete: A review. *Applied Clay Science*, 43(3-4), 392-400.
- [10]. E. E. Berry, & V. M. Malhotra, (1980, March). Fly ash for use in concrete-a critical review. In *Journal Proceedings* (Vol. 77, No. 2, pp. 59-73).
- [11]. T. Hemalatha, & A. Ramaswamy, (2017). A review on fly ash characteristics-Towards promoting high volume utilization in developing sustainable concrete. *Journal of cleaner production*, 147, 546-559.
- [12]. P.K. Mehta, (2004, May). High-performance, high-volume fly ash concrete for sustainable development. In *Proceedings of the international workshop on sustainable development and concrete technology* (pp. 3-14). Ames, IA, USA: Iowa State University.
- [13]. A.D.N.A.N. Oner, S. Akyuz, & R. Yildiz, (2005). An experimental study on strength development of concrete containing fly ash and optimum usage of fly ash in concrete. *Cement and Concrete Research*, 35(6), 1165-1171.



- [14]. J. Paya, M.V. Borrachero, J. Monzo, E. Peris-Mora, & F. Amahjour, (2001). Enhanced conductivity measurement techniques for evaluation of fly ash pozzolanic activity. *Cement and Concrete research*, 31(1), 41-49.
- [15]. S. Goni, A. Guerrero, M.P. Luxan, & A. Macías, (2003). Activation of the fly ash pozzolanic reaction by hydrothermal conditions. *Cement and Concrete Research*, 33(9), 1399-1405.
- [16]. R. Snellings, H. Kazemi-Kamyab, P. Nielsen, & L. Van den Abeele, (2021). Classification and milling increase fly ash pozzolanic reactivity. *Frontiers in Built Environment*, 7, 670996.
- [17]. J. Zhao, D. Wang, X. Wang, S. Liao, & H. Lin, (2015). Ultrafine grinding of fly ash with grinding aids: Impact on particle characteristics of ultrafine fly ash and properties of blended cement containing ultrafine fly ash. *Construction and Building Materials*, 78, 250-259.
- [18]. P.K. De Maeijer, B. Craeye, R. Snellings, H. Kazemi-Kamyab, M. Loots, K. Janssens, & G. Nuyts, (2020). Effect of ultra-fine fly ash on concrete performance and durability. *Construction and Building Materials*, 263, 120493.
- [19]. E. Mulder, (1996). Pre-treatment of MSWI fly ash for useful application. *Waste Management*, 16(1-3), 181-184.
- [20]. S. Jala, & D. Goyal, (2006). Fly ash as a soil ameliorant for improving crop production—a review. *Bioresource technology*, 97(9), 1136-1147.
- [21]. A.C. Chang, L.J. Lund, A.L. Page, & J.E. Warneke, (1977). Physical properties of fly ash-amended soils (Vol. 6, No. 3, pp. 267-270). American Society of Agronomy, Crop Science Society of America, and Soil Science Society of America.
- [22]. F. Mushtaq, M. Zahid, I.A. Bhatti, S. Nasir, & T. Hussain, (2019). Possible applications of coal fly ash in wastewater treatment. *Journal of environmental management*, 240, 27-46.
- [23]. A. Dwivedi, & M. K. Jain, (2014). Fly ash—waste management and overview: A Review. *Recent Research in Science and Technology*, 6(1).
- [24]. K. Prakash, & A. Sridharan, (2009). Beneficial properties of coal ashes and effective solid waste management. *Practice periodical of hazardous, toxic, and radioactive waste management*, 13(4), 239-248.
- [25]. G. Jayarajan, & S. Arivalagan, (2021). An experimental studies of geopolymer concrete incorporated with fly-ash & GGBS. *Materials Today: Proceedings*, 45, 6915-6920.
- [26]. M. B., Ali, R., Saidur, & M. S. Hossain, (2011). A review on emission analysis in cement industries. *Renewable and Sustainable Energy Reviews*, 15(5), 2252-2261.
- [27]. A., Bosoaga, O., Masek, & J. E. Oakey, (2009). CO2 capture technologies for cement industry. *Energy procedia*, 1(1), 133-140.
- [28]. H. G., Van Oss, & A. C. Padovani, (2003). Cement manufacture and the environment part II: environmental challenges and opportunities. *Journal of Industrial ecology*, 7(1), 93-126.
- [29]. E., Benhelal, G., Zahedi, E., Shamsaei, & A. Bahadori, (2013). Global strategies and potentials to curb CO2 emissions in cement industry. *Journal of cleaner production*, 51, 142-161.
- [30]. K. S., Devi, V. V., Lakshmi, & A. (Alakanandana, 2017). Impacts of cement industry on environment-an overview. *Asia Pac. J. Res*, 1, 156-161.
- [31]. U. Ozcan, & S. Gungor, (2019). *Surdurulebilir Bir Yontem/Betonda Puzolan Kullanimi. Avrupa Bilim ve Teknoloji Dergisi*, (15), 176-182.
- [32]. B.E. Scheetz, & R. Earle, (1998). Utilization of fly ash. *Current Opinion in Solid State and Materials Science*, 3(5), 510-520.
- [33]. J. P., Prashanth, P. V., Sivapullaiah, & A. Sridharan, (2001). Pozzolanic fly ash as a hydraulic barrier in land fills. *Engineering Geology*, 60(1-4), 245-252.
- [34]. M., Saafi, L., Tang, J.,, Fung, M. Rahman, & J. Liggat, (2015). Enhanced properties of graphene/fly ash geopolymeric composite cement. *Cement and Concrete Research*, 67, 292-299.
- [35]. Y., Hefni, Y., Abd El Zaher, & M. A. Wahab, (2018). Influence of activation of fly ash on the mechanical properties of concrete. *Construction and Building Materials*, 172, 728-734.
- [36]. I. B., Topcu & M. Canbaz, (2007). Effect of different fibers on the mechanical properties of concrete containing fly ash. *Construction and Building Materials*, 21(7), 1486-1491.
- [37]. M. M., Roshani, S. H., Kargar, V., Farhangi, & M. Karakouzian, (2021). Predicting the effect of fly ash on concrete's mechanical properties by ann. *Sustainability*, 13(3), 1469.
- [38]. A. K. Saha (2018). Effect of class F fly ash on the durability properties of concrete. *Sustainable environment research*, 28(1), 25-31.
- [39]. N. Schwarz, H. Cam, & N. Neithalath, (2008). Influence of a fine glass powder on the durability characteristics of concrete and its comparison to fly ash. *Cement and Concrete Composites*, 30(6), 486-496.
- [40]. P. Nath, & P. Sarker, (2011). Effect of fly ash on the durability properties of high strength concrete. *Procedia Engineering*, 14, 1149-1156.
- [41]. Y.S. Yoon, J.P. Won, S. K. Woo, & Y.C. Song, (2002). Enhanced durability performance of fly ash concrete for concrete-faced rockfill dam application. *Cement and Concrete Research*, 32(1), 23-30.
- [42]. V.P. Kumar, & D.R. Prasad, (2019). Influence of supplementary cementitious materials on strength and durability characteristics of concrete. *Advances in concrete construction*, 7(2), 75.
- [43]. M. Harilal, V.R. Rathish, B. Anandkumar, R.P. George, M.H.S. Mohammed, J. Philip, & G. Amarendra, (2019). High performance green concrete (HPGC) with improved strength and chloride ion penetration resistance by synergistic action of fly ash, nanoparticles and corrosion inhibitor. *Construction and Building Materials*, 198, 299-312.
- [44]. K. Chintalapudi, & R. M. R. Pannem, (2021). Enhanced Strength, Microstructure, and Thermal properties of Portland Pozzolana Fly ash-based cement composites by reinforcing Graphene Oxide nanosheets. *Journal of Building Engineering*, 42, 102521.



Effect of Boron Waste on Mechanical and Durability Properties of Concrete

Oznur Biricik¹, Suleyman Ozen², Ali Mardani³

Abstract

It was emphasized that 8% of the CO₂ emission that causes global warming occurs during cement production. In addition, the consumption of natural resources used in cement production increases due to the increase in cement demand with the widespread use of concreting. In this context, studies on alternative binders continue in order to reduce cement production and consumption. Today, besides the use of mineral additives such as blast furnace slag, fly ash and silica fume as binders in concrete mixtures, studies on the disposal and sustainability of other industrial wastes are continuing. One of the wastes generated in the industry is formed in boron plants. It is important to evaluate boron wastes especially in Turkey, which has significant boron reserves in the world. Studies on the use of boron wastes in concrete mixtures have recently become widespread. In this study, a comprehensive literature search was conducted on the effect of boron waste usage on the fresh state, mechanical, durability and radiation absorption properties of cementitious systems. In this context, with the increase in the use of boron waste and the increase in its usage rate, the radiation absorption properties of cementitious systems, their resistance to high temperatures and freeze-thaw have improved. However, with the addition of waste, the fresh water requirement and setting time of the mixtures increased. In terms of compressive strength, if the boron wastes in the mixtures exceed 10%, their compressive strength generally decreased.

Keywords: Boron waste, cementitious systems, sustainability, strength, durability performance

1. INTRODUCTION

Cement production exceeds 4 million tons per year due to the increase in the need for concrete in infrastructure and residential constructions [1]. Since cement production, which is responsible for 8% of the CO₂ emitted in the world, causes important problems such as global warming and climate change, the use of sustainable binder materials, which are less harmful to the environment, is being investigated in many countries to reduce cement consumption [2]. In this direction, the use of different mineral additives such as fly ash, silica fume and blast furnace slag by substituting and activating them instead of cement has become widespread in concrete production [3,4]. In addition to these materials, the use of different types of materials in concrete, which is a waste of a production process and creates environmental and storage problems, continues to be investigated [5]. In addition to the fact that the materials to be used do not adversely affect the fresh state properties, mechanical properties and durability performance of the concrete, the fact that it provides benefits for its performance increases its preferability [6]. In addition, the increase in energy demand with the developing

¹ Department of Civil Engineering, Faculty of Engineering, Bursa Uludag University, Bursa, Turkey, oznurbiricik@uludag.edu.tr , 0000-0003-4884-7350

² Department of Civil Engineering, Faculty of Engineering, Bursa Technical University, Bursa, Turkey, suleyman.ozen@btu.edu.tr, 0000-0001-5522-427X

³ Corresponding author: Department of Civil Engineering, Faculty of Engineering, Bursa Uludag University, Bursa, Turkey, ali.mardani16@gmail.com/alimardani@uludag.edu.tr, 0000-0003-0326-5015

technology and the construction of nuclear power plants for this purpose, the high strength and durability performance of concrete mixtures, as well as radiation absorption and nuclear waste storage expectations are increasing. In this context, boron ore has recently gained an increasing momentum among the materials that can be used for the improvement of some properties of concrete and radiation absorption.

Boron is used in various areas of industry such as agriculture, cleaning, ceramics, glass, insulation, health and energy. Turkey has the largest boron deposits worldwide with a share of 72% (851 Mt) in terms of B_2O_3 content [7]. During the processing of boron in industrial areas, about 400000 tons/year of different types of solid boron-containing wastes are generated [8]. Excessive amounts of waste cause serious environmental and costly storage problems [9]. The B_2O_3 content in these wastes usually ranges from 11% to 25% by weight, depending on the starting minerals and processing conditions. Turkey's commercial boron ores are colemanite, tincal and ulexite. After colemanite is extracted and concentrated in the concentrate plant, it is reacted with sulfuric acid to obtain boric acid. Concentration plant waste is called colemanite concentrator waste and boric acid plant waste is called borogypsum. Colemanite concentrator waste and borogypsum contain approximately 6.3% and 4.2% B_2O_3 , respectively. It was declared that the amount of CO_2 released during the heat treatment of boron-derived wastes is lower than in cement production. The loss on ignition value of boron-derived wastes below $1000^\circ C$ obtained by XRF analysis is about 30% by weight due to the removal of both H_2O and CO_2 , while a higher amount of CO_2 is released (the cement content is 57.5% by weight on average) during conventional cement production [10]

Kok et al. [11] stated that boron wastes provide protection against gamma rays and thermal neutrons in concrete mixtures. In addition to this feature, it was stated that geopolymerization accelerated and compressive strength increased by adding geopolymer to concrete mixtures for the immobilization of nuclear boron wastes [12]. In this context, recent studies on the effects of boron use on the radiation absorption, fresh state properties, compressive strength, freeze-thaw and high temperature resistance of concrete are presented in this study.

Radiation absorption properties

The photon attenuation coefficient is an important parameter for characterizing the penetration and diffusion of X- and gamma-rays in multi-element materials. Photon attenuation coefficients are essential in a variety of nuclear science, technology and medical applications. The mass attenuation coefficient, l/q , is a measure of the average number of interactions between the photons and the matter occurring per unit area thickness of the substance under investigation [13]. The fact that radiation can be harmful has led to the development of a wide variety of shields to protect against it [13]. A larger amount of shielding material is required for nuclear radiation shielding. Therefore, examining the radiation flux propagation in shielding materials is a basic requirement for shield design [13]. Good shielding should have a high absorption cross section for radiation and at the same time, the irradiation effects on its mechanical and optical properties should be small. The mass attenuation coefficients depend on the chemical composition of the absorbing material and the energy of the gamma rays. In this context, the use of materials such as waste boron in nuclear shield concrete mixtures should be investigated. The radiation permeability of the concrete produced by using boroplaster and colemanite concentrator wastes for 59.54 and 80.99 keV gamma rays was measured and it was investigated whether adding

these boron-containing wastes to cement as a protective material would be beneficial. It was emphasized that both boron waste types are effective in preventing radiation transmission. As a result, it was reported that boron wastes add gamma ray shielding properties to the cementitious mixture [13]. Many studies were conducted on the radiation shielding properties of concretes containing colemanite and ulexite as aggregate additives. In the study carried out by Oto and Gur [14], the mass attenuation coefficients of concrete containing ulexite and ulexite concentrator wastes were examined, and it was declared that both materials could be used for gamma ray protection at concentrations below 10%. Binici et al. [15], the linear absorption coefficient increased from 0.07 cm^{-1} to 0.24 cm^{-1} by adding 10% waste barite to the control mixture. By adding 0.25% and 0.75% colemanite to the control mixture, the said value was measured as 0.08 cm^{-1} and 0.05 cm^{-1} . As a result, it is seen that barite wastes are effective in preventing radiation transmission, the said effect is low for colemanite and these materials are promising materials for gamma ray shielding in mortars. It was observed that the linear absorption coefficient increased from 0.24 cm^{-1} to 0.69 cm^{-1} with the increase in barite usage rate from 2.5% to 10%. It was emphasized that high amounts of barite (90%) containing BaSO_4 are effective in shielding gamma rays.

Effect on fresh state properties

The use of boron-derived materials in cementitious systems significantly affects the fresh state properties of the mixtures. The increase in boron waste replacement ratio from 1% to 7% in mortar mixtures containing boron waste adversely affected the fresh state properties of the mixtures and increased the need for water reducing admixtures for adequate workability [16,17]. It was stated that the use of boron waste generally causes an increase in rheological parameters (viscosity and shear stress). It was reported that the mixture containing 1.0% boron waste behaves similarly to the reference mixture in terms of some rheological parameters, but with the said ratio increasing to 1.5, 2.0, 2.5%, the static and dynamic shear stress and plastic viscosity values together exceed the reference mixture values over time [18]. In addition, the increase in colemanite waste content in mortar mixtures negatively affected the time-dependent slump flow performance. Similar to the slump-spreading behavior in terms of rheological properties, an increase was observed in all three of the viscosity, static and dynamic shear stress values with the use of waste boron. It was declared that this increase has become more evident especially with the use of waste boron at high rates. Similarly, in another study, the slump values decreased from 220 mm to 200 mm when the water/binder ratio was 0.6, and from 40 mm to 8 mm when the water/binder ratio was 0.5, with 15% waste boron replacement in the control mixture [19]. It was observed that the effect of boron on fresh state properties is greater in mixtures with low water/binder ratio. It was reported that this negative effect is due to the high loss on ignition of the waste boron and the clay minerals in it and to increase the friction between the cement grains [17].

Erdogmus [20] and Gencel et al. [21] suggested that the setting times increase with the increase in the amount of waste boron and the effect of the B_2O_3 component in cementitious systems. Borates such as soluble boric acid react with the calcium compounds of Portland cement and cause the formation of insoluble calcium borate compounds such as $2\text{CaO}\cdot 3\text{B}_2\text{O}_3\cdot 8\text{H}_2\text{O}$ and $\text{CaO}\cdot \text{B}_2\text{O}_3\cdot 6\text{H}_2\text{O}$ under high pH conditions [12]. These calcium borate compounds accumulate on the surface of cement particles and slow down or prevent hydration reactions

[16]. In this context, the setting of portland cement is delayed and its early age mechanical properties are weakened [22].

Shen et al. [23], it was reported that borax significantly delays the early hydration and setting time of calcium sulfoaluminate (CSA) cement containing different proportions of gypsum. It was reported that the use of an appropriate amount of borax as a retarder is beneficial for the development of advanced age strength of CSA cements. While the early strength of borax mortars decreased in mixtures containing 5% gypsum, improvements were observed in the mechanical properties of mixtures containing 15% and 20% gypsum. It was emphasized that this is due to the fact that borax prevents the hydration of ye'elimit and the depletion of plaster in 1 day. It was stated that the effect of borax on ettringite formation is related to the gypsum content of CSA cements.

It was stated that the use of boric acid and borate is a solution to the problem of magnesium phosphate cement reacting too quickly. Borax is the most commonly used set retarder and its retarding effect is related to the ratio of boron to magnesium [24]. For example, it was stated that 5% and 10% borax magnesium phosphate cement pastes reach their final setting temperature in 18 minutes and 22 minutes, respectively [25]. It was found that boron-containing compounds can effectively control the reaction rate of magnesium phosphate cement [26]. Magnesium phosphate cement material has good interfacial bonding properties. With the application of borax, the reaction rate of magnesium phosphate cement with extremely high early strength becomes controllable. Thus, the possibility of emergency repair and reinforcement of magnesium phosphate cement for roads, airport runways, bridges and military repair materials was also investigated [27].

Effect on strength properties

Boron waste materials affect the setting times of cementitious systems as well as the mechanical properties of early and advanced ages. Final compressive strength in cementitious systems containing waste boron is also relatively low (2 ± 0.3 MPa) due to the delay of setting of calcium borate compounds. Fabian et al. [28], the use of cementitious mixtures for the disposal of nuclear waste was investigated. As a result of the study, it was emphasized that the leakage of nuclear wastes is less with the increase in the compressive strength of concrete mixtures. In addition, it was stated that the 28-day compressive strength value decreased from 42.57 MPa to 37.51 MPa with the increase of boron waste amount (boric acid) from 50 g/l to 250 g/l. It was declared that the use of geopolymer waste forms is more beneficial than cement waste forms for the immobilization of radioactive wastes [29]. In general, geopolymers exhibited higher compressive strength than cement, despite shorter curing days with the same waste load [30]. According to the Japan Atomic Energy Agency, metakaolin-based geopolymers are superior to portland cement for immobilization of sewage sludge ash containing ^{137}Cs [29]. It was determined that the amount of radioactive cesium ($<0.1\%$) leached in geopolymers is approximately 300 times lower than that in cement [29]. Kim et al. [12], a phosphate-based geopolymer waste storage mixture was investigated for the immobilization of radioactive boron waste. All geopolymers met the landfill acceptance criteria (3.45 MPa), despite the short setting time. It was declared that curing at high temperatures (at 60 and 90°C) compared to room temperature increases the 7-day compressive strength of geopolymers and the maximum compressive strength is obtained in a geopolymer containing 40% by weight waste boron. XRD,



MAS NMR and SEM analysis results of the geopolymer with the highest compressive strength and the reaction product prepared under high temperature curing conditions showed that the crystalline phases in boron waste were transformed into amorphous boron phosphate phase and 4-coordinated boron was included in the geopolymer structure. Therefore, high temperature curing conditions lead to direct precipitation of the amorphous boron phosphate phase and accelerated geopolymerization, resulting in higher compressive strength as the boron waste content increases. These results show that phosphate-based geopolymers are promising waste form candidates for the immobilization of waste boron and other radioactive wastes, which are difficult to immobilize using conventional cement or alkali-activated materials. However, it was observed that the 7-day compressive strength of geopolymers decreased as the amount of waste boron in the mixture increased. It was assumed that the consumption of an acidic activator by the boron phosphate reaction results in low compressive strength.

The effect of the use of waste boron materials obtained from the concentrated borax unit (CW1) and borax pentahydrate unit (CW2) in mortars on the strength was investigated by Ozdemir et al. [31]. These waste borates were used in mortar mixtures with 1, 2.5, 5 and 10% cement substitutes. Mortar containing 1% CW1 has a higher 28-day compressive strength than the control mixture. However, the mechanical properties of the mortar were adversely affected as the use of waste boron and the rate of B_2O_3 in waste boron increased. Mortar mixes containing up to 5% CW1 ($B_2O_3=22.48\%$) and 10% CW2 ($B_2O_3=8.23\%$) met TS24 (1985) standard minimum compressive strength requirements (32.5 MPa). As a result, it was suggested that these wastes can be replaced by cement up to 5% and 10%, respectively. Similar results were found by Gencil et al. [21] has also been observed. Durgun et al. [17], the 28-day compressive strength of all samples containing 1, 3, 5 and 7% waste boron was lower than the control sample. While the difference between the control sample and the waste boron added samples was closed in the 56-day samples, the sample containing 5% waste boron had a higher compressive strength than the control sample. In another study, it was observed that there was a decrease in early strength in mortar mixtures with boron waste substituted for natural gypsum compared to the control sample. However, setting times were not significantly affected [32].

The use of boron wastes in different types of cementitious systems was studied by various researchers. In a study, the incorporation of boric acid and boron oxide from boron waste into raw meal for the production of belite cement and the effect of boron as a part of clinker on belite crystals were investigated. Three types of clinker were prepared by adding 1.5% by weight boric acid (BC_BA1.5) and 1.0% (BC_BW1) and 6.5% (BC_BW6.5) boron waste in the whole mixture. According to the development of free lime content and microstructure of the clinkers, firing was carried out at 1330°C, 1350°C and 1310°C for BC_BA1.5, BC_BW1 and BC_BW6.5, respectively. In Figure 1, optical microscope images of clinkers formed at 1320°C firing temperature are given. Boron addition helped stabilize the upper belite polymorphs as well as lowering the clinkerization temperature. As a result of the study, with the addition of 1% and 1.5% boron, the 28-day compressive strength values were declared to be 60 MPa and 52.7 MPa, respectively. It was emphasized that the increased molten phase caused the deterioration of hydraulic properties due to the formation of higher amounts of C_3BS in the clinker. The 28-day compressive strength varied depending on the type of belite crystals in the clinker rather than the content. The results show that although the increase in the use of boron oxide in

certain cements affects the strengths somewhat negatively, it may be beneficial in terms of lowering the firing temperature of the cement in the kiln [7].

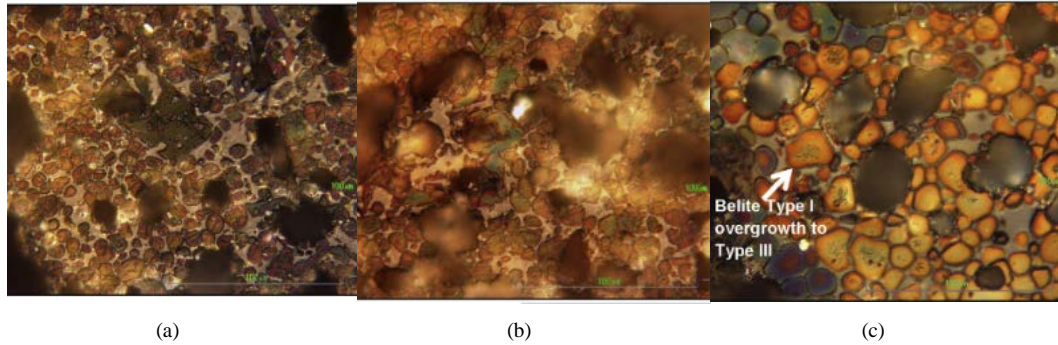


Figure 1. Optical microscope images of clinker formed at 1320°C firing temperature: a) BC_BA1.5, b) BC_BW1 c) BC_BW6.5 [7]

In some studies, boron wastes were calcined at high temperature and used to improve their properties. In a study, ground heat-treated (1 hour 800 degrees 10°C/min) boron-derived wastes with different particle sizes (larger, closer and smaller median particles) than Portland cement were used instead of Portland cement at a rate of 25% by weight. In addition, the compositions and microstructures of the hydration products were found to be similar for all mortars. However, it was stated that the strength of 7- and 28-day cement mortars does not always increase with the reduction of particle size of ground heat-treated boron wastes. Compared to cement, coarser ground heat-treated boron wastes resulted in a high strength loss as expected (42.5% reduction). However, the smaller median particle size of ground heat-treated boron wastes reduced the strength of the mortars due to the waste's non-reactivity and lower packing density. Ground heat-treated boron tailings with a median particle size comparable to that of cement reduced the strength to only 6.3% of that of the reference mortar. It was associated with a higher particle size range of ground heat-treated boron wastes, which provided the same packing density as the reference mortar due to the filling effect. Environmentally friendly cement mortars can be produced using boron wastes, which cause serious environmental problems in terms of compressive strength and costly storage problems, by replacing 25% by weight of Portland cement with ground heat-treated boron wastes. In summary, not only the median particle size of cement substitutes, but also the particle size range plays a critical role in the filler density and therefore the strength of cement mortars. Therefore, the use of non-reactive fillers with a slightly wider range of particle size may be beneficial for other studies focused on increasing the strength of reinforced concrete mortars. Data obtained from microstructural analysis and compression test showed that ground heat treated boron wastes can be replaced with cement at a rate of 25% by weight for 1 hour at 800°C [10].

In addition, recently, it has become widespread to investigate the usability of boron wastes in alkali-activated geopolymer systems. In the study conducted by Yon and Karatas [33], self-compacting alkali-activated mortar samples were produced using 0-25% boron waste and granulated blast furnace slag. The samples were cured at 60 and 100°C for 3 days. As a result, it was determined that the mechanical and durability properties of the samples decreased with the high use of boron waste in the mixtures. According to this study, it was suggested

that up to 10% boron waste can be used in self-compacting alkali-activated mortar in terms of both mechanical and durability performances. In particular, it showed that the addition of waste boron caused greater sensitivity to the curing temperature at 100°C in compressive strength compared to 60°C. It can be said that the main reasons for low compressive strength for waste boron samples are increased water demand for waste boron content, low CaO: SiO₂ and SiO₂: Al₂O₃ and slowing of binder hydration. The presence of calcium aids in curing by improving CSH and CASH and coexists with NASH in the geopolymer matrix [34]. Also, the increase in curing temperature (from 60°C to 100°C) affects the C-S-H gel, which causes the self-compacting alkaline active mortar to be porous with many cracks [35]. Therefore, high amount of calcium activated binder in NH-NS showed lower strength at 100°C [33]. Similarly, in the study examining the effect of waste boron replacement ratio (0, 10, 20, 30, 40%) on the compressive strength of alkali-activated mortars, it was declared that the mixture containing 90% metakaolin and 10% waste boron showed the best performance [36].

Effect on freeze-thaw resistance

The effect of boron wastes on the freeze-thaw resistance of cementitious systems was investigated. In the study carried out by Erdogmus [20], the effect of samples containing 6% silica fume and 2-12% colemanite on the dissolution resistance was investigated. While the strength loss was 14.9% in the mixture without colemanite waste after freeze-thaw cycles, it was reported that this ratio was 14.5-28.3%, respectively, in mixtures containing 2-8% colemanite. For 10% and 12% ratios, it was stated that the said ratio exceeded the 30% strength loss limit specified in ASTM C666 with 39.4% and 53.3%. Similar results were also observed in the study conducted by Topcu and Boga [37]. It was stated by the researchers that the decrease in the flexural strength of the mortar sample containing 3% and 10% waste colemanite after freeze-thaw was 10% and 20%, respectively.

The effect of using boron wastes (0-25%) in granulated blast furnace slag and self-compacting alkali activated mortar on permeability and freeze-thaw resistance was investigated. It was reported that with the increase in boron waste utilization rate (5, 10, 15%), the sorptivity coefficient and porosity increased, the pores became more independent, and during the freeze-thaw cycles, the external liquid entered the pores of the mortar more easily, causing the sample to disperse [33]. Similar results were observed by Erdogmus [20]. In a study examining the 1-year durability performance of alkali-activated mortars containing 90% metakaolin and 10% boron waste, it was declared that the freeze-thaw resistance was appropriate [38]. It was stated by the researchers that the main reason for this is that the compact structure of the matrix is resistant to freezing and thawing effects and provides a good degree of adhesion.

Effect on high temperature resistance

The strength of concrete after exposure to high temperatures is important in terms of durability performance. It was declared that the high temperature resistance is not adversely affected by the use of waste boron [36]. It was declared that the strength preservation performance of concrete mixtures containing 1, 3 and 5% colemanite wastes is better after being exposed to 200-1000°C [39]. In addition, it was declared that the cement mixture on which the pumice aggregate in lightweight concrete mixtures is coated contains colemanite and that the high temperature resistance of lightweight concrete samples improves with the increase of this content [40]. With

the increase in temperature, the enlargement of the sample pore structure and the water evaporation in the matrices increase. With the loss of mass, additional voids are formed. These additional gaps are the reason for the decrease in ultrasonic pulse velocity results. Dehydration and moisture loss in samples produced at high temperatures lead to weight loss and microstructure damage. The colemanite substitution reduced the weight loss after high temperatures. According to the results, up to 10% substitution of colemanite resulted in an improvement in strength properties and ultrasonic transmission rate test results, and this amount of improvement decreased at higher substitution rates [41].

CONCLUSION

The following results were obtained when the use of boron waste in cementitious systems and the effects on fresh state, mechanical properties and durability performance were examined together.

- It was understood that boron wastes are promising materials in terms of benefiting the properties of cementitious systems by preventing radiation transmission and shielding gamma rays.
- The water requirement and setting time of cementitious systems increased with the use of boron waste and the increase in its usage rate.
- When the use of boron waste exceeds the order of 10%, their compressive strength generally decreases. In this context, it was understood that more suitable results can be obtained by using the waste when calcining at high temperatures.
- It was understood that the freeze-thaw resistance decreases as a result of the increase in the porosity of the cementitious systems with the use of boron.
- It was declared that boron waste improves the resistance of cementitious systems against high temperatures.

Data Availability Statement

All data, models, and code generated or used during the study appear in the submitted article.

Funding

This research did not receive any specific grant from funding agencies in the public, commercial, or not-for-profit sectors.

Conflicts of Interest/Competing Interests

The authors declare that they have no known competing financial interests or personal relationships that could have appeared to influence the work reported in this paper.

REFERENCES

- [1]. Mehta, K. P. (2001). Reducing the environmental impact of concrete. *Concrete international*, 23(10), 61-66.
- [2]. United States Geological Survey (Eua). Departamento do Interior. (2020). Mineral commodity summaries 2020. 06.02. 2020, Reston, VA; <https://pubs.er.usgs.gov/publication/mcs2020>.
- [3]. Gopalakrishna, B., & Dinakar, P. (2023). Mix design development of fly ash-GGBS based recycled aggregate geopolymer concrete. *Journal of Building Engineering*, 63, 105551.
- [4]. Bahmani, H., & Mostofinejad, D. (2023). A review of engineering properties of ultra-high-performance geopolymer concrete. *Developments in the Built Environment*, 100126.
- [5]. Ram, K., Serdar, M., Londono-Zuluaga, D., & Scrivener, K. (2023). Does carbon footprint reduction impair mechanical properties and service life of concrete?. *Materials and Structures*, 56(1), 6.
- [6]. Tahwia, A. M., El-Far, O., & Amin, M. (2022). Characteristics of sustainable high strength concrete incorporating eco-friendly materials. *Innovative Infrastructure Solutions*, 7, 1-13.
- [7]. Koumpouri, D., & Angelopoulos, G. N. (2016). Effect of boron waste and boric acid addition on the production of low energy belite cement. *Cement and Concrete Composites*, 68, 1-8.
- [8]. Christogerou, A., Kavas, T., Pontikes, Y., Koyas, S., Tabak, Y., & Angelopoulos, G. N. (2009). Use of boron wastes in the production of heavy clay ceramics. *Ceramics International*, 35(1), 447-452.
- [9]. Ulutas, D., Bayrakci, E., Cokaygil, Z., Ozkan, A., Guney, Y., & Banar, M. (2014). Geotechnical, chemical and structural characterization of waste clay from boron production. *Athens Journal of Technology Engineering*, 1(3), 171-179.
- [10]. Koroglu, L., Kaman, D. O., & Ayas, E. (2021). Optimizing the particle size distribution of heat-treated boron derivative wastes in cement mortars as Portland cement replacements. *Construction and Building Materials*, 282, 122640.
- [11]. Kok, S., Turetken, M. S., Oksuzer, N., & Gokce, H. S. (2023). Effect of elevated temperature on radiation shielding properties of cement and geopolymer mortars including barite aggregate and colemanite powder. *Materialia*, 101693.
- [12]. Kim, B., Kang, J., Shin, Y., Yeo, T. M., & Um, W. (2022). Immobilization mechanism of radioactive borate waste in phosphate-based geopolymer waste forms. *Cement and Concrete Research*, 161, 106959.
- [13]. Demir, D., & Keles, G. (2006). Radiation transmission of concrete including boron waste for 59.54 and 80.99 keV gamma rays. *Nuclear Instruments and Methods in Physics Research Section B: Beam Interactions with Materials and Atoms*, 245(2), 501-504.
- [14]. Oto, B., & Gur, A. (2013). Determination of mass attenuation coefficients of concretes containing ulexite and ulexite concentrator waste. *Annals of Nuclear Energy*, 59, 72-74.
- [15]. Binici, H., Aksogan, O., Sevinc, A. H., & Kucukonder, A. (2014). Mechanical and radioactivity shielding performances of mortars made with colemanite, barite, ground basaltic pumice and ground blast furnace slag. *Construction and Building Materials*, 50, 177-183.
- [16]. Ozen, S., Durgun, M. Y., Kobya, V., Karakuzu, K., & Mardani-Aghabaglou, A. (2022). Effect of Colemanite Ore Wastes Utilization on Fresh Properties and Compressive Strength of Cementitious Systems. *Arabian Journal for Science and Engineering*, 1-15.



- [17]. Durgun, M. Y., Ozen, S., Karakuzu, K., Kobya, V., Bayqra, S. H., & Mardani-Aghabaglou, A. (2022). Effect of high temperature on polypropylene fiber-reinforced mortars containing colemanite wastes. *Construction and Building Materials*, 316, 125827.
- [18]. Seker, O., & Durgun, M. Y. (2022). Investigation of the effects of colemanite and colemanite concentrator wastes on the rheological and hardened properties of self-compacting concrete. *Archives of Civil and Mechanical Engineering*, 23(1), 50.
- [19]. Sevim, U. K., Ozturk, M., Bankir, M. B., & Aydin, U. (2017). Utilization of colemanite waste in concrete design. *International Journal of Advanced Engineering Research and Science (IJAERS)*, 12.
- [20]. Erdogmus, E. (2014). Combined effect of waste colemanite and silica fume on properties of cement mortar. *Science and Engineering of Composite Materials*, 21(3), 369-375.
- [21]. Osman, G., Witold, B., Cengiz, O., & Muuml; min, F. (2010). An investigation on the concrete properties containing colemanite. *International Journal of Physical Sciences*, 5(3), 216-225.
- [22]. Palomo, A., & dela Fuente, J. L. (2003). Alkali-activated cementitious materials: Alternative matrices for the immobilisation of hazardous wastes: Part I. Stabilisation of boron. *Cement and Concrete Research*, 33(2), 281-288.
- [23]. Shen, Y., Zhang, W., Zhu, H., LI, J., & Shi, S. (2023). Effect of Borax on Calcium Sulfoaluminate Cement Properties. *Ceramics–Silikáty*, 67(1), 10-19.
- [24]. Zheng, Y., Zhou, Y., Huang, X., & Luo, H. (2022). Effect of raw materials and proportion on mechanical properties of magnesium phosphate cement. *Journal of Road Engineering*.
- [25]. Yang, J., & Qian, C. (2010). Effect of borax on hydration and hardening properties of magnesium and potassium phosphate cement pastes. *Journal of Wuhan University of Technology-Mater. Sci. Ed.*, 25, 613-618.
- [26]. Qin, J., Qian, J., Dai, X., You, C., Ma, H., & Li, Z. (2021). Effect of water content on microstructure and properties of magnesium potassium phosphate cement pastes with different magnesia-to-phosphate ratios. *Journal of the American Ceramic Society*, 104(6), 2799-2819.
- [27]. Qin, J., 2019. Study on Preparation and Mechanical Behavior of Ultra-high Strength Magnesium Phosphate Cement Composites (PhD thesis). Chongqing University, Chongqing.
- [28]. Fabian, M., Tolnai, I., Kis, Z., & Szilagyi, V. (2022). Characterization of Simulated Liquid Radioactive Waste in a New Type of Cement Mixture. *ACS omega*, 7(41), 36108-36116.
- [29]. Kozai, N., Sato, J., Osugi, T., Shimoyama, I., Sekine, Y., Sakamoto, F., & Ohnuki, T. (2021). Sewage sludge ash contaminated with radiocesium: Solidification with alkaline-reacted metakaolinite (geopolymer) and Portland cement. *Journal of Hazardous Materials*, 416, 125965.
- [30]. Lee, J., Kim, B., Kang, J., Kang, J., Kim, W. S., & Um, W. (2020). Comparative Study Between Geopolymer and Cement Waste Forms for Solidification of Corrosive Sludge. *Journal of Nuclear Fuel Cycle and Waste Technology (JNFCWT)*, 18(4), 465-479.
- [31]. Ozdemir, M., & Ozturk, N. U. (2003). Utilization of clay wastes containing boron as cement additives. *Cement and Concrete Research*, 33(10), 1659-1661.
- [32]. Olgun, A. S. I. M., Kavas, T., Erdogan, Y., & Once, G. (2007). Physico-chemical characteristics of chemically activated cement containing boron. *Building and environment*, 42(6), 2384-2395.



- [33]. Yon, M. S., & Karatas, M. (2022). Evaluation of the mechanical properties and durability of self-compacting alkali-activated mortar made from boron waste and granulated blast furnace slag. *Journal of Building Engineering*, 61, 105263.
- [34]. Phoo-ngernkham, T., Hanjitsuwan, S., Suksiripattanapong, C., Thumrongvut, J., Suebsuk, J., & Sookasem, S. (2016). Flexural strength of notched concrete beam filled with alkali-activated binders under different types of alkali solutions. *Construction and Building Materials*, 127, 673-678.
- [35]. Huseien, G. F., Mirza, J., Ismail, M., & Hussin, M. W. (2016). Influence of different curing temperatures and alkali activators on properties of GBFS geopolymer mortars containing fly ash and palm-oil fuel ash. *Construction and Building Materials*, 125, 1229-1240.
- [36]. Celik, A., Yilmaz, K., Canpolat, O., Al-Mashhadani, M. M., Aygormez, Y., & Uysal, M. (2018). High-temperature behavior and mechanical characteristics of boron waste additive metakaolin based geopolymer composites reinforced with synthetic fibers. *Construction and Building Materials*, 187, 1190-1203.
- [37]. Aygormez, Y., Canpolat, O., & Al-mashhadani, M. M. (2020). Assessment of geopolymer composites durability at one year age. *Journal of Building Engineering*, 32, 101453.
- [38]. Durgun, M. Y., & Sevinc, A. H. (2019). High temperature resistance of concretes with GGBFS, waste glass powder, and colemanite ore wastes after different cooling conditions. *Construction and Building Materials*, 196, 66-81.
- [39]. Bideci, O. S. (2016). The effect of high temperature on lightweight concretes produced with colemanite coated pumice aggregates. *Construction and Building Materials*, 113, 631-640.
- [40]. Ali, N., Canpolat, O., Aygormez, Y., & Al-Mashhadani, M. M. (2020). Evaluation of the 12–24 mm basalt fibers and boron waste on reinforced metakaolin-based geopolymer. *Construction and Building Materials*, 251, 118976.
- [41]. Topcu, I. B., & Boga, A. R. (2010). Effect of boron waste on the properties of mortar and concrete. *Waste management & research*, 28(7), 626-633.

Investigation of Thermal Performance of a Ground Coupled Carbonated Soft Drink Cooling System with an Underground Thermal Energy Storage Tank

Ahmed Wshyar Rasool¹, Hatem Hasan Ismaeel², Recep Yumrutas³

Abstract

This study investigates the thermal performance of a ground coupled carbonated soft drink cooling system with an underground thermal energy storage tank. The system is composed of three main components: a chiller unit, a thermal energy storage (TES) tank, and a syrup room to be cooled. An analytical model was developed to determine the thermal performance parameters of the system using Duhamel's superposition and dimensionless variables to solve the transient heat transfer problem around the TES tank. The analytical model includes energy expressions for the main components as well as a solution to the heat transfer problem surrounding the TES tank. The hourly temperature variation of water in the TES tank and other performance parameters, such as Coefficient of Performance (COP), are calculated. To do this, a simulation model was developed using MATLAB software. The study investigated the effect of various system parameters such as the size of the underground thermal energy storage tank, soil type, and Carnot factor on the thermal performance of the system. The findings reveal that granite is the most efficient type of soil for the cooling process and that COP increases with increasing Carnot Factor and tank size. The results indicate that the ground coupled carbonated soft drink cooling system with an underground thermal energy storage tank is a feasible and energy-efficient solution for providing cooling for carbonated soft drinks. The system has the potential to reduce energy consumption and greenhouse gas emissions associated with traditional cooling systems.

Keywords: Duhamel's superposition; Energy; Energy storage; Ground coupled chiller; Syrup room; TES.

¹ Department of Mechanical Engineering, Gaziantep University, Gaziantep, 27310, Turkey. ahmed.wshyar@alumni.ais.edu.krd

² Department of Energy Engineering, Technical College of Engineering, Duhok Polytechnic University, Duhok, Iraq. hatem.hasan@dpu.edu.krd

³ Department of Mechanical Engineering, Gaziantep University, Gaziantep, 27310, Turkey. yumrutas@gantep.edu.tr



1. INTRODUCTION

Chillers are heat transfer devices used to extract heat from a fluid or process by a vapor-compression refrigeration cycle and exhaust that heat into the atmosphere or surrounding environment. There are two conventional types of chillers, based on their condensation processes, used in the various industrial and residential applications. Air-cooled chillers exchange heat with the ambience during the condensation process, and water-cooled chillers use cooling towers to which heat is rejected. An important application in which both types of chillers have been used is the cooling of Carbonated Soft Drinks (CSD). A viable potential solution to this problem is the application of ground coupled cooling systems. Ground coupled cooling systems can operate at higher COP values in summer since heat is rejected to a sufficient depth of ground where the temperature is lower and relatively constant.

Nomenclature

c	specific heat of earth ($\text{kJ kg}^{-1} \text{K}^{-1}$)
c_{pa}	specific heat of air ($\text{kJ kg}^{-1} \text{K}^{-1}$)
c_w	specific heat of water ($\text{kJ kg}^{-1} \text{K}^{-1}$)
k	thermal conductivity of earth ($\text{W m}^{-1} \text{K}^{-1}$)
P	dimensionless, $P = \frac{\rho_w c_w}{3\rho c}$
q	dimensionless heat transfer to the tank
Q	heat transfer to the tank (W)
\dot{Q}_L	heat gain to the syrup room (W)
r	radial distance from the tank centre (m)
R	tank radius (m)
x	dimensionless radial distance
t	time (s)
T	earth temperature (K)
T_a	ambient air temperature (K)
T_o	outside design air temperature (K)
T_w	water temperature in the tank (K)
T_c	water temperature in fan coil unit (K)
T_∞	deep ground temperature (K)
u	dimensionless parameter for design condition
$(UA)_H$	product of heat transfer coefficient and area of syrup room (W K^{-1})
$(UA)_{FC}$	product of heat transfer coefficient and area for fan coil (W K^{-1})
V	volume of the tank (m^3)
w	dimensionless compressor work
W	compressor input power (W)

Greek Letters

α	thermal diffusivity of the soil ($\text{m}^2 \text{s}^{-1}$)
β	Carnot factor
η_c	Carnot efficiency
ϕ	dimensionless temperature for earth, $\frac{T-T_\infty}{T_\infty}$
ϕ	dimensionless design inside air temperature
ϕ_a	dimensionless ambient air temperature
ϕ_w	dimensionless water temperature in the tank
ψ	dimensionless temperature
γ	dimensionless parameter, $4\pi Rk/(UA)_H$
ρ	density of soil (kg m^{-3})
ρ_w	water density (kg m^{-3})
τ	dimensionless time, $\tau = \frac{\alpha t}{R^2}$



Ground coupled heat pump systems use the same principle in winter to get higher COP values over air source systems by using higher heat sink temperatures of the ground. Accordingly, ground coupled cooling systems have high potential to prove to be energy efficient systems in the industry and could provide an alternative to conventional chiller systems, especially in the food and beverage production sectors.

There have been several research and experimental work done to improve the COP of cooling systems in industries and buildings as well as investigations on ground coupled heat pump systems for the optimization of thermal energy storage systems. Rosen et al. [1] evaluated cold thermal storage systems in terms of energy and exergy analyses. Yumrutas et al. [2] determined the annual periodic performance of a space cooling system employing a spherical underground thermal energy storage tank and a ground coupled chiller system by developing a computational model. De Swardt and Meyer [3] conducted an experimental and simulation based comparison between the performances of a conventional air source heat pump system and a reversible ground coupled heat pump connected to a municipality water reticulation system for both cooling and heating applications. Their results indicated the validity of using ground source heat pumps to optimize the consumption of energy in the air conditioning sector. Kuyumcu et al. [4] developed an analytical model to obtain the long

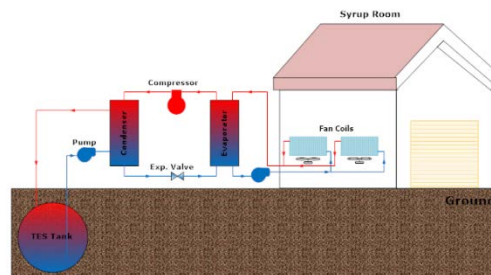


Fig.1 Schematic of the Cooling System with Underground Spherical TES Tank

Fig.2 Schematic of the Energy Balance around the TES tank

period performance of a swimming pool heating system by utilizing waste or surplus heat energy that is rejected from a chiller unit of an ice rink and subsequently stored in an underground thermal energy storage (TES) tank using Duhamel's superposition and similarity techniques. They found that it takes the swimming pool heating system five to seven years to attain regular operation. Also, the outcomes demonstrated that the heating system's effectiveness is at its peak when the ice rink surface area is 475 m² and the swimming pool area is 625 m². Zogou and Stamatelos [5] discovered that warmer Mediterranean conditions are well suited for heating and cooling applications of heat pump systems after studying the effects of climatic conditions on their performance. Yumrutas and Unsal [6] developed an analytical and computational model based on hourly operation to determine performance parameters of a house heating system utilizing a heat pump and a spherical underground TES tank. Tutumlu et al. [7] developed an analytical and computational model for an ice rink cooling system with a spherical underground TES tank and obtained the solution of the thermal energy storage tank problem using a similarity transformation and Duhamel superposition techniques. Ismael and Yumrutas



[8] investigated the performance of a solar assisted heat pump wheat drying system with underground thermal energy storage tank by developing a mathematical model to find performance parameters on an hourly basis. The results indicate that the system reaches periodic operation from fifth year onward and that earth type has significant impact on the performance of the system. Soyulu et al. [9] investigated the effects and effectiveness of evaporative cooling on air-cooled chiller systems; their findings illustrate that the COP of the system increased by reducing the inlet air temperature of the air-cooled condenser by pre cooling the air entering the condenser. However, it is also evident that it was more difficult to cool the air when relative humidity of the outside air increased, leading to a decrease in the COP of the system. Thus, evaporative cooling is most effective in hot and dry climates when the effectiveness of the evaporative cooler is highest to provide a useful solution to decrease condenser inlet air temperature. Yang et. al. [10] performed an analytical and experimental investigation on the application of water mist evaporative pre-cooling to air-cooled chillers to improve the chiller plant efficiency. Their experimental results showed that the inlet condenser air temperature with water mist pre-cooling could drop by up to 9.4 K from the ambient air temperature. The pre-cooled condenser air enabled a drop of the condensing temperature by up to 7.2 K, and the chiller coefficient of performance (COP) could be improved in varying degrees by up to 18.6%.

2. Modeling of the System

The system under study is represented schematically in Figure 1 and consists of a chiller that uses a vapor compression refrigeration cycle, a spherical underground thermal energy storage (TES) tank, and the syrup room that needs to be cooled. The refrigeration cycle uses the TES tank as a heat sink. Heat is transferred to water in the TES tank by the refrigerant as it absorbs heat from the cooled space in the evaporator, compresses in the compressor, and releases heat. It is assumed that the chiller is a water-to-water type, where water circulates in the fan-coil unit of the evaporator and heat is rejected to storage water in the condenser. Because the TES tank's water temperature is lower than the surrounding air's temperature and experiences fewer temperature changes than an air source system, this ground-coupled space cooling system is anticipated to have greater coefficient of performance (COP) values than an air source system. The system is considered to be installed in Erbil-Iraq.

2.1 Solution of the Transient Temperature Distribution Outside the TES Tank

It is presumed that the TES tank is spherical, water-filled, and situated underground. The water in the tank is considered to be fully mixed at a spatially aggregated time-varying temperature $T_w(t)$. At the beginning, the tank is at the deep ground temperature T_∞ . The earth is thought to have a uniform structure and stable thermal characteristics. The periodic transient heat transfer issue outside the spherical TES tank can be written as a one-dimensional partial differential equation with boundary and initial conditions using the spherical coordinate system:

$$\frac{\partial^2 T}{\partial r^2} + \frac{2}{r} \frac{\partial T}{\partial r} = \frac{1}{\alpha} \frac{\partial T}{\partial t} \quad (1)$$

$$T(R, t) = T_w(t) \quad (2)$$

$$T(\infty, t) = T_\infty \quad (3)$$

$$T(r, 0) = T_\infty \quad (4)$$

The energy transferred to the tank is equal to the energy gain in the tank and the heat loss from the tank through conduction to the earth around it. The equation below can be used to express this relationship:

$$Q = \rho_w c_w V_w \frac{dT_w}{dt} - kA \frac{\partial T}{\partial r}(R, t) \quad (5)$$

where ρ_w , c_w , and V_w stand for the volume, density, and specific heat of the water in the tank, respectively, and k , R , and A stand for the radius, surface area, and thermal conductivity of the soil surrounding the tank, respectively.

The following variables can be used to define the transient heat transport issue outlined by equations (1) through (5) in a dimensionless form:

$$x = \frac{r}{R} \quad \tau = \frac{\alpha t}{R^2} \quad q = \frac{Q}{4\pi R k T_\infty} \quad p = \frac{\rho_w c_w}{3\rho c}$$



$$\begin{aligned}\phi &= \frac{T-T_\infty}{T_\infty} & \phi_w &= \frac{T_w-T_\infty}{T_\infty} \\ \phi_a &= \frac{T_a-T_\infty}{T_\infty}\end{aligned}\quad (6)$$

the variables x , τ , ϕ , and q in the equations denote the dimensionless parameters of radial distance, time duration, temperature, and net energy transmitted to the tank, respectively. Moreover, r and c stand for the density and the specific heat of the ground, correspondingly. The letters "w" and "a" stand for water and surrounding air, respectively. The following expressions can be generated by substituting these equations into the expressions given in Eqs. (1) through (6), and simplified using the following transformation:

$$\psi(x, \tau) = x\phi(x, \tau) \quad (7)$$

$$\frac{\partial^2 \psi}{\partial x^2} = \frac{\partial \psi}{\partial \tau} \quad (8)$$

$$\psi(1, \tau) = \phi_w(\tau) \quad (9)$$

$$\psi(\infty, \tau) = 0 \quad (10)$$

$$\psi(x, 0) = 0 \quad (12)$$

$$q = p \frac{d\phi_w}{d\tau} - \frac{\partial \phi}{\partial x}(1, \tau) \quad (13)$$

Using Duhamel's superposition approach, the following unsteady temperature distribution in the ground surrounding the TES tank is obtained:

$$\psi(x, \tau) = \phi_w(0) \left\{ 1 - \operatorname{erf} \left(\frac{x-1}{2\sqrt{\tau}} \right) \right\} + \int_0^\tau \frac{d\phi_w(\xi)}{d\xi} \left\{ 1 - \operatorname{erf} \left(\frac{x-1}{2\sqrt{\tau}} \right) \right\} d\xi \quad (14)$$

differentiating ϕ with regards to x , at $x=1$, and solving in dimensionless form for the temperature of water in the tank at the n th time increment, we get:

$$\begin{aligned}\phi_w(\tau_n) &= q(\tau_n) + \left[\frac{P}{\Delta\tau} + \frac{1}{\sqrt{\pi\Delta\tau}} \right] \phi_w(\tau_{n-1}) - \sum_{i=1}^{n-2} \frac{\phi_w(\tau_{i+1}) - \phi_w(\tau_i)}{\sqrt{\pi\Delta\tau}(n-i)} / 1 + \frac{P}{\Delta\tau} \\ &+ \frac{1}{\sqrt{\pi\Delta\tau}}\end{aligned}\quad (15)$$

To determine the hourly dimensionless water temperature, Equ. (15) is used, where $q(\tau)$ is the net dimensionless heat input rate to the tank.

2.2 Modeling of the Chiller Unit

The evaporator, compressor, condenser, and expansion device are the four parts that make up the refrigeration process that powers the cooling system. The condenser transfers heat to the TES tank, while the evaporator takes heat from the syrup room to be cooled. It is vital that the chiller must absorb all of the heat the house produces so the cooling load can be expressed as:

$$Q_L(t) = (UA)_H(T_a - T_i) \quad (16)$$

where T_a is the average of the highest summer design temperature and T_i is the interior design temperature, and $(UA)_H$ is the product of the total heat transfer coefficient for the storage and the heat transfer area.

The fan-coil unit's specifications can also be used to express the cooling load as follows:

$$Q_L(t) = (UA)_{FC}(T_i - T_c) \quad (17)$$

T_c is the average water temperature inside the fan-coil unit, and $(UA)_{FC}$ is the multiplication of the cooling system's overall heat transfer coefficient by the heat transfer area.

The chiller's COP is expressed by:

$$COP = \frac{Q_L(t)}{W(t)} = \frac{Q_L(t)}{Q_H(t) - Q_L(t)} \quad (18)$$



As a function of Carnot efficiency, COP may be given as:

$$COP = \beta \frac{T_c}{T_w - T_c} \quad (19)$$

where β is the Carnot factor, which ranges from 0 to 1. T_c can be solved for by combining Equ. (16) and Equ. (17). Plugging it into Equ. (19) and converting it into dimensionless form, yields:

$$COP = \beta \left[\frac{u(\phi_i - \phi_a(\tau)) + \phi_i + 1}{u(\phi_a(\tau) - \phi_i) + \phi_w(\tau) - \phi_i} \right] \quad (20)$$

The compressor's work may be expressed as:

$$W(t) = \frac{Q_L(t)}{COP} = \frac{(UA)_H(T_a(t) - T_i)}{COP} \quad (21)$$

By plugging Equ. (20) into Equ. (21) and converting the temperatures into dimensionless form, we get:

$$w(t) = \frac{W(t)}{(UA)_H T_\infty} = \frac{(\phi_a(t) - \phi_i) \cdot [u(\phi_a(t) - \phi_i) + \phi_w(t) - \phi_i]}{\beta [u(\phi_i - \phi_a(t)) + \phi_i + 1]} \quad (22)$$

The parameter u may be expressed as:

$$u = \frac{(UA)_H}{(UA)_{HE}} = \frac{T_i - T_c}{T_a - T_i} \quad (23)$$

2.3 Modeling of the Syrup Room

To obtain the overall heat transfer coefficient and calculate the cooling load for the syrup storage room, the following equations are used:

$$Q_{(\tau)} = U * A * (T_o(t) - T_i) \quad (24)$$

Where $Q_{(\tau)}$, U , A , $T_o(t)$, and T_i are the heat gain (W/h), overall heat transfer coefficient (W/m².°C), surface area of the cold storage room (m²), outside temperature of atmosphere air (°C), and inside temperature of cold storage air (°C), respectively.

To find the overall heat transfer coefficient for the syrup room, the following equations and data are used:

$$U = \frac{1}{R_{total}} \quad (25)$$

$$R_{total} = \frac{1}{h_i} + \frac{X_1}{K_{Al}} + \frac{X_2}{K_{Foam}} + \frac{X_3}{K_{Al}} + \frac{1}{h_o} \quad (26)$$

R_{total} , h_i , X_1 , K_{Al} , X_2 , K_{Foam} , X_3 , and h_o are over all thermal resistance, convective heat transfer coefficient of inside air, aluminum plate thickness, thermal conductivity of aluminum, polyisocyanurate foam thickness, thermal conductivity of the foam, aluminum plate thickness, and convective heat transfer coefficient of outside air, respectively. Transmission load is the heat that is transferred into the refrigerated space through its surface. The size of the syrup room is 41 m length x 9.75 m width x 12 m height. The total area of the walls and roof is equal to: 1617.75 m².

3. Input Data and Computational Procedure

In the part before, an analytical model was established, and a MATLAB computer program was made based on this model for numerical computations. The program is used to compute the hourly coefficient of performance of the chiller as well as the temperature distribution in the earth surrounding the storage tank, and transient temperature of water in the storage tank.

The starting storage temperature is considered to be 15°C, the same as the deep earth temperature at the beginning of the calculations, and the summer indoor design air temperature is assumed to be 25°C. With the Photovoltaic Geographical Information System (PVGIS) Online Tool, the average hourly outdoor air temperature may be determined. The average value obtained for each month represents the highest ambient air

temperature. The product of the overall heat transfer coefficient and the area of the syrup room (UA_H) is determined to be $705 \text{ W/}^\circ\text{C}$, with the summer cooling load being roughly 15 kW .

Based on design conditions, the u value in Eqs. (20) and (22) is calculated as 1.2. Zogou and Stamatelos [13] noted that small electric heat pumps typically have CF ratings between 0.30 and 0.50. Three CF values (0.30, 0.40, and 0.50) were consequently used in this study. Unless otherwise stated, the study has assumed a CF value of 0.4 and a tank volume of 400 m^3 for all computations. The water in the TES tank is thought to be evenly mixed. The water has a specific heat of $4.18 \text{ kJ/kg}^\circ\text{C}$ and a density of 1000 kg/m^3 , respectively. The water temperature is considered to be $15 \text{ }^\circ\text{C}$, the temperature of the deep ground, at the beginning of the system's operation. Three types of soil are taken into account in the study: limestone, clay, and granite, which evaluates the effect of soil type on system performance.

4. Results and Discussions

Due to different thermophysical qualities, the performance parameters of each earth surrounding the TES tank change. The TES tank's water temperature variation is one of these performance criteria. As a result, the storage temperature affects every performance parameter.

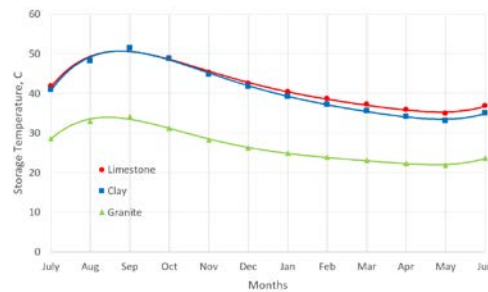


Fig.3 Effect of Soil Type on Annual Variation of Water Temperature in the TES Tank during the Tenth Year

These properties have led to the observation that materials with lower thermal conductivity and diffusivity, like limestone, inhibit the transfer and dispersion of heat from the TES (thermal energy storage) tank to the surrounding ground. Figures 4 and 5 show the effects of the soil types on the TES tank storage temperature and the COP for the ten years of operation, respectively. It is evident from these figures that granite is the most efficient type of soil for the cooling system. This is mainly due to its thermos-physical properties of having higher thermal conductivity and thermal diffusivity, allowing faster heat rejection into the surrounding earth. It should be noted, however, that the soil type for the real case at the power plant location is clay, which operates with reasonable values and is used in most of the following figures.

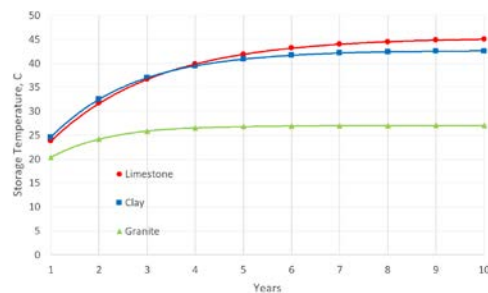


Fig.4 Annual Storage Temperature Variations for Different Earth Types

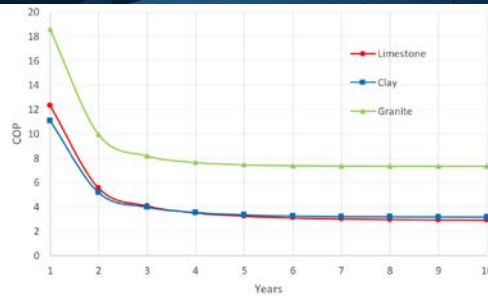


Fig.5 Effect of Soil Types on COP for Ten Years of Operation

The annual variations in the tank's water temperature are shown in Figure 6 for years one, five, and ten. A rapid temperature swing occurs in the tank from the first year of operation. Although the temperature steadily rises until the fifth year of operation, it then stays almost constant. As a result, it may be said that the system transitions to an annually periodic regime in the fifth year. As it can be observed, the values of years 5 and 10 are almost identical, meaning that the temperature does not undergo much change from the fifth year onward.

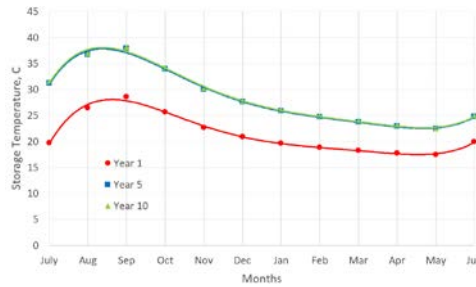


Fig.6 TES Tank Temperature Variations with Operation Time for Three Years

The progression toward an annual periodic regime is also shown in Figure 7. The temperature varies notably, especially in the first and second years, but after the fifth onward, when the storage temperatures are comparable to those of the sixth year, it stabilizes. These numbers give us crucial information about how long the transient period lasts until we get to the annually periodic phase.

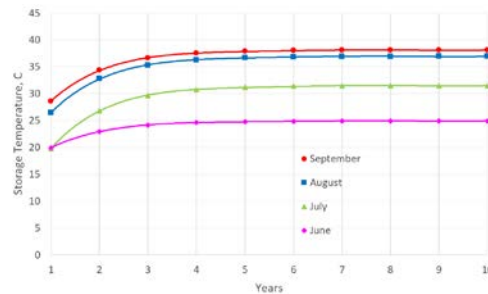


Fig.7 Storage Temperature Variations with Operating Time for Cooling Months

The volume of the TES tank has an impact on the system's performance. Figures 8 and 9 have been supplied to examine how tank volume affects storage temperature. Figure 8 shows the annual oscillations in the TES tank's water temperature with respect to tank volume. The graph shows that the storage temperature and the amplitude of water temperature both decrease as tank volume grows. The highest storage temperatures are found at the end of the summer season in the smallest tank sizes. By the end of August, the storage temperature rises to about 30 °C when the storage capacity is 400 m³.

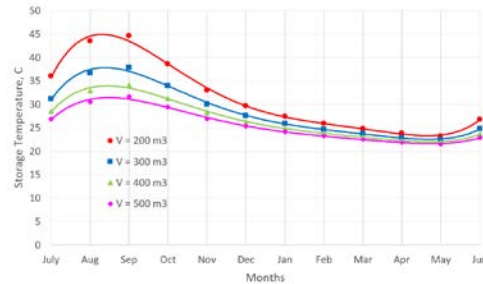


Fig.8 Annual Temperature Variation of Storage Water with Tank Volume in the Fifth Year

Larger tanks are preferable because they allow for higher heat dissipation from TES tank to surrounding earth, which keeps the storage temperature lower. It is obvious that the storage temperature decreases with tank size. While choosing the right tank size, however, economic factors should be taken into account because choosing a larger tank implies a higher initial cost. A TES tank with a volume of 400 m^3 is appropriate because less storage space is needed and a lower initial investment is preferred.

The relationship between tank volume and storage temperature is shown in Figure 9, which shows the yearly variation in storage temperature for tanks with sizes of 200, 300, 400, and 500 m^3 . The graph illustrates that the temperature is relatively lower in the first three years but increases afterward and stabilizes after the fifth year onward. As shown in Figure 10, the COP of the heat pump will drop as the temperature rises with decreasing volume.

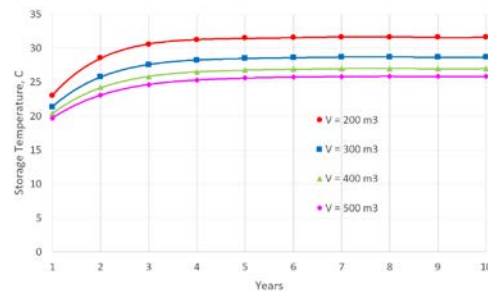


Fig.9 Variation of TES Tank Temperature during September

5. Conclusions

The thermal performance of a CSD cooling system that uses an underground TES tank was examined in this study. The system's components were expressed theoretically, and the performance characteristics of the system were constructed using a mathematical model. To evaluate the effect of input parameters on the system performance, a MATLAB program was developed. The analytical model discussed in this study is useful for forecasting the long-term performance of a refrigeration system for industrial applications in CSD cooling of a storage, that includes an underground spherical TES tank. In order to estimate storage tank temperatures and COP of the heat pump, the model takes into account a variety of system factors, including Carnot factor and storage volume. According to the findings, this system operates at a higher thermodynamic efficiency than conventional air source refrigeration systems. The following is a summary of the study's main conclusions:

Performance indicators like the water temperature in the TES tank and the COP of the heat pump for the load gradually rise from the beginning of the cooling operation until the fifth year, when it runs on a periodic basis. According to the study, it takes about five years for the system parameters taken into account in the research to establish an annually periodic operating regime.

The type of earth or thermos-physical properties of the geological structure around the underground TES tank have a significant impact on the cooling system's performance. As a result, it is suggested that a suitable location is carefully picked for the installation of such cooling systems.

When the storage size is reduced, the temperature amplitude increases.

With a cooling load of approximately 15 kW, a heat pump's COP ranging from 4 to 15, and a clay earth type, a storage tank volume of 400 m^3 is deemed to be an appropriate amount for chilling the syrup room for the climatic circumstances of Erbil's Coca-Cola Plant.

References

- [1]. Rosen, M. A., Pedinelli, N., & Dincer, I. (1999). Energy and exergy analyses of cold thermal storage systems. *International Journal of Energy Research*, 23(12), 1029–1038.
- [2]. Yumrutas, R., Kanoglu, M., Bolatturk, A., & Bedir, M. S. (2005). Computational model for a ground coupled space cooling system with an underground energy storage tank. *Energy and Buildings*, 37(4), 353–360.
- [3]. De Swardt, C. A., & Meyer, J. P. (2001). A performance comparison between an air-source and a ground-source reversible heat pump. *International Journal of Energy Research*, 25(10), 899–910.
- [4]. Kuyumcu, M. E., Tutumlu, H., & Yumrutas, R. (2016). Performance of a swimming pool heating system by utilizing waste energy rejected from an ice rink with an energy storage tank. *Energy Conversion and Management*, 121, 349–357.
- [5]. Zogou, O., & Stamatelos, A. (1998). Effect of climatic conditions on the design optimization of heat pump systems for space heating and cooling. *Energy Conversion and Management*, 39(7), 609–622.
- [6]. Yumrutas, R., Unsal, M (2012). *Energy Education Science and Technology Part A: Energy Science and Research 2012* Volume 28(2): 669-682
- [7]. Tutumlu, H., Yumrutas, R., & Yildirim, M. (2017). Investigating thermal performance of an ice rink cooling system with an underground thermal storage tank. *Energy Exploration & Exploitation*, 36(2), 314–334.
- [8]. Hasan Ismaeel, H., & Yumrutas, R. (2020). Investigation of a solar assisted heat pump wheat drying system with underground thermal energy storage tank. *Solar Energy*, 199, 538–551.
- [9]. Soylu, S.K., Atmaca, I., & Dogan, A. (2016). Investigation of Evaporative Cooling Effectiveness on The Performance of Air – Cooled Chillers.
- [10]. Yang, J., Chan, K. T., Wu, X., Yang, X., & Zhang, H. (2012). Performance enhancement of air-cooled chillers with water mist: Experimental and analytical investigation. *Applied Thermal Engineering*, 40, 114–120.

Land Cover And Land Use Classification Of Patch-Based Denoised Sar Images

Elif Meseci¹, Caner Ozcan^{2}, Buse Yaren Tekin³*

Abstract

Land cover and land use information contributes to the research of important environmental issues such as the change of forest areas on the earth over the years, the determination of the increase and decrease in the amount of water, the detection of irregularities on the earth, the determination of damage after natural disasters. Synthetic Aperture Radar (SAR) systems, which can provide images in all weather conditions without being affected by changes in weather events, are preferred for obtaining images. Classification of SAR images is crucial to the analysis of these images. Developing technology allows the recording and interpretation of many high-dimensional SAR images. Since SAR images represent large areas, the objects in the image take up a very small area. The study includes the use of a patch-based approach to classifying these areas. In the proposed study, despeckling was applied to remove speckle noise which may occur in SAR images due to scattering. Denoised and original SAR images were classified with the deep learning algorithm, and comparative results of the classification performance of the noise filtering were obtained. Experimental results have proven that the despeckling significantly impacts classification performance.

Keywords: synthetic aperture radar (SAR); remote sensing; deep learning; land classification; image processing; despeckling

1. INTRODUCTION

Synthetic Aperture Radar (SAR) is frequently used in applications such as geographical, biological, and physical surveys of the Earth and tracking changes in landforms. It is a high-resolution radar system that can be used on manned and unmanned aerial platforms and is preferred because it is not affected by factors such as weather conditions [1]. The SAR imaging system is based on the idea of using an antenna array instead of a large antenna to achieve high resolution [2]. In addition, this imaging system, which is not affected by the light factor, has advantages such as adaptability to all weather conditions. However, SAR imagery is harder to interpret than optical imagery [3]. The SAR system is integrated into a satellite or aircraft and is moved forwards in orbit at a certain speed, and during this movement, it sends signals to the Earth for a certain period of time. The reflected signals from the transmitted signals are collected by the radar system, recorded in the appropriate format, and combined. In this way, artificial aperture radar images are created. However, signals reflected from a large number of scatterers in the image pixels can create bright spots in the image. Such situations that may occur in images make it difficult to detect objects. The fact that SAR images represent a wide area is another factor that makes it difficult to analyze, interpret and search with the human eye. Such

¹ Zonguldak Bulent Ecevit University, Department of Computer Engineering, Zonguldak, Turkey, elifmeseci@beun.edu.tr

² Corresponding author: Karabuk University, Department of Software Engineering, Karabuk, Turkey. canerozcan@karabuk.edu.tr

³ Kastamonu University, Department of Computer Technologies, Kastamonu, Turkey, bytekin@kastamonu.edu.tr

situations reveal the need for deep learning models that make the analysis process efficient and provide high accuracy in object detection.

Deep learning models are frequently used in tasks such as image classification and object detection. Automatic feature extraction of deep learning models, a subtype of machine learning approach, enables it to get ahead of machine learning models [4]. Deep Neural Networks (DNNs) are defined as artificial neural networks with additional depth, that is, with an increasing number of hidden layers between the input and output layers [5]. Convolutional Neural Networks (CNNs) are a subcategory of DNNs that allow complex data to go through mathematical operations. CNNs are computationally efficient models with special convolution and pooling operations for detecting objects by analyzing images. CNNs can solve computational complexity and high dimensionality problems by applying various convolution functions to the pixels of the images. The ability of CNNs to classify using fewer parameters compared to other neural networks ensures that they are trained in a shorter time and have less computational complexity [6]. Thanks to these advantages, CNNs are used in the classification of SAR images. When the literature is examined, it has been seen that deep learning models are used on SAR images in many studies, such as the detection of military vehicles, target recognition system, detection of ships, detection of oil spills, land use classification, bridge detection system [3],[7]-[10].

The primary purpose of the study is to evaluate the effect on performance of using the despeckling as a pre-process in the classification of SAR images. In the study, the classification of five different land use and land cover classes is carried out: alongside, building, vegetation, road, and water. The SAR image in which the dataset was created was taken from the publicly available TerraSAR-X spotlight image archive. The acquired SAR image is divided into classes following a patch-based approach by clipping it into smaller pieces with distinctive and independent features. In order to compare the images divided into classes, a separate dataset was created by applying the despeckling, which removes the speckle noise caused by natural factors, such as light, in the SAR images. The classification model was trained on denoised and original datasets under the same conditions and parameters. The performance of the classification model was then evaluated by measuring its accuracy, precision, recall and, f1-score metrics. Thus, the extent to which the classification performance can be improved by pre-processing the SAR images with the despeckling has been investigated.

2. MATERIALS AND METHODS

2.1. Dataset and Pre-processing

Images with open-source access in the TerraSar-X Spotlight image archive were used in the study. Although these images have high resolution and high dimensions, they include areas in five different land cover and use categories: alongside, building, vegetation, road, and water classified. Detecting and classifying these areas in images representing high-dimensional and large areas, such as SAR images, is a challenging task. In the study, a patch-based approach was followed so that these areas could be taught to the model, and the model could focus on objects by avoiding unnecessary feature learning. While following the patch-based approach, attention was paid to the fact that the images obtained were independent and had different features. In this context, in the algorithm created by using the sliding window method to divide the image into patches, it is ensured that the patches contain pixels different from each other. According to the coordinate information of the images divided into patches, the categories they belong to were determined. Then the data set was created by dividing them into categories of alongside, building, vegetation, road, and water. The dataset comprises 7200 images from five classes, including 5040 images train, 1440 images validation, and 720 images test set. Each class consists of the same number of images, and Figure 1 shows examples of each class.

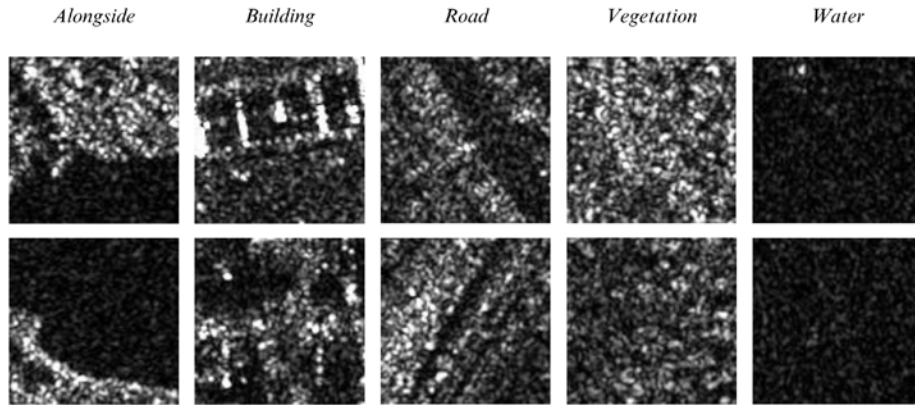


Figure 1. Example images of each class from the dataset

2.2. Speckle Filtering

Speckle filtering has been inevitable when dealing with applications involving amplitude or intensity images obtained by other systems, especially SAR images [11]. In this study, Sparsity Driven Despeckling (SDD) [12], a successful SAR noise removal filter that has made a significant contribution in the literature, was used. SDD method preserves features such as edge and point scattering in images, provides a successful smoothing function in homogeneous regions, and applies the total variation approach using different norms. Therefore, the speckle filtering structure is considered a step before generating the feature vectors. The SDD filter attached to three parameters that control the despeckling level. In addition, the SDD method proposes a method that makes it possible to make the total variation regulator term as l_0 -norm, fractional norm, and l_1 -norm [12].

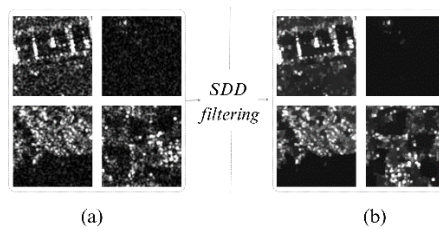


Figure 2. Example images from the unfiltered dataset and the SDD filtered dataset. (a) Raw images of the original dataset, (b) pre-processed images of the original dataset.

Figure 2 shows sample class images from the original dataset, which were then pre-processed with the SDD filter for despeckle. Accordingly, it was concluded that the speckles in the pre-processed SAR images were eliminated to a certain extent. In particular, the difficulty of detecting changes in SAR images has been addressed due to the complex nature of the terrain environment and the fact that SAR images suffer from speckle noise [14]. The performance results of noiseless and noisy images were obtained and compared by choosing the same parameters for the model architecture determined for this study.

2.3. Model Architecture

The architecture of the Inception-ResNet-v2 [13] CNN model proposed for this study is given in Figure 3. The Inception-ResNet-v2 model is a variation of the Inception network and consists of deep CNN layers. The model is highly configurable and has an architecture of many possible changes in the number of filters in the various layers that do not affect the quality of the fully trained network. The second version of the selected network is because of the use of more suitable Inception blocks than the original Inception network. It is followed by a filter expansion layer (1×1 convolution) used to match the input depth before adding each

Inception block. This is necessary to compensate for the dimensionality reduction caused by the Inception block [13].

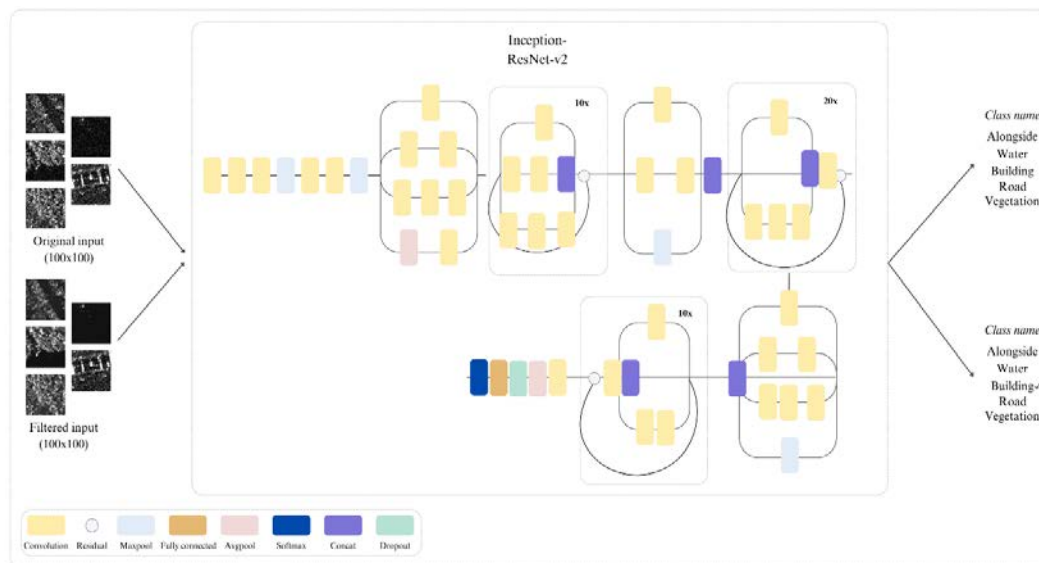


Figure 3. Visualization of Inception-ResNet-v2 model architecture

Combined with the ResNet architecture of residual blocks, the Inception model uses batch normalization only on top of traditional layers. The neural network whose visualization is given in Figure 3 has 54,336,736 parameters. The model is 164 layers deep. It is also known that the residual blocks in the mesh provide a better understanding of the image of the deeper mesh [14]. As in Figure 3, which includes the layers of the proposed network in detail, the SAR images given as input to the neural network are provided in 100x100 dimensions. The first layers in the network consist of 3 standard convolutional layers and a maximum pooling layer, then again two convolutional layers and a maximum pooling layer. In the next step, the convolved structure, an initial convolution, surrounds and combines simultaneously using filters of different sizes for each convolution operation. The convolved layers in the figure are repeated 10 or 20 times. In this case, the network uses dropout layers to drop random weights to avoid overfitting [14].

3. RESULTS AND DISCUSSION

In order to determine the experimental findings in this study, the NVIDIA Tesla T4 graphics card of the Colaboratory tool offered by Google is used. The pre-trained Inception-ResNet-v2 model was trained on both the original and SDD-filtered datasets. All parameters used during the training were adjusted in the same way to be suitable for comparison. In addition, to compare the classification performances, two datasets consist of exactly the same data; one dataset consists of original images, while the other dataset consists of images with SDD filtering. Thus, it is possible to examine the effect of the SDD filter, which performs despeckling on SAR images, on classification performance. The performance measurement metrics of the classification model on the dataset consisting of original images are given in Table 1. The precision, recall, and f1-score metrics values for each class were given, and the accuracy value of the classification model was calculated as 91.16%. In addition, the overall precision, recall, and f1-score metrics of the classification model on all classes are 90.87%, 90.61%, and 90.67%, respectively.

Table 1. Performance metrics of classification on unfiltered data

	Precision (%)	Recall (%)	F1-score (%)
alongside	86.00	84.04	85.01
building	94.84	99.15	96.94
road	89.20	95.83	92.40
vegetation	86.21	80.36	83.18
water	98.11	93.67	95.84

The performance measurement metrics of the classification model on the dataset consisting of SDD-filtered images are given in Table 2. Precision, recall, and f1-score metrics of each class are given, and the classification model has an accuracy of 93.4%. In addition, the overall precision, recall, and f1-score metrics of the classification model on all classes are 93.16%, 92.99%, and 93.05%, respectively.

Table 2. Performance metrics of classification on filtered data

	Precision (%)	Recall (%)	F1-score (%)
alongside	88.10	84.64	86.34
building	94.59	99.43	96.95
road	99.07	96.08	97.55
vegetation	91.06	90.46	90.76
water	93.00	94.32	93.65

According to the results obtained, it is seen that the accuracy of the model increased by 2.24%, precision by 2.29%, recall by 2.38%, and f1-score value increased by 2.38% with the application of the SDD filter. It has been observed that there is a significant performance difference between the classification of speckle-free images and the classification of SDD-filtered images. The study clearly demonstrates that the application of the SDD filter improves classification performance in challenging tasks such as the classification of SAR images.

4. CONCLUSION

The study focused on two main challenges in the classification of SAR images. The fact that SAR images detect a large area is a factor that makes it difficult to detect objects in the image. To overcome this difficulty, a patch-based approach is proposed in the study. In this way, the model is enabled to learn more details in the

images. Another challenge is speckle noise in SAR images due to various natural factors. To overcome this difficulty, despeckling has been applied. Thus, the model is trained with denoised images of land cover and use areas, free of speckle noise. Although many studies have been examined in the literature, and there are studies that try different ways to overcome these problems, the difference in performance has yet to be revealed as much as achieved in this study. In addition, since a patch-based approach was followed in this study, it is predicted that a successful result can be obtained on different images regardless of the image size. In addition, this study confirmed how practical pre-processing steps on the image can be for classification performance. In future studies and researches, it is aimed to achieve higher success by minimizing the current error rate in the classification of SAR images.

ACKNOWLEDGEMENT

This study is supported by Karabuk University Scientific Research Projects Unit with the project number KBUBAP-23-YL-027.

REFERENCES

- [1]. Z. Wu, B. Hou, and L. Jiao, "Multiscale CNN with autoencoder regularization joint contextual attention network for SAR image classification", *IEEE Transactions on Geoscience and Remote Sensing* 59.2, pp. 1200-1213, 2020.
- [2]. J. C. Curlander and R. N. McDonough, *Synthetic Aperture Radar: Systems and Signal Processing*, New York: Wiley, 1991.
- [3]. L. Chen, T. Weng, J. Xing, Z. Pan, Z. Yuan, X. Xing and P. Zhang, "A new deep learning network for automatic bridge detection from sar images based on balanced and attention mechanism", *Remote Sensing* 12(3), 441, 2020.
- [4]. X. Huang, B. Zhang, W. Perrie, Y. Lu and C. Wang, "A novel deep learning method for marine oil spill detection from satellite synthetic aperture radar imagery", *Marine Pollution Bulletin* 179, 113666, 2022.
- [5]. Marco Casini, *Building automation systems*, In Woodhead Publishing Series in Civil and Structural Engineering, pp 525-581, 2022.
- [6]. A. Passah, S. N. Sur, B. Paul and D. Kandar, "Sar image classification: A Comprehensive study and analysis", *IEEE Access* 10, 20385–20399, 2022.
- [7]. J. Pei, Y. Huang, W. Huo, Y. Zhang, J. Yang and T. S. Yeo, "SAR Automatic Target Recognition Based on Multiview Deep Learning Framework", *IEEE Transactions on Geoscience and Remote Sensing*, vol. 56, no. 4, pp. 2196-2210, 2018.
- [8]. H. Furukawa, "Deep learning for target classification from sar imagery: Data augmentation and translation invariance", arXiv preprint, Article Title 9arXiv:1708.07920, 2017.
- [9]. M. Krestenitis, G. Orfanidis, K. Ioannidis, K. Avgerinakis, S. Vrochidis, and I. Kompatsiaris, "Oil Spill Identification from Satellite Images Using Deep Neural Networks", *Remote Sensing*, vol. 11, no. 15, p. 1762, Jul. 2019.
- [10]. Z. Wu, B. Hou, B. Ren, Z. Ren, S. Wang and L. Jiao, "A deep detection network based on interaction of instance segmentation and object detection for sar images", *Remote Sensing* 13(13), 2582, 2021.
- [11]. F. Lattari, B. Gonzalez Leon, F. Asaro, A. Rucci, C. Prati and M. Matteucci, "Deep learning for SAR image despeckling", *Remote Sensing*, 11(13), 1532, 2019.
- [12]. C. Ozcan, B. Sen and F. Nar, "Sparsity-driven despeckling for SAR images", *IEEE Geoscience and Remote Sensing Letters*, 13(1), 115-119, 2015.
- [13]. C. Szegedy, S. Ioffe, V. Vanhoucke and A. Alemi, "Inception-v4, inception-resnet and the impact of residual connections on learning", *Proceedings of the AAAI conference on artificial intelligence* (Vol. 31, No. 1), 2017.
- [14]. Y. Bhatia, A. Bajpayee, D. Raghuvanshi and H. Mittal, "Image captioning using Google's inception-resnet-v2 and recurrent neural network", *2019 Twelfth International Conference on Contemporary Computing (IC3)*, pp. 1-6, IEEE, 2019.

Analysis Of Y-Balance Test Data Used In Sports Sciences With Machine Learning Methods

Suheda Cilek^{1}, Caner Ozcan², Bahar Ates³*

Abstract

The Y-Balance Test (YBT) is a popular method used to evaluate the dynamic balance and functional mobility of athletes. However, it is crucial to perform the test correctly to obtain accurate results. For precise measurement of YBT data, a separate measurement should be conducted for each individual, and the test grid and equipment must be set up correctly. Clear instructions and a standardized protocol must be followed to avoid misleading results, which can lead to incorrect information being used to design training programs to improve athletes' performance and reduce injury risks. To address this challenge, a study was conducted using supervised learning methods to explore YBT data, perform preprocessing steps, and conduct a comparative analysis of different machine learning models' performance in predicting YBT data. The study predicted YBT values, which require individual measurements, using different machine learning methods based on determining features such as age, gender, and training age. The experimental results demonstrated that the predicted YBT values can aid in designing training programs that can enhance athletes' performance and reduce injury risks. Overall, the findings of the study highlight the importance of accurate YBT data measurement and the potential of machine learning methods in predicting YBT values based on an individual of specific features. This approach can provide valuable insights to coaches, trainers, and healthcare professionals to create tailored training programs that can improve athletes of balance and mobility while minimizing injury risks.

Keywords: Y-Balance Test (YBT); Machine Learning; Regression; Prediction; Sport; Analysis

1. INTRODUCTION

The Y-Balance Test (YBT) is a widely used clinical test to assess dynamic balance and neuromuscular control in athletes and patients with lower extremity injuries.[1] It involves standing on one foot and reaching as far as possible in different directions (anterior, posteromedial, and posterolateral) while maintaining balance. The YBT has been shown to have good reliability and validity and is commonly used to assess and monitor progress in rehabilitation programs.[2] Incorrect YBT results can lead to negative outcomes such as delaying rehabilitation program for the patient, ineffective treatment, and even further injury. The YBT is a test that should be carefully and accurately administered by a trained clinician with experience in the test and an understanding of how to properly set up and apply it. Those measuring the Y-balance value require a reliable and consistent testing environment. In addition, they must measure 3 separate reach distances in the anterior, posterolateral, and posteromedial directions. This process is a time and attention-consuming practice for the person administering the test. The idea of using machine learning methods to predict YBT results is important in terms of test sensitivity and accuracy, as it can help prevent errors and accurately guide athletes towards appropriate treatment by analyzing the factors that influence test results.

¹ Karabuk University, Department of Computer Engineering, Karabuk, Turkey, suhedacilek@gmail.com

² Corresponding author: Karabuk University, Department of Software Engineering, Karabuk, Turkey. canerozcan@karabuk.edu.tr

³ Usak University, Faculty of Sports Science, Usak, Turkey, bahar.ates@usak.edu.tr



In recent years, machine learning techniques have been widely used in the medical field. Machine learning is a subfield of artificial intelligence and improves performance on certain tasks by learning from data using mathematical models. These algorithms identify patterns and relationships in data and use them to make predictions or make decisions for new data. YBT is a balance test in which variable factors are effective on the results. These factors include variables such as age, gender, height, weight and training age. Studies investigating the effects on YBT performance indicate that factors (such as limb, gender, and anthropometric characteristics) play an important role. Machine learning techniques can also be used to predict long jumps using characteristics of people, such as age, gender, sport branches and body weight.[3]

The relationship between balance ability and the risk of sports injuries has also been established in many cases.[4] Studies have shown that poor balance is associated with an increased risk of lower extremity injury.[5] Non-contact injuries account for approximately 20% of all injuries sustained during play and approximately 40% of injuries sustained during training.[6] For these reasons, the use of screening tests measuring lower extremity balance may help sports physicians to identify athletes at risk of injury.[7] In addition, the importance of balance tests in the prevention of ankle and knee injuries and in the evaluation of decisions to return to sports is emphasized in clinical practice. The safety of YBT has been studied in various populations and moderate to high quality evidence has been reported as a reliable test of dynamic neuromuscular control.[8] It has been reported that the test is a reliable tool for pre-adolescent, late adolescence and adult athletes. It has also been reported to be a reliable tool to assess dynamic balance in women in early adolescence.[9] Recent research has used a variety of techniques, such as generalized regression neural networks and deep learning approaches, to predict YBT performance. In a sample of healthy individuals, long jump estimation was made using machine learning techniques such as multiple linear regression, using the characteristics of individuals such as age, gender, branch, and body weight.[10] Another study used a deep learning approach to predict YBT performance and found that the model was able to accurately predict scores on the test.[11] Other studies have investigated the effect of factors such as limb, gender, and anthropometric characteristics on YBT performance. For example, limb and gender factors were found to have a significant effect on YBT performance.[12] Similarly, anthropometric characteristics such as height and weight were found to be associated with YBT performance in children participating in a wide range of sports.[13] In addition to predicting YBT performance, several studies have also investigated the effects of regular exercise on YBT performance. It found that regular Pilates exercise improved the performance of YBT in women compared to sedentary women.[14] Machine learning techniques were used to analyze the relationship between soft tissue injury risk and YBT performance in elite futsal players.[15]

This article discusses the use of machine learning algorithms to analyze the factors that determine the performance of children participating in sports during the YBT. In our study, we examined the effects of variables such as age, gender, training age, Body Mass Index (BMI), and branch knowledge of the athletes on the YBT results. Our objective was to develop a method that could determine the factors affecting the dynamic balance abilities of children using the data obtained from the YBT results and to create personalized training programs based on these factors. Additionally, we evaluated the performances of different regression algorithms in this study and compared the results with criteria such as Root Mean Square Error (RMSE). As a result, we identified which regression algorithm provided better estimations of the balance abilities of children participating in sports. These findings will enable children to follow a more effective way to develop their training programs and enhance their dynamic balance abilities.

2. MATERIALS AND METHODS

2.1. Dataset and Pre-processing

In this study, a data set containing dynamic balance data of child athletes aged 6-17 was used. A total of 216 children, aged 6-17 years from different sports clubs were included in the present study. The participants were allocated into 8 groups based on their regular sports participation: football, basketball, tennis, volleyball, handball, gymnastic, swimming and teakwando. While creating the data set, participants' known neurological, mental, orthopedic, vestibular, and systemic etc. It was sought that he did not have a disease or a problem that prevented the completion of the dynamic balance test and that he had not done any vigorous exercise before the study. Prior to the tests, participants were given a practice session to familiarize themselves with all test procedures. In the test session, the anthropometric characteristics and dynamic balances of the participants were evaluated. Personal information, height and weight measurements of each participant were recorded in the data set. After a three-minute warm-up period, participants did an adequate warm-up with movements such as jumping and standing walking and six trial exercises on each leg in each of the three lying directions. During the practice trials, researchers emphasized the importance of maintaining a one-legged

stance while performing desired movements in three directions (anterior, posteromedial, and posterolateral) to reach both legs, as depicted in Figure 1. To account for individual variations in leg length, the anterior, posteromedial, and posterolateral values were normalized by dividing them by leg length. The resulting normalized values were represented as percentages (%), for both the right and left legs, as shown in Figure 2. The mean of the normalized anterior values for both legs was labeled as ANT%AVG, while the mean of the normalized posteromedial and posterolateral values for both legs was labeled as PM%AVG and PL%AVG, respectively. Finally, the average of ANT%AVG, PM%AVG, and PL%AVG values was calculated to obtain TOTAL%AVG.

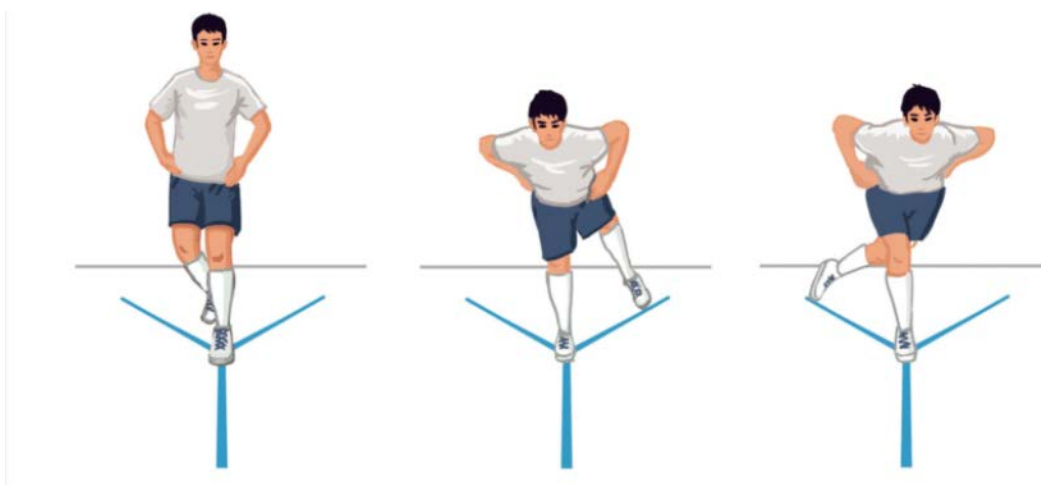


Figure 1. Direction of Y-Balance Test (Anterior, Posteromedial, Posterolateral).[16]

Dataset preprocessing is important for the correct interpretation of machine operating studies data. A data set including age, gender, training age, body mass index and branch knowledge characteristics used for the YBT was used. The preprocessing usage of the dataset is as follows: First, unnecessary columns are removed. Categorical sections can be expanded numerically, especially the branch information feature has been converted with the "One-Hot Encoding" method. While scaling the data, age, training age, body mass index and branch information were scaled with the "Standard Scaler" method. The gender feature was scaled with the "Label Encoder" method. This use of preprocessing has been made so that it can be correctly interpreted by the automatic machine use inferences.

Gender	Branch	Age	BMI	Training Age	Right-ANTR%	Left-ANTR%	ANT%AVG	Right-PM%	Left-PM%	PM%AVG	Right-PL%	Left-PL%	PL%AVG	TOTALAVG%
F	Tennis	7	15,3846	2	56,34	59,15	57,75	91,08	84,51	87,79	75,59	58,69	67,14	70,89
F	Gymnastics	10	17,1163	7	67,11	68,89	68,00	99,56	114,67	107,11	103,11	92,44	97,78	90,96
M	Teakwando	8	14,1233	1	64,62	63,59	64,10	118,97	123,08	121,03	120,00	125,13	122,56	102,56
F	Volleyball	11	17,4191	1	55,31	52,75	54,03	97,07	100,73	98,90	76,56	71,06	73,81	75,58
M	Basketball	10	17,8571	4	44,00	45,78	44,89	71,11	64,89	68,00	54,67	57,33	56,00	56,30
M	Handball	11	17,0799	2	56,44	59,56	58,00	104,44	107,11	105,78	106,67	98,22	102,44	88,74
M	Football	9	16,1377	1	42,13	39,81	40,97	59,72	56,94	58,33	56,94	62,50	59,72	53,01
F	Swimming	12	21,7738	6	62,96	66,26	64,61	108,23	120,58	114,40	111,11	110,70	110,91	96,64

Figure 2. Dataset with Y-balance test values and personal characteristics.

2.2. Machine Learning Algorithms

Analysis of YBT results was performed with machine learning. For this analysis, the results were compared using different machine learning regression algorithms. Regression analysis is a popular supervised learning technique in machine learning used to predict a continuous numerical value based on one or more input variables. In this study, the most widely used and proven performance Decision Tree, Random Forest Regression algorithms and Lazy Predict library were used to analyze YBT data. Random forest regression algorithm is an ensemble learning method that creates multiple decision trees and combines their predictions to increase accuracy and reduce overfitting.[17] The decision tree algorithm is a non-parametric method that

creates a tree-like model for decision making by dividing the data into different subgroups according to their characteristics.[18] Lazy Predict is a library developed in the Python programming language that allows us to quickly evaluate the performance of multiple models in a given dataset.[19] In this study, we used the implementation of these algorithms available in the scikit-learn library in Python. Considering how personal characteristics may affect the result, 6 different models, right and left, were created for 3 different reach distances measured in YBT. Each model performed regression analysis for a different direction. This method showed that YBT analysis can be done by creating different models using different personal characteristics. The results showed that YBT results could be predicted using personal characteristics. results of algorithms; It is measured by the Root Mean Squared Error (RMSE), which provides a general idea of how much the predicted values deviate from the true values.

3. RESULTS AND DISCUSSION

In this study, the YBT results of individuals were analyzed using various personal characteristics such as age, BMI, years of education, and branch. Different machine learning regression algorithms such as Decision Tree, Random Forest Regression and Lazy Predictor library were used to predict the YBT results. In YBT testing, the Lazy Predictor library provided a fast and efficient way to evaluate the performance of multiple models in a given dataset. The results showed that constructing different models for each aspect with different personal characteristics is a promising method for estimating YBT outcomes. Among the different algorithms used, the Random Forest Regression algorithm showed the lowest RMSE values for the right-anterior, right-posteromedial, and right-posterolateral directions. As can be seen in Table 1, Table 2, Table 3 and Table 4, when one balance measures were given in addition to personal characteristics, the RMSE value of the remaining balance measurements decreased. These results show that experts can estimate YBT values by using the personal characteristics of individuals, and they can also reach approximate values by making only one measurement from one leg in order to increase the accuracy and reliability of the results.

Table 1. RMSE results of predicted YBT values using Age, BMI, Training Year, Branche

Features	Predicted	RMSE
Age, BMI, Training Year, Branche	Right-Anterior%	12.68
	Left-Anterior%	14.18
	Right-Posteromedial%	14.06
	Left-Posteromedial%	20.79
	Right-Posterolateral%	12.45
	Left-Posterolateral%	16.22

In Table 1, the RMSE results of the YBT values predicted using Age, BMI, Training Year, and Branche values, along with the predicted attributes, are presented. Right-Posterolateral% showed the best performance with the lowest RMSE value.

Table 2. RMSE results of predicted YBT values using Age, BMI, Training Year, Branche, Right-Anterior%

Features	Predicted Features	RMSE
Age, BMI, Training Year, Branche, Right-Anterior%	Left-Anterior%	4.93
	Right-Posteromedial%	8.65
	Left-Posteromedial%	18.35
	Right-Posterolateral%	8.53
	Left-Posterolateral%	13.07

In Table 2, in addition to Age, BMI, Training Year, and Branche values, information of the right leg anterior value was also used. Improvements were observed in the RMSE values of the predicted YBT values.

Table 3. RMSE results of predicted YBT values using Age, BMI, Training Year, Branche, Right-Posteromedial%

Features	Predicted Features	RMSE
Age, BMI, Training Year, Branche, Right-Posteromedial%	Right-Anterior%	9.71
	Left-Anterior%	10.18
	Left-Posteromedial%	10.52
	Right-Posterolateral%	6.96
	Left-Posterolateral%	11.66

In Table 3, in addition to Age, BMI, Training Year, and Branche values, information on the right leg posteromedial value was also used. The predicted YBT values showed improvement in their RMSE values compared to those in Table 1. However, there was an only increase observed in the anterior values when compared to those in Table 2.

Table 4. RMSE results of predicted TOTALORT% values using different features

Features	Predicted Features	RMSE
Age, BMI, Training Year, Branche	Total Average% ((Anterior Average% + Posteromedial Average% + Posterolateral Average%) / 3)	7.78
Age, BMI, Training Year, Branche, Right-Anterior%		5.89
Age, BMI, Training Year, Branche, Right-Posteromedial%		8.46
Age, BMI, Training Year, Branche, Right-Posterolateral%		5.69

The predicted results of the Total Average% value used as a pathway for determining the interventions required to improve an individual of balance and balance performance are presented in Table 4. In this case, it has been observed that the Total Average% value can be estimated by giving only personal characteristics, and the results can be improved by giving only 1 additional direction information on personal characteristics.

4. CONCLUSION

In this study, the YBT test was analyzed using regression analysis to investigate the effect of various personal characteristics such as age, gender, BMI and educational age on right-left anterior, posteromedial and posterolateral values. Machine learning algorithms were utilized and the Random Forest Regression algorithm was found to be the most effective. In addition, the study found that the use of YBT values measured by obtaining only one-way reach information instead of six measurements can increase the applicability and evaluability of the test. The Total Average % calculated by averaging the YBT data was also found to be useful for disability risk estimation. The study showed that expanding the dataset to include a wider range of samples can further improve the analysis results.

ACKNOWLEDGEMENT

This study is supported by Karabuk University Scientific Research Projects Unit with the project number KBUBAP-23-YL-040.

REFERENCES

- [1]. Plisky, Phillip J et al. "The reliability of an instrumented device for measuring components of the star excursion balance test." *North American journal of sports physical therapy : NAJSPT* vol. 4,2 (2009): 92-9.
- [2]. Gribble, Phillip A et al. "Using the Star Excursion Balance Test to assess dynamic postural-control deficits and outcomes in lower extremity injury: a literature and systematic review." *Journal of athletic training* vol. 47,3 (2012): 339-57. doi:10.4085/1062-6050-47.3.08

- [3]. Ucar, Mehmet, Incetas, Murat Onur, Bayraktar, Ismail, & Cilli, Mehmet. "Using Machine Learning Algorithms for Jumping Distance Prediction of Male Long Jumpers." *Journal of Intelligent Systems: Theory and Applications*, vol. 5, no. 2, 2022, pp. 145-152. <https://doi.org/10.38016/jista.1078474>.
- [4]. Engquist, Katherine D et al. "Performance Comparison of Student-Athletes and General College Students on the Functional Movement Screen and the Y Balance Test." *Journal of strength and conditioning research* vol. 29,8 (2015): 2296-303. doi:10.1519/JSC.0000000000000906
- [5]. Ates, B. , Cetin, E. , Yarim, I. "Kadin Sporcularda Denge Yetenegi ve Denge Antrenmanlari" . *Gaziantep Universitesi Spor Bilimleri Dergisi 2* (2017) : 66-79 <https://dergipark.org.tr/tr/pub/gaunjss/issue/29859/321612>
- [6]. Hootman, Jennifer M et al. "Epidemiology of collegiate injuries for 15 sports: summary and recommendations for injury prevention initiatives." *Journal of athletic training* vol. 42,2 (2007): 311-9.
- [7]. Lai, Wilson C et al. "Lower Quarter Y-Balance Test Scores and Lower Extremity Injury in NCAA Division I Athletes." *Orthopaedic journal of sports medicine* vol. 5,8 2325967117723666. 8 Aug. 2017, doi:10.1177/2325967117723666
- [8]. Plisky, Phillip et al. "Systematic Review and Meta-Analysis of the Y-Balance Test Lower Quarter: Reliability, Discriminant Validity, and Predictive Validity." *International journal of sports physical therapy* vol. 16,5 1190-1209. 1 Oct. 2021, doi:10.26603/001c.27634
- [9]. Greenberg, Eric T. et al. "INTERRATER AND TEST-RETEST RELIABILITY OF THE Y BALANCE TEST IN HEALTHY, EARLY ADOLESCENT FEMALE ATHLETES." *International journal of sports physical therapy* 14 2 (2019): 204-213 .
- [10]. Akay, M. F., Ates, B., & Ozciloglu, M. M. (n.d.). Prediction of Y-Balance Test Performance Using Generalized Regression Neural Network. In Proceedings of the 1st International Conference on Life and Engineering Sciences, Kyrenia, Cyprus, 2-6 September 2018.
- [11]. Gil-Martín, Manuel et al. "Scoring Performance on the Y-Balance Test Using a Deep Learning Approach." *Sensors (Basel, Switzerland)* vol. 21,21 7110. 26 Oct. 2021, doi:10.3390/s21217110
- [12]. Riemann, Bryan and George Davies. "Limb, Sex, and Anthropometric Factors Influencing Normative Data for the Biodex Balance System SD Athlete Single Leg Stability Test." *Athletic Training & Sports Health Care*, vol. 5, 2013, pp. 224-232. doi: 10.3928/19425864-20130827-02
- [13]. Opstoel, Katrijn et al. "Anthropometric characteristics, physical fitness and motor coordination of 9 to 11 year old children participating in a wide range of sports." *PloS one* vol. 10,5 e0126282. 15 May. 2015, doi:10.1371/journal.pone.0126282
- [14]. OZTURK, Mehmet & Ates, Bahar. (2019). Duzenli pilates egzersizi yapan kadinlar ile sedanter kadinlarda Y denge testi performansinin karsilastirilmasi. *Ege Tip Bilimleri Dergisi*. 2. 2-7. 10.33713/egtb.510183.
- [15]. Ruiz-Pérez, Iñaki et al. "A Field-Based Approach to Determine Soft Tissue Injury Risk in Elite Futsal Using Novel Machine Learning Techniques." *Frontiers in psychology* vol. 12 610210. 5 Feb. 2021, doi:10.3389/fpsyg.2021.610210
- [16]. Guo, Zhenxiang et al. "The Effect of 6-Week Combined Balance and Plyometric Training on Change of Direction Performance of Elite Badminton Players." *Frontiers in Psychology*, vol. 12, 2021, article 684964. doi: 10.3389/fpsyg.2021.684964.
- [17]. Breiman, Leo. "Random Forests." *Machine Learning*, vol. 45, no. 1, 2001, pp. 5-32.
- [18]. Quinlan, J. Ross. "Induction of Decision Trees." *Machine Learning*, vol. 1, no. 1, 1986, pp. 81-106.
- [19]. "Lazypredict." Read the Docs, 2021, <https://lazypredict.readthedocs.io/en/latest/>.

Fire Risk Assessment in High-Rise Buildings with Combustible Aluminum Composite Panels

Mousa Al-Dghaimat^{1*}, Awad Saad¹, Osama Abuzeid²

Abstract

This paper aims at presenting a novel model of the Aluminum Composite Panels (ACPs) cladding system. The main objective of this work is to find the air gap and the suitable and economical number of fire barriers between the external wall of the high-rise buildings and the ACPs used for cladding.

For this purpose, a simulated fire experiment was conducted using Grasshopper and Galapagos software. The integrated novel model of ACPs proposed changes in the material used, like wet and hot insulations using special latest products like Fenomastic hygiene emulsion paint.

The input parameters used to investigate the validity of the proposed numerical model are the initial fire temperature, the facade material elements, the facade elements' properties, the elements' fire resistance, and the time.

As a result, the optimal value for the air gap is 111 mm. Furthermore, using four barriers in the air cavity plays a major role in neutralizing and limiting the fire spread to the external facades, minimizing the risk, and reducing harmful effects to the inhabitants of the high-rise buildings.

These findings and results will contribute to improving and enhancing the behavior of the fire flame in high-rise buildings, in addition, to eliminating the fire risk for the habitant's life in the high levels of tall buildings and conserving the environmental periphery including neighboring buildings, human beings, vehicles, and all other equipment and materials.

Keywords: Aluminium Composite Panels ACPs, High-rise buildings, cavity fire barriers, air gap, Galapagos.

1. INTRODUCTION

Many fire accidents have occurred worldwide in recent years, resulting in many deaths, serious injuries, and a great loss of money and buildings. In the architecture and civil engineering sector, a lot of research has been carried out in the last three decades relating to Aluminum Composite Panels ACPs as external cladding systems, and to the depth of the air gap and fire cavity barriers. After an extensive study of the existing tall buildings, whether in the UAE or other countries, it was found that most of them have been clad with aluminum composite panels. Fires spreading due to building cladding have risen to a global average of 4.8 per annum. "Fig.1" shows fire incidents worldwide every five years from 1990–2019 ([1] - 2]).

¹* Corresponding author: Mousa Al-dghaimat: Faculty of Architecture, Sudan University for Science & Technology, Sudan, Mousa.63@hotmail.com.

² Professor, School of Engineering, The University of Jordan, Jordan

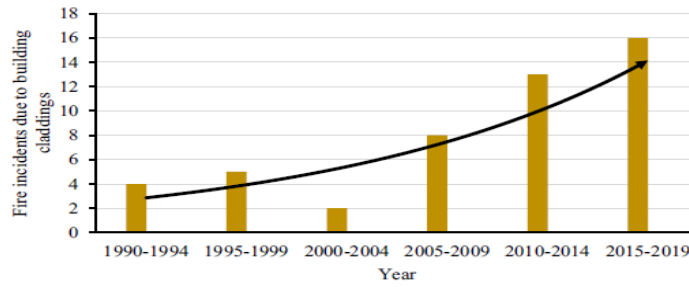


Figure 1: statistical data of fire incidents worldwide every five years from 1990–2019 ([1] - [2]).

Recent dramatic events happened around the world (Mermoz Tower in Roubaix, France, 2012; Polat Tower in Istanbul, Turkey, 2012; Lacrosse Tower in Melbourne, Australia, 2014; and Grenfell Tower in London, UK, 2017) remind us of the importance of addressing fire issues as a whole and clearly highlight the major role played by facade cladding and the associated insulation as fire propagation vectors. In UAE fire breaks at Torch and Marina Tower in Dubai in 2017, a fire at Al Baker residential tower in Sharjah in 2012, a fire in Residential Building No. 1 in Ajman in 2016, and a fire in Address Hotel in Dubai in 2016 [2,3].

The damages resulting from these fires are large and costly, whether human, psychological, or material, the largest example of this topic is the Grenfell Tower in the United Kingdom in 2017, which resulted in the death of more than 70 residents and the displacement of all residents of the tower in addition to its complete burning and damage [4].

"TABLE 1" provides a non-exhaustive list of the fires that have happened internationally because of combustible facade systems, and "Fig.2" shows and provides an illustrative map of the location of fires that engulfed all around the world [5].

From the schedule and map, it is clear that the Arab Gulf States gained the biggest number of fires, This is what encouraged to search and focus on finding a solution to this phenomenon, which is spread in general around the world and in the UAE in particular, because of its distinction in building tall towers, the latest of which is Sheikh Khalifa Tower, number one in the world until today ([2]-[5]).



Figure 2: A fire incident involving exterior facade systems all around the world [5].

Table 1: Shows a non-exhaustive list of the fires that have happened globally.

Country	City	Fire incidents involving the façade assembly on the exterior of a building							
UAE	Dubai	2017	2016	2016	2015	2012	2012	2008	2007
	Ajman		2016						
	Abu Dhabi		2016						
	Sharjah		2015	2012	2010				
Qatar	Doha		2010						
Russia	Grozny		2013						
Australia	Melbourne		2014						
	Fairfield		2002						
China	Shenyang		2016						
	Beijing		2011	2010	2009	2008			
Azerbaijan	Baku		2015						
Turkey	Istanbul		2012						
Thailand	Bangkok		2012						
Bangladesh	Dhaka		2016	2012					
USA	Atlantic City		2007						
	Reno		1997						
	Philadelphia		1991						
Hungary	Miskolc		2009						
France	Dijon		2010						
	Epinay-sur seine		2016						
	Lille		2016						
	Roubaix		2012						
Belgium	Neder-over-Heembeek		2016						
Germany	Berlin		2016						
	Munich		2005						
Spain	Ovideo		1996						
Canada	Winnipeg		2016						
S. Korea	Busa		1990						
UK	Liverpool		2010						
	Irvine		1991						
	Hereford		1999						
	London		2017	1993					
Japan	Hiroshima		1996						
Indonesia	Jakarta		2015						

The unique advantages and characteristics of ACPs made them the first choice for architects and engineers working in architectural design, and the construction sector in general. After using these panels for cladding extensively, especially in high-rise towers, in contemporary cities like New York, Tokyo, Dubai ...etc. It was found that there are still several disadvantages related to such panels. Such disadvantages result from the use of flammable materials in its components and the presence of an air cavity that helps in the spread of vertical fire flame and defects in fixing them on the facades.... etc.

A specific focus on the external facade system and ACP insulation is necessary for the UAE material requirements. The nature of fire spread with ACP cladding materials containing combustible core materials raises concern over the safety of building occupants and firefighters ([4]–[6]). The presence of the air cavity led to the emergence of a serious problem, which assists the rapid spread of vertical fire flames in the event of a fire on the upper floors and apartments, which exposes buildings and their inhabitants to the danger of fire [4].

Some studies appeared recently to solve the problem of air cavities [7-12], and a little bit researchers presented solutions by installing fire barriers and suggested one or two barriers, but the problem still exists, and the number of fires is increasing, moreover, the problem is getting worse day by day, posing a great threat to lives and buildings alike.

The fire behavior of ventilated cladding systems made of aluminum composite panels ACPs has become a topic of concern, the fire performance of a cladding system comprises not only the cladding panel and the insulant but also air cavities, cavity barriers, and mounting and fastening elements. In a real fire, all these components interact significantly. It was also confirmed that the Grenfell Tower fire in (UK, 2017), where there were installed barriers; however, the installation geometry of the cladding system developed an interconnected network of cladding cavities, allowing the fire to spread rapidly. Moreover, the transition to the mode where the flames filled the entire cavity width was observed to occur at the cavity width of 0.03m and 0.04 in the experimental tests. The visual observations clearly indicated that the flame heights increased with reduced width [13].

Mineral wool fire stops barriers (at least 50 mm thick) are required for buildings of three or more stories fitted with combustible external insulation. The fire stop barriers must be installed to the cladding at intervals of not more than two stories [4].

“As observed in real high-rise building fire incidents, flames can eject from many windows over multiple floors and the interactions between multiple fire plumes are very complex. This needs to be studied further and more deeply: the ejected flame interaction of multiple windows with different arrangements and wind conditions is suggested to be further considered.” [14].

The conducted experiment it was found that the results indicate that, without a barrier, fire starting at the middle of the wall generated a higher peak. The heat release rate HRR was higher at the bottom, which was, in turn, higher than that at the top. When the insulation panel below the barrier was 1 m high, the upward fire spread from the bottom could be stopped by 40 cm, but not 30 cm, barriers. However, when the insulation panel below the barrier was 2 m high, even the 40-cm barriers failed. Lastly, the downward fire spread from above could not be stopped by a 40-cm barrier due to the dripping of burning plastics. The study highlights the limitations of horizontal fire barriers in preventing vertical fire spread over exposed B2-grade polystyrene insulation and establishes protocols for further investigations [15].

When the fire inside the cabin develops to be in its most severe stage, flames may escape from the openings, forming outer flames, also known as Interface fires. Structural parapets (e.g., balconies, eaves, and overhangs) greatly influence the vertical spread of the opening spill column. Numerical investigations show this chamber fire and prevailing ventilation conditions. Strongly influences indoor fire behavior through oxygen availability. And the development of flame emanating from the outside because of natural factors such as wind and high temperature ([16-19]).

“Aluminum composite panels could melt in high temperatures, and flame and hot gases could enter the cavity between the panels and insulations. The use of fire stops between the outer panels and inner insulation materials was found to be effective to control the fire spread in the cavity” [20].

The gap depth is the subject matter of many works but, it still needs more in-depth studies to find the optimal and safe depth that will be suitable enough to use in the recent high-rise buildings.

In accordance with what has been achieved by development and progress in the design of high-rise buildings in general and the external facades in terms of aesthetics first, and then their compliance with the conditions of sustainability such as energy saving, thermal insulation, etc., there are still many challenges that architects and designers face in designing their high-rise projects. Represented in the danger of fires and the rapid spread of their flames in high-rise residential buildings.

One of the main factors for the spread of vertical flames in skyscrapers was the presence of gaps or cavities in most models used until today. Furthermore, and to the importance and seriousness of this phenomenon, it was decided to focus on in-depth research using the most contemporary scientific means to find the best solutions for it [2].

By reviewing the previous literature and many others, it has become clear that the use of fire barriers in air cavities is effective and gives positive results, but it is not sufficient to prevent the spread of fires in general and the spread of vertical flames in particular, and based on all of the above, this study was enumerated, where they conducted a simulation test of a novel proposed model based on the theory EA and using the Grasshopper and Galapagos applications. So, a novel model for ACPs is developed and investigated to minimize the fire risk in a high-rise building. A varying number of fire barriers, accompanied by various dimensions of the air gap, were used. To get the optimum gap space and the economical number of fire barriers, an evolutionary algorithm EA was proposed and performed using Rhinoceros, Grasshopper, and Galapagos.

2. MODEL CONSTRUCTION

This simulation experiment test aims to examine, improve, and develop the exterior wall assemblies that are cladded by ACP's material system, in compliance with applications and laboratory tests approved globally as BS8414 part 1 & 2, ISO 13785 part 1 & 2, NFPA 285, SP105, CAN/ULCS134, DIN 4102-20.

2.4 Installation way of ACPs and joints between Panels.

Aluminum Composite panels (ACPs) are typically installed on exterior walls on steel channels or battens/top hats, [20]. This creates an air gap of around 40 mm between the next surface within the external wall cavity (typically sarking or other weather resistive barrier) and the cladding. The panels are typically fastened to the steel battens by either of the following two methods:

2.4.1 Flat stick method - Flat cut ACP panels adhered to steel battens using double-sided adhesive tape.

2.4.2. Cassette mount method - The edges of the panels are folded at right angles and are rivet or screw fixed to aluminum or steel channels or clips which are in turn screw fastened to the exterior wall.

Sealant is normally applied to the gaps between panels, this is called "face sealing". The Cassette mount method of installation typically forms a ventilated facade/rain screen with an air gap separating the ACP from the supporting wall behind. However, ACP can be incorporated into other forms of construction including pre-manufactured unitized curtain wall facade panels.

"Fig.3 (a)" shows three-dimensional images of the model, including the method of installing and fixing the composite aluminum sheets on metal supports fixed to the block wall, in addition to installing fire barriers and thermal insulation in their specified places [21].

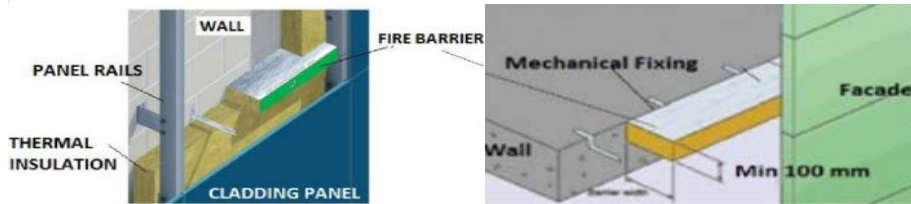
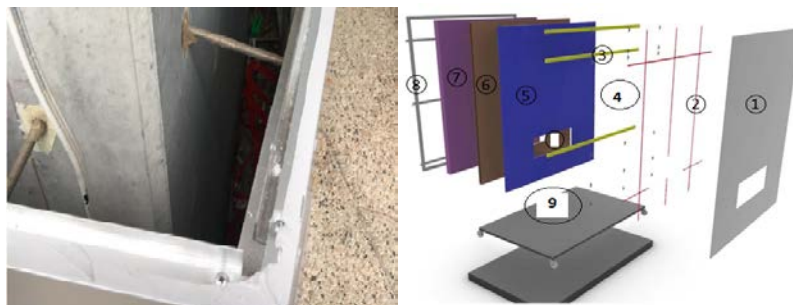


Figure 3 (a): three-dimensional images of the model [21].

One of the main factors for the spread of vertical flames in skyscrapers was the presence of gaps or cavities in most models used until today.

The air gap between the Aluminum Composite Panels ACPs and the external wall is a major factor in fire extension on the facade of high-rise buildings, it is playing a very important role to prevent vertical fire flame spread, more than one problem was found in this position, the first being depth of the cavity. The horizontal fire barriers using 300 mm high non-combustible insulation were effective to delay the fire spread on exterior walls [20]. The air gap is also considered as a leveling monitor to adjust the defects in the civil works in the external walls." Fig.3 b" presents the size of air (cavity gap) between the wall and ACP which is more than 300 mm [22].



3 (b): Cassette mount installation of ACP onto the wall (photo by CSIRO) [22]. 3 (c): Layers and specifications of the novel model.

"Fig.3 b" shows the components of the novel model as the followings:

- 1- 4MM THK aluminum composite panel FR-A2.
- 2- Vertical/horizontal runners: 40X40X3MM. alum. hollow square tube fixed to the panel rails brackets.

- 3- Cavity fire barrier depth 111 mm*height 57 mm*long variable recompressed stone wool density 80 kg/m³.
- 4- Gap (Air Cavity) 111mm.
- 5- Thermal insulation 50 MM mineral wool.insulation density 24KG/ M3.
- 6- Fenomastic hygiene emulsion silk paint.
- 7- 200 MM block wall fixed to the metal frame.
- 8- Steel frame supporting block wall.
- 9- Model base.

3. METHODOLOGY AND RESULTS

In this paper, the conducted simulation test was focused accurately to find the optimal depth using the Evolutionary Algorithm Theory. In addition to finding the Economical Number of Fire Barriers. The test has been done in cooperation with the CALI-S. T professionals and designers, (Jordan, USA).

3.1. Evolutionary Algorithm Implementation [2]

The main objective of the work is the limitation of fire spread within the insulated facade of high-rise buildings. Observations and experience show that facades have a large potential to contribute to the spread of fire between floors and apartments of residential buildings. Many reports on fire accidents prove that the presence of a cavity (gap) assists spreading of vertical flames in high-rise buildings. Therefore, studying and analyzing the 'facade in the fire' - scenario helps to develop safety methods and potential mitigating strategies,[9].

Rhino and Grasshopper software packages were used as an integrated computer design tool with an algorithmic method to achieve a fully automated design, variants creation, and considering parametric modular coordination. Parametric modeling tools can simplify a wide range of possible concepts for optimal design exploration by allowing the automatic generation of a group of alternative design solutions to achieve the optimal genome model [23].

The optimal design of Aluminum composite panels (ACPs) that can minimize the vertical fire flame and fire risk in high-rise buildings while maximizing safety and durability is challenging and expensive to perform due to the complexities and constraints encountered.

Computational costs of such constraints manifest themselves in many indices of complexity, namely the availability of many combustible materials in commercial wall assemblies. These assemblies include exterior insulation, metal composite claddings, high-pressure laminates, and weather-resistive barriers. Likewise, modeling complexity deals with the methods used to find a solution to the problem at hand. Simple models admit closed-form solutions while the more complex ones require robust optimization or finite element models. Furthermore, thermal loads of ACPs are highly sensitive to geometric tolerances and imperfections. One of the most significant parameters is the air cavity (gap) between the external wall of the high-rise buildings and the ACPs used for cladding. While there is still no good way to incorporate imperfections in the design because their amplitudes and shapes are not known, designers often concentrate only on the cavity (gap), the most critical scenario for design optimization. In compliance with this last requirement, the optimum cavity (gap), an evolutionary algorithm (EA) in accompany of parametric design were adopted within the integrated platform of Rhino 3D, Grasshopper, and Galapagos software, "Fig.4 and Fig.5" [22].

This process is supported by Galapagos which uses genetic fitness to eliminate unwanted characteristics (here larger cavity (gap) size) and to select genes (here member sizes and properties) that evolved towards genetic success (here minimum cavity (gap) size). A unique feature of this optimization is the efficient reduction of variables that were genetically modified [24]. The application of evolutionary algorithms to structural optimization allows a huge reduction of time and computational effort. In general, EAs search a multi-dimensional space for points according to a predefined fitness function, then use some selection mechanism to discard unfavorable points, making the working set better [25].

To achieve a fully automated design, variants creation, and considering parametric modular coordination, Rhino, and Grasshopper software packages were used as an integrated computer design tool with an algorithmic method. Parametric modeling tools can simplify a wide range of possible concepts for optimal design

exploration by allowing the automatic generation of a group of alternative design solutions to achieve the optimal genome model [23].

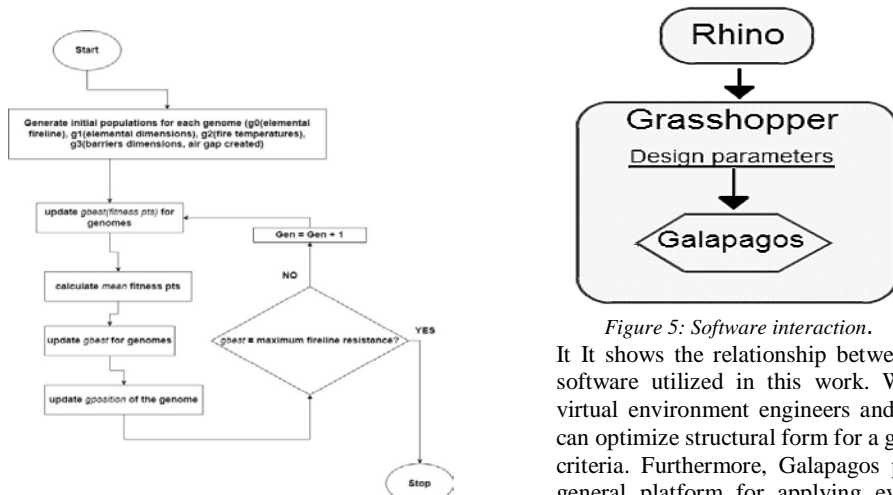


Figure 4: Flowchart of the proposed algorithm.

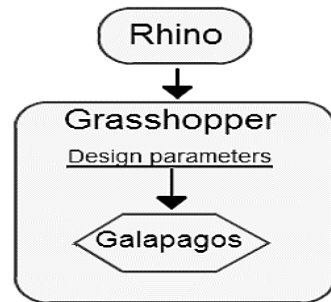


Figure 5: Software interaction.

It shows the relationship between various software utilized in this work. Within this virtual environment engineers and architects can optimize structural form for a given set of criteria. Furthermore, Galapagos provides a general platform for applying evolutionary algorithms for use in a variety of solutions problems by non-programmers [26].

Grasshopper software starts with standard input as shown in " Fig.6"(exploded bar). The design parameters shown are defined to Galapagos via C-Sharp (a programming language). This will be explained thoroughly in the following:

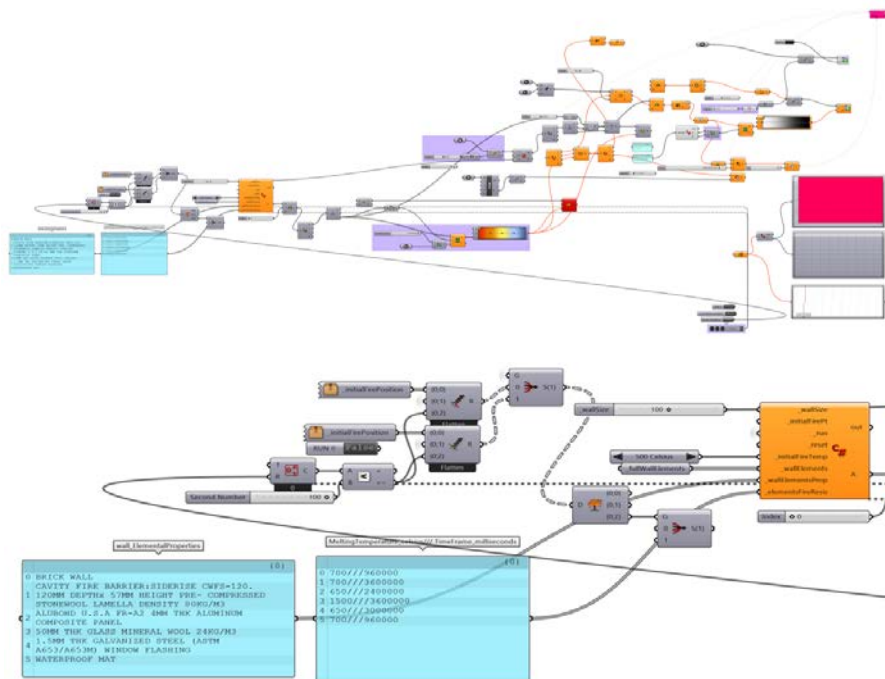


Figure 6: Parametric relationships chart within the grasshopper program (part of the figure is exploded to make it clear).

Galapagos, the solver, starts with a random “population” of sets of input values. These sets of input values are plugged into the model (using C-sharp) and the results are evaluated relative to the target value, i.e., the optimum gap (OG): Finding the optimum gap is computationally demanding and many iterations were performed. In this text, two sample iterations in the vicinity of the optimum gap are presented. In the first

sample, the air gap is assumed to be 70 mm, then EA runs for the whole input parameters for 45min (the time of experiment recommended by NFPA 285). The data recorded on the external layer and resistance pressure show that the results are not promising, and the facade will collapse after 17min because the air pressure between the barriers and the compounding structure of the facade will lead to internal explosive pressure. In the second sample, the air gap is assumed to be 150 mm, then again, the EA runs for the whole input parameters for 45min. The data recorded on the external layer and resistance pressure show that vertical fire extrapolation growth will increase by 12.1%, leading to external explosive pressure in the upper levels after 26 min, because of the oxygen volatility between the barriers. As the result of EA, the optimum value for the air gap is 111mm which holds the most precise values for the equation to reach the targeted fitness point with ~40.27 min.

3.2. Economical Number of Fire Barriers [4]

Five consecutive simulation tests were performed, and each test takes about 45 minutes. The first one is performed assuming no barriers. The next four were performed adding one barrier each time. In addition to the fire barriers that are located and installed all around the openings such as doors or windows "Fig. 7".

The barriers proposed were sufficient and effective in suffocating, seizing, and controlling the spreading of the vertical fire flame.

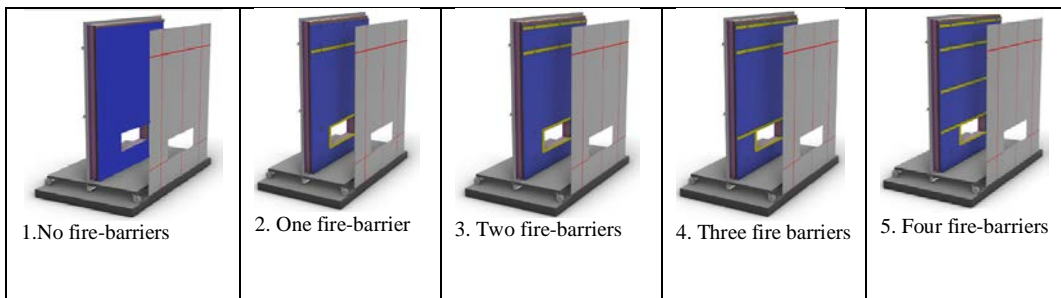


Figure 7: Positions of fire barriers throughout the simulation test.

Adding new barriers will suppress flame propagation, but it is not recommended to use a great number of barriers because of economic and technical purposes.

"Fig.8" shows the flame height versus time for the fire cases shown in "Fig.7" where the number of cavity barriers changed.

With no barriers, as shown in line diagram number (1), results indicate the highest level of the fire flame, which reaches five-meter and a little bit more, that no fire barriers used.

With one fire barrier as shown in line diagram number (2), results indicate that it is 1.00 m lower than not using any fire barrier.

When using 2- barriers as shown in line diagram number (3) present a small difference, in the height of the flame lower than when using one barrier.

Using three fire barriers, as shown in line diagram No. (4), it was found that the height of the fire didn't exceed 2.50 m.

When using 4 barriers, as shown in line diagram No. (5), a significant decrease in flame height and control of the fire, in general, was observed.

Therefore, this proves that the use of 4 fire barriers is sufficient to reduce the risk of fire spreading, isolating, and suffocating in general and neutralizing the risk of vertical fire flame.

For practical and economical purposes, it is not recommended to use more than 4 barriers at this distance.

Flame Height (cm)

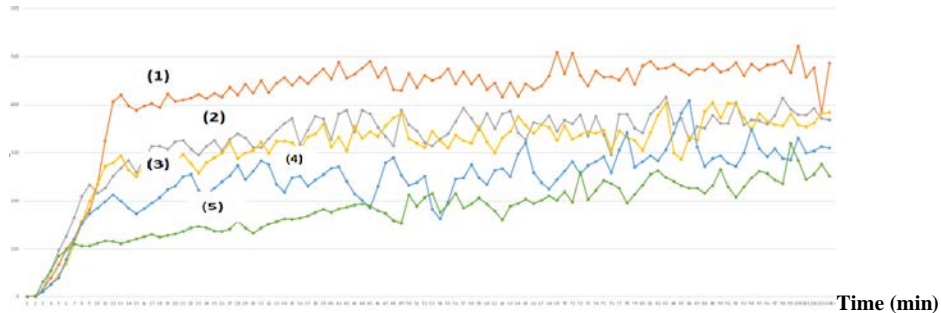
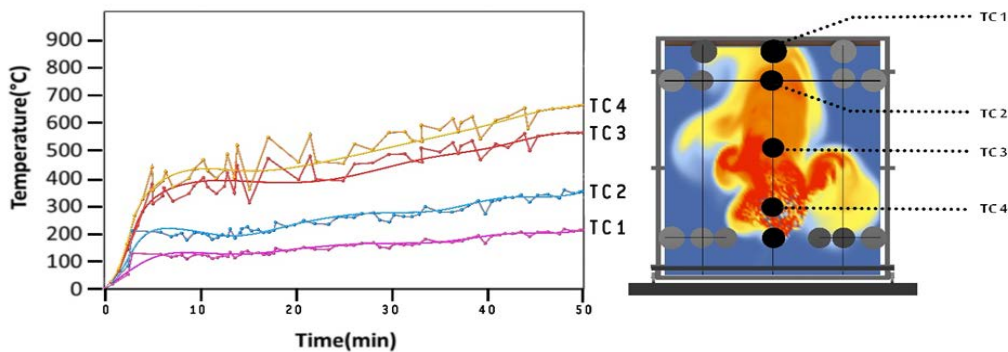


Figure 8: Flame heights versus time with various numbers of cavity barriers.

1. No Cavity Barrier, 2. 1-Barrier used, 3. 2-Barrier used, 4. 3-Barrier used, 5. 4-Barrier used



9 (a). Shows the temperature variation, with recorded at each thermos couple TC.

9 (b). Shows the positions of the adjusted thermocouples (TC1,2,3,4) where the flame ature is recorded.

It is clear from "Fig.9", that (TC1) recorded the lowest temperature, it raises within 5 minutes up to 140 °C, and very slowly developed to a maximum of 190 °C within 50 minutes.

(TC2) records show that the temperature raises up to 220 °C within 5 min. similar to TC1, but it gradually developed up to 300 °C within 50 minutes.

The record of (TC3) shows an overshoot of up to 370 °C within 5 minutes. In the next 50 minutes, the temperature was raised up to approximately 500 °C.

The data presented in "Fig.10" are recorded in the existence of 4 - fire barriers. This gives additional proof of the importance of such a barrier.

In conclusion, "TABLE 2" presents a comparison between the proposed and tested novel model and the traditional model (classical). The novel model contains all the materials and elements that were tested through conducting the simulation test for the experiment, and it is the one that succeeded in passing all stages of the experiment, which gave promising results in reducing the problem of the spread of fire from one floor to another and eliminating the problem of spreading vertical flame.

Table 2: Shows the New Main Hypothesis (Novel model) Compared with the (Traditional) ACP System

Serial No.	Design Parameters of ACPs	Traditional Model	Proposed and Tested Novel Model
1.	ACPs itself combustible with polyurethane core	- Old traditional model	
2.	ACPs are noncombustible with a mineral core A2	- The latest product of ACPs A2	ACPs noncombustible mineral core A2
3.	Waterproofing system	- Classic Bitumen Paint	Fenomastic hygiene emulsion silk paint.
4.	Heat insulation system	1. Rock wool 2. Polystyrene foam	Mineral wool.
5.	The gap between the wall and ACPs.	The size of the gap allowed up to 300mm.	The optimal gap (cavity) thickness is 111mm.
6.	Joints between Panels.	1. Not closed properly 2. Mastic used is flammable	.Prolastik matt silicone sealant.
7.	(Cavity barriers) (Compressed stone wool size up to 300mm *57mm).	1 or 2 barriers are used. horizontal fire rated.	Fire barriers used are 4. (Compressed stone wool size 57mm *111mm).

4. CONCLUSIONS

Overall, based on the results have been gained from the simulation test, by using evolutionary algorithm assessment as discussed, an important consideration which supporting and enhancing the generated genomes that improve the efficiency, choosing the best solutions, and focusing on the best-generated genomes that will improve the novel model of ACPs to minimize the risk of vertical fire flame in a high-rise building.

Although the obtained results are promising and made a qualitative and quantitative leap in the world of the construction industry, the subject needs more research and scrutiny to obtain an ideal model that contains all safety elements for the high-rise buildings, their occupants, and the surrounding environment. The results also, show that a 4 number of cavity barriers are required to be used in external wall assemblies to reduce and control fire spread. Its contribution in reducing the vertical flame is considerable to confine, suffocate, and control the fire and prevent it from spreading.

In addition, it works to discourage and prevent the spread of vertical fire flames that lead to the transmission of fire to the upper floors in tall buildings, which poses a great danger to lives and property.

ACKNOWLEDGMENT

I would like to express my special appreciation and thanks to my advisors Professor Dr. Awad Saad and Prof. Dr. Osama Abuzeid. This work would not have been possible without their generous support, and I will keep on trusting them for my full life.

REFERENCES

- [1]. Bonner M.& ReinG. (2020) List of Facade Fires (1990 – 2020).
- [2]. Al-Dghaimat M., Saad A., and Abuzeid O. (2023). High Rise Buildings with Combustible Exterior Wall Assemblies: The Optimum Size of Cavity (Gap) between the Wall and the Cladding. International Journal of Engineering Science Invention (IJESI). V12: (2), pp. 35-47.
- [3]. Dréan, V., Girardin, B., Guillaume, E., & Fateh, T. (2019). Numerical simulation of the fire behaviour of facade equipped with aluminium composite material-based claddings-Model validation at large scale. Fire and Materials, 43(8), 981-1002.
- [4]. Al-Dghaimat M., Saad A., and Abuzeid O. (2023). High-Rise Buildings with Combustible Exterior Wall Assemblies: Effect of the Number of cavity fire barriers on Upward Flame Spread. International Journal of Engineering Science Invention (IJESI). V 12: (4) PP 49-56.
- [5]. Lamont, S., &Ingolfsson, S. (2018). High Rise Buildings with Combustible Exterior Wall Assemblies: Fire Risk Assessment TooNational Fire Protection Association Report.
- [6]. Almarzooqi, A., Alzubaidi, A., and Alkatheeri, S. (2022). Fire Hazards by Aluminum Composite Cladding in High-Rise Buildings.
- [7]. Hossain, M.D., Hassan, M.K., Yuen, A.C.Y., He, Y.; Saha, S., and Hittini, W. (2021) Flame behavior, fire hazard and fire testing approach for lightweight composite claddings—A review. J. Struct. Fire Eng. 2021, 12, 257–292.
- [8]. Hossain, M.D., Saha, S., Hassan, M.K., Yuen, A.C.Y., Wang, C., Hittini, W., George, L., and Wuhler, R. (2022) Testing of aluminum composite panels in a cone calorimeter: A new specimen preparation method. Polym. Test. 2022, 106, 107454
- [9]. White, N., and Delichatsios, M. (2015). Fire Hazards of Exterior Wall Assemblies Containing Combustible Components; Springer: Cham, Switzerland,
- [10]. Chen, T., Yuen, A., Yeoh, G., Yang, W. and Chan, Q. (2019) Fire risk assessment of combustible exterior cladding using a collective numerical database. Fire, 2, 11.
- [11]. Hossain, M.D., Hassan, M.K., Akl, M., Pathirana, S., Rahnamayiezekavat, P., Douglas, G., Bhat, T., and Saha, S. (2022) Fire Behaviour of Insulation Panels Commonly Used in High-Rise Buildings. Fire, 5, 81.
- [12]. Hossain, M.D., Saha, S., Hassan, M.K., Yuen, A.C.Y., Wang, C., and Hittini, W. (2021) Influencing factors in small-scale fire testing of aluminium composite panels. In Proceedings of the 12th Asia-Oceania Symposium on Fire Science and Technology (AOSFST), Brisbane, Australia, 7–9 December.
- [13]. Kamrul, H., Dilawar, H., Michael, G., Rahnamayiezekavat, P., Douglas, G., Sameera, P. and Swapan S., (2022) Numerical Investigations on the Influencing Factors of Rapid Fire Spread of Flammable Cladding in a High-Rise Building.
- [14]. Sun, X., Tang, F., Lu, K., Ren, F., Shi, C., Merci, B., and Hu, L. (2023). Fundamentals of window-ejected fire plumes from under-ventilated compartment fires: Recent progress and perspectives. Progress in Energy and Combustion Science, 94, 101039.
- [15]. Zhou, L., Chen, A., Liu, X., and Zhang, F. (2016). The effectiveness of horizontal barriers in preventing fire spread on vertical insulation panels made of polystyrene foams. Fire Technology, 52(3), 649-662.
- [16]. Duny, M., Dhima, D., Garo, J. P., and Wang, H. Y. (2019). Numerical and theoretical evaluations of a full-scale compartment fire with an externally venting flame. Fire Technology, 55, 2087-2113.
- [17]. Xing, X., Zhang, J., and Li Y (2013) A computational study on structural barrier to vertical spread of window spill plume along building exterior facade. Proceed Eng 52:475–482
- [18]. Duny, M., Dhima, D., Garo, JP., and Wang HY. (2015) Numerical investigation on window ejected facade flames. In: Proceedings of international fire safety symposium, pp 463–472
- [19]. Martinez, B. (2013) Contribution to the study by numerical simulation of a fire plume coming out through a window on facade—application to the comprehension of the wind influence on an eventually stack effect. In: Proceedings of 1st international seminar for fire safety of facades, p 03004.
- [20]. Peng, L., Ni, Z., & Huang, X. (2013). Review on the fire safety of exterior wall claddings in high-rise buildings in China. Procedia Engineering, 62, 663-670.
- [21]. <https://www.bluechipgroup.net.au/facade-cladding-perth/aluminium-composite-panel-perth.html>.
- [22]. White, N. (2020): Fire performance and test methods for ACP external wall cladding.
- [23]. Trissi, S. M. S., Kayali, M. N., & Darwish, A. H. (2021). Sustainable Architectural Design of the Residential Compound Towers in Aleppo City Using the Genetic Algorithm: 126-147, (5)5, *مجلة العلوم الهندسية وتكنولوجيا المعلومات*.
- [24]. Gerbo, E. J., &Saliklis, E. P. 2014. Optimizing a Trussed Frame Subjected to Wind Using Rhino, Grasshopper, Karamba and Galapagos. In Proceedings of IASS Annual Symposia (Vol. 2014, No. 13, pp. 1-7).
- [25]. Kruchten, N. J. 2003. Galapagos: a Distributed Parallel Evolutionary Algorithm Development Platform, BSc dissertation, University of Toronto. <https://doi.org/10.1016/j.jhazmat.2018.12.077>. (<https://www.sciencedirect.com/science/article/pii/S0304389418312275>).
- [26]. Ruten, D (2010). "Evolutionary Principles applied to Problem Solving, <https://www.grasshopper3d.com/profiles/blogs/evolutionary-principles>"

Analysis of Multi-Level Parabolic Leaf Spring Systems Designed by using Different Materials

Mehmet Bahadir Cetinkaya ¹, Muhammed Isci ²

Abstract

The deformations that may occur on multi-level parabolic leaf spring systems due to the external effects such as vibration and force should be analyzed before the system designed. In this work, ANSYS based modal and deformation analyzes have been carried out for 10-7 parabolic leaf spring systems designed by using the Stainless Steel, Titanium Alloy and Aluminum Alloy materials. From the deformation analyzes realized under the force values of 1000 N, 3000 N and 5000 N, it was observed that the maximum total deformation values were obtained for Aluminum Alloy material and the relevant deformations were obtained as 2.7620 e-5 m, 8.2861 e-5 m and 1.3810 e-4 m, respectively. In order to analyze the effects of the different materials on the resonance frequencies, the modal analyzes were also realized under the 5000 N force value. The modal analyzes results represent that the resonance frequency value intervals were emerged as [141.3 Hz-515.14 Hz] for Stainless Steel material, [128.66 Hz-471.47 Hz] for Titanium Alloy material and [142.89 Hz-522.97 Hz] for Aluminum Alloy material.

Keywords: Leaf Spring System, Total Deformation Analysis, Modal Analysis

1. INTRODUCTION

The material properties of a leaf spring system directly affect the attenuation performance of the relevant system in terms of the disruptive effects such as stress, strain, deflection and deformation. Modal analysis and deformation analysis may usually offer effective results in performance analysis of the leaf spring systems against these disruptive effects. In literature, there are several number of works presenting detailed analyzes of leaf spring systems according to material properties. In [1], theoretical and ANSYS based modal analyzes of a multi-level leaf spring systems made of E-glass/epoxy, graphite/epoxy, carbon/epoxy and Kevlar/epoxy composite materials were performed. In work [2], ANSYS based analyzes of a multi-level steel leaf spring system and a mono composite leaf spring system both having the same load carrying capacity were carried out. In another work, a detailed ANSYS based performance comparison have been realized between the suspension behaviors of kenaf and hemp reinforced epoxy composite leaf spring system and the steel and synthetic fiber composite leaf spring system [3]. The authors in [4] performed fatigue analyzes and modal analyzes of mono leaf spring systems made of E-glass and natural fibers and then compared the results to that of 65Si7 steel material. Tadesse and Fatoba were computed the maximum displacements and the von Mises stress values for different material properties via the CATIAVR9 and ANSYS software and then compared the results both among themselves and with the literature [5]. In [6], leaf spring systems made of composite materials such as carbon epoxy, bamboo polyester, E-glass/epoxy and graphite epoxy were analyzed and their performances were compared to that of traditional steel leaf spring systems by using CATIAVR9 and ANSYS software. In work [7], dynamic analyzes of mono leaf spring systems composed of different materials such as FRP, titanium alloy, super bainite and structural steel were carried out. In another work, as a result of the performance comparison between the composite materials used in leaf spring systems it was found that the fractures usually occurring in the main direction instead of the shear direction [8]. Finally, the design processes and performance

¹ Corresponding author: Erciyes University, Department of Mechatronics Engineering, 38039, Melikgazi/Kayseri, Turkey. cetinkaya@erciyes.edu.tr

² Kayseri University, Department of Machine and Metal Technologies, 38280, Talas/Kayseri, Turkey. muhammedisci@kayseri.edu.tr

comparisons of multi-level leaf spring systems made of AISI 6150 steel, Ti-6Al-4V alloy and S-Glass fiber composite materials were analyzed in [9].

In this work, ANSYS based modal and deformation analyzes were realized for 10-7 parabolic leaf spring systems made of Stainless Steel, Titanium Alloy and Aluminum Alloy materials. The deformation analyzes were carried out under the force values of 1000 N, 3000 N and 5000 N. Furthermore, in order to determine the resonance frequencies modal analyzes were carried out for the first 6 Mode (Mode 1, Mode 2, ..., Mode 6) under the 5000 N force value.

2. MATERIALS AND METHODS

The strength of leaf spring systems against internal and external disruptive factors is extremely important. On the other hand, the material properties have a direct effect on the system strength and the variety of materials that can be preferred in the design of leaf spring systems is quite high. The 10-7 multi-level parabolic leaf spring system used in this work consists of 10 leaves in the upper leaf spring system and 7 leaves in the lower leaf spring system as shown in Figure 1.

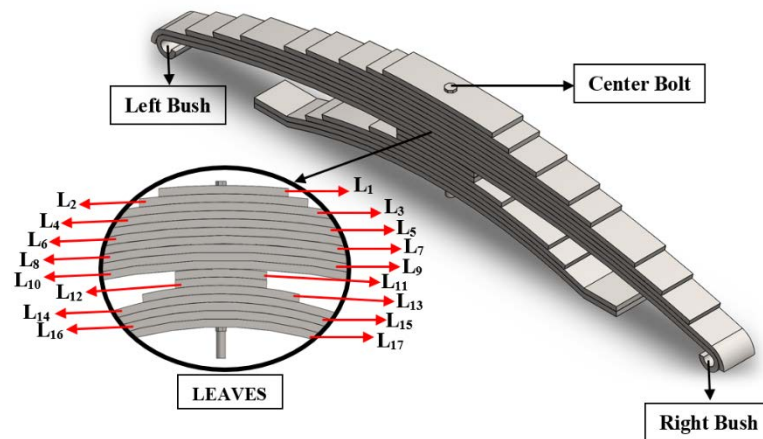


Figure 1. 10-7 multi-level parabolic leaf spring system structure

The material properties of the multi-level parabolic leaf spring system given in Figure 1 and having double bushes are represented in Table 1.

Table 1. Material properties of the 10-7 multi-level parabolic leaf spring system

Structure of the Leaf Spring System		
	Upper Leaves (mm)	Lower Leaves (mm)
Length of leaves, L	L ₁ = 200 L ₈ = 937 mm	L ₁₁ = 235 mm
	L ₂ = 260 L ₉ = 150 mm	L ₁₂ = 405 mm
	L ₃ = 365 L ₁₀ = 150 mm	L ₁₃ = 475 mm
	L ₄ = 485	L ₁₄ = 675 mm
	L ₅ = 555	L ₁₅ = 675 mm
	L ₆ = 725	L ₁₆ = 150 mm
	L ₇ = 830	L ₁₇ = 150 mm
Width of each leaf	57 mm	
Thickness of each leaf	8 mm	

The structural properties of Stainless Steel, Aluminum Alloy and Titanium Alloy materials used in the design of the 10-7 leaf spring system are given in Table 2 below. The design of the leaf spring system was realized by

using the SOLIDWORKS 2016 software. On the other hand, ANSYS Workbench 18.1 software was used to realize the deformation and resonance frequency analyzes. While performing the deformation analysis, the force values of 1000 N, 3000 N and 5000 N were applied to the *Center Bolt* region shown in Figure 1.

Table 2. The structural properties of the materials used in the design of leaf spring system

Property	Material Type		
	Stainless Steel	Aluminum Alloy	Titanium Alloy
Density (kg/m ³)	7750	2770	4620
Poisson's Ratio	0.31	0.33	0.36
Young's Modulus (Pascal)	1.930 e+11	7.100 e+10	9.600 e+10
Bulk Modulus (Pascal)	1.693 e+11	6.960 e+10	1.142 e+11
Shear Modulus (Pascal)	7.366 e+10	2.669 e+10	3.529 e+10
Tensile Yield Strength (Pascal)	2.070 e+08	2.800 e+08	9.300 e+08
Tensile Ultimate Strength (Pascal)	5.860 e+08	3.100 e+08	1.070 e+09

3. RESULTS AND DISCUSSION

In ANSYS based analysis the physical system analyzed firstly decomposed into smaller parts in order to obtain more accurate results. By means of this process, named Meshing, more reliable results could be provided. In the MESH processes performed for all leaf spring system structures, the value of the Element Size and Body Number parameters were taken as 7.7×10^{-3} and 18, respectively. The meshing image used in the simulations is shown with Figure 2.

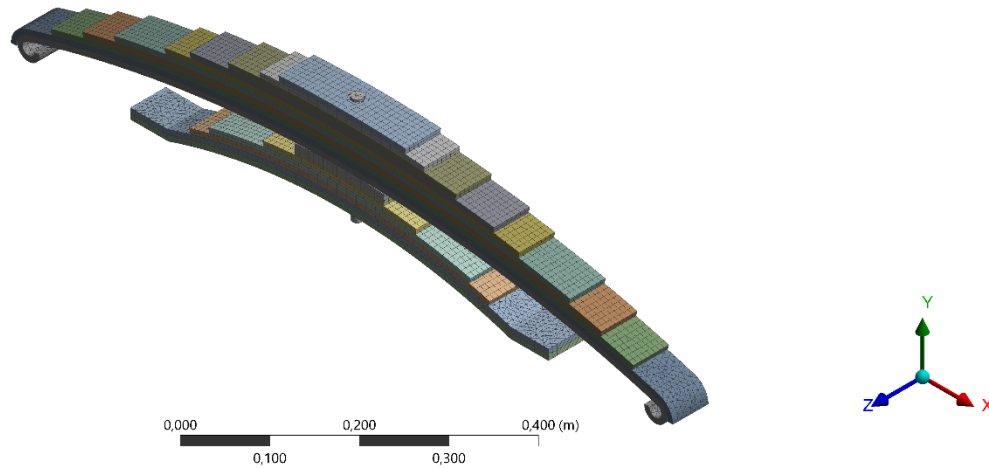


Figure 2. 10-7 leaf spring system meshing

The maximum total deformation values emerged as a result of the force values applied to the multi-level parabolic leaf spring systems made of Stainless Steel, Aluminum Alloy and Titanium Alloy materials are given in Table 3.

Table 3. The maximum total deformation values emerged for three different materials

MATERIAL	FORCE VALUES (Newton)			TOTAL DEFORMATIONS (m)
	1000 N	3000 N	5000 N	
Stainless Steel	1.0167 e-5	3.0501 e-5	5.0835 e-5	
Titanium Alloy	2.0405 e-5	6.1216 e-5	1.0203 e-4	
Aluminum Alloy	2.7620 e-5	8.2861 e-5	1.3810 e-4	

According to the values given in Table 3, it can be expressed that the leaf spring system made of Aluminum Alloy material exposes to the maximum deformation. In other words, it has been determined that the Aluminum Alloy leaf spring system shows less strength at all force values than the systems designed with other materials. However, the highest material strength was produced by the leaf spring system made of Stainless Steel material.

The resonance frequency defines the frequency value at which the amplitude of the system output begins to disturb. The resonance frequency values obtained for six different modes under the 5000 N force are given in Figure 3. From the figure, it can be seen that Titanium Alloy material produces the lowest resonance frequency values in all mode shapes. On the other hand, the highest resonance frequency values in all mode shapes were produced by the Aluminum Alloy material. Namely, Aluminum Alloy material based leaf spring systems will expose to deformation at higher frequencies to that of the other two structures. Finally, it can also be seen that the resonance frequency values emerged for the Stainless Steel and the Aluminum Alloy materials are too close to each other.

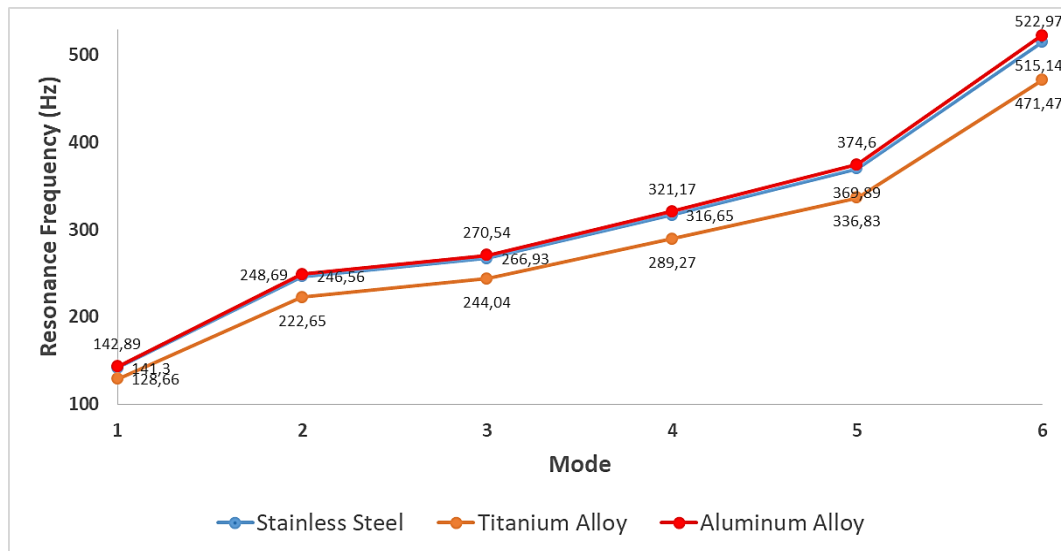


Figure 3. Mode to mode resonance frequency variations

4. CONCLUSIONS

In this work, the detailed deformation analyzes of the leaf spring systems made of Stainless Steel, Aluminum Alloy and Titanium Alloy materials were realized under different force values and then the modal analyzes were applied separately to each of the 6 different modes to obtain the relevant resonance frequencies. The results obtained for deformation analyzes represent that the highest total deformation values were emerged for the leaf spring systems made of Aluminum Alloy. Thus, the Aluminum Alloy material was determined as the lowest strength material in terms of the deformation. However, it was also observed that the Stainless Steel based materials were able to reach to the highest strength levels. According to the modal analyzes results, it is

seen that the Titanium Alloy material produces the minimum resonance frequency values for each of the 6 mode and this represents that Titanium Alloy material will reach to the resonance at lower frequencies when compared to other two materials. In general, it can also be concluded that leaf spring systems made of Stainless Steel and Aluminum Alloy materials will produce similar resonance frequencies in all mode shapes.

REFERENCES

- [1]. P. S. Rao, and R. Venkatesh, "Modal and harmonic analysis of leaf spring using composite materials," *Int. J. Novel Res. Electrical Mechanical Engineering*, Vol. 2, pp. 67-75. Dec. 2015.
- [2]. M. A. Kumar, T. N. Charyulu, C. Ramesh, "Design optimization of leaf spring," *Int. J. Engineering Res. App.*, Vol. 2, pp. 759-765, Dec. 2012.
- [3]. M. A. Faiyaz, , C. S. Hassan, M. M. Nazer, N. F. Abdullah, "Suspension behaviour of kenaf and hemp fibre composites leaf spring using finite element analysis," *Materials Today: Proceedings*, Feb. 2023.
- [4]. A. P. Venkatesh, S. Padmanabhan, C. A. Rufus, H. M. Lukmaan, A. A. Rahman, "Exploration of fatigue and modal analysis on mono leaf suspension made by natural composite materials," *Materials Today: Proceedings*, Vol. 47, pp. 4262-4267, May. 2021.
- [5]. B. A. Tadesse, O. Fatoba, "Theoretical and finite element analysis (FEA) of coated composite leaf spring for heavy-duty truck application," *Materials Today: Proceedings*, Vol. 62, pp. 4283-4290, May. 2022.
- [6]. B. A. Tadesse, O. Fatoba, "Design optimization and numerical analyses of composite leaf spring in a heavy-duty truck vehicle," *Materials Today: Proceedings*, Vol. 62, pp. 2814-2821. Mar. 2022.
- [7]. C. D. Bhatt, M. Nadarajan, R. Balaji, A. Selokar, "Leaf spring model for heavy load vehicle using solid works and ANSYS analysis," *Materials Today: Proceedings*, Vol. 33, pp. 4764-4770, Sept. 2020.
- [8]. P. B. Satasiya, M. Parikh, D. Dodiya, S. Tirole, "Optimization of a Leaf Spring by Ansys Software," *Int. J. Tech. Res. Engineering*, Vol. 6, pp. 5452-5454, May. 2019.
- [9]. S. Shamim, J. Anwer, "Design and optimization of automotive multi-leaf spring by finite element method," *Int. J. Res. Aeronautical Mech. Engineering*, Vol. 2, pp. 46-54. Aug. 2014.

BIOGRAPHY



MEHMET BAHADIR CETINKAYA was born in Kayseri, Turkey, in 1978. He received the B.S., M.S. and Ph.D. degrees in Electrical and Electronics Engineering Department from Erciyes University, Turkey, in 2001, 2004 and 2010, respectively. From 2002 to 2010 he was a Research Assistant in the department of Electrical and Electronics Engineering at Erciyes University. From 2010 to 2015 he was an Assistant Prof. Dr. at the same department. From 2015-2023 he worked as an Assistant Prof. Dr. at Mechatronics Engineering Department. In February 2023 he received the Associate Prof. Dr. degree in Electrical and Electronics Engineering science area. His current research interests include Artificial Intelligence, Biomedical Image Processing, Sensors and Mechatronic Systems.



MUHAMMED ISCI was born in Corum, Turkey in 1995. He received his two B.S. degrees in 2018 and 2019 in Mechatronics Engineering and Mathematics Department from Erciyes University. He received his M.S. degree in 2020 in Mechatronics Engineering Department from Erciyes University. He is also continuing his Ph.D. studies at the same department. From 2018 to 2020, he worked as a Mechatronics Engineer at Dener Machine Company. Since 2021, he has been working as a Lecturer at Machine and Metal Technologies Department in Technical Sciences Vocational College at Kayseri University. His research interests include Artificial Intelligence based analysis of Vibration and Force in mechanical systems.

Wind Turbine Power Estimation Based on ANFIS Under Changing Air Density And Wind Speed Conditions

Goksel Gokkus¹

Abstract

Within the scope of the study, a mathematical model of a wind turbine (WT) with a power value of 600kW, which is in the power range used extensively today, was created in a simulation environment. An Adaptive Neuro-Fuzzy Inference system (ANFIS) model was also created in the same simulation environment. The training of ANFIS was made using the data of a real wind turbine, which provides similar power values with the mathematical model. Air density and wind speed and output power values of the wind turbine were used in the training of ANFIS. In the next step, wind speed and air density data of Nevsehir province were transferred to the simulation environment. Both the mathematical wind turbine model and the Fuzzy Inference System (FIS) model created as a result of ANFIS training were run on the same data set. Both generated models were run at the same time in the simulation environment and the power data produced were compared. It has been observed that the ANFIS model, which has achieved a great deal of success on non-linear systems, predicts the wind turbine output power value within the scope of the study more than 90% correctly. As a result of the obtained comparison, it has been observed that the farthest error value, at which the training with ANFIS is differentiated according to the mathematical model, is around 10%.

Keywords: Wind Turbine Power Estimation, ANFIS

1. INTRODUCTION

It is a fact that energy consumption moves in parallel with this in developing societies with rising living standards. Industrialization and developments in production technologies accelerate the increase in energy demand. It is estimated that the demand for energy will increase even more with the idea of using electric vehicles instead of internal combustion engines by 2050 with the zero emission movement of the participating countries in accordance with the Paris climate agreement. Today, energy needs are mostly met from fossil resources and their derivatives. The most important factor in the use of these resources is the ease of energy conversion and adaptation to existing systems. For example, we can use fossil fuels such as fuel oil to power transportation vehicles, while at the same time we can generate electricity or use it for heating. The use of fossil fuels in daily life is widespread. However, the wastes generated during and after the use of these resources have negative consequences on the environment. The heat generated during the energy conversion process is one of the main ones. Others are gaseous waste. These waste gases remain suspended in the air, creating a greenhouse effect and causing further warming of the Earth and climatic changes. These effects and the changes that occur are known by the leaders of the world countries and conscious people and various steps are taken in this sense. For example, energy systems used outside of critical areas can be provided from renewable energy, and electric vehicles using hydrogen batteries, batteries and electric motors instead of internal combustion engines. In addition to these movements, tax reductions and incentives provided by countries to their citizens to turn to alternative energy sources can also be counted. Alternative energy sources are resources that draw their power and potential from nature and constantly renew themselves. Because of their potential, their energy is infinite. They can be found in the air, land and sea and have many forms. Solar energy and wind energy are the leading renewable energy sources and these two sources have the largest share in renewable energy production. Today, two methods, thermal and photovoltaic (PV) methods, are used in the conversion of solar energy into electrical energy. With the thermal method, solar energy is first converted into heat energy and then into steam power and electrical energy on steam turbines. In electricity generation with the photovoltaic method, photovoltaic cells working with the photovoltaic effect are used. Photovoltaic cells are transducers that convert solar energy into electrical energy. Photovoltaic cells act as a current source. PV panels are formed by connecting multiple PV cells in series and parallel, and it is possible to reach very high power values by connecting the panels in

series and parallel with the same logic. Although solar energy has a very high energy potential, it may not provide energy every hour of the day and every day of the year. Another energy source that stands out among renewable energy sources is wind energy [1].

Wind turbines are used to generate electricity from wind energy. Today's wind turbines are the modernization of the windmills of the past. In the past, windmills were used for various purposes such as grinding grain, drawing water from water wells and processing timber. With the increasing use of electrical energy, it has become capable of generating electricity. Wind turbines are an ideal resource for off-grid locations and rural settlements and are also used as a design tool in modern buildings. Wind turbines come in many types in terms of their axis, number of blades and aerodynamic structure. In addition, wind turbines can be produced up to megawatt level in terms of power ranges. In order to benefit from wind turbines to the maximum extent, mountain elevations, coastlines and off-shore applications, which are referred to as off-shore, are seen today. Wind turbines are an energy conversion system that requires initial investment costs. For this reason, it is necessary to have various meteorological and geographical information about the area to be installed in order to make maximum use of these systems and to pay back the investment costs in a short time. In order to profit from wind turbines, the wind speed of the area where the turbine will be installed is required to be above an average annual value of 7 m/s. Wind turbines are one of the most studied energy types and academic studies include topics such as wind turbine control and maximum power point tracking. These studies also include topics such as power estimation, fault detection and optimization in wind turbines. In addition, the increase in the installation of wind farms with large-scale wind turbines has led to a remarkable increase in wind turbine failures [2]. The variable and unpredictable characteristic of wind is the most important challenge in wind energy utilization. For the safety of the wind turbine and the efficiency of the wind energy conversion system, it is crucial to optimize the operation of the wind turbine [3]. For this purpose, various methods have been used to improve the quality and efficiency of the wind energy system. Power estimation in wind turbines is one of the methods used to obtain maximum energy from the turbine. In addition, estimation of the power curve is also required to calculate the power output of a wind turbine [4]. The wind turbine power curve shows the relationship between wind speed and power output. Modeling the wind turbine power curve can be used as a tool for monitoring, forecasting and error control of wind energy [5-7].

2. MATERIALS AND METHODS

2.1. Mathematical model of wind turbine

As the heated air rises, a low air pressure is created in this area. This low air pressure zone is filled with air again, that is, there is an air flow towards the low air pressure zone and wind is formed during this event. Wind energy has a huge potential. However, wind energy is a natural energy source that is not under human control [8]. In addition, wind energy is unlimited, clean and non-territorial. Wind turbines are systems that convert kinetic energy into mechanical energy and then into electrical energy. The mechanical power produced by wind turbines is calculated by Equation (2).

$$P = \frac{1}{2} A \rho V^3 \quad (1)$$

$$P = \frac{1}{2} A \rho V^3 C_p(\alpha, \beta) \quad (2)$$

$$C_p = \frac{P_m}{P} \quad (3)$$

Where A is rotor swept area in m^2 , V is wind speed in m/s , ρ is air density in kg/m^3 , C_p is power co-efficiency, P_m is wind turbine output power in W , α is tip speed ratio (TSR), β is blade pitch angle in $^\circ$. Within the scope of the study, a wind turbine model is created using Equations (2) and (3).

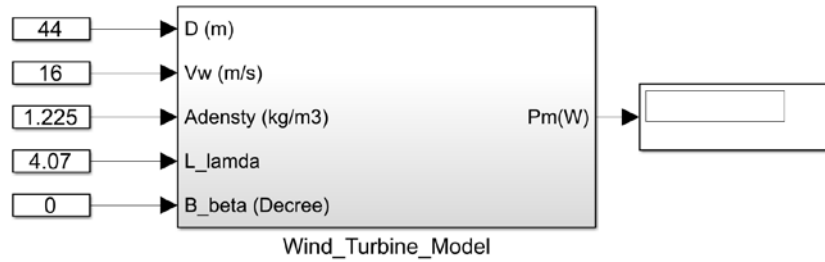


Figure 2. Wind turbine model created within the scope of the study

In this model, rotor blade diameter D , wind speed Wv , and air density ρ are used as input parameters. The model is given in Figure 1. The design parameters of the wind turbine model are given in Table 1. These parameters are published in open source.

Table 2. Electrical and mechanical data of the V44-600 wind turbine in the study [9]

Parameters	Value	Unit
Rated Power	600	kW
Rated Wind Speed	16	m/s
Survival Wind Speed	52	m/s
Cut-in Wind Speed	4.5	m/s
Cut-out Wind Speed	20	m/s
Rotor diameter	44	m
Swept area	1521	m ²
Number of blades	3	Pieces
Rotor maximum speed	28	U/min
Tip speed	65	m/s
Rotor material	GFK/Epoxy	-
Gear box ratio	1:51	-
Generator Type	Asynchronous	-
Generator maximum speed	1650	U/min
Generator voltage	690	V
Grid connection	Thyristor	-
Frequency	50	Hz

2.2. Training and design phases of ANFIS

Power estimation techniques in wind turbines provide very good dynamic responses and can do so without the need for turbine parameters [10]. For this purpose, machine learning methods are frequently used. The mechanical output power of WT's successfully Predicted using input variables such as wind speed, rotor angular speed, power coefficient (C_p) and blade pitch [11]. ANFIS is used for fault detection and fault diagnosis of systems such as wind turbines [12]. ANFIS is a fuzzy model that facilitates adaptation and learning within a flexible system framework and ANFIS does not require expert knowledge to build the modeling system [13],

nor does it need a mathematical formulation. ANFIS is more practical than existing systems with its two-input structure [14] and is a type of neural network that shows better learning and prediction capabilities [15]. In this study, ANFIS, one of the intelligent techniques, is used to predict the output power of a wind turbine. Electrical and meteorological data of a real wind turbine are used in the training of ANFIS. The real wind turbine data used in the training is given in Table 2. According to this table, the air density varies between 1.06 and 1.27Kg/m³. The wind speed varies between 4.5-20 m/s, which are the values given in Figure 2 and cover the operating regions of the wind turbine. On the other hand, the mechanical power output of the wind turbine varies between 0 and 600kw and this variation is shown in Figure 2.

Table 2. Wind and power data of the V44-600 wind turbine in the study [9]

Wind Speed	Air Density								
	1.06	1.09	1.12	1.15	1.18	1.21	1.225	1.24	1.27
4.5	0	0	0	0	0	0	0	0	0
5	24.7	25.8	26.8	27.8	28.9	29.9	30.4	31.0	32.0
6	65.2	67.4	69.9	71.8	74.0	76.2	77.3	78.4	80.6
7	115	119	123	126	130	134	135	137	141
8	176	181	187	192	198	203	206	209	214
9	246	253	261	268	275	283	287	290	298
10	320	329	338	348	357	366	371	375	384
11	393	404	415	425	436	445	450	454	463
12	461	471	482	492	503	511	514	518	525
13	517	525	534	542	551	556	558	560	565
14	557	563	568	573	579	581	582	584	586
15	581	584	587	589	592	593	594	594	595
16	593	594	595	596	598	598	598	598	599
17	598	598	598	599	599	599	599	600	600
18	600	600	600	600	600	600	600	600	600
19-20	600	600	600	600	600	600	600	600	600

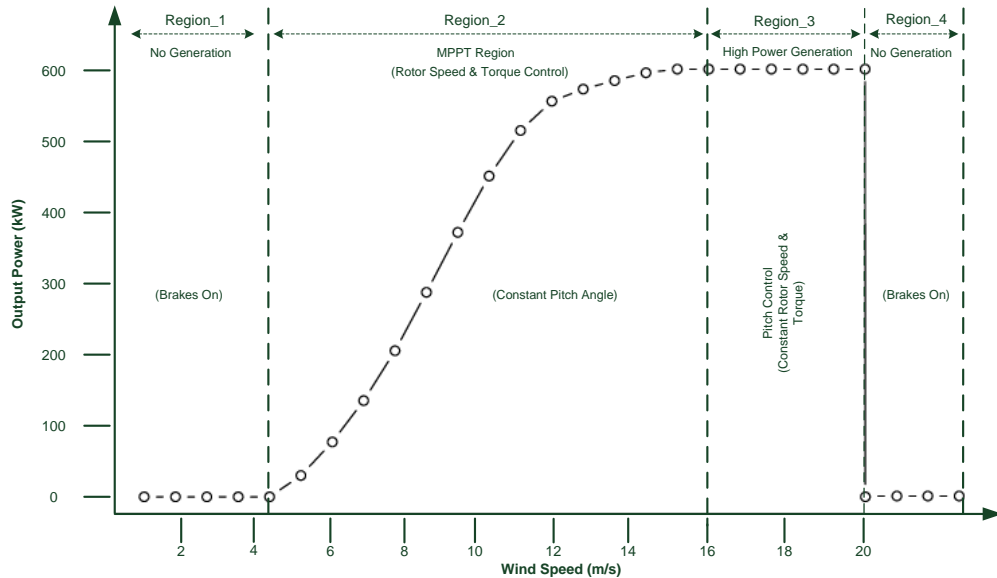


Figure 2. Power curve and operating regions graph of the wind turbine used in ANFIS training

- **Region 1:** In this area wind speed is too low to generate power or is much lower than the desired value. According to the manufacturer, the wind turbine is disabled at wind speeds below 4.5 m/s, and according to the company, the lower wind cut value of the V44-600 model is 4.5 m/s.
- **Region 2:** The wind speed in this area is higher than the lower cut value and less than the optimum value. In other words, the wind speed varies between 5-16 m/s. In this area, it is possible to produce mechanical power and therefore electrical energy. The wind turbine is constantly controlled by various methods in this area, and it is aimed to produce maximum power from the turbine. This field is also called the MPPT field.
- **Region 3:** In this area wind turbine produces the highest power and energy. The rotor speed of the wind turbine is fixed in this area, ensuring that the power produced is at the maximum rate. The rotor speed of the turbine is fixed by methods such as blade angle control, variable TSR, and variable C_p .
- **Region 4:** Wind speed in this area is determined by the manufacturer and includes the risks if the wind turbine continues to operate. If the wind speed exceeds 20 m/s, the braking process is activated, preventing structural damage to the components under pressure or to the wind turbine.

A simplified block diagram of the ANFIS training process is given in Figure 3. According to this block diagram, real wind turbine data is trained with anfisedit and a Fuzzy Interface System (FIS) file is generated as a result of the training.

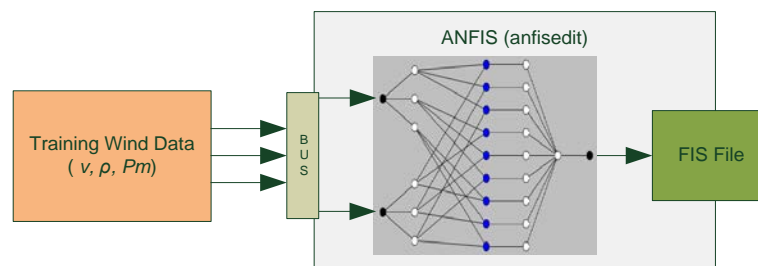


Figure 3. Simplified block diagram of the training process of ANFIS within the scope of the study

The structural layers of ANFIS and the parameters used in its design are given in Figure 4. According to Figure 4, ANFIS consists of 5 layers, 2 input and 1 output parameters.

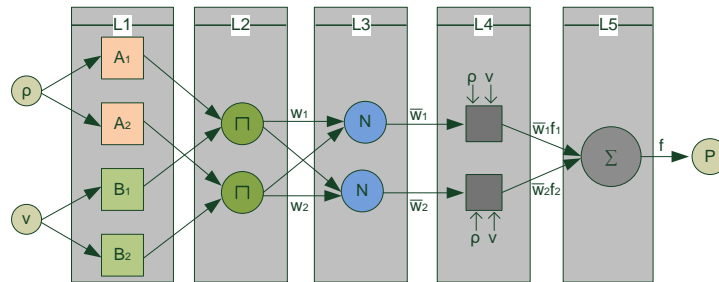


Figure 4. Structural layers and design parameters of ANFIS

The input and output parameters of the FIS file produced as a result of ANFIS training are given in Figure 5.

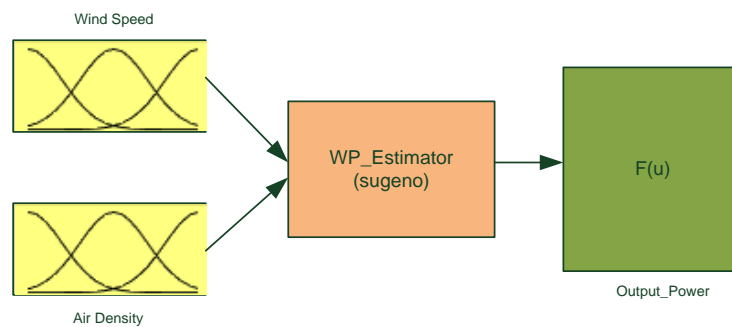


Figure 5. Input and output parameters of the FIS file produced as a result of ANFIS training

3. RESULTS AND DISCUSSION

Within the scope of the study, a mathematical model of the V44-600 model, which is a product of Vestas Company, has been created. The mathematical model was created using the actual design parameters of the V44-600 model. The wind speed, air density and output power data in Table 2, which contains the actual data of the V44-600 model, were used. Before using the actual data of the turbine in ANFIS training, the repetitive data that may cause errors were removed. As a result of the removal of repetitions, a data set consisting of 154 units was created. With this data set, the FIS file was generated as a result of the training. The generated FIS file was run over the Fuzzy Logic Controller using real wind speed and air density profiles. In order to fulfill this purpose, a model was created and the model is given in Figure 6.

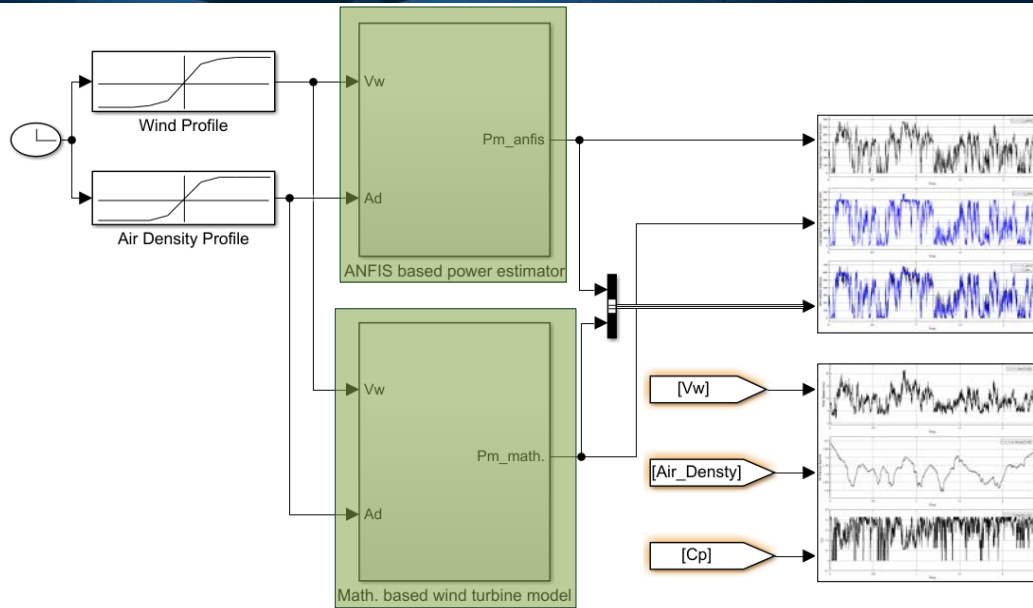


Figure 6. Simulation environment where both models are run together

Figure 7 shows the real wind speed and air density profiles of Nevsehir province, the mathematical and ANFIS-based wind turbine model in which these profiles are applied simultaneously. The graph of the air density profile used as an input parameter during the study process is given in Figure 7. According to this graph, the air density varies between 1.1792 and 1.2088 Kg/m³

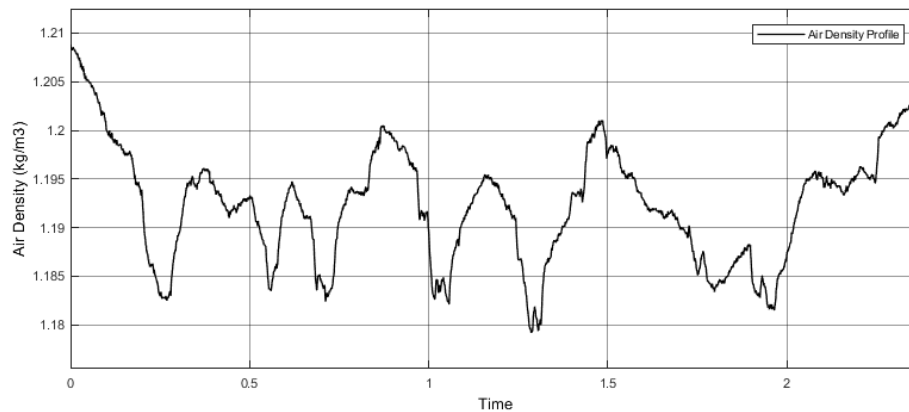


Figure 7. Graph of the air density profile used in the test phase of ANFIS

When Figure 7 is analyzed, it is seen that the limit values of the air density used during the training of ANFIS (Table 2) cover the air density used in the test phase. Figure 8 shows the wind speed graph used in the test phase of ANFIS. The minimum value of the wind speed used in the test phase is 1.8 m/s and the maximum value is 21.5 m/s.

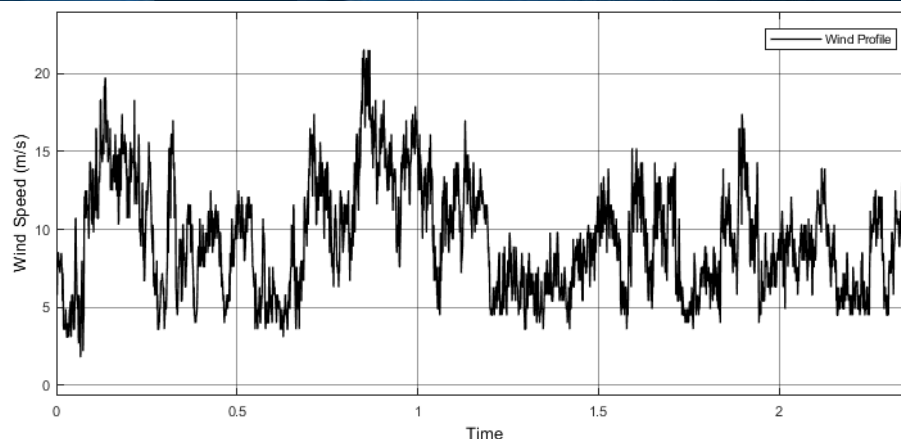


Figure 8. Graph of the wind speed profile used in the test stage of ANFIS

When the upper and lower values of the graph given in Figure 8 are analyzed; it can be seen that the wind speed used in the training stage of ANFIS (Table 2) is out of the training data in certain regions where the wind speed used in the test stage does not cover the wind speed.

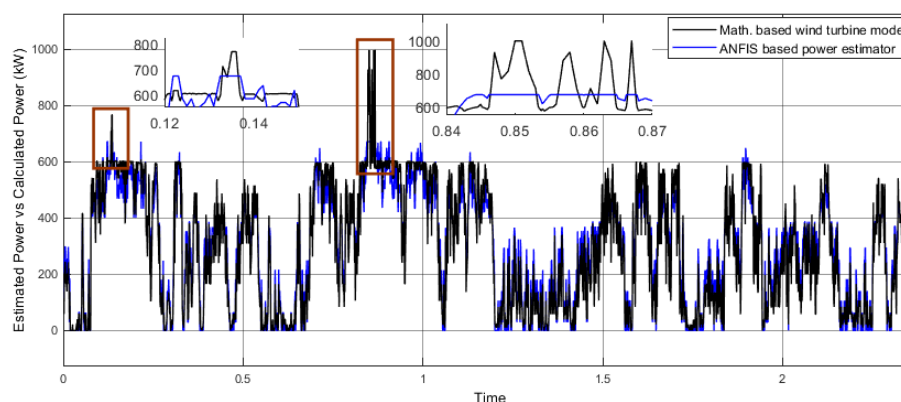


Figure 9. Graph of the mechanical output power produced by the mathematical model and ANFIS model

The mechanical output power curves obtained as a result of running the mathematical model and ANFIS-based model in the environment given in Figure 6 are given in Figure 9. Here, the blue colored line represents the mechanical output power produced by the ANFIS-based model, while the mechanical output power curve produced by the mathematical model is black.

4. CONCLUSIONS

In this paper, a study has been carried out on wind energy, one of the most studied energy sources, and wind turbines that can generate electrical energy from this energy. Within the scope of the study, a mathematical model of a wind turbine with a power value of 600kW was developed. An ANFIS based model was also developed in the same environment and with the same power value. The ANFIS model was trained on a real wind turbine data. In the next stage, both models were run in the same environment and at the same time. Wind speed and air density data, which are atmospheric parameters of Nevsehir province, were used as input for both models. The output power values obtained as a result of the study were compared. As can be seen from the output power graph given in Figure 9, although both models are designed over a power value of 600 kW, it is observed that the mathematical model produces values well above 600kW in some places (shown in visual detail in Figure 9). However, it is seen that the ANFIS based model produces more realistic output power values under the same conditions. In addition to this It has been observed that the ANFIS model, which has achieved a great deal of success on non-linear systems, predicts the wind turbine output power value within the scope of the study more than 90% correctly. As a result of the obtained comparison, it has been observed that the farthest error value, at which the training with ANFIS is differentiated according to the mathematical model, is around 10%.

REFERENCES

- [1]. S. Tumse, A. Ilhan, M. Bilgili, and B. Sahin, "Estimation of wind turbine output power using soft computing models," (in English), *Energy Sources Part a-Recovery Utilization and Environmental Effects*, vol. 44, no. 2, pp. 3757-3786, Jun 15 2022.
- [2]. Q. Zhou, T. T. Xiong, M. B. Wang, C. M. Xiang, and Q. P. Xu, "Diagnosis and Early Warning of Wind Turbine Faults Based on Cluster Analysis Theory and Modified ANFIS," (in English), *Energies*, vol. 10, no. 7, Jul 2017.
- [3]. A. B. Asghar and X. D. Liu, "Estimation of wind turbine power coefficient by adaptive neuro-fuzzy methodology," (in English), *Neurocomputing*, vol. 238, pp. 227-233, May 17 2017.
- [4]. M. Javadi, A. M. Malysheff, D. Wu, C. Q. Kang, and J. N. Jiang, "An Algorithm for Practical Power Curve Estimation of Wind Turbines," (in English), *Csee Journal of Power and Energy Systems*, vol. 4, no. 1, pp. 93-102, Mar 2018.
- [5]. S. Seo, S. D. Oh, and H. Y. Kwak, "Wind turbine power curve modeling using maximum likelihood estimation method," (in English), *Renewable Energy*, vol. 136, pp. 1164-1169, Jun 2019.
- [6]. J. Yan, H. Zhang, Y. Q. Liu, S. Han, and L. Li, "Uncertainty estimation for wind energy conversion by probabilistic wind turbine power curve modelling," (in English), *Applied Energy*, vol. 239, pp. 1356-1370, Apr 1 2019.
- [7]. L. G. M. Souza and D. C. Santos, "A Performance Comparison of Robust Models in Wind Turbines Power Curve Estimation: A Case Study," (in English), *Neural Processing Letters*, vol. 54, no. 4, pp. 3375-3400, Aug 2022.
- [8]. N. Labeled, I. Attoui, S. Makhoulfi, A. Bouraiou, and M. S. Bouakkaz, "PSO Based Fractional Order PI Controller and ANFIS Algorithm for Wind Turbine System Control and Diagnosis," (in English), *Journal of Electrical Engineering & Technology*, Nov 23 2022.
- [9]. thewindpower. V44/600. Available: <https://media.mwps.world/static/2011/03/Technical-description-Vestas-600-kW.pdf>
- [10]. J. M. Guerrero, C. Lumberras, D. Reigosa, D. Fernandez, F. Briz, and C. B. Charro, "Accurate Rotor Speed Estimation for Low-Power Wind Turbines," (in English), *Ieee Transactions on Power Electronics*, vol. 35, no. 1, pp. 373-381, Jan 2020.
- [11]. M. Y. Javed, I. A. Khurshid, A. B. Asghar, S. T. H. Rizvi, K. Shahid, and K. Ejsmont, "An Efficient Estimation of Wind Turbine Output Power Using Neural Networks," (in English), *Energies*, vol. 15, no. 14, Jul 2022.
- [12]. B. Chen, P. C. Matthews, and P. J. Tavner, "Wind turbine pitch faults prognosis using a-priori knowledge-based ANFIS", *Expert Systems with Applications*, vol. 40, no. 17, pp. 6863-6876, Dec 1 2013.
- [13]. M. Morshedizadeh, M. Kordestani, R. Cariveau, D. S. K. Ting, and M. Saif, "Power production prediction of wind turbines using a fusion of MLP and ANFIS networks," (in English), *Iet Renewable Power Generation*, vol. 12, no. 9, pp. 1025-1033, Jul 9 2018.
- [14]. N. M. L. Phan, D. N. Tung, T. N. Thanh, and N. T. T. Vu, "ANFIS Wind Speed Estimator-Based Output Feedback Near-Optimal MPPT Control for PMSG Wind Turbine," (in English), *Journal of Control Automation and Electrical Systems*, Dec 24 2022.
- [15]. M. R. Sarkar, S. Julai, C. W. Tong, and S. F. Toha, "Effectiveness of Nature-Inspired Algorithms using ANFIS for Blade Design Optimization and Wind Turbine Efficiency," (in English), *Symmetry-Basel*, vol. 11, no. 4, Apr 2019.

Investigation of the Electrochemical Behavior of a Pillar[5]arene Derivative on the Glassy Carbon Electrode Surface

Tugce Gover¹

Abstract

Glassy carbon (GC) electrode surface was modified with gelatin/azido-pillar[5]arene, and the electrochemical behavior of ascorbic acid (AA) was investigated on these new surface. To improve the efficiency of electrode, the electrode surface was modified and optimum conditions for AA determination were established. Electrochemical experiments were performed at different modification techniques, pH values, the concentrations of AA and scan rates. The usability of the proposed modified electrode for the determination of AA was investigated using square wave voltammetry (SWV). The gelatin/azido-pillar[5]arene/GC modified electrode exhibited a good repeatability, stability and sensitivity for the determination of AA.

Keywords: Pillar[5]arene, electrochemical method, electrode modification

1. INTRODUCTION

Pillarenes are macrocyclic compounds composed of hydroquinone units linked by methylene bridges at para positions [1]. Although pillar[5]arene shows electrochemical activity related to the oxidation of hydroquinone units, the number of studies on its use in electrochemical sensors is very few [2].

Ascorbic acid (AA), known for its reducing properties, is easily oxidized to dehydroascorbic acid. It is a powerful antioxidant and fights against free radical-induced diseases. Excess ascorbic acid can irritate the stomach, and oxalic acid, one of its metabolites, causes problems in the kidneys. Sometimes, excess amounts of ascorbic acid can result in the inhibition of natural processes occurring in food and can cause a deterioration of taste/aroma [3-5]. Thus, the determination of ascorbic acid has become important.

Chromatography [6], voltammetry [7], fluorometry [8] and potentiometric titration [9] can be given as examples of analysis methods used in AA determination studies reported in the literature. Voltammetry is an electrochemical method. Electrochemical methods are among the most attractive and convenient methods because they do not require preliminary preparation, are simple and fast, and allow determination with inexpensive equipment [10].

The aim of this study is to investigate the electrochemical behavior of ascorbic acid with a voltammetric sensor, gelatin/azidopillar[5]arene modified glassy carbon electrode. The electrochemical behavior of azidopillar[5]arene (Figure 1) synthesized for the first time by Kursunlu and his research group [11] was investigated by electrochemical technique on the GC electrode surface (Figure 2).

¹Selcuk University, Faculty of Pharmacy, Department of Analytical Chemistry, 42130, Konya, TURKEY.
tugce.gover@selcuk.edu.tr



Figure 1. Structure of Azidopillar[5]arene

2. EXPERIMENTAL

2.1. Chemicals and Reagents

In this study, the chemicals obtained from the related companies were used directly without a purification process. Sodium dihydrogen phosphate dihydrate ($\text{NaH}_2\text{PO}_4 \cdot 2\text{H}_2\text{O}$) and sodium acetate trihydrate ($\text{C}_2\text{H}_3\text{NaO}_2 \cdot 3\text{H}_2\text{O}$) were supplied from VWR. Hydrochloric acid (HCl), boric acid and ortho-phosphoric acid (85 %) were supplied from Merck. Tetrabutylammonium tetrafluoroborate (TBATFB) (99 %) and Sodium Hydroxide (NaOH) were supplied from Sigma-Aldrich. Acetonitrile (CH_3CN) ($\geq 99.9\%$) was supplied from Isolab. Potassium hexacyanoferrate (III) ($\text{K}_3[\text{Fe}(\text{CN})_6]$) was supplied from Alfa Aesar. Sodium hydrogen phosphate (Na_2HPO_4) and l (+) ascorbic acid were supplied from (John Townsend Baker, Gliwice, Poland). Potassium chloride (KCl) and acetic acid (CH_3COOH) were supplied from Riedel-de Haën. Aluminum oxide (Al_2O_3) was supplied from Nanografi Company. Gelatin powder was supplied from Doga Ilac Hammaddeleri. Ultra-pure water and freshly prepared solutions were used throughout the experiment. All solutions were stored in the refrigerator.

2.2. Instrumentation and Other Equipment

CHI 660C electrochemical analyzer device was used in the electrochemical examination of experiments. Three-electrode cell system was used which includes the working (BAS model MF-2012 GC), reference $\text{Ag}/\text{AgCl}/(\text{sat. KCl})$ used in aqueous media, or Ag/Ag^+ (in 10 mM AgNO_3), used in non-aqueous media) and counter (platinum wire) electrodes.

During the study, special care was taken that the calibration of all used devices was done at certain time periods. Bandelin RK 100 model ultrasonic bath was used for cleaning electrode surfaces. JENWAY 3010 model pH meter was used at room temperature for pH adjustments of prepared solutions.

2.3. Preparation of Modified Electrode

The GC electrode was washed with pure water and cleaned in a circular direction with the suspension of alumina polishing powder of $0.05\ \mu\text{m}$ dimension on the velvet surface. At the end of the alumina powder process, electrodes were sonicated in pure water and acetonitrile for three minutes, respectively [12].

- Modified solid contact electrode with azido-pillar[5]arene was prepared by potentiodynamic polymerization.

Electropolymerization of azido-pillar[5]arene on the GC electrode surface was performed at 5 cycles in the potential range $-1.5\ \text{V}/+2.0\ \text{V}$ at the scan rate of $100\ \text{mV/s}$ in $1.0 \times 10^{-3}\ \text{mM}$ azido-pillar[5]arene prepared in CH_3CN containing $0.1\ \text{M}$ tetrabutylammonium tetrafluoroborate (TBATFB) (Figure 2). The surface prepared after this step was defined as azido-pillar[5]arene/GC electrode.

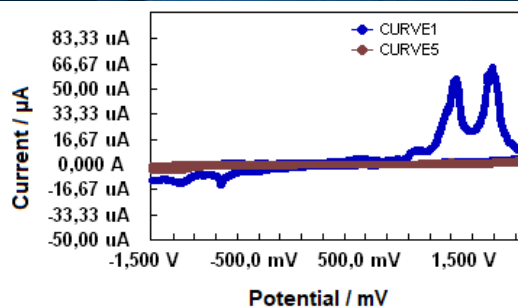
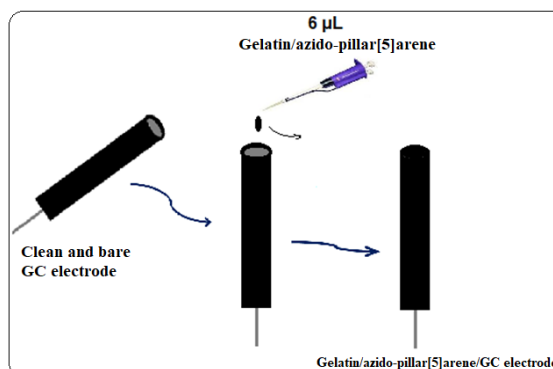


Figure 2. The cyclic voltammograms on the GC electrode surface of azidopillar[5]arene dissolved in CH_3CN containing 0.1 M TBATFB at 5 cycles. Blue line:1st cycle and red line:5th cycle (The scan rate is 100 mV/s).

- GC electrode modification by drop-dry method

The electrode surface was modified by the drop dry method [13]. After 10 mg of Gelatin powder was dissolved in 1 mL of distilled water, it was mixed in a sonicator in a hot environment for half an hour. A solution was prepared by adding 1 mg of azidopillar[5]arene to this mixture [14]. 6 μL of this mixture was dropped to the cleaned GC electrode surface, and then the electrode surface was waited to dry at room temperature. The surface prepared after this step was defined as gelatin/azido-pillar[5]arene/GC electrode (Scheme 1).



Scheme 1: Preparation of the electrode surface by drop dry method

3.RESULTS AND DISCUSSION

3.1.Characterization of Modified Electrode by Cyclic Voltammetry

In the characterization of the modified electrode surfaces, the $K_3Fe(CN)_6$ molecule is generally used as an electrochemical probe. The cyclic voltammograms of $Fe(CN)_6^{3-}$ molecule on the bare and modified electrode surfaces were taken and the bare and modified electrode surfaces were compared. Figure 3 is the cyclic voltammogram of $Fe(CN)_6^{3-}$ molecule on modified GC electrode by electropolymerization. Figure 4 is the cyclic voltammogram of $Fe(CN)_6^{3-}$ molecule on modified GC electrode by drop dry method. As seen from Figures 3 and 4, the difference in peak currents of $Fe(CN)_6^{3-}$ on the electrode surfaces indicates that the GC electrode surface has been modified.

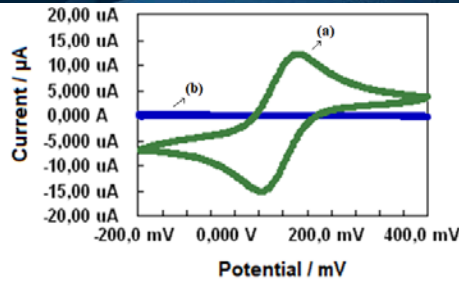


Figure 3: The cyclic voltammograms of 1.0 mM of $\text{Fe}(\text{CN})_6^{3-}$ in Britton-Robinson buffer (pH 2.0) of (a) bare GC electrode and (b) azido-pillar[5]arene/GC electrode modified at 5 cycles. (Scan rate: 100 mV/s)

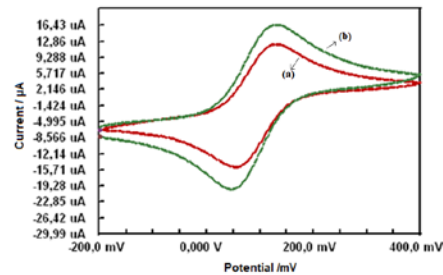


Figure 4: The cyclic voltammograms of 1.0 mM of $\text{Fe}(\text{CN})_6^{3-}$ in Britton-Robinson buffer (pH 2.0) of (a) bare GC electrode and (b) gelatin/azido-pillar[5]arene/GC electrode modified by drop dry method (Scan rate: 100 mV/s)

As can be seen from the voltammograms obtained from Figure 4, the higher peak current of the modified electrode enables the determination of the amount of ascorbic acid [10, 15].

3.2. Effect of pH Value

The electrochemical oxidation of ascorbic acid in pH 5.0, 6.0, 7.0 and 8.0 phosphate buffer solution was studied using differential pulse voltammetry (DPV) technique. Figure 5 and 6 show the effect of pH value on the oxidation peak current of ascorbic acid. pH 8.0 phosphate buffer solution was used for the determination of ascorbic acid to achieve higher sensitivity.

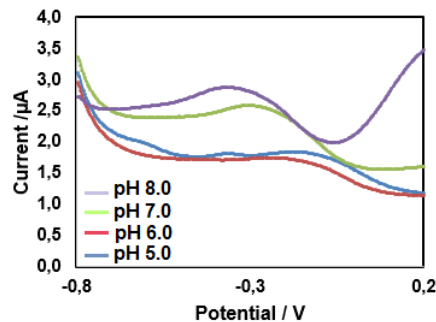


Figure 5: Differential pulse voltammograms in the presence of 1 mM ascorbic acid in 0.1 M phosphate buffer solution at various pH values on gelatin/azido-pillar[5]arene/GC electrode (Scan Rate: 100 mV/s)

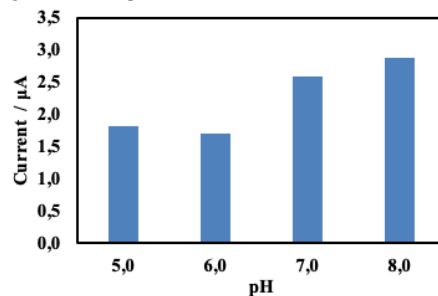


Figure 6: Current graph against various pH values

The highest peak current value was obtained in pH 8.0 phosphate buffer solution. Therefore, pH 8.0 was chosen as the most suitable medium.

3.3. Effect of the Scan Rate

To determine whether the electrochemical process of AA on the modified glassy carbon electrode surface is diffusion-controlled or adsorption-controlled, a scan rate study was performed. For this purpose, cyclic voltammograms of 2.0×10^{-3} M AA in pH 8.0 phosphate buffer solution were taken at different scan rates between 25 mV/s and 300 mV/s. The $\log v$ - $\log I$ graph is given in Figure 7. The slope value of the $\log I$ vs. $\log v$ graphs gives information on either diffusion or adsorption control of the redox processes.

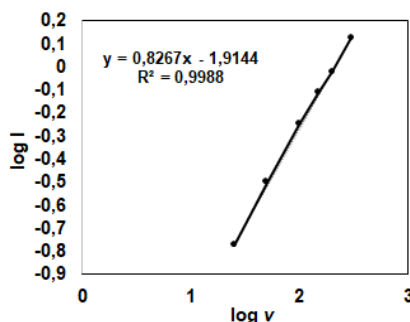


Figure 7: The graph of $\log I$ versus $\log v$ of 2.0×10^{-3} M AA in pH 8.0 phosphate buffer solution (Scan rates: 25, 50, 100, 150, 200, 300 mV/s)

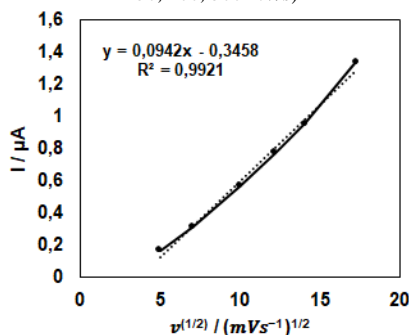


Figure 8: The graph of current versus square root of scanning rate of 2.0×10^{-3} M AA in pH 8.0 phosphate buffer solution (Scan rates: 25, 50, 100, 150, 200, 300 mV/s)

In diffusion-controlled processes, the slope value of 0.5 is the theoretical value [10]. As seen in Figure 7, the slope being different from 0.5 indicates that the electron transfer reaction is not diffusion controlled. The fact that the slope of the graph obtained by plotting the logarithm of the scan rate versus the logarithm of the peak current was different from 0.5 and showed an increase approaching 1.0 revealed that the transfer was not only diffusion controlled but also adsorption controlled. As seen in Figure 8, it is seen that the graph obtained by plotting the peak current versus the square root of the scan rate is linear when the R^2 value in the graph is close to 1 [16].

3.4. Analytical Performance and Calibration Curve of the Modified Electrode

The analytical performance of the modified electrode was investigated (Figure 9). From the voltammograms given in Figure 9, it is seen that the peak current values increase with increasing AA concentration.

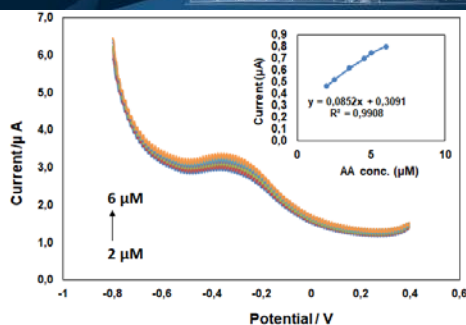


Figure 9: Square wave voltammograms and calibration graph of different concentrations (2 μM ; 2.5 μM ; 3.5 μM ; 4.5 μM ; 5 μM ; 6 μM) of ascorbic acid in 0.1 M phosphate buffer solution (pH 8.0).

CONCLUSION

In this study, a gelatin/azido-pillar[5]arene-modified glassy carbon electrode was used for the determination of AA. The preparation of this sensor is a simple and quick process. The proposed sensor provided sensitivity, short measurement time, ease of preparation, good accuracy and good analytical performance. Due to these features, it provides a good alternative to the existing studies in the literature in terms of AA determination.

ACKNOWLEDGMENT

I am grateful for laboratory material and equipment support to Prof. Dr. Salih Zeki Bas, Prof. Dr. Mustafa Ozmen and Prof. Dr. Ahmed Nuri Kursunlu.

REFERENCES

- [1]. J.-F. Chen, Q. Lin, H. Yao, Y.-M. Zhang, and T.-B. Wei, "Pillar[5]arene-based multifunctional supramolecular hydrogel: multistimuli responsiveness, self-healing, fluorescence sensing, and conductivity", *Mater. Chem. Front.*, vol. 2, pp. 999-1003, 2018.
- [2]. V.A. Smolko, D.N. Shurpik, R.V. Shamagsumova, A.V. Porfireva, V.G. Evtugyn, L.S. Yakimova, I.I. Stoikov, and G.A. Evtugyn. "Electrochemical Behavior of Pillar[5]Arene on Glassy Carbon Electrode and Its Interaction with Cu^{2+} and Ag^+ Ions", *Electrochim. Acta*, vol. 147, pp. 726–734, 2014.
- [3]. C.S. Erdurak-Kilic, B. Uslu, B. Dogan, U. Ozgen, S.A. Ozkan, M. Coskun, "Anodic voltammetric behavior of ascorbic acid and its selective determination in pharmaceutical dosage forms and some Rosa species of Turkey", *J. Anal. Chem.*, vol. 61, pp. 1113-1120, 2006.
- [4]. A. Hodgkinson, Oxalic acid in biology and medicine, Academic Press, London, UK, 1977.
- [5]. J. Wawrzyniak, A. Ryniecki and W. Zembrzuski, "Application of voltammetry to determine vitamin C in apple juices", *Acta Sci. Pol. Technol. Aliment.*, vol. 4(2), pp. 5-16, 2005.
- [6]. D. Ivanović, A. Popović, D. Radulović and M. Medenica, "Reversed-phase ion-pair HPLC determination of some water-soluble vitamins in pharmaceuticals", *J. Pharm. Biomed. Anal.*, vol 18(6), pp 999-1004, 1999.
- [7]. C. Bravo-Díaz and E. González-Romero, "A novel method for the determination of vitamin C in natural orange juices by electrochemical monitoring of dediazonation of 3-methylbenzenediazonium tetrafluoroborate", *Anal. Chim. Acta*, vol. 385(1-3), pp 373-384, 1999.
- [8]. Y. Dilgin and G. Nisli, "Fluorimetric determination of ascorbic acid in vitamin C tablets using Methylene Blue", *Chem. Pharm. Bull.*, vol. 53(10), pp. 1251-1254, 2005.
- [9]. G. S. Sastry and G. G. Rao, "Oxidimetric determination of ascorbic acid with potassium hexacyanoferrate(III) in acid medium", *Talanta*, vol. 19(2), pp. 212-214, 1972.
- [10]. T. Tabanlıgil Calam. "The Voltammetric Determination of Epinephrine on an Au Electrode Modified with Electropolymerized 3,5-Diamino-1,2,4-Triazole Film", *GU J Sci, Part C*, vol. 7(4), pp. 985-998, 2019.
- [11]. K. Atacan, A.N. Kursunlu and M. Ozmen. "Preparation of pillar[5]arene immobilized trypsin and its application in microwave-assisted digestion of Cytochrome c", *Mater. Sci. Eng. C*, vol. 94, pp. 886–893, 2019.
- [12]. T. Govar and Z. Yazicigil, "Electrochemical study of 6-(ferrocenyl)hexanethiol on gold electrode surface in non-aqueous media", *Surf. Interfaces*, vol. 13, pp. 163-167, 2018.
- [13]. N. Ndebele, J. Mack, and T. Nyokong, "A 3,5-DistyrylBODIPY Dye Functionalized with Boronic Acid Groups for Direct Electrochemical Glucose Sensing", *Electroanalysis*, vol. 31, pp. 137–145, 2019.
- [14]. Z. O. Erdogan, A. N. Kursunlu, S. Kucukkolbasi. "Pillar [5] arene Based Non-Enzymatic and Enzymatic Tyramine Sensor", *IEEE Sensors Journal*, vol. 21(5), pp. 5728-5735, 2020.
- [15]. F. Agin. "Guaifenesinin poli(Nil Mavisi) ile modifiye edilmiş camsi karbon elektrot ile voltametrik analizi ve farmasotik dozaj formundan tayini", *Karadeniz Chem. Sci. Tech.*, vol. 02, pp. 27-31, 2018.
- [16]. Y. Oztekin and Z. Yazicigil. "1,10-Fenantrolin Mono Hidrat'ın Elektrokimyasal Modifikasyonu ve Karakterizasyonu", *S.U. Fen Ed. Fak. Fen Derg.*, vol. 31, pp. 1-8, 2008.



BIOGRAPHY

Tugce Gover was born in Konya, Turkey. She received the Ph.D. degree from Ankara University, Ankara, Turkey, in 2017. She works as an assistant professor at Selcuk University. Her research interests include construction of electrochemical sensors and biosensors in analytical chemistry.

Forest Fire Detection Using Unmanned Aerial Vehicle Images and Deep Learning

Fatma Ozge Ozkok^{1,2}, Yucel Batu Salman²

Abstract

Forests are the most important source of oxygen and have an essential role in the life of living things. Therefore, it is necessary to protect forests for ecological balance. However, forest fires disrupt the environmental balance and cause severe damage to forests. While forest fires are easy to put out when they first appear, it isn't easy to put out when they spread over large areas. Recently, images obtained from unmanned aerial vehicles have been used to detect forest fires by detecting fire and smoke in large areas. Deep learning algorithms provide faster and more accurate analysis of these images. This study uses the End to End Object Detection with Transformers (DETR) algorithm, a robust deep learning algorithm. Experimental studies show that the DETR algorithm has promising results in detecting forest fires.

Keywords: deep learning, object detection, detr, forest fire, unmanned aerial vehicle images

1. INTRODUCTION

Forests are one of the most essential parts of our planet. They are the primary source of oxygen and the habitat of many living things. Moreover, they provide clean air and water resources. In addition to its environmental contributions, it also contributes to the economy with its wood products. On the other hand, deforestation affects all residing things negatively. Therefore, the protection of forests has significant importance [1,2].

Forest fires are devastating disaster that causes critical damage to forests. It can quickly spread over a large area with wind and other weather conditions. It is challenging to extinguish large-area fires. However, it is easier to put out if the fire is noticed when it starts. So that the harmful effects of fire can be reduced [1-4].

In recent years, large areas can be quickly analyzed thanks to unmanned aerial vehicles (UAV). For this reason, successful results are obtained in many fields, such as agriculture, agriculture, and the defense industry, especially forest fires. UAVs can enter narrow and dangerous places that pilots cannot reach. For this reason, it is pretty successful and reliable in monitoring forest fires. However, it is also crucial to correctly analyze these images obtained from unmanned aerial vehicles [5,6].

Deep learning has emerged as a sub-field of machine learning. It is used for classification, object detection, and pattern identification in different data types, such as images, signals, and text. The performance of deep learning methods, especially in image processing, has accelerated technological developments in various fields. It is also frequently used in analyzing UAV images [7-9].

End-to-End Object Detection with Transformers (DETR) algorithm is a deep learning algorithm that uses state-of-the-art transformers techniques for object detection [10]. The algorithm provides powerful object detection performance in UAV images.

In the study, we focus on the detection of smoke using UAV imagery and the DETR algorithm. The rest of the paper is organized as follows: Section 2 presents related works. Section 3 introduces the DETR algorithm ms. Section 4 gives the experimental results, and Section 5 presents the conclusions and future works.

¹ Corresponding author: Erciyes University, Department of Computer Engineering, Kayseri, Turkey
fozgeozkok@erciyes.edu.tr

² Bahcesehir University, Department of Computer Engineering, Istanbul, Turkey

2. RELATED WORKS

Forest fire monitoring and detection techniques can be categorized as digital image processing and deep learning [11]

In the literature, digital image processing methods are successfully used. For example, Vipin proposed a rule-based color model for fire pixel classification. The model using RGB and YCbCr color spaces detects fire and nonfire images [12]. Chen et al. also developed a method to detect forest fires and reduce false alarm rates. The method focuses on the segmentation of images using k-means algorithm [13]. Xiao et al. identified fire using continuous image sampling provided by a CCD camera and color information of pixels [14]. Surit and Chatwiriya proposed a 4-step method that detects smoke in a forest fire. The first step of the method is to detect changing areas. The second step is to segment the area of change from the image. The third step is to analyze static and dynamic characteristics [15]. They finally detect whether there is smoke in the picture. Although these studies are successful in their fields, they do not have the advantages of deep learning algorithms when the number of data increases or more complex data needs to be analyzed.

Recently, deep learning has been used successfully in monitoring and detecting forest fires, as in many other fields. For example, Zheng et al. proposed a convolutional neural network (CNN) model to detect forest fires in real-time. This model can automatically extract features from images thanks to CNN [16]. Xue et al. developed an improved YOLO5 algorithm to identify small forest fire targets [17]. Kinaneva proposed a framework to detect forest fires using UAVs early. Their framework comprises a UAV with cameras and a neural network model [18]. Liu et al. developed a two-level forest fire detection method based on deep learning. In this model, a high amount of training data was produced using the general advanced networks (GAN). Then, histogram of oriented gradient (HOG) and Adaboost algorithms were used for preliminary definition. Finally, forest fire pictures were analyzed with high performance using the CNN and support vector machine algorithm (SVM) classifier [19]. Although CNN-based methods are dominant in object detection, it has been seen that transformer-based methods are also successful recently.

DETR is one of the transformer-based object detection methods that has shown successful application performance [20-23]. The algorithm also has a simple feed-forward network. Therefore, it can detect objects successfully and quickly with less prior knowledge [24]. For these reasons, a DETR-based object identification algorithm was used in the study to detect forest fires.

3. MATERIAL METHODS

3.1. Datasets

A forest fire dataset consisting of 737 images was used in this study. The dataset was partitioned into 516 training, 147 validation, and 74 test images. In this dataset, smoke is used to detect fire. The dataset was obtained from the Roboflow website [25].

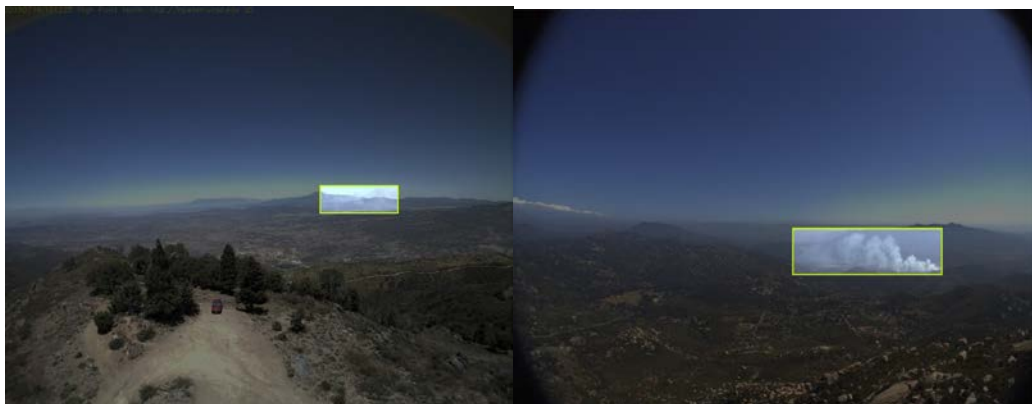


Figure 3: Images from the forest fire dataset

3.2.DETR

The DETR is a state-of-the-art algorithm for object detection. The algorithm consists of two parts: CNN backbone and transformer (Figure 2). The CNN backbone is used for the 2D representation of images. In this layer, the features of the images are extracted and given to the transformer layer. As a result of the transformer layer, class, and bounding box or no-object class are determined [10].

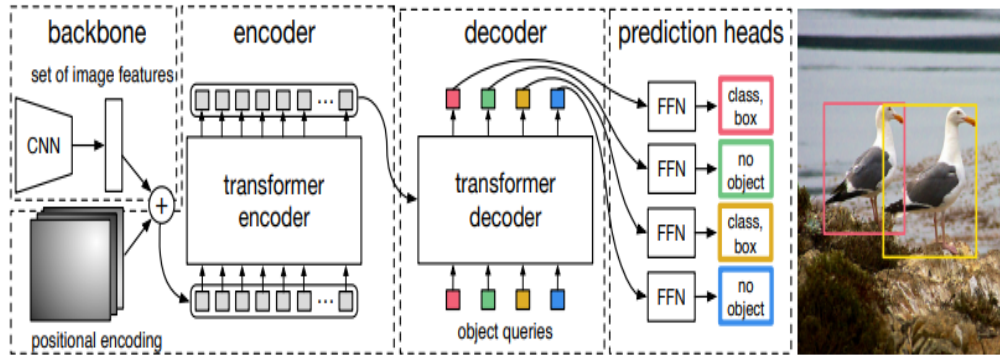


Figure 4 The architecture of DETR [10]

The detailed architectures of the encoder-decoder layers are given in Figure 3. The features of the image are given as input to the encoder. The encoder consists of multi-head self-attention and feed-forward networks (FFN). Self-attention layers focus on the model's relevant image regions and capture general contextual information.

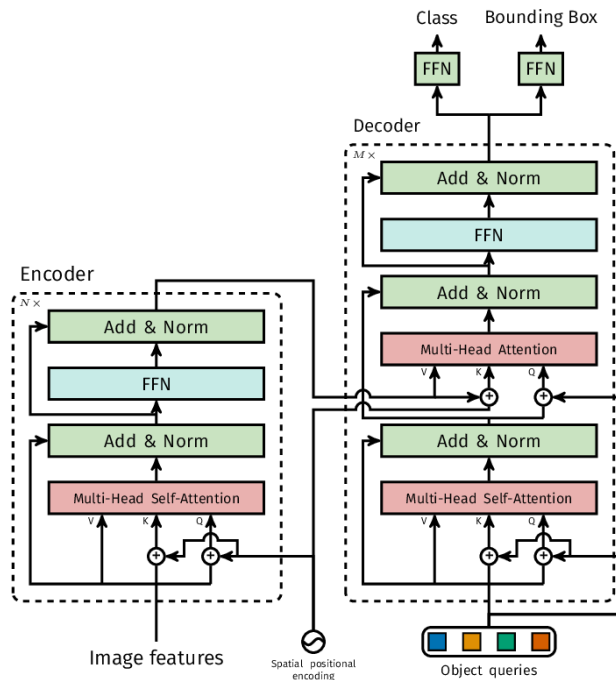


Figure 5 Encoder-Decoder Architecture [10]

The output of the encoder and object queries are given to the decoder. The decoder consists of multi-head self-attention, multi-head attention, and feed-forward networks. The attention layers are used to refine object queries. The FFN layer determines the class label and bounding box.

4.RESULTS AND DISCUSSION

The proposed method aims to detect smoke in the forest fire dataset using DETR algorithm. Experiments were conducted using Google Colab framework with GPU T4. The hyperparameters of DETR were selected as follows.

- Learning rate : 1e-4,
- Learning rate of backbone :1e-5,
- Batch size : 2
- Weight_decay: 1e-4
- Epochs: 60
- Learning rate of drop: 200

Figure 4 shows the average recall results of the experiment. Classes were detected without error. The best result is obtained with 89.4% success. The algorithm is more successful at detecting large smoke.

```
Averaged stats: class_error: 0.00  loss: 3.8580 (5.0528)  loss_ce: 0.0020 (0.0255)
Average Precision (AP) @[ IoU=0.50:0.95 | area= all | maxDets=100 ] = 0.407
Average Precision (AP) @[ IoU=0.50 | area= all | maxDets=100 ] = 0.894
Average Precision (AP) @[ IoU=0.75 | area= all | maxDets=100 ] = 0.308
Average Precision (AP) @[ IoU=0.50:0.95 | area= small | maxDets=100 ] = 0.257
Average Precision (AP) @[ IoU=0.50:0.95 | area=medium | maxDets=100 ] = 0.385
Average Precision (AP) @[ IoU=0.50:0.95 | area= large | maxDets=100 ] = 0.561
Average Recall (AR) @[ IoU=0.50:0.95 | area= all | maxDets= 1 ] = 0.483
Average Recall (AR) @[ IoU=0.50:0.95 | area= all | maxDets= 10 ] = 0.549
Average Recall (AR) @[ IoU=0.50:0.95 | area= all | maxDets=100 ] = 0.603
Average Recall (AR) @[ IoU=0.50:0.95 | area= small | maxDets=100 ] = 0.454
Average Recall (AR) @[ IoU=0.50:0.95 | area=medium | maxDets=100 ] = 0.561
Average Recall (AR) @[ IoU=0.50:0.95 | area= large | maxDets=100 ] = 0.742
```

Figure 6 The average results of the experiment

Figure 5 shows an example of smoke detection in the dataset.



Figure 7.The detection of smoke

Figure 6 shows graphs of the experiment's loss and mAP results. As the epoch number increases, the error decreases and the average accuracy increases. As a result, the loss rate approaches 0 and the mAP approaches 1.

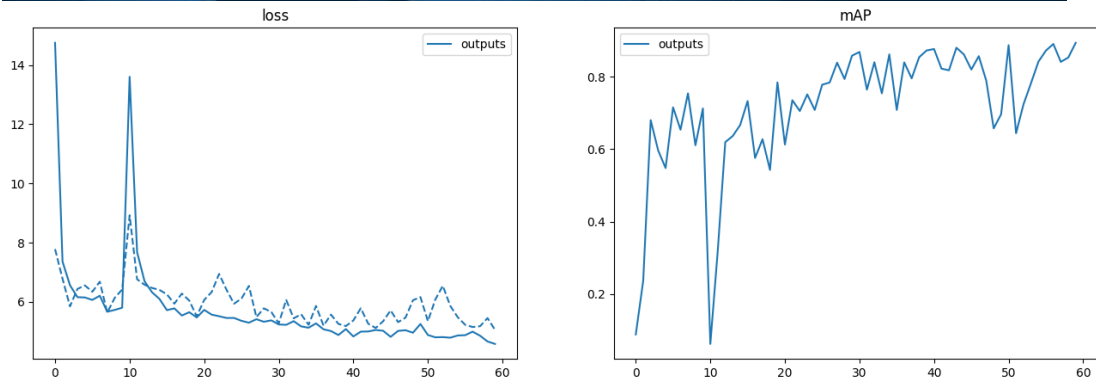


Figure 8 Loss and mAP Graphs

Figure 7 shows the loss graphs of the experiment. As the epoch number increases, the losses decrease.

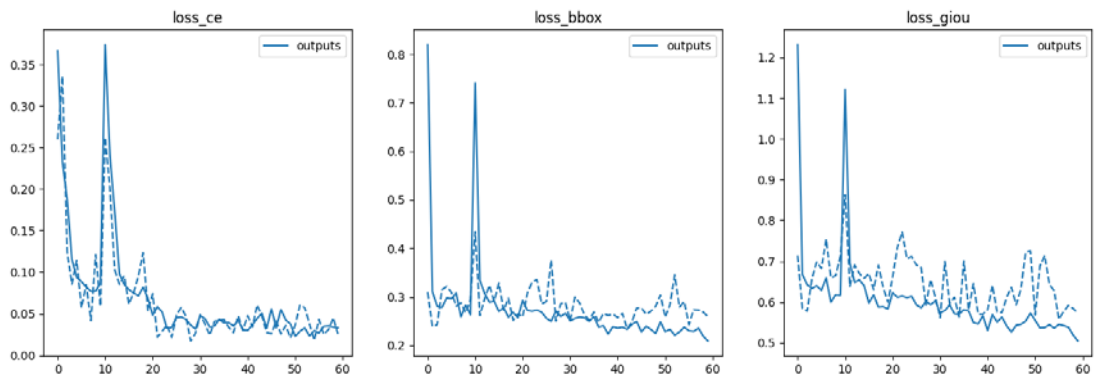


Figure 9 Loss graphs

Figure 8 shows the class error and cardinality error graphs of the experiment. As the epoch number increases, the errors decrease.

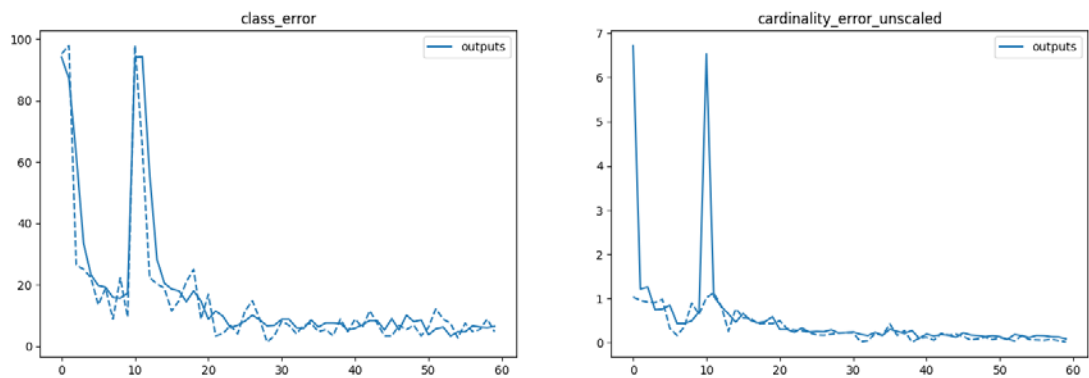


Figure 10 Class error and cardinality error graphs

CONCLUSIONS

Forests are an indispensable part of our planet. However, forest fires significantly destroy them. If fires can be put out when smoke first rises, the spread of fires can be prevented. Thanks to unmanned aerial vehicles, images can be collected from forests, and fire can be detected by analyzing these images with deep learning methods. In this study, forest fire detection was performed with the DETR algorithm, which is an object detection algorithm with transformers. Experimental results show that the DETR algorithm is successful in forest fire detection.

In future works, we plan to develop a DETR-based deep learning method to improve object detection results in smaller objects datasets.

ACKNOWLEDGMENT

This study was funded by Scientific Research Projects Commission of Bahcesehir University Project number: BAP.2022-02.18. In addition, this study was supported by the Scientific and Technological Research Council of Turkey (TUBITAK) with the BIDEB-2218 program.

REFERENCES

- [1] Flannigan, M. D., Stocks, B. J., & Wotton, B. M. (2000). Climate change and forest fires. *Science of the total environment*, 262(3), 221-229.
- [2] Sastry, N. (2002). Forest fires, air pollution, and mortality in Southeast Asia. *Demography*, 39(1), 1-23.
- [3] Sanford Jr, R. L., Saldarriaga, J., Clark, K. E., Uhl, C., & Herrera, R. (1985). Amazon rain-forest fires. *Science*, 227(4682), 53-55.
- [4] Whitlock, C. (2004). Forests, fires and climate. *Nature*, 432(7013), 28-29.
- [5] Newcome, L. R. (2004). Unmanned aviation: a brief history of unmanned aerial vehicles. Aiaa.
- [6] Valavanis, K. P. (Ed.). (2008). *Advances in unmanned aerial vehicles: state of the art and the road to autonomy*.
- [7] Learning, D. (2020). Deep learning. High-dimensional fuzzy clustering.
- [8] Srivastava, S., Divekar, A. V., Anilkumar, C., Naik, I., Kulkarni, V., & Pattabiraman, V. (2021). Comparative analysis of deep learning image detection algorithms. *Journal of Big Data*, 8(1), 1-27.
- [9] Osco, L. P., Junior, J. M., Ramos, A. P. M., de Castro Jorge, L. A., Fatholahi, S. N., de Andrade Silva, J., & Li, J. (2021). A review on deep learning in UAV remote sensing. *International Journal of Applied Earth Observation and Geoinformation*, 102, 102456.
- [10] Carion, N., Massa, F., Synnaeve, G., Usunier, N., Kirillov, A., & Zagoruyko, S. (2020). End-to-end object detection with transformers. In *Computer Vision–ECCV 2020: 16th European Conference, Glasgow, UK, August 23–28, 2020, Proceedings, Part I 16* (pp. 213-229). Springer International Publishing.
- [11] Xue, Z., Lin, H., & Wang, F. (2022). A small target forest fire detection model based on YOLOv5 improvement. *Forests*, 13(8), 1332.
- [12] Vipin, V. (2012). Image processing based forest fire detection. *International Journal of Emerging Technology and Advanced Engineering*, 2(2), 87-95.
- [13] Chen, R., Luo, Y., & Alsharif, M. R. (2013). Forest Fire Detection Algorithm Based on Digital Image. *J. Softw.*, 8(8), 1897-1905.
- [14] Xiao, J., Li, J., & Zhang, J. (2009, October). The identification of forest fire based on digital image processing. In *2009 2nd International Congress on Image and Signal Processing* (pp. 1-5). IEEE.
- [15] Surit, S., & Chatwiriya, W. (2011, May). Forest fire smoke detection in video based on digital image processing approach with static and dynamic characteristic analysis. In *2011 First ACIS/JNU International Conference on Computers, Networks, Systems and Industrial Engineering* (pp. 35-39). IEEE.
- [16] Zheng, X., Chen, F., Lou, L., Cheng, P., & Huang, Y. (2022). Real-Time Detection of Full-Scale Forest Fire Smoke Based on Deep Convolution Neural Network. *Remote Sensing*, 14(3), 536.
- [17] Xue, Z., Lin, H., & Wang, F. (2022). A small target forest fire detection model based on YOLOv5 improvement. *Forests*, 13(8), 1332.
- [18] Kinaneva, D., Hristov, G., Raychev, J., & Zahariev, P. (2019, May). Early forest fire detection using drones and artificial intelligence. In *2019 42nd International Convention on Information and Communication Technology, Electronics and Microelectronics (MIPRO)* (pp. 1060-1065). IEEE.

- [19] Liu, Z., Zhang, K., Wang, C., & Huang, S. (2020). Research on the identification method for the forest fire based on deep learning. *Optik*, 223, 165491.
- [20] Shanliang, L., Yunlong, L., Jingyi, Q., & Renbiao, W. (2022, April). Airport UAV and birds detection based on deformable DETR. In *Journal of Physics: Conference Series* (Vol. 2253, No. 1, p. 012024). IOP Publishing.
- [21] Wang, D., Li, Z., Du, X., Ma, Z., & Liu, X. (2022). Farmland Obstacle Detection from the Perspective of UAVs Based on Non-local Deformable DETR. *Agriculture*, 12(12), 1983.
- [22] Lin, M., Li, C., Bu, X., Sun, M., Lin, C., Yan, J., ... & Deng, Z. (2020). Detr for crowd pedestrian detection. arXiv preprint arXiv:2012.06785.
- [23] Zheng, A., Zhang, Y., Zhang, X., Qi, X., & Sun, J. (2022). Progressive end-to-end object detection in crowded scenes. In *Proceedings of the IEEE/CVF Conference on Computer Vision and Pattern Recognition* (pp. 857-866).
- [24] Arkin, E., Yadikar, N., Xu, X., Aysa, A., & Ubul, K. (2022). A survey: object detection methods from CNN to transformer. *Multimedia Tools and Applications*, 1-31.
- [25] Dwyer, B., Nelson, J. (2022), Solawetz, J., et. al. Roboflow (Version 1.0) [Software]. Available from <https://roboflow.com>. computer vision.



Performance analysis comparison for a ground source heat pump with and without using solar collectors

Ghadir Chahid¹, Hatem Hasan Ismaeel², Recep Yumrutas³

Abstract

Underground storage tanks are used to efficiently store thermal energy for domestic and commercial heating systems. This study compares two systems; The first consists of an underground storage tank, a heat pump, and a building to be heated. The second system consists of the same components with adding solar collectors (SC). An analytical model of each system is developed to find the performance parameters of the heating systems. The Coefficient of Performance COP, the temperature of the storage tank, and solar energy are part of the main performance parameters. Time-dependent water temperature in the tank is obtained by calculating the heat transfer from the storage tank to the surrounding earth hourly. A MATLAB program is prepared for computing all performance parameters of the heating systems. In the fifth year of operation, the comparison results showed adding the SC led to increasing the temperature of the tank by at least 10.2 °C; it also showed an increase in the value of COP around 1.8. These findings were obtained for a tank volume of 400 m³, a Carnot efficiency of 40%, and a house in Gaziantep. As evidenced by a temperature increase and coefficient of Performance COP, the addition of solar collectors SC has a significant impact on the system.

Keywords: seasonal thermal energy storage tank, ground source heat pump, solar energy, comparison.

1. INTRODUCTION

Recently, there is increasing interest in renewable energies as an alternative to fossil fuels. The use of heat pumps for heating and cooling is one of the best options for saving energy and preserving the environment, as these systems rely on heat extracted from renewable sources such as outside air, ground water, or ground. The principle of thermal storage for heat pumps began to be used in the last decade of the last century, as thermal storage technologies were developed to increase the efficiency of using thermal energy and save costs by benefiting from solar energy. Since then, these technologies have been improved and developed to include wider uses in heating and cooling homes, buildings, and industries. Research in this field varied between experimental and theoretical studies, and included an analysis of materials and designs, determining thermal loads, and improving control systems. Recent research in this field has shown the effectiveness of thermal storage technologies in increasing energy efficiency and improving the overall performance of heat pumps.

Several studies have analyzed the performance of various solar thermal energy storage systems. Yumrutas and Unsal [1] proposed a model for determining the performance of a solar aided heat pump space heating system with seasonal energy storage in a hemispherical tank, and found that the type of earth and storage depth have a minor impact on the system's annual energy fractions. Meanwhile, Rodríguez-Hidalgo et al. [2] found that the size of the storage tank is a crucial factor in determining the performance of a solar plant, particularly when the ratio of the volume of the storage tank (V) to the area of the solar collector (A) is less than 0.05 m. They found that the optimum storage tank size is $V/A = 0.08$ m. Bermed tanks were found to be more economically efficient than completely buried tanks, according to Dincer and Rosen [3], even though they may not perform as well in reducing thermal losses. Bermed tanks require less excavation, resulting in lower initial costs, and provide easy access for maintenance purposes. Ucar and enalli [4] compared the

¹ Department of Mechanical Engineering, Gaziantep University, Gaziantep, 27310, Turkey. ghadir.chahid@gmail.com

² Department of Energy Engineering, Technical College of Engineering, Duhok Polytechnic University, Duhok, Iraq. hatem.hasan@dpu.edu.krd

³ Department of Mechanical Engineering, Gaziantep University, Gaziantep, 27310, Turkey. yumrutas@gantep.edu.tr

thermal performances and economic savings of central solar heating system with three types of seasonal storage. The study found that the solar savings of a system with an underground storage tank were higher than other storage systems, and that heat loss from a tank without insulation on the ground was higher than that of a tank with insulation. Caliskan et al. [5] analyzed different types of thermal energy storage (TES) systems for building applications under different environmental temperatures and found that the most sustainable TES system is the aquifer TES, while the least sustainable system is the latent TES.

Nomenclature			
ρ_w	density of water (kg.m ⁻³)	T_h	temperature of the radiator used in the house (K)
c_w	specific heat of the water (kJ.kg ⁻¹ .K ⁻¹)	ϕ_w	dimensionless water temperature in the tank (-)
V_w	volume of the water (m ³)	ϕ_i	dimensionless inside design air temperature (-)
V	volume of the tank (m ³)	ϕ_a	dimensionless ambient air temperature (-)
A	area of the tank (m ²)	ϕ_0	constant (-)
A_c	area of the solar collectors (m ²)	q	dimensionless net energy charge to the tank (-)
R	radius of the tank (m)	q_h	dimensionless heat requirement of the house (-)
r	radial distance from the tank center (m)	q_u	dimensionless useful solar energy (-)
T_w	water temperature in the tank (K)	τ	dimensionless time (-)
T_∞	earth temperature (K)	w	dimensionless heat pump work (-)
T_i	inside design air temperature (K)	γ	dimensionless parameter (-)
T_a	ambient air temperature (K)	u	dimensionless parameter (-)
k	thermal conductivity (W.m ⁻¹ .K ⁻¹)	x	dimensionless radial distance (-)

Other studies have focused on optimizing various design parameters for solar thermal energy storage systems. Chung et al. [6] found that a Central Solar Heating Plant with Seasonal Storage could supply 39% of the total heat energy required by a greenhouse and office building, and future expansion may require enlarging the collector area. Zhang et al. [7] suggested that optimizing the thickness of the insulating cover and properly designing the volume of the water pond are crucial design parameters that affect the performance of a space heating and cooling system with surface water seasonal energy storage. Wang and Qi [8] analyzed the performance of underground thermal storage in a SGCHPS for a residential building and found that the efficiency of underground thermal storage strongly depends on solar radiation intensity and the ratio between the water tank volume and the area of solar collectors. The study suggested a reasonable ratio between tank volume and collector area of 20-40 L/m² for optimal performance. The efficiency of underground thermal storage was found to be over 40% and 70% based on total radiation and absorbed solar energy, respectively. Qu et al. [9] proposed an optimal solar cooling and heating system for the Intelligent Workplace with a 4 m³ storage tank and constant temperature control. With NS orientation, the system could provide 39% cooling and 20% heating, saving 100 kW h/ m² and 34 kW h/ m² annually. With EW orientation, it could provide 37% cooling and 29% heating, saving 74 kW h/m² and 61 kW h/m² annually.

2. DESCRIPTION OF THE SYSTEM

Figure 1. (a) displays the schematic diagram of a heating system with a ground-coupled heat pump. On the other hand, Figure 1. (b) illustrates a heating system that uses both solar assistance and a ground-coupled heat pump.

There are three mainly circuits in these two systems: 1) the circuit of water in the underground buried storage tank with a small circulating pump; 2) the refrigerant circuit of the heat pump, equipped with an expansion valve and driven by a compressor; 3) the radiator circuit which distributes heat to the house. A heat storage tank associated with a heat pump is an essential part of the heating system. The Thermal Energy Storage (TES) tank is assumed to be spherical in shape, buried underground and filled with water as the storage medium. The main objective of water storage is to take advantage of the earth's heat, as the heat is absorbed from the soil and transferred to the thermal storage tank, as well as retaining the collected solar heat during the summer to provide heating of the place in the winter months, when adding SC. The heat pump absorbs

the heat from the ground tank through the evaporator and delivers it to the place to be heated through the condenser. The heat pump operates when the ambient temperature is lower than the designed temperature in the place to be heated. Heat is supplied to the house by means of water radiators. The design heating load of the house is 10 Kw.

In the second system, solar collectors are coupled to the underground storage tank. The solar energy is used to heat the fluid that circulates inside the collectors, then converts it into thermal energy that is delivered to the tank.

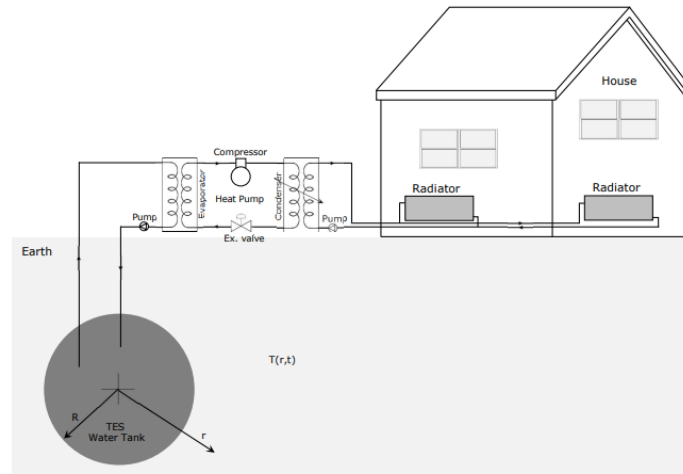


Figure 11. (a) Heating system with ground-coupled heat pump

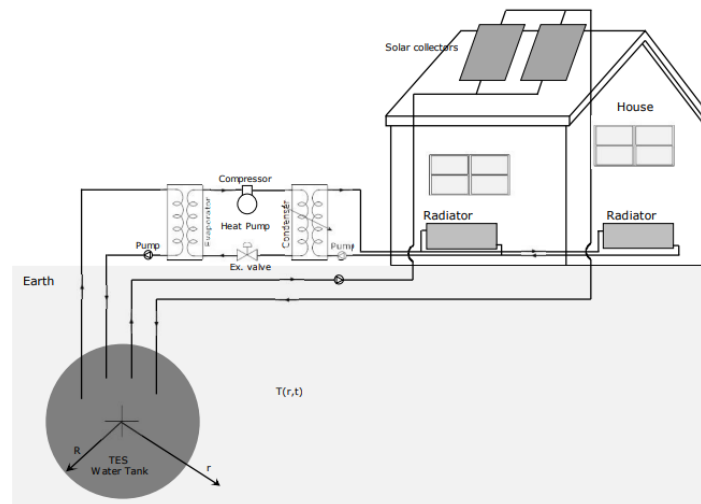


Figure 1. (b) heating system with solar assisted and ground coupled heat pump

3. MODELING OF THE SYSTEM

3.1. Solution of the transient heat transfer problem for the TES tank:

Many assumptions were made to simplify this study, such as assuming a constant temperature of 15 °C for the earth and considering the soil to be homogeneous with constant thermophysical properties. The present study also assumes that the TES tank is located deep in the Earth's surface and thus the three-dimensional

transient heat transfer problem can be simplified to a one-dimensional transient heat transfer problem in spherical coordinates. This simplification makes the heat transfer problem easier to analyze and study.

This section will develop an expression for calculating the water temperature in the TES tank as a function of time. The initial and boundary conditions of the transient temperature field problem inside the earth outside the spherical TES tank are expressed in spherical coordinates as follows:

$$\frac{\partial^2 T}{\partial r^2} + \frac{2}{r} \frac{\partial T}{\partial r} = \frac{1}{\alpha} \frac{\partial T}{\partial t} \quad (1)$$

$$T(R, t) = T_w(t) \quad (2)$$

$$T(\infty, t) = T_\infty \quad (3)$$

$$T(r, 0) = T_\infty \quad (4)$$

By using following dimensionless radial distance (x), time (τ) and temperature (ϕ) the dimensionless form of Eq. (1) can be obtained as:

$$\begin{aligned} x &= \frac{r}{R} & q &= \frac{Q}{4\pi R k T_\infty} & p &= \frac{\rho_w c_w}{3\rho c} & \tau &= \frac{\alpha t}{R^2} \\ \phi &= \frac{T - T_\infty}{T_\infty} & \phi_w &= \frac{T_w(t) - T_\infty}{T_\infty} & \phi_a(\tau) &= \frac{T_a(t) - T_\infty}{T_\infty} & \phi_i & \\ & & &= \frac{T_i - T_\infty}{T_\infty} & & & & \end{aligned} \quad (5)$$

$$\frac{\partial^2 \phi}{\partial x^2} + \frac{2}{x} \frac{\partial \phi}{\partial x} = \frac{\partial \phi}{\partial \tau} \quad (6)$$

$$\phi(1, \tau) = \phi_w(\tau) \quad (7)$$

$$\phi(\infty, \tau) = 0 \quad (8)$$

$$\phi(x, 0) = 0 \quad (9)$$

The energy balance for the storage tank is defined as:

$$Q = \rho_w c_w V_w \frac{dT_w}{dt} - kA \frac{\partial T}{\partial r}(R, t) \quad (10)$$

Using dimensionless parameters in Eq. (5) gives:

$$q = p \frac{d\phi_w(\tau)}{d\tau} - \frac{\partial \phi}{\partial x}(1, \tau) \quad (11)$$

Eq. (6) can be further simplified by applying the following transformation:

$$\psi(x, \tau) = x \cdot \phi(x, \tau) \quad (12)$$

$$\frac{\partial \psi}{\partial x} = x \cdot \frac{\partial \phi}{\partial x} + \phi(x, \tau) \quad (13)$$

$$\frac{\partial^2 \psi}{\partial x^2} = \frac{\partial \psi}{\partial \tau} \quad (14)$$

$$\psi(1, \tau) = \phi_w(\tau) \quad (15)$$

$$\psi(\infty, \tau) = 0 \quad (16)$$

$$\psi(x, 0) = 0 \quad (17)$$

Using Eq. (12) and Eq. (13) in Eq. (11) gives:

$$q = p \frac{d\phi_w(\tau)}{d\tau} - \frac{\partial \psi}{\partial x}(1, \tau) + \phi_w(\tau) \quad (18)$$

The following similarity transformation is used to solve this dimensionless transient heat transfer problem:

$$\eta = \frac{x-1}{2\sqrt{\tau}} \quad (19)$$

The solution of the resulting transformation for the constant ϕ_0 is:

$$\psi(x, \tau) = \phi_0 \left\{ 1 - \operatorname{Erf} \left[\frac{x-1}{2\sqrt{\tau}} \right] \right\} \quad (20)$$

The general solution is obtained as:

$$\psi(x, \tau) = \phi_w(0) \left\{ 1 - \operatorname{Erf} \left[\frac{x-1}{2\sqrt{\tau}} \right] \right\} + \int_0^\tau \left\{ \frac{d\phi_w(\xi)}{d\xi} \right\} \left\{ \frac{x-1}{2\sqrt{\tau-\xi}} \right\} \quad (21)$$

The following integro-differential equation can be obtained by differentiating the general solution with respect to dimensionless variable x , evaluating the result at $x=1$, and substituting it into (18):

$$q = p \frac{d\phi_w}{d\tau} + \phi_w(\tau) + \int_0^\tau \left\{ \frac{d\phi_w(\xi)}{d\xi} \right\} \left\{ \frac{d\xi}{\pi\sqrt{\tau-\xi}} \right\} \quad (22)$$

The finite difference form of Eq. (22) is given as follows:

$$\phi_w(\tau_n) \left[\frac{p}{\Delta\tau} + \frac{1}{\sqrt{\pi\Delta\tau}} \right] \phi_w(\tau_{n-1}) - \sum_{i=1}^{n-2} \frac{\phi_w(\tau_{n+1}) - \phi_w(\tau_i)}{\sqrt{\pi\Delta\tau}(n-i)} = \frac{q(\tau_n)}{1 + \frac{p}{\Delta\tau} + \frac{1}{\sqrt{\pi\Delta\tau}}} \quad (23)$$

The dimensionless water temperature in the TES tank can be determined using Eq. (23).

The $q(\tau)$ term in Eq. (23) is equal to the difference between heat pump work and the heat requirement of the house, which can be given as:

$$q(\tau) = \frac{w(\tau)}{\gamma} - q_h(\tau) \quad (24)$$

where $w(\tau)$ and $q_h(\tau)$ represent the dimensionless heat pump work and heat requirement of the house during heating season. ($\gamma = (4\pi Rk)/(UA)_h$) is a dimensionless parameter.

3.2. Energy requirement of the house:

Energy needs of the house in heating season can be expressed as:

$$\begin{aligned} Q_h(t) \\ &= (UA)_h [T_i - T_a(t)] \end{aligned} \quad (25)$$

Where: $(UA)_h$ is the (UA) value of the house, T_i is the inside design air temperature, and $T_a(t)$ is the hourly ambient air temperature.

The energy requirement of the house can also be expressed as:

$$\begin{aligned} Q_h(t) = (UA)_{he} [T_h(t) \\ - T_i] \end{aligned} \quad (26)$$

Where: $(UA)_{he}$ is the (UA) value of the load side heat exchanger used in the house and T_h is the temperature of the load side heat exchanger used in the house.

The effects of the heat capacity of the building were ignored based on the simplification mentioned in a previous study [10].

3.3. Energy requirement of the heat pump:

The heat loss in the condenser of the heat pump can be expressed as:

$$\begin{aligned} Q_h(t) \\ &= W(t) \cdot COP \end{aligned} \quad (27)$$

$$\begin{aligned} COP &= \frac{Q_h(t)}{W(t)} \\ &= \frac{Q_h(t)}{Q_h(t) - Q_L(t)} \end{aligned} \quad (28)$$

Where COP is the coefficient of performance of the heat pump for space heating. COP can be also given as:

$$\begin{aligned} COP \\ &= \eta_c \cdot COP_c \end{aligned} \quad (29)$$

Where η_c is known as a ratio of actual COP of a heat pump to Carnot COP. Carnot COP at any time is given as a function of source temperature T_w and sink temperature T_h :

$$\begin{aligned} COP_c \\ &= \frac{T_h(t)}{T_h(t) - T_w(t)} \end{aligned} \quad (30)$$

$$\begin{aligned} COP \\ &= \eta_c \cdot \frac{T_h(t)}{T_h(t) - T_w(t)} \end{aligned} \quad (31)$$

Rearranging Eq. (31) and using dimensionless temperatures and (u) parameter in Eq. (32) gives:

$$u = \frac{(UA)_h}{(UA)_{he}} = \frac{T_h(t) - T_i}{T_i - T_a(t)} \quad (32)$$

$$\begin{aligned} COP \\ &= \eta_c \cdot \frac{u[\phi_i - \phi_a(\tau)] + \phi_i + 1}{u[\phi_i - \phi_a(\tau)] + \phi_i - \phi_w(\tau)} \end{aligned} \quad (33)$$

This is the dimensionless form of the COP of the heat pump.

To find the work of the heat pump Eq. (27) can be written as:

$$\begin{aligned} Q_h(t) = (UA)_h T_\infty [\phi_i \\ - \phi_a(\tau)] \end{aligned} \quad (34)$$

Using Eq. (33) and Eq. (34) in Eq. (27) gives:

$$W(t) = (UA)_h T_\infty [\phi_i - \phi_a(\tau)] \cdot \frac{\{u[\phi_i - \phi_a(\tau)] + \phi_i - \phi_w(\tau)\}}{\eta_c \{u[\phi_i - \phi_a(\tau)] + \phi_i + 1\}} \quad (35)$$

The dimensionless form of the heat pump work $w(\tau)$ is defined as:

$$\begin{aligned} w(\tau) &= \frac{W(t)}{(UA)_h T_\infty} \end{aligned} \quad (36)$$

$$= \frac{w(\tau)}{\frac{[\phi_i - \phi_a(\tau)] \cdot \{u[\phi_i - \phi_a(\tau)] + \phi_i - \phi_w(\tau)\}}{\eta_c \{u[\phi_i - \phi_a(\tau)] + \phi_i + 1\}}} \quad (37)$$

3.4. solar energy collection rate

The hourly useful energy collection rate $Q_u(t)$ can be calculated by the formula mentioned in Duffie and Beckman [11]:

$$Q_u(t) = \eta_{col}(t) \cdot I_T(t) \quad (38)$$

Where; $I_T(t)$ is the hourly radiation on the tilted solar collector which is given by:

$$I_T(t) = R \cdot I(t) \quad (39)$$

Where R is the ratio of total radiation on the tilted surface to that on a horizontal surface. It can be estimated by:

$$R = \left(1 - \frac{I_b(t)}{I(t)}\right) R_b + \frac{I_d(t)}{I(t)} \left(\frac{1 + \cos \beta}{2}\right) + \rho \left(\frac{1 - \cos \beta}{2}\right) \quad (40)$$

Where; β is the slope angle of the surface ($\beta = 37.1^\circ$) and ρ is the ground albedo which is taken 0.7 in February, 0.3 in January, and 0.1 in the rest of the year. R_b is the ratio of beam radiation on a tilted surface to that on a horizontal surface. $\frac{I_d(t)}{I(t)}$ is the ratio of diffuse radiation to total radiation on horizontal surface. $\frac{I_b(t)}{I(t)}$ is the ratio of beam radiation to total radiation on horizontal surface

$\eta_{col}(t)$ is the efficiency of the flat plate solar collector which is estimated by Yumrutas and Kaska [12] as:

$$\eta_{col}(t) = 0.72 - 0.64 \frac{T_w(t) - T_a(t)}{I_T(t)} \quad (41)$$

Where; $T_w(t)$ is the inlet fluid temperature which is equal to the storage tank temperature. ($T_w(0) = 15^\circ\text{C}$).

By adding the solar collectors SC, the dimensionless net heat input rate to the TES tank in Eq. (24) becomes:

$$q(\tau) = q_u(\tau) + \frac{w(\tau)}{\gamma} - q_h(\tau) \quad (42)$$

which will be used in Eq. (23) in order to calculate the hourly water temperature in TES tank.

4. INPUT DATA AND COMPUTATIONAL PROCEDURE

This study compares two heating systems; ground coupled heat pump with and without adding solar collectors. The input data used in each component of these two systems is presented in this section.

4.1. Heat pump parameters and House heating load

CE values ranging from 0.30 to 0.50 for small electric heat pumps were reported by Zogou and Stamatelos [13]. As a result, the present study took into account three CE values (0.30, 0.40, and 0.50) in accordance

with their findings. The (UA) value of the house was considered to be 345W/°C. The value of (u) mentioned in Eq. (32) was considered equal to 1.2.

4.2. Thermal storage tank

In this study, the tank volume was assumed to be 400 m³, with an initial water temperature equal to the ground temperature, $T_w(0) = 15^\circ\text{C}$. A density of 1000 kg/m³ and a specific heat of 4.18 kJ/kg.°C were assigned to the water. The soil surrounding the tank was assumed to be granite, and its physical properties are listed in Table (1).

4.3. Solar collectors

The purpose of connecting the system to the solar collectors is to compare its parameters with the other system. The solar collectors are directly connected to the storage tank, with an area of 20 m² and a slope angle of $\beta=37.1^\circ$, which is equivalent to the angle of latitude. The solar constant is 1353 W/m². Hourly outside temperatures and solar radiation were obtained from the Meteorological Authority in Gaziantep.

4.4. Procedure of the computation

The dimensionless heat requirement for the house, which changes hourly as a result of the change in the ambient air temperature, is calculated along with the pump work through Eq. (37) depending on the initial tank temperature ($T_w(0) = 15^\circ\text{C}$). Next, the dimensionless net heat input to the tank is calculated using Eq. (24), and finally, the coefficient of performance COP is determined over ten years to obtain the annual periodic operating condition. If SC are added, the net heat input to the tank is calculated using a different equation (42), and the same process is repeated to obtain the required system parameters.

Table 3. Thermophysical characteristics of geological formations as described by [14].

Ground Type	Conductivity, (W/m K)	Diffusivity, (m ² /s)	Specific Heat, (J/kg K)	Heat Capacity, (kJ/m ³ K)
Coarse	0.519	1.39×10^{-7}	1842	3772
Limestone	1.3	5.75×10^{-7}	900	2250
Granite	3.0	14.00×10^{-7}	820	2164.8

5. RESULTS AND DISCUSSION

The results were obtained from the analytical calculations that were applied to the MATLAB program. The effect of Carnot coefficient, volume of thermal storage tank and type of the earth on system coefficient performance and changes in tank temperatures are studied and discussed in this section.

Fig. 2 and Fig. 3 display the impact of the Carnot efficiency CE on tank temperature variations and coefficient of performances in the fifth year of operation, for both systems with and without adding SC. The findings in Fig. 2 reveal the advantages of adding solar collectors to the heating system. Specifically, the water temperature in the tank increased by at least 10.2 °C when SC were added. Fig. 2 also shows the inverse relationship between CE values and tank temperature in the two systems. As the CE value of the heat pump rises, the water temperature decreases when the required heat load remains constant. Whereas, when the system is attached to the solar collectors, the energy gained from the solar energy compensates for the decrease in temperature caused by the increase in CE. Thus, the effect of CE on tank water temperature when SC is added to the system is minimal.

In Figure 3, the increase in COP values when solar collectors are added to the heating system is clearly visible, as the values increased by no less than 1.8. It shows that when using a pump with CE = 0.4, COP value for the system with SC was at 4.75 in the first year of operation, and the value continued to increase until it settled at approximately 5.41 in the fifth year of operation, While in the system without SC, the COP values continued to decrease for the same pump specifications after the first year of operation until it settled at approximately 3.6 in the fifth year of operation. An increase in the CE value leads to an increase in the COP value, which leads to an increase in the amount of heat extracted from the tank Q_L for the same required heat load Q_H , and therefore the temperature of the tank decreases.

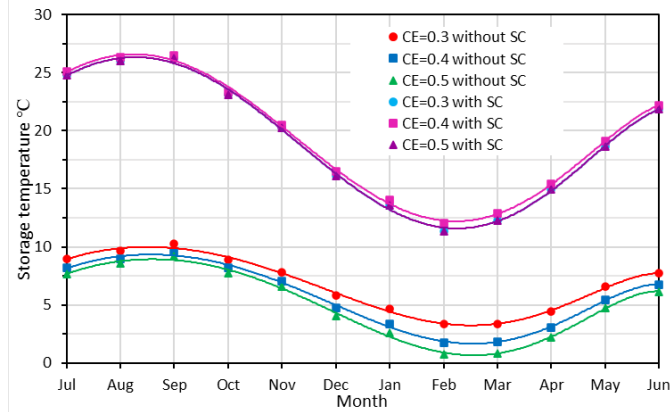


Fig. 2 The effect of CE on the annual variation of water temperature in the TES tank in the fifth year of operation. ($v=400$, granite)

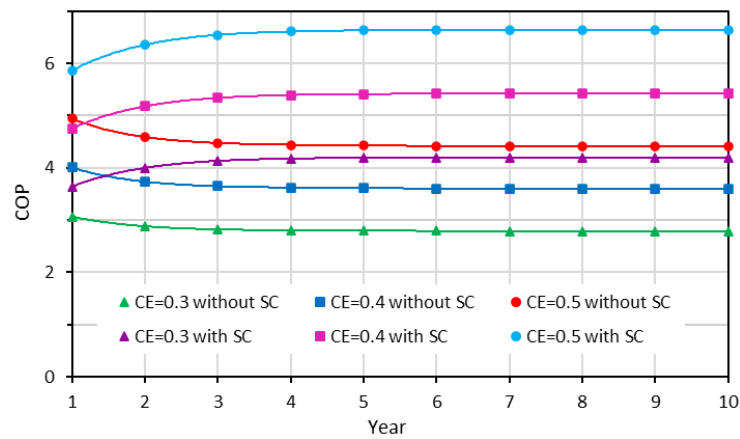


Fig. 3 The effect of CE on the COP of the heat pump. ($v=400\text{ m}^3$, Granite)

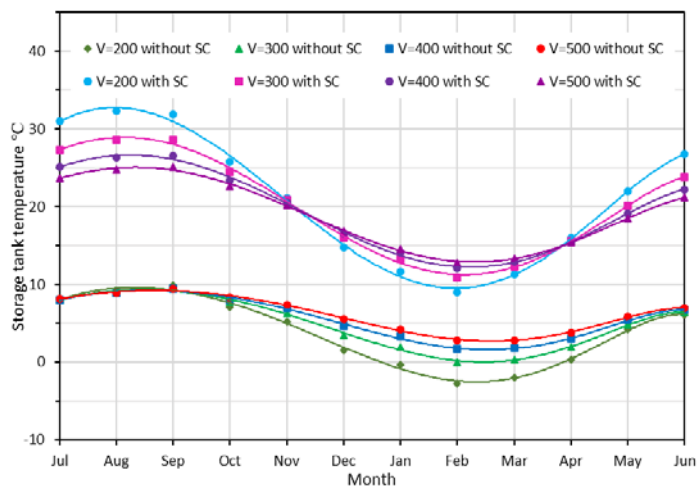


Fig. 4 Effect of storage volume on annual temperature variation of water temperature in the TES tank during tenth year (Granite, $CE=0.4$).

Fig. 4 shows the effect of the volume of the tank on the water temperatures of the tank, as the results show the slight effect of it, especially in the heating season, for volumes that exceed 300 m^3 .

It is also clear that the use of volumes below 300 m^3 is ineffective for the system without SC, as the results approached zero degrees and reached below zero when using a tank of 200 m^3 .

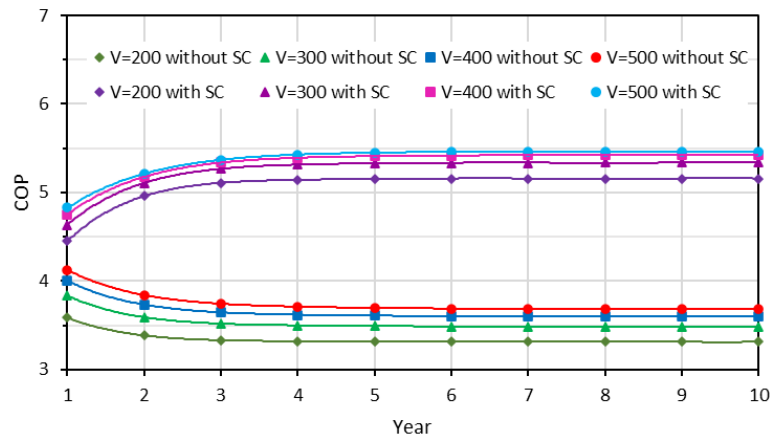


Fig. 5 Variation of COP with TES tank volume and operation time (Granite, CE=0.4).

Fig.5 shows the effect of volume of the tank on COP where it is shown that the larger the volume the higher the COP value for both systems. Increasing the volume of the tank means increasing the amount of sensible energy of the water times the amount of energy lost through thermal conductivity and thus increasing the net energy of the tank Eq.(10), Which is the heat source for the heat pump. This increasing leads to an increase in the COP of the heat pump for the same required heat load (sink).

The second observation in Fig.5 is that at the beginning of operation, the tank volume of 500 m³ recorded the highest COP value in both systems, as the COP value in the system with SC in the first year of operation was 4.8 and continued to increase until it stabilized in the fifth year at approximately at 5.45. Also in the system without SC, the tank volume of 500 m³ recorded the highest value of COP in the first year of operation at the value of 4.1, but it continued to decrease until it stabilized at a value of 3.7 in the fifth year of operation. The addition of SC to the system compensates for the decrease in the degree of the tank water temperature, which helps to increase the COP value in the first years of operation, unlike what happened in the other system.

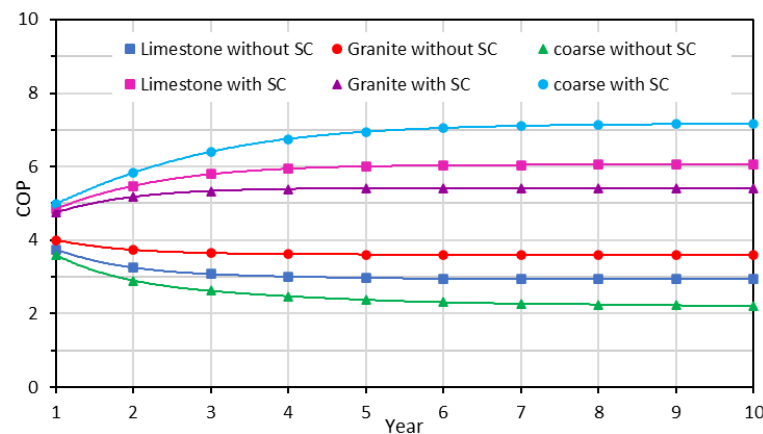


Fig. 6 Variation of COP with earth type and operation time (Granite, CE=0.4).

The results presented in Fig. 6 indicate that the lower thermal conductivity coefficient and thermal diffusivity of the soil surrounding the thermal storage tank, leads to higher coefficient of performance in the system with SC. A low thermal conductivity coefficient of the surrounding soil leads to slower heat transfer, which can positively impact the efficiency of the heat pump, as the storage tank is able to retain the temperature it gained from solar energy for a longer period.



In the system without solar collectors, as the thermal conductivity and thermal diffusivity of the surrounding soil decrease, the ability of the soil to transfer heat to the storage tank decreases. This leads to a decrease in the coefficient of performance (COP) of the heat pump, as shown in Fig. 6.

6. CONCLUSIONS

The study compared two heating systems, one with an underground storage tank and a heat pump, and the other with the addition of solar collectors. The performance parameters of the heating systems, such as COP, temperature of the storage tank, and solar energy were analyzed using an analytical model and MATLAB program. The impact of Carnot efficiency, volume of thermal storage tank, and type of earth on system performance parameters were studied. Results showed that adding solar collectors to the heating system increased the water temperature in the tank by at least 10.2 °C and significantly increased the COP values. Increasing the volume of the tank led to an increase in the COP value for both systems, and increasing the diffusivity and conductivity coefficient of the soil increased the performance coefficient in the system without solar collectors. Overall, the results indicate that adding solar collectors to the heating system is beneficial and can compensate for the decrease in temperature caused by the increased Carnot efficiency of the heat pump, particularly when using soils with low conductivity coefficient and low thermal diffusivity.

REFERENCES

- [1]. Yumrutas, R., Unsal M., Analysis of solar aided heat pump systems with seasonal thermal energy storage in surface tanks. *Energy* 2000;25:1231–43.
- [2]. Rodríguez-Hidalgo MC, Rodríguez-Aumente PA, Lecuona A, Legrand M, Ventas R. Domestic hot water consumption vs. solar thermal energy storage: the optimum size of the storage tank. *Appl Energy* 2012;97:897–906.
- [3]. Dincer I, Rosen MA. *Thermal energy storage: Systems and applications*. New York, US: John Wiley & Son; 2002.
- [4]. Ucar A, Inalli M. Thermal and economic comparisons of solar heating systems with seasonal storage used in building heating. *Renewable Energy* 2008;33:2532–9.
- [5]. Caliskan H, Dincer I, Hepbasli A. Thermodynamic analyses and assessments of various thermal energy storage systems for buildings. *Energy Convers Manage* 2012;62:109–22.
- [6]. Chung, M., Park, J., Yoon, H.K., 1998. Simulation of a central solar heating system with seasonal storage in Korea. *Solar Energy* 64 (4–6), 163–178.
- [7]. Zhang, H.F., Ge, X.S., Ye, H., 2007. Modeling of space heating and cooling system with seasonal energy storage. *Energy* 32, 51– 58.
- [8]. Wang, H., Qi, C., 2008. Performance study of underground thermal storage in a solar-ground coupled heat pump system for residential buildings. *Energy and Buildings* 40, 1278–1286.
- [9]. Qu, M., Yin, H., Archer, David H., 2010. A solar thermal cooling and heating system for a building: experimental and model-based performance analysis and design. *Solar Energy* 84, 166–182.
- [10]. Yumrutas, R., Unsal, M., 2000. Analysis of solar aided heat pump systems with seasonal thermal energy storage in surface tanks. *Energy* 25, 1231–1243.
- [11]. Duffie, J.A., Beckman, W.A., 1991. *Solar Engineering of Thermal Process*. John Willey and Sons, New York.
- [12]. Yumrutas, R., Kaska, O., 2004. Experimental investigation of thermal performance of a solar assisted heat pump system with an energy storage. *International Journal of Energy Research* 28, 163–175.
- [13]. Zogou, O., Stamatelos, A., 1998. Effect of climatic conditions on the design optimization of heat pump systems for space heating and cooling. *Energy Convers. Manage.* 39, 609–622.
- [14]. Ozisik, M.N., 1985. *Heat transfer: A basic approach*. McGraw-Hill, New York.

The comparative petiole anatomy of some *Hedysarum* species (Fabaceae) in Turkey

Burcu Yilmaz Citak¹

Abstract

This paper was designed to analyze the petiole anatomical characteristics of six *Hedysarum* species in Turkey. Paraffine method was applied to obtain cross sections of petiole or handmade sections were used to made anatomical analysis. The cross sections taken from petiole of studied species had an epidermis layer with oval-rectangular shaped. There was a large median bundle in all examined species with smaller lateral two bundles. Collenchymatic tissue changeable from 4 to 8 layered was located in the corners of petiole especially over the vascular bundles in studied species. Multilacunar and trilacunar petiole types were detected to separate species each other. The pith region of petiole had oval shaped parenchymatic cells that in different size. The petiole anatomical characteristics of *Hedysarum* species were showed that the *Subacaulia* and *Crinifera* sections have trilacunar petiole type the most primitive type in *Hedysarum* genus however *Multicaulia* section has multilacunar type which is advanced one. In conclusion, the median and lateral bundles size and their patterns are the most constructive petiole anatomical character to separate *Hedysarum* species has been determined.

Keywords: *Hedysarum*, Leguminosae, Taxonomy, Sweet Vetch, Systematic

1. INTRODUCTION

Fabaceae called as legumes is third largest flowering plant family is comprised with about 19,500 species in about 751 genera. This large family exhibits a high level of species diversity and evolutionary success in various ecosystems worldwide like alpine and arctic meadows, stony grasslands, deserts, and seashores [1]. Within the genus *Hedysarum* 45 taxa recognized for the circum-Mediterranean areas by Greuter et al. (1989), among them 33 are present in the eastern Mediterranean [2].

In Turkey alone, 22 taxa of *Hedysarum* were recognized by Hedge (1979) and with the addition of new taxa, the number of genus is reached to 26 species [3],[4],[5], [6],[7]. Of which, 14 are endemics to Turkey, and the endemism ratio of the genus is 63.3%. Hedge (1979) separated *Hedysarum* into five sections (*Hedysarum*, *Obscura*, *Multicaulia*, *Subacaulia*, and *Crinifera*) in Flora of Turkey. The classification of sections of *Hedysarum* is also quite problematic.

Angiosperms have long used anatomical properties to categorize species at different taxonomic levels and to identify their taxonomic relationships [8]. Petiole vascular systems are often complex and offer a variety of features that can prove to be of essential diagnostic value. The central area of the petiole is the most reliable from which a single portion can be cut for comparative analysis [9]. Several studies on petiole anatomy are systematically important in a variety of clades at various taxonomic levels [10],[11],[12].

Petiole anatomy is thought to be important in determining the number, length, and width of vascular bundles in the abaxial epidermis, adaxial epidermis, parenchyma, and collenchyma cells [10]. Some researchers from around the globe have studied the petiole anatomy of *Hedysarum* genus [10],[13],[14].

This is the second detailed study of *Hedysarum* petiole vasculature and their taxonomic relevance using microscopic visualization. This study also described the significant petiole micromorphological traits which will contribute to the anatomy of the Fabaceae species for their accurate identification.

¹ Corresponding author: Selcuk University, Department of Biology, 42130, Selcuklu/Konya, Turkey.
burcuyilmaz@selcuk.edu.tr

MATERIALS AND METHODS

2.1. Plant Materials

The plant specimens used in current study were collected during 2018 and 2021 from various localities in Turkey. The information about the voucher specimens is given in Table 1. The anatomical samples of the examined species were stored in the Plant Anatomy Laboratory of Biology Department of University of Selcuk, Konya, Turkey.

Table 1. The locality information about examined species.

Species	Subgenus	Collector number	Locality
<i>H. varium</i> subsp. <i>varium</i>	Multicaulia	B. Citak-149	Karaman, Ayranci, 2013
<i>H. varium</i> subsp. <i>syriacum</i>	Multicaulia	B. Citak-151	Aksaray, 2012
<i>H. laxum</i>	Multicaulia	B. Citak-366	Adana: Tufanbeyli, 2021
<i>H. pestalozzae</i>	Multicaulia	B. Citak-160	Karaman: Ayranci, 2013
<i>H. nitidum</i>	Multicaulia	B. Citak-369	Erzincan: Resadiye, 2021
<i>H. turcicum</i>	Subacaulia	B. Citak-357	Yozgat: Bogazliyan, 2022
<i>H. pannosum</i> *	Crinifera	H. Dural-3500-B. Citak	Konya: Kizoren, 2011

*the information obtained from [10].

2.2. Anatomical methods

The paraffin method which has been added some modifications was used to make the permanent anatomical slides [15]. For each taxon, five plant samples were used and the experiments were done at least two times. Firstly the petiole pieces were treated through an increasing alcohol series to remove the water from the tissues. As the next step, a portion of paraffin was added to small glass flasks. The paraffin blocks were obtained and 12–16- μ m-thick transverse sections were cut using a Thermo Scientific microtome with disposable blades. Under a light microscope (Leica DM 1000), the best sections were chosen and photographed at magnifications of 10x, 20x, and 40x. The measurements, which were made with the Kameram 21 software programme, were based on at least 20 or more cells per specimen. The mean values of the measurements of all of the investigated taxa were given.

2.3. Numerical analysis

For the statistical analysis, the qualitative and quantitative characters were scored. A total of 6 discriminative petiole anatomical characters were used to evaluate the taxonomical similarities of the studied *Hedysarum* species (Table 2). A data matrix was set using the recorded qualitative and quantitative characters. Based on the anatomical characters, the coefficients of correlation among the six species were determined and these species were grouped using the clustering analysis method (unweighted pair group method with arithmetic mean, UPGMA, dissimilarity, standardized variables). The clustering analysis was based on Gower's (1971) general coefficient similarity [16], which was used directly with a mixture of character types (binary, qualitative, and quantitative). Untransformed, centered, and unstandardized data were used to create a covariance matrix. MVSP 3.22 software was used for all of the computations.

3. RESULTS AND DISCUSSION

3.1. The petiole anatomical properties

The shape of petiole cross section is oval in *H. varium* subsp. *varium*, *H. varium* subsp. *syriacum*, *H. laxum*, *H. pestalozzae*, and *H. nitidum* which have been taken from the median parts of the petiole. *H. turcicum* has triangular shaped petiole. In anatomy of petiole of *Hedysarum* species, three nodal types, unilacunar, trilacunar, and multilacunar types, were recorded by Watari (1934) in Leguminosae [17]. The trilacunar type was most common in the family, but the unilacunar type was only recorded in some species in tribe Genisteae, and the multilacunar type was sporadically found in subfamilies Caesalpinioideae and Papilionoideae [17]. The trilacunar type was inferred to be the more primitive type in Leguminosae [18] and this type is the most common in *Hedysarum* genus. Watari (1934) emphasized that "the petiolar base is one of the most important regions in

the vascular course of foliar organs of Leguminosae." He classified branching patterns of the vascular bundles at the petiolar bases into three types based on the number of leaf traces and whether the traces are fused or free. Choi et al. (1999) had announced a pattern of petiole in *Hedysarum* species (Fig 1). The member of Subacaulia section have three leaf traces with free organization and Multicaulia section have more than three ones according to this literature.

In petiole transverse sections, the epidermis is composed of one layer and epidermal cells of both surfaces are rectangular to oval and have trichomes in studied species (Fig. 2). *H. pannosum* from Crinifera section was studied by the author in a previous study [10] and the same results were conducted. *H. cappadocicum* is another species in Subacaulia section was reported with three leaf traces in petiole [14] as observed in *H. turcicum* in current study.

Collenchyma cells located in the corners of petiole are composed of 4-7 layers. Cortex parenchymatic cells which are presented under the epidermis are orbicular shaped and are composed of 8-9 layers in studied species. There are three large primary collateral vascular bundles in the corners of the petioles, with small secondary bundles among them. On the median vascular bundles there is large sclerenchyma tissue shaped like an arc and also secondary vascular bundles have sclerenchyma (Fig. 2). The pith is composed of parenchymatic cells which are orbicular shaped with changeable sizes (Fig. 2).

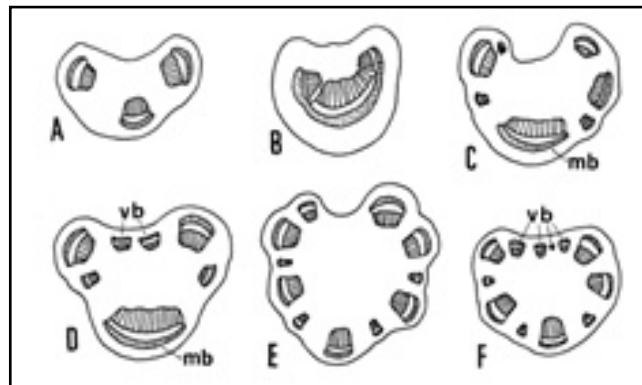


Figure 12. The petiole pattern in *Hedysarum* genus according to Choi et al. (1999).

3.2. Numerical analysis results

The dendrogram created from the cluster analysis using the UPGMA based on the 6 petiole anatomical variables of the six *Hedysarum* species is presented in Fig. 3. This dendrogram reflected the similarities among the examined species. The dendrogram revealed two main groups: Group A (with 40% similarity) comprised only one species *H. nitidum* which is a distinct *Hedysarum* species in this group. Group B (with 68% similarity) comprised the remaining five species of studied *Hedysarum* species. Group B consisted of two main subclusters, which were described further as Clusters B1 and B2. Cluster B1 included subspecies of *H. pannosum* and *H. turcicum* (with 76% similarity) with a trilacunar type petiole. Cluster B2 included two subgroups called as C and D. Group C includes *H. pestalozzae* and *H. varium* subsp. *syriacum* (with 88% similarity). Group D included *H. laxum* and *H. varium* subsp. *varium* (with 89% similarity).

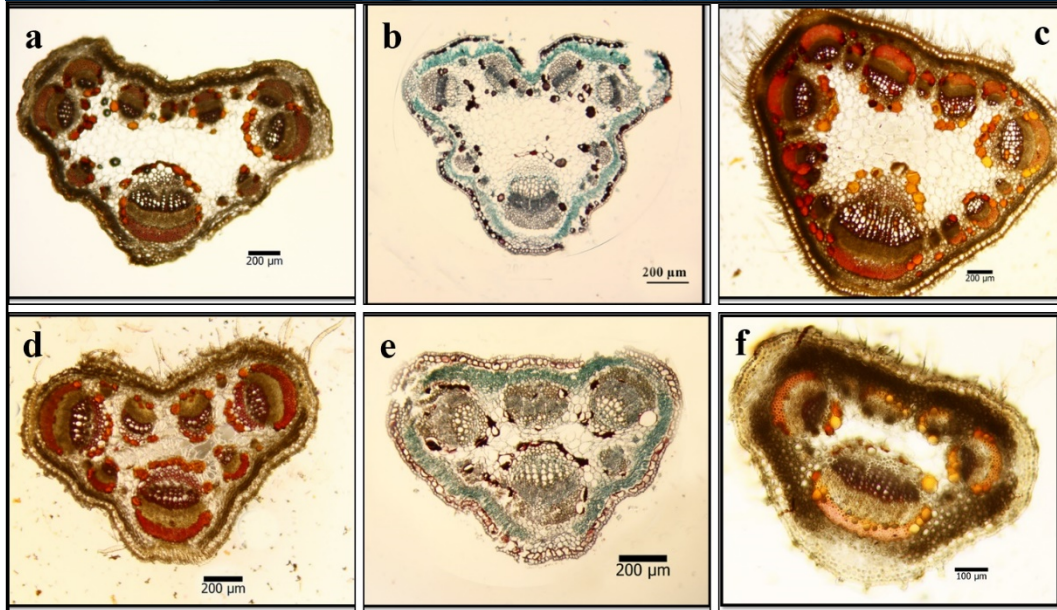


Figure 2. The petiole pattern in *Hedysarum* genus a. *Hedysarum varium* subsp. *varium*, b. *Hedysarum varium* subsp. *syriacum*, c. *H. nitidum*, d. *H. laxum*, e. *H. pestalozzae*, f. *H. turcicum*

Table 2. The petiole characters used in numerical analysis

Species	Petiole type	Median bundle length(μm)	The number of vascular bundles	Pith cells(μm)	Collenchyma(μm)	Ventral bundle(μm)
<i>H. varium</i> subsp. <i>varium</i>	1	499.9	10	89.74	84.04	398.7
<i>H. varium</i> subsp. <i>syriacum</i>	1	362.3	7	53.55	70	230.5
<i>H. laxum</i>	1	465.23	8	72.48	72.13	382.38
<i>H. pestalozzae</i>	1	378.64	6	77.23	63.59	324.8
<i>H. nitidum</i>	1	882.97	16	147.57	106.67	560.09
<i>H. turcicum</i>	0	253.84	9	63.68	46.35	180.44
<i>H. pannosum</i> *	0	232.2	7	48.2	152.2	178.3

*the information obtained from Dural & Citak (2015)

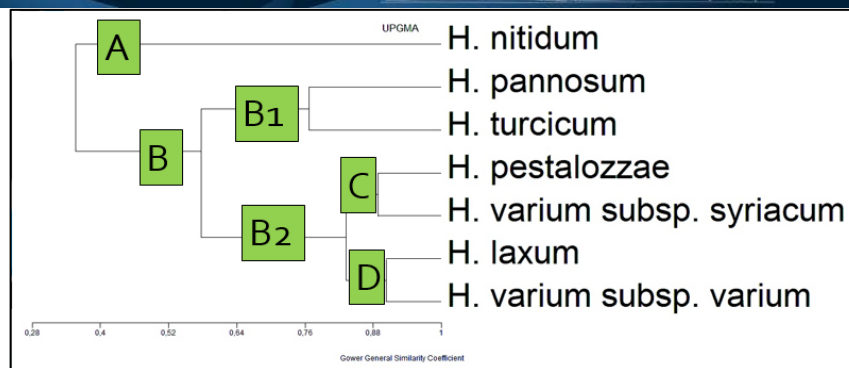


Figure 3. Dendrogram based on petiole anatomical properties showing the similarity and distance between *Hedysarum* species.

4. CONCLUSION

The anatomical results of this study showed that Subacaulia and Crinifera sections have trilacunar petiole type the most primitive type in *Hedysarum* genus however Multicaulia section has multilacunar type which is advanced one.

In conclusion, the median and lateral bundles size and their patterns are the most useful petiole anatomical character to separate *Hedysarum* species has been determined.

REFERENCES

- [1]. B. Choi and H. Ohashi, "Generic criteria and an infrageneric system for *Hedysarum* and related genera (Papilionoideae-Leguminosae)," *Taxon*, vol. 52, pp. 567–576, Aug. 2003.
- [2]. W., Greuter, H. M. Burdet, and G. Long, Eds., *Linum L., Med-Checklist, Dicotyledones, (Lauraceae-Rhamnaceae)*. Conservatoire et Jardin Botaniques, Geneva. 1989, Vol. 4.
- [3]. P.H., Davis, Ed., *Hedysarum, Flora of Turkey and the East Aegean Islands*, Edinburgh: Edinburgh University Press, 1970, vol 3.
- [4]. I. Baskose, A. E. Yaprak, and B. Akyildirim, "*Hedysarum ketenoglui* (Fabaceae-Hedysareae), a new species from southern Turkey," *Phytotaxa*, vol. 357, pp. 291–297, June 2018.
- [5]. Z. Aytac, B. K. Igci, and T. S. Koruklu, "*Hedysarum nallihanse* (Fabaceae): A new species from Turkey," *Phytotaxa*, vol. 471, pp. 276–282, Nov. 2020.
- [6]. E. Hamzaoglu, and M. Koc, "*Hedysarum turcicum* (Hedysareae, Fabaceae), a new species from Turkey," *Phytotaxa*, vol. 428, pp. 1–6, Jan. 2020.
- [7]. A. Kandemir, E. Sevindik, F. Yildiz, H. I. Turkoglu, and B. Yildiz, "A new species of *Hedysarum* (Fabaceae) from Turkey," *Phytotaxa*, vol. 587, pp. 12–20, March, 2023.
- [8]. A. B. Okwuchukwu, and O. C. Uwabukeonye, "Taxonomic significance of stem and petiole anatomy of three white varieties of *Vigna unguiculata* (L.) Walp.," *Archives of Agriculture and Environmental Science*, vol. 2, pp. 109–112, June, 2017.
- [9]. N. Talip, D. F. Cutler, A. S. Ahmad Puad, B. S. Ismail, A. R. Ruzi, and A. A. Ahmad Juhari, "Diagnostic and systematic significance of petiole anatomy in the identification of *Hopea* species (Dipterocarpaceae)," *South African Journal of Botany*, vol. 111, pp. 111–125, 2017.
- [10]. H. Dural, and B. Y. Citak, "Morphology and anatomy of *Hedysarum pannosum* (Boiss.) Boiss. (Fabaceae)," *Acta Botanica Croatica*, vol. 74, pp. 19–29, 2015.
- [11]. P. D. Abeyasinghe, and T. Scharaschkin, "Taxonomic value of the petiole anatomy in the genus *Cinnamomum* (Lauraceae) found in Sri Lanka," *Ruhuna Journal of Science*, vol. 10, 1–17, 2019.
- [12]. A. Akhtar, A. Mushtaq, M. Tariq, A.M. Khan, M. Arfan, Q. Abbas, M. Zafar, S. Sultana, R. Batool, A. Fatima, S. Khan, S. A. Ullah, and A. Khan, "Microscopic characterization of petiole anatomy of Asteraceous taxa of Western Himalaya-Pakistan," *Microscopy Research and Technique*, vol. 2, pp. 591–606, 2021.
- [13]. B. Choi, and H. Ohashi, "Pollen morphology and taxonomy of *Hedysarum* and its related genera of the tribe Hedysareae (Leguminosae: Papilionoideae)," *J. Jap. Bot.*, vol. 71, pp. 191–213, 1996.
- [14]. M. Tekin, and Y. Akyol. "Endemik *Hedysarum cappadocicum* Boiss. (Fabaceae) Turunun Anatomik Ozellikleri," *Anadolu Universitesi Bilim ve Teknoloji Dergisi C- Yasam Bilimleri ve Biyoteknoloji*, vol. 7, pp. 207–213, 2018.
- [15]. D. A. Johansen, *Plant Microtechnique*. Mcgraw-Hill Book Company, London, 1940.



- [16].P. H. Sneath, and R.R. Sokal. Numerical Taxonomy, The principles and practice of numerical classification. 1st Ed. San Francisco, Ca, USA, Wh Freeman, 1973.
- [17].S. Watari, "Anatomical studies on some leguminous leaves with special reference to the vascular system in petioles and rachises," Journal of the Faculty of Science, University of Tokyo, Section III Botany, vol. 4, pp. 225–365, 1934.
- [18].R. M., Polhill, and P. H. Raven, Eds., Papilionoideae: Advances in legume systematics, part 1, 367–370. Kew: Royal Botanic Gardens, 1981.

BIOGRAPHY

Burcu Yilmaz Citak received B.Sc. and Ph.D. degrees in biology from the Faculty of Science, University of Selcuk, Konya, Turkey, in 2011 and 2018, respectively. Her areas of interest include plant anatomy, palynology and plant systematics.

A Preliminary Study on Potentiodynamic Polarisation Behaviour of UNS S32760 Duplex Stainless Steel

*Burcin Ozbay Kisasoz*¹

Abstract

Duplex stainless steels (DSSs) possess higher mechanical properties and corrosion resistance owing to dual-phase microstructure. DSSs have an approximately equal amount of ferrite and austenite phases. The ferrite phase provides mechanical strength and resistance to pitting corrosion, while the austenite phase provides ductility and general corrosion resistance. The desired ferrite and austenite phase balance can be achieved by the solution treatment applied above 1000 °C. Application of solution treatment at high temperatures or long periods at proper treatment temperature causes an excessive increase in ferrite ratio. An increase in ferrite content causes brittleness in the structure and a decrease in general corrosion resistance. In this study, the influence of solution treatment duration on the corrosion properties of the UNS S32760 duplex stainless steel is investigated. Solution treatments are applied at 1050 °C for 30 minutes, 60 minutes and 90 minutes. Then corrosion resistance and pitting potential of the samples are investigated by potentiodynamic polarization and electrochemical impedance spectroscopy tests, respectively. It is revealed that the solution treatment process is critical for the corrosion properties of the UNS S32760 duplex stainless steel alloy.

Keywords: Duplex stainless steels, solution treatment, corrosion, pitting.

1. INTRODUCTION

Duplex stainless steels (DSSs) are one of the main types of stainless steels with a dual-phase structure. The dual-phase microstructure consists of a nearly equal amount of ferrite and austenite phases [1-3]. The ferrite phase ensures pitting resistance and mechanical strength, while the austenite phase ensures general corrosion resistance and ductility. The DSSs have been used in desalination, shipbuilding, and the petrochemical industry because of enhanced mechanical properties and superior corrosion resistance [4-6].

Solution treatment (ST) is applied to the DSSs for achieving the phase balance. The ST provides the dissolution of inclusions and secondary phases, besides obtaining desired ferrite and austenite proportion. The ST process temperature is critical for obtaining desired microstructure. A lower ST temperature is insufficient for the dissolution of secondary phases and, a higher ST temperature causes the formation of excessive ferrite and deteriorates the corrosion properties [7-10].

This study investigates the influence of ST duration on the electrochemical corrosion behaviour of UNS S32760 at 1050 °C. Potentiodynamic polarization and electrochemical impedance techniques have been studied to reveal corrosion behaviour.

2. MATERIAL AND METHOD

UNS S32760 super duplex stainless steel alloy was used in the experimental studies. The chemical compositions of the alloy was given in Table 1.

¹ Fatih Sultan Mehmet Vakif University, Aluminium Test Training and Research Center (ALUTEAM), Istanbul, Turkey.
burcinozbay@gmail.com

Table 4. Sample table

Chemical composition					
Cr	Ni	Mo	Mn	Si	C
25.850	6.850	3.670	0.530	0.390	0.022
Cu	W	P	S	N	Fe
0.680	0.691	0.028	0.001	0.264	Bal.

The samples were heated to solution treatment temperature with a 6 °C/min heating regime and annealed at 1050 °C for 30 min, 60 min and 90 min followed by quenching. Solution-treated samples were polished at 1 μm following the grinding up to 2000 grids. All samples were etched by the electrolytic etching method in 10% wt. KOH solution. The microstructure investigations were carried out by optical microscopy (OM-Nikon Eclipse MA100).

All electrochemical corrosion tests were performed with Ivium Compactstat. The device consisted of a triple electrode system, including a reference electrode (Ag/AgCl solution), a working electrode (test sample), and a counter electrode (platinum). The potential of the reference electrode was determined as 0.065 mV, while the surface area ratio of the counter electrode and working electrode was 4. The corrosion behavior of the examined samples was investigated by potentiodynamic polarization (PP), and electrochemical impedance spectroscopy (EIS) tests. Prior to the polarization experiments, an open circuit potential (OCP) of the samples was determined by holding samples in a 3.5% NaCl solution.

3. RESULTS AND DISCUSSION

The microstructure of the initial UNS S32760 alloy was given in Fig. 1. The microstructure consists of ferrite (α) and austenite (γ) phases. The dark phase indicates ferrite, and the white phase indicates austenite. The initial ferrite and austenite ratios are 52% and 48%, respectively.

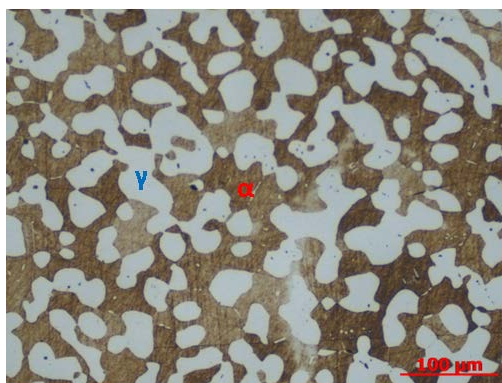


Figure 13. Microstructure of the initial alloy

Potentiodynamic polarization curves and the test result were given in Fig. 2 and Table 2, respectively. It was clearly observed that a drastic change occurred in the potentiodynamic polarization behaviour of the studied alloy after solution treated at 1050 °C for 90 min. The enhanced treatment time caused an increase in the ferrite content of the alloy and adversely affected the corrosion properties. When the polarization curves were examined, it was observed that the samples treated for 30 minutes and 60 minutes exhibited similar polarization behaviour. However, a different potentiodynamic polarization behaviour was observed in the sample treated for 90 minutes. Especially, the sample treated for 90 minutes showed a considerably higher corrosion rate value compared to the other samples, as seen in Table 2.

Fig. 3 shows the Nyquist and Bode plots of the samples tested in 3.5% NaCl solution. Generally, the Nyquist plots demonstrated a randel-like feature. The Nyquist plot of the sample treated for 30 min exhibited a nearly

linear characteristic that can be attributed to the passive surface. On the other hand, the impedance value of the samples treated for 60 min and 90 min was decreased as seen in Fig. 3a. Especially the remarkable decrease in the impedance value of the sample treated for 90 min can be related to the excessive ferrite phase which may promote the pitting corrosion. Accordingly, the impedance value was decreased due to the corrosion of the sample treated for 90 min. Fig. 3b shows the phase angle bode plots of the examined samples. The maximum peak angles for all samples were observed in the medium frequency range which was attributed to the chromium oxide protective film. Also, that phenomenon was more apparent for the short time of corrosion exposure.

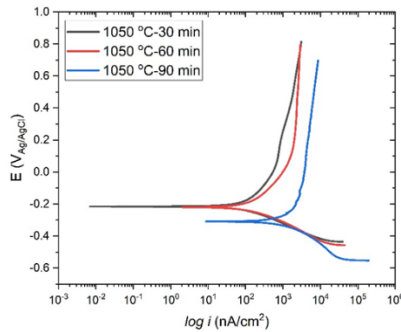


Figure 2. Potentiodynamic polarization curves of the studied samples

Table 2. Potentiodynamic polarization test results

Solution treatment duration (min)	E_{corr} (V)	i_{corr} (A/cm ²)	Corrosion rate (mm/year)
30 min	-0.2152	8.785×10^{-8}	0.001019
60 min	-0.2234	16.410×10^{-8}	0.001902
90 min	-0.3093	107.400×10^{-8}	0.01245

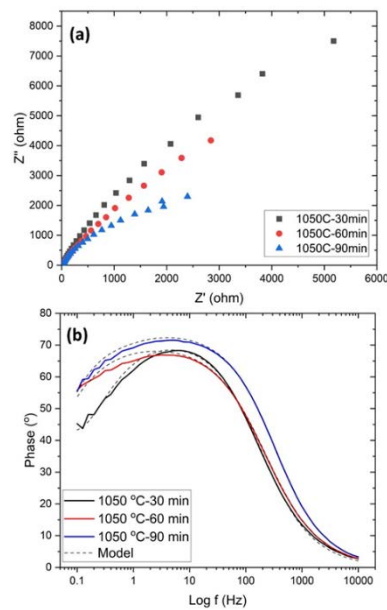


Figure 3. EIS test results; a) Nyquist plots, b) Phase angle bode plots

Corrosion damage of the sample can be seen in Fig. 4. Light microscopy images taken from the corrosion surfaces are compatible with the corrosion test results. As the heat treatment time increases, the pits formed on the surface of the material grow and corrosion damage increases. As mentioned before, as the solution treatment time increases, the ferrite-austenite balance that provides optimum material properties is disrupted and corrosion properties are adversely affected. As the solution treatment time increased to 90 minutes, the pitting rate on the corrosion surface increased up to 4.755%.

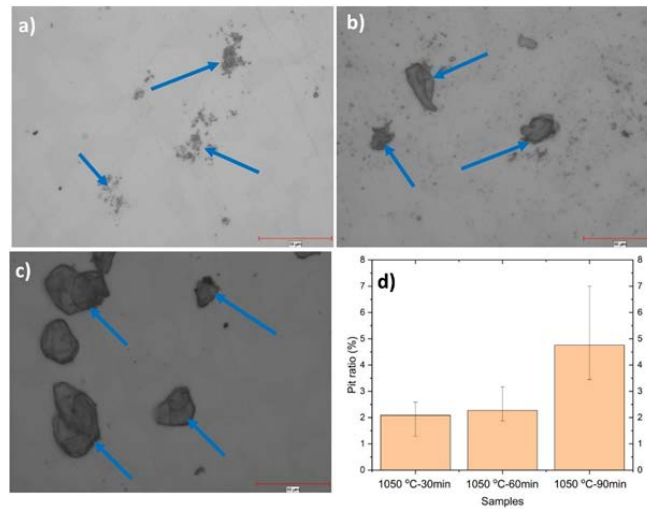


Figure 4. Micrographs of the samples following the corrosion tests a) ST for 30 min, b) ST for 60 min, c) ST for 90 min, d) Pit ratio graph

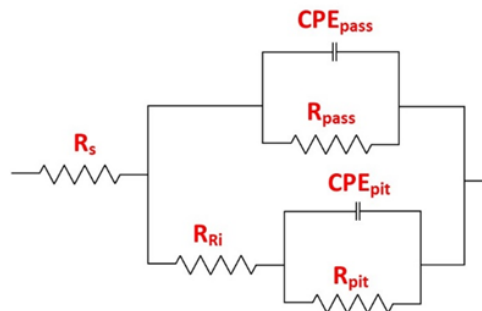


Figure 5. Equivalent circuit for the EIS results

The equivalent electrical circuit used to fit the impedance data was given in Fig. 5. Measured capacitance was often not ideal and Q was determined as the constant phase element (CPE_{pass} and CPE_{pit}). R_s is the electrolyte resistance in 3.5% wt. NaCl solution, and R_{pass} is the charge transfer resistance for the passive layer. Moreover, R_{Ri} and R_{pit} solution and charge resistance of the pit, respectively. In the samples, significant pitting corrosion occurred, as indicated in the light microscopy observations. Thus, a double-layered model was observed at the interface owing to the formation of stable pits parallel to the passive surface.

CONCLUSION

The enhanced treatment time caused an increase in the ferrite content of the alloy and adversely affected the corrosion properties.

The sample treated for 90 minutes showed a considerably higher corrosion rate value compared to the other samples.

The impedance value was decreased due to the corrosion of the sample treated at 1050 °C for 90 min.

The maximum peak angles for all samples were observed in the medium frequency range which was attributed to the chromium oxide protective film.

As the heat treatment time increases, the pits formed on the surface of the material grow and corrosion damage increases.

A double-layered model was observed at the interface owing to the formation of pits on the surface.

REFERENCES

- [1]. C. Donik, A. Kocijan, D. Mandrino, I. Paulin, M. Jenko, and B. Pihlar, "Initial oxidation of duplex stainless steel," *Appl Surf Sci*, vol. 255, pp. 7056-7061, May 2009.
- [2]. G. Yalciner, G. Ozer, A. Kisasoz, and A. Karaaslan, "Influence of the phase balance and cooling conditions on the microstructure and corrosion behavior of solution-treated 1.4462 duplex stainless steel," *Mater Res Express*, vol. 6, no. 12, 2019.
- [3]. M. Pohl and O. Storz, "Sigma-phase in duplex-stainless steels," *Zeitschrift fur Metallkunde*, vol. 95, no. 7, pp. 631-638, 2004.
- [4]. H. Hwang and Y. Park, "Effects of Heat Treatment on the Phase Ratio and Corrosion Resistance of Duplex Stainless Steel," *Mater Trans*, vol. 50, no. 6, pp. 1548-1552, 2009.
- [5]. A. Kisasoz, A. Karaaslan, and Y. Bayrak, "Effect of etching methods in metallographic studies of duplex stainless steel 2205," *Metal Science and Heat Treatment*, vol. 58, no. 11-12, 2017.
- [6]. R. Badji, M. Bouabdallah, B. Bacroix, C. Kahloun, K. Bettahar, and N. Kherrouba, "Effect of solution treatment temperature on the precipitation kinetic of σ -phase in 2205 duplex stainless steel welds," *Materials Science and Engineering A*, vol. 496, no. 1-2, pp. 447-454, 2008.
- [7]. V. A. Hosseini, L. Karlsson, S. Wessman, and N. Fuertes, "Effect of sigma phase morphology on the degradation of properties in a super duplex stainless steel," *Materials*, vol. 11, no. 6, Jun. 2018.
- [8]. S. Li, Y. Wang, H. Zhang, S. Li, G. Wang, and X. Wang, "Effects of prior solution treatment on thermal aging behavior of duplex stainless steels," *Journal of Nuclear Materials*, vol. 441, no. 1-3, pp. 337-342, 2013.
- [9]. Y. Zhou and D. L. Engelberg, "Application of bipolar electrochemistry to assess the ambient temperature corrosion resistance of solution annealed type 2205 duplex stainless steel," *Mater Chem Phys*, vol. 275, Jan. 2022.
- [10]. S. Li, Y. Wang, and X. Wang, "Effects of ferrite content on the mechanical properties of thermal aged duplex stainless steels," *Materials Science and Engineering A*, vol. 625, pp. 186-193, Feb. 2015.

Analysis of the Combined Usage of Plasticizer and Accelerator Effects on Microstructure for Mortar

Murat Timur¹, Ilker Bekir Topcu²

Abstract

During the production process of mortar many of additives can be used jointly to obtain efficient workability properties. In this situation strength of mortar depends on the correct ratio of admixtures. This study focuses on analysing of mortar samples that have three different doses of sodium lignosulphonate based plasticizer (%1 -1,5-3) and calcium nitrate based set accelerator (%0,5-1-2) admixture combinations. The water-cement ratio is selected as 0.50 for the mortar production. Various effects in the strength and durability are investigated by experimental methods. Scanning electron microscope (SEM) images were obtained at the range of magnification 500x to 4000x for observations. In the investigation unit weight, ultrasonic pulse velocity, compressive strength, setting time tests and microstructure analysis tests were performed in three different dosage mixtures and the obtained data were evaluated. As a result of the tests carried out, the use of the admixtures in different dosages caused decrease in compressive strength maximum 7,27 MPa in 28 day samples. It has been observed that %1 plasticizer and %0,5 accelerator combination which has the minimum doses reach the highest compressive strength for 28 days (39,8 MPa). Therefore, as a result the coexistence of additives must be sensitively controlled and the required dosage adjustments must be made in production.

Keywords: Accelerator, dosage, microstructure, plasticizer, SEM

1. INTRODUCTION

With the improvement of the chemical investigations variety of methods have been developed to meet the needs in terms of developing technology with the manufacture of concrete. The most important of these by using the chemicals of concrete samples on the property is the path to be taken. Chemical additives are put into operation in a very serious way in the last ten years as it is known for it [1]. Impermeability of concrete, reducing the amount of water used, accelerating or reducing the setting time, improving workability are important issues. In addition chemical additives and so many subjects frost resistance has become an indispensable element of concrete [2]. Therefore, this situation led to the spread of the use of the contributions. Spreading this frequency of use as a result of using the wrong usage or mixed in a way that allows the use of two requested feature at the same time [23-24]. However, using a combination of admixtures non-compatible with each other can result in the formation of unpredictable effects [14]. Chemical additives are mismatch in some cases cause unwanted effects or causes to achieve low proportions of results. Combined use of certain chemical additives as a result of producing concrete with desired properties is concerned. Certainly compatibility with each other of such users is the subject of a serious investigation [26-27]. The wide variety of contributions, which are still in use complicates our matters. The unclear terms of concrete that available admixtures on market makes this topic worth investigating.

The additives made by a new generation of plasticizers and setting time studies give different results than conventional additive [3]. Even in studies of plasticizer used cement types of chemical additives and compatibility with mineral additives research has been reported that physical and chemical modification [4-23-29]. However, any anti-corrosion chemical additives in various chemical changes in the properties of concrete

¹ Corresponding author: Eskişehir Osmangazi University, Faculty of Engineering and Architecture, Civil Engineering Department, 2648 Eskişehir, Turkey. murattimur81@gmail.com

² Eskişehir Osmangazi University, Faculty of Engineering and Architecture, Civil Engineering Department, 2648 Eskişehir, Turkey. ilkerbt@ogu.edu.tr

strength values even if the interference with his additives and included the amount of air changes [5-20] shows us proportional differences can reveal different aspects of the use of additives and changes on concrete and mortar. In other investigation self-levelling screed properties was examined successfully [11]. It was observed that the collapse of the self-leveling mortar although the use of chemical and mineral additives to be used in the successful design and the serious improvement in resistance values [6]. However, it became clear that in lignosulphonate and naphthalene sulphate based agent in high dosages study the negative adverse effects of voice transmission speeds and strenght decreasing have been investigated [7].

Because of plenty of research area, many works were produced about additives. Habib et al. [17] researched effect of some chemical admixtures on the physico-chemical and reological properties of oil well cement pastes. Shanthappa et al. [18] studied effect of addition of combination of admixtures on the properties of self compacting concrete subjected to sulphate attack. Recalde et al. [19] investigated combination of lignosulfonate and AMPS®-co-NNDMA water retention agent—an example for dual synergistic interaction between admixtures in cement. Many tests and essays shows that preventing expansion and shrinkage admixtures in equal proportions is effective that shrinkage is in the normal values [8]. This situation is the result of the positive use of the contributions. To give you one other example water-reducing and retarding additives often use to extend the workability of concrete and so that the water / cement ratio to reduce and it is possible to increase the resistance at high temperatures. Retarders prolongs the ability to settle the concrete, accelerators are used to accelerate the hydration process. In studies amixture of plasticizer and retardant and accelerating additives have been tried.

Thus, regenerative mortar mixtures have been studied in preparation [9]. Such mixtures provide the most convenient examples are used for rapid concrete repair. Additives to obtain a combination of a great range of properties are used in combination is provided. Selecting contribution and making the dose adjustment for concrete to be produced requires the presence of many trials. This requires reducing the number of statistically these experiments [10]. Therefore, in this case shows that the right dose admixture combinations is so sensitive and also shows the multiplicity of experimental studies. In this study the most widely used type of chemical additives using together and investigate the effects of micro concrete.

2. MATERIALS and METHODS

2.1. Materials

Samples generated from experiments in the study CEM I 42.5 Portland cement as binding material is used. The chemical and physical properties of cement are given in Table 1 and Table 2. Chemical additives for mortar specimens prepared using standard sand and tap water is provided by applying different proportions to obtain different characteristics of the samples. The data obtained by ensuring that the standard of the materials used have also tried to prevent the affected lot of material differences. Information about the standard sand Limak West Cement firm belongs Norman sold as sand RILEM Chemburea standard sand is weighs 1350 g density and loose unit weight used in preparing the assay mixture in Table 3. The chemical analysis of potable tap water used is given in Table 5. Grace products company contributions are preferred. Wrda 35 as a plasticizer, Daraset 580 is the accelerator has been used. Chemical properties of the additive are given in Table 4.

Table 1. Chemical properties of cement

SiO ₂	CaO	Al ₂ O ₃	Fe ₂ O ₃	MgO	Na ₂ O	K ₂ O	SO ₂	LOI
19.65	62.14	5.34	2.89	1.34	0.35	0.7	3.05	3.75

Table 2. Physical properties of cement

Spec.gravity	Blaine, cm ² /g	Compressive strenght, MPa
3.14	3490	44 (7day) 57.2 (28day)

Table 3. Specific gravity and loose unit weight of standart sand

Loose unit weight kg/m ³	Specific gravity
1350	2550

Table 4. Properties of chemical admixtures

Properties	Wrda 35	Daraset 580
Content		Calciumnitrate
Color	Darkbrown	Brown
State	Liquid	Liquid
Density	1.108 g/ml	1.161 g/ml
Ph	10.0	8.8
Clorit%		<0.1

Table 5. Properties of chemical admixtures

Ph	Na ₂ O	K ₂ O	Cl	SO ₄	Zn	Pb	P ₂ O ₅	NO ₃	Fd
7.3	52	11	66	80	5.06	0.05	1.5	0.1	30.1

2.2 Method and Tests

In this study, the utilization rate of creation is currently used chemical additives and combinations of additives in accordance with the frequency mixing mortar effects evaluated. When the other components of the chemical additives are constant (standard sand and water at the same rate and the same kind cement), chemical additives replaced. The water-cement ratio is selected as 0.50 for the mortar production. Using accelerator and plasticizer admixtures, different samples are obtained. Three combinations are prepared. These are made by plasticizer and accelerator admixtures. Each set is a combination of a control sample sets and even 3 sets will be prepared at various dosages. Different doses recommended optimal dose of preparing the chemical additives that considered as a combination dosage.

Table 6. The dosages of admixtures according to combinations

Combination	Accelerator %	Plasticizer %
1	0,5	1
2	1	1,5
3	2	3

The optimal rate of 50% for the second dose combination is increased or reduced state. In the third dose combination of 2 or 3 levels increased or reduced combination was prepared. Dosages are given in Table 6. The samples 4x4x16 cm 3-cast in the mold was made. With the product mixtures, fresh state tests; such as unit weight, flowability and setting time were conducted. Also in order to observe hardened state properties ultrasonic pulse velocity, flexural and compressive strenght tests were conducted. At the last part of the work micro structure inspections, Scanning electron microscope (SEM) was conducted.

3. RESULTS and DISCUSSION

3.1. Fresh Mortar Properties

3.1.1 Fresh Unit Weight and Flowability (Flow Table)

Unit weight values are given in Table 7 combination mixture dosages are given in Table 6. It was observed that decreasing arc occurs in results when the mixture dosage rates increase. It is known that some air content can be found when the plasticizer used in concrete. So unit weight of mixtures are in low degree if we compare to control sample. In combination 3, %5 admixture ratio is used totally and the lowest value obtained in this sample. Flowability test results depending on admixture combinations are given in Table 7. As expected with the using of plasticizer admixture flow rate increased. When the ratio rises, flow degrees rise paralel in value. Flowability test diameters were varied from 12 to 19 cm. The key point of the graphic is combination 2 that has %1,5 plasticizer. From this value degree increases highly.

Table 7. Fresh unit weight variation and flow diameter results

Combination	Unit weight, kg/dm	Flow diameter, cm
control	2,22	12,1
1	2,17	15,1
2	2,15	15,9
3	2,11	18,1

3.1.2 Setting Times

Initial and final setting time values are given in Figure 1. Accelerator and plasticizer were used together in samples, so we saw that accelerator limits the effect of high dosage plasticizer. We expect that when the accelerator rise initial and final setting time decrease but the negative effect of plasticizer increases the values. Because of %3 plasticizer ratio is over from %2 accelerator ratio, accelerator is only limits the plasticizer.

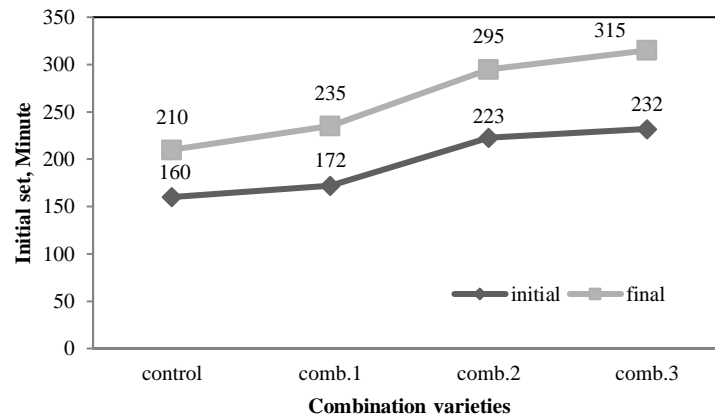


Figure 1. Initial and final setting time variation

3.2 Hardened Mortar Properties

3.2.1 Ultrasonic Pulse Velocity

Ultrasonic velocity test results at the age of 3 to 28 days are presented in Figure 2. Ultrasonic pulse velocity values are varying from 3,77 km/s to 5,12 km/s. Common result is velocity increase with the days. Another inference is all mixture combinations did not reach the control sample. We can say that usage of mix-tures decrease the ultrasonic pulse velocity depending on the usage ratio irregardless of which additive is used.

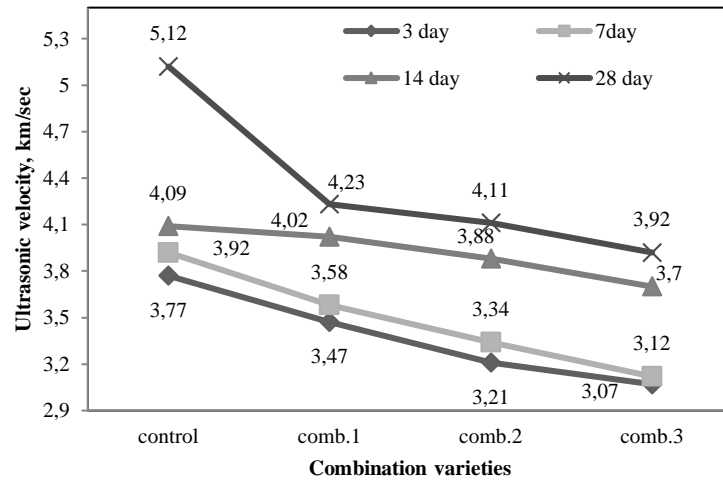


Figure 2. Ultrasonic velocity variation

3.2.2 Flexural Strength

Flexural strength values at the age of 3day to 28 day are given in Figure 3. In all samples, flexural strength value is lower than control sample. Flexural strength is weak in concrete but using admixtures decreases the strength value in accordance with the ratio of additives. Results obtained in 28day about 4,53 to 5,44 MPa.

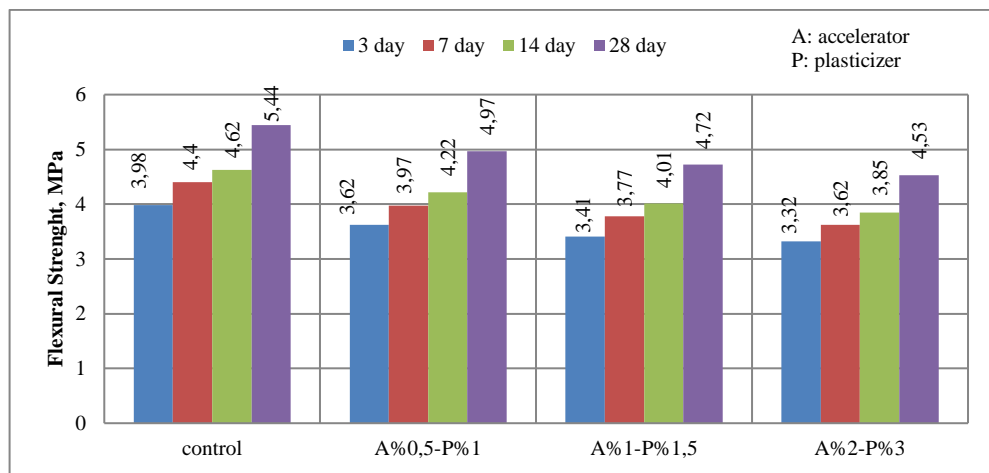


Figure 3. Flexural strength values

3.2.3 Compressive Strength

Compressive strength tests were conducted at the age of 3-7-14-28 days old specimens. For all combinations and control sample results are given in Figure 4. Strength values change according to admixture ratio about 21,78 MPa to 43,55 MPa. Control sample gained the highest value. Generally increasing additive decrease the strength but in combination 2 mixture some early day strength values is similar to control sample. Also this value decrease in 28 day results. According to the graph values obtained that increasing optimum dosage mixture that productive company recommended scaled up the early day strength values.

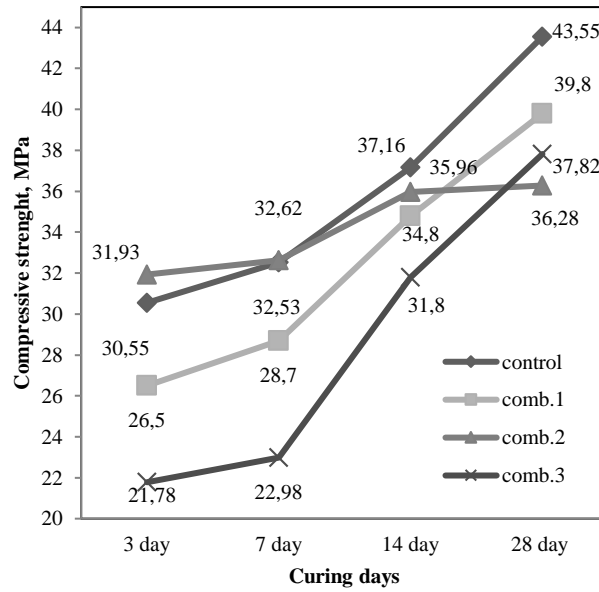


Figure 4. Compressive strenght values

3.2.4 Scanning Electron Microscope (SEM) Analysis

All combinations and control sample SEM images are given in Fig.5-6-7. In Fig. 5 control sample SEM image strong CSH structure easily can be seen in 28days. According to this image the other combination images can comment that it is weak structure or not. But in Figure 6 and Figure 7 magnification of 1500x, we can obtain poor CSH structure in this high dosage samples.

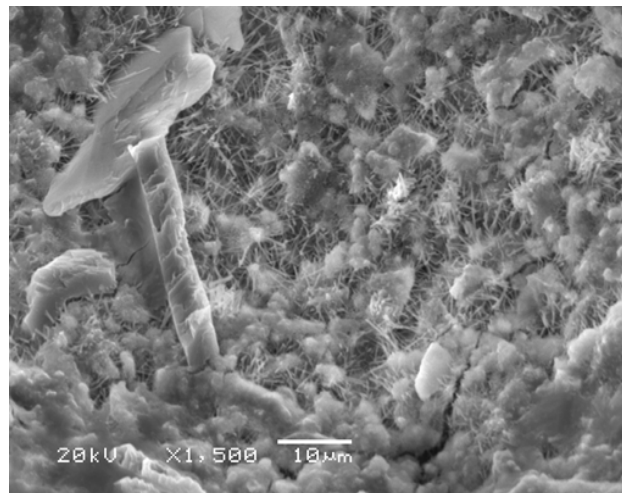


Figure 5. SEM image (magnification 1500x) of control sample

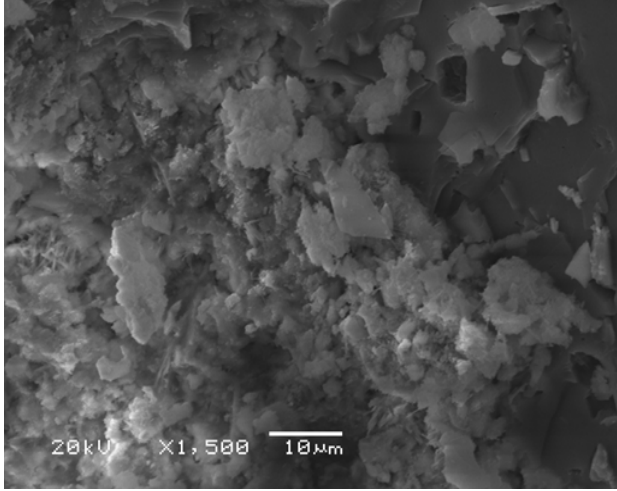


Figure 6. SEM image (magnification 1500x) of combination 2

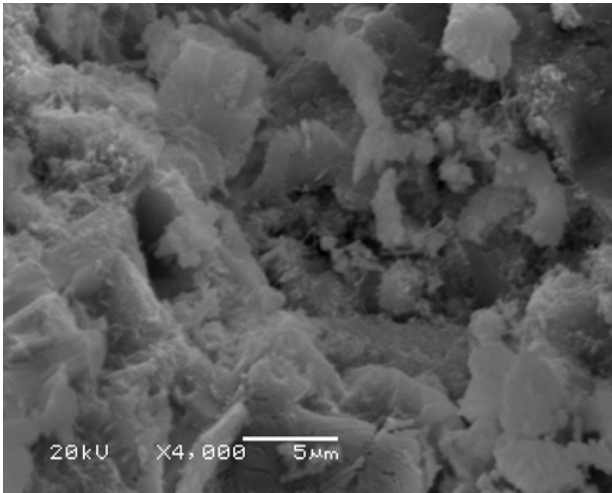


Figure 7. SEM image (magnification 4000x) of combination 1

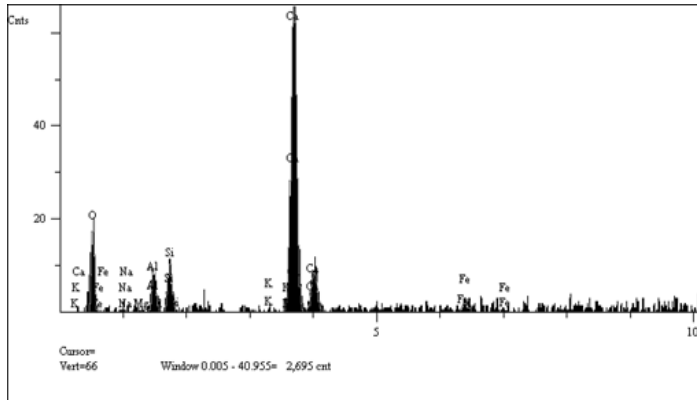


Figure 8. EDX graphic analysis of control sample

Component	Mole Conc.	Conc.	
Al	3.479	4.163	
Fe	1.133	2.807	
O	69.209	49.110	
Si	3.742	4.661	
Ca	21.429	38.091	
Mg	0.378	0.407	
K	0.167	0.289	
Na	0.464	0.473	
Total	100.000	100.000	

CONCLUSIONS

Experimental study was carried out with the following results:

- With the increasing of admixture ratios fresh unit weight values decreased entirely. Especially the existence of admixtures more than %3 totally, it was decreased the results significantly.
- Using of plasticizer in all admixture combinations flowability was increased if compare with the control samples results as expected.
- We expect that when the accelerator rise initial and final setting time decrease but the negative effect of plasticizer increases the values. But it was received that accelerator limits the effect of high dosage plasticizer.
- According to the hardened tests; ultrasound pulse velocity, flexural strength, compressive strength results shows us it is general decreasing in all samples. Control sample results are higher than others proportional with dosage of admixtures. So we can say that using combination of admixtures in several doses changes the expected strength.
- SEM and BET analyses support strength decrease. Comparing with the control sample combinations have poor CSH structure. But in optimum dosage, this reducing effect in strength decreases than others.

As a result of the experiments and investigations, combining accelerator and plasticizer admixtures in different dosages cause negative effect in fresh and hardened state properties of concrete. Especially in overdose of combinations, negative effect shows itself strongly. So usage of combination accelerator and plasticizer admixtures must be limited and controlled in manufacturing.

REFERENCES

- [1]. V.S. Ramachandran, Concrete Admixtures Handbook, Elsevier (1996) , <http://dx.doi.org/10.1016/B978-081551373-5.50001-5>
- [2]. Concrete Admixtures Market by Type Global Trends & Forecast to 2019, (n.d.). <http://www.Researchandmarkets.com/research/6psp98/concrete> (accessed January 11, 2016)
- [3]. B. Felekoğlu, K. Tosun, B. Baradan, Compability of A Polycar-boxylate-based Superplasticiser with

- Different Set-Controlling Admixtures, *Constr. Build. Mater.* 25(2011)1466-1473
- [4]. O.B. Montes, M. Palacios, P. Rivilla, F. Puer-tas ,Compability Between Superplasticizer Admixtures and Cements with Mineral Additions, *Constr. Build. Mater.* 31 (2012) 300-309
- [5]. G. De Schutter, L. Luo, Effect of Corrosion Inhibiting Admixtures on Concrete Properties, *Constr. Build. Mater.* 18 (2004) 483-489
- [6]. I.B.Topçu, T. Uygunoglu, Influence of mineral additive type on slump -flow and yield stress of self-consolidating mortar, *Scien. Resear. Essays* 5 (2010) 1492–1500
- [7]. I.B. Topçu , Ö. Ateşin, Effect of high dosage lignosulphonate and naphthalene sulphonate based plasticizer usage on micro concrete properties, *Construction and Building Materials* 116 (2016) 321–325
- [8]. M.J. Oliveira, A.B. Riberio, F.G. Branco, Combined effect of ex-pansive and shrinkage reducing admixtures to control autogenous shrinkage in self-compacting concrete, *Constr. Build. Mater.* 52 (2014) 267–275
- [9]. T. Meagher, N. Shanahan, D. Buidens, K.A. Riding, A. Zayed, Ef-fects of chloride and chloride-free accelerators combined with typical admixtures on the early-age cracking risk of concrete repair slabs, *Constr. Build. Mater.* 94 (2015) 270–279
- [10]. B.E. Jimma, P.R. Rangaraju, Chemical admix-tures dose optimization in pervious concrete paste selection–A statistical approach, *Constr. Build. Mater.* 101 (2015) 1047–1058
- [11]. M. Canbaz, İ.B. Topçu, Ö. Ateşin, Effect of admixture ratio and aggregate type on self-leveling screed properties, *Constr. Build. Mater.* 116 (2016) 321-325, [http:// dx.doi.org/10.1016/j.conbuildmat.2016.04.084](http://dx.doi.org/10.1016/j.conbuildmat.2016.04.084)
- [12]. B. Łażniewska-Piekarczyk, Investigations on the relationship between porosity and strength of admixtures modified high performance self-compacting concrete, *Journ. Civil Eng. Management.* 22:4 (2016) 520-528, [http:// dx. doi.org/10.3846/13923730.2014.897978](http://dx.doi.org/10.3846/13923730.2014.897978)
- [13]. S. Liu, M. Rao, J. Wei, Z. Gao, W. Zhou, Q. Li, Study on strength and microstructure of cement-based materials containing combi- nation mineral admixtures, *Advan. in Mater. Sci. And Eng.* (2016) doi:[http://dx.doi.org/ 10.1155/2016/7243670](http://dx.doi.org/10.1155/2016/7243670)
- [14]. N. Shanahan, D. Buidens, K.A. Riding, A. Zayed, Effect of Chloride-based accelerator in the presence of water-reducing and retarding admixture on autogenous shrinkage, *Jour. Am. Ceram. Soc.* 99 (2016) 2147-2158, doi: 10.1111/jace.14221
- [15]. M. Stehlik, Enhancing the durability of con- crete made of concrete recyclate by additives and admixtures, *Journ. Civil Eng. Mana- gement.* 20:2 (2014) 270-27, [http:// dx. doi.org/10.3846/13923730.2013.802708](http://dx.doi.org/10.3846/13923730.2013.802708)
- [16]. C. Wang, K. Tan, X. Xu, P. Wang, Effect of activators, admixtures and temperature on the early hydration performance of desulfurization ash, *Constr. Build. Mater.* 70 (2014) 322–331, [http://dx.doi.org/10.1016/j.conbuildmat. 2014.07.095](http://dx.doi.org/10.1016/j.conbuildmat.2014.07.095)
- [17]. A.O. Habib, I. Aiad, T.A. Youssef, A.M. Abd El-Aziz, Effect of some chemical admixtures on the physico-chemical and rheological properties of oil well cement pastes, *Constr. Build. Mater.* 120 (2016) 80–88, [http:// dx. doi.org/10.1016/j.conbuildmat.2016.05.044](http://dx.doi.org/10.1016/j.conbuildmat.2016.05.044)
- [18]. B.C. Shanthappa, M.C. Prahallada, K.B. Pra-kash, Effect of addition of combination of admixtures on the properties of self compacting concrete subjected to sulphate attack, *I-Manager's Journal on Civil Engineering*, 2:4 (2012) 34-39, [https:// search. Proquest.com/docview/1473897815?accountid=16716](https://search.Proquest.com/docview/1473897815?accountid=16716)
- [19]. N. Recalde Lummer, J. Plank, Combination of lignosulfonate and AMPS®-co-NNDMA water retention agent—An example for dual synergistic interaction between admixtures in cement, *Constr. Build. Mater.* 42 (2012) 728–735
- [20]. B. Łażniewska-Piekarczyk, The influence of admixtures type on the air-voids parameters of non-air-entrained and air-entrained high performance SCC, *Constr. Build. Mater.* 41 (2013) 109–124, [http://dx.doi.org/ 10. 1016 /j.conbuildmat.2012.11.086](http://dx.doi.org/10.1016/j.conbuildmat.2012.11.086)
- [22]. M.J. Olivera, A.B. Riberio, F.G. Branco, Com-bined effect of expansive and shrinkage reducing admixtures to control autogenous shrinkage in self-compacting concrete, *Constr. Build. Mater.* 52 (2014) 267–275, [http://dx. doi.org/ 10.1016/j.conbuildmat. 2013.11.033](http://dx.doi.org/10.1016/j.conbuildmat.2013.11.033)
- [23]. B. Nematollahi, J. Sanjayan, Effect of diffe- rent superplasticizers and activator combi-nations on workability and strength of fly ash based geopolymer, *Materials&Design* 57(2014)667–672,[http:// dx. doi.org /10.1016 /j.matdes.2014.01.064](http://dx.doi.org/10.1016/j.matdes.2014.01.064)
- [24]. A.M. Rashad, A comprehensive overview about the influence of different additives on the properties of alkali-activated slag – A guide for Civil Engineer, *Constr. Build. Mater.* 47 (2013) 29–55, [http://dx.doi.org/ 10.1016 /j.conbuildmat.2013.04.011](http://dx.doi.org/10.1016/j.conbuildmat.2013.04.011)



- [25]. U.S Yılmaz, H. Turken, The effects of various curing materials on the compressive strength characteristic of the concretes produced with multiple chemical admixtures, *Scientia Iranica.Transaction E Industrial Engineering*, 19:1 (2012) 77–83, <https://search.proquest.com/docview/1021186302?accountid=16716>
- [26]. M.S. Meddah, M. Suzuki, R. Sato, Influence of a combination of expansive and shrinkage-reducing admixture on autogenous deformation and self-stress of silica fume high-performance concrete, *Constr. Build. Mater.* 25 (2011) 239–250, <http://dx.doi.org/10.1016/j.conbuildmat.2010.06.033>
- [27]. B. Felekoğlu, H. Sarikahya, Effect of chemical structure of polycarboxylate-based superplasticizers on workability retention of self-compacting concrete, *Constr. Build. Mater.* 22 (2008) 1972–1980, <http://dx.doi.org/10.1016/j.conbuildmat.2007.07.005>
- [28]. S.A. Civjan, J.M. LaFave, J. Trybulski, D. Lovett, J. Lima, D.W. Pfeifer, Effectiveness of corrosion inhibiting admixture combinations in structural concrete, *Constr. Build. Mater.* 27 (2005) 688–703, <http://dx.doi.org/10.1016/j.cemconcomp.2004.07.007>
- [29]. M. Palacios, F. Puertas, Effect of superplasticizer and shrinkage-reducing admixtures on alkali-activated slag pastes and mortars, *Constr. Build. Mater.* 35 (2005) 1358–1367, <http://dx.doi.org/10.1016/j.cemconres.2004.10.014>
- [30]. C. Maltese, C. Pistolesi, A. Lolli, A. Bravo, T. Cerulli, D. Salvioni, Combined effect of expansive and shrinkage reducing admixtures to obtain stable and durable mortars, *Constr. Build. Mater.* 35 (2005) 2244–2251, <http://dx.doi.org/10.1016/j.cemconres.2004.11.021>



Utilization of PVC Wastes on Concrete Bicycle Roads

Hasan Baylavli¹

Abstract

*Polyvinyl-chlorine (PVC) is a material with a wide range of utilities such as construction, packaging, medical materials, and the automotive sector. Because these materials have much time to disappear in nature, it is vital to utilize PVC chip wastes. Concrete was applied on the roads of the Northern campus of Hittites University. PVC chips obtained from door and window manufacturing shops have been added to the concrete mix of concrete bicycle roads. PVC chips were utilized in the concrete by eliminating 0,5 mm aperture size. PVC chips have been added into the transit-mixer from the concrete plant to the construction site. PVC chips were used in the mixture of concrete in the ratio of 1-3 and 5 kg/m³. The largest aggregate size in the mixture is 22.4 mm. The addition of PVC chip to the concrete mix reduced the precipitation value of fresh concrete from 190 mm to 150 mm. The addition of PVC chip has slightly increased the air void ratio of the fresh concrete. Hardened concrete tests, compression resistance, tensile splitting strength, and modulus of elasticity were performed. PVC has been compared with the additive control concrete sample. 5 kg/m³ PVC chip, which was added to the mixture, has reduced pressure resistance by about 11%. It can be stated that the PVC chip contributes positively to the tensile splitting strength and elasticity module values of the concrete. Apart from these tests, firstly, modulus of elasticity tests was carried out on 15*30 cm cylinder samples. Then, compression resistance and tensile splitting strength tests were conducted on the same samples. In the modulus of elasticity test, variations in compression and tensile splittings strengths of examples exposed to repeated compression loads were examined. After the test of elasticity modulus, the compression resistance and tensile-splitting strengths of the samples have decreased. It has been concluded that very thin PVC chip wastes can be utilized in a concrete mix.*

Keywords: PVC wastes, concrete, compressive strength, elasticity modül, tensile splitting strength

1. INTRODUCTION

PVC is a building material used in many sectors. Since the usage area is very large, PVC wastes are increasing day by day. These wastes have a very long time to disappear in nature. Therefore, it is important to use these wastes in recycling. [1-8]. Many researchers have used various plastic wastes as aggregates in self-compacting concrete [9]. Waste plastic bag fibers were used in self-compacting concrete. Waste plastic fibers reduced the slump flow value of fresh concrete. As the fiber length increased, the separation in the L-Box test increased. [10]. Usage of the plastic waste as fine aggregate has an acceptable impact on workability compared to the coarse plastic waste aggregate [11]. The addition of PET fibers to SCC has reduced slump flow time and T50 values, may be due to the shape and dosage of the fibers [12]. When plastic aggregate was replaced with fine aggregate, it increased the compressive strength compared to coarse plastic waste aggregate [10]. The increase in the amount of plastic waste decreased the 28-day and 90-day compressive strength of high-strength self-compacting concrete. [13]. Addition of 0.1% PPF to self compacting concrete increased the tensile strength of concrete by 16% to 32%. [14]. Fine aggregate was partially replaced with waste plastic (LDPE) and used in concrete production. Concrete specimens were cast to estimate the concrete strength. Replacing of fine aggregate by 5%-20% with plastic waste, the strength in compression of the plastic concrete is observed to reduce by about 35 to 50%. [15]. In one study has been employed to come up with the eco-friendly concrete by using the plastic waste to promote the sustainability. plastic waste has shown to decrease the compressive strength and anomalous behavior was observed in case of split tensile strength. plastic waste has shown to decrease the compressive strength and anomalous behavior was observed in case of split tensile strength. [16].

In one research investigates the effect of utilizing Incinerated Solid Waste (ISW) and Recycled Plastic Waste (RPW) as a partial replacement for cement and fine aggregate. Workability decreased as cement and fine aggregate replacement increased. The experimental investigation concluded that up to 20% of fine aggregate and 15% of cement replacement with ISW rendered better concrete strength. [17]. In one research, experimental investigations were conducted to study the performance of the concrete mechanical properties, and reinforced concrete (RC) beam contained FPWA as a partial substitute of the NSG. The use of FPWA in the concrete mix decreased the workability, bending, shear, tensile and compressive strengths of fresh concrete. [18]. The properties of recycled aggregate and waste plastic fiber concrete were investigated. Adding recycled aggregates to waste plastic fiber concrete significantly increased its workability. It also increased the water absorption, compressive strength and tensile strength of the hardened concrete. [19]. The feasibility study of recycled plastic waste as fine aggregate in concrete was investigated. In this experimental study, the concrete of M30 grade of concrete is partially replaced with two types of recycled plastic such as PET and PP individually by different percentages as 5%, 10%, 15%, 20% and 25%. The split tensile strength and flexural strength concrete with PET increases till 10% replacement. The compressive strength concrete with PET plastic increases up to 10% beyond that it decreases. [20].

In this study, PVC chips obtained from door and window manufacturing shops have been added to the concrete mix of concrete bicycle roads. PVC chips have been added into the transit-mixer from the concrete plant to the construction site. Experimental study was carried out in field concrete application. Mechanical properties of concrete with PVC waste additives were investigated. There are many different kinds of waste from PVC products. There are different recovery, recycling and disposal options for each resulting waste product group. PVC waste can be evaluated in two categories.

1. Pre-consumption (Industrial and / or Commercial PVC wastes),

These are wastes such as burrs, ullages and sawdust that occur during the PVC production stage. This type of waste is easier to recover and collect from a single point.

2. Post-consumption PVC wastes

Post-consumption waste is more difficult to collect for recycling. Wastes such as pipes, window frames, packaging waste are examples of this group. These wastes are often mixed with other wastes. Some of the post-consumption PVC wastes are sent to the landfills. Another portion is disposed of by incinerating for energy recovery. In this study, the utilization of pre-consumption PVC wastes in concrete was investigated.

2.MATERIALS AND METHODS

PVC wastes were collected from PVC door and window manufacturing workshops. The collected wastes were sieved to separate them into certain sizes. PVC chips were utilized in the concrete by eliminating 0,5 mm aperture size. PVC chips have been added into the transit-mixer from the concrete plant to the construction site. Mixing ratios are given in Table 1. PVC chips were used in the mixture of concrete in the ratio of 1-3 and 5 kg/m³. The largest aggregates size in the mixture is 22,4 mm. Chemical additive hyperplasticizer was used. PVC wastes were used in three different ratios in the concrete mixture. Together with the witness concrete, four series of concrete were produced. Mixing codes are given in Table 2.



Figure 1. Screened PVC waste

Table 5. Mixings Ratios

Ingredients	Mixing Ratios
Sand (0-2 mm)	230 kg/m ³
Fine aggregate (2-4 mm)	880 kg/m ³
Crushed Stone (4-12 mm)	250 kg/m ³
Crushed Stone (12-22,4 mm)	560 kg/m ³
Cement	300 kg/m ³
PVC Wastes	1-3-5
Water	165 kg/m ³
Admixture	%0,8
Water-cement ratio	0,54
Unit Weight	2385 kg/m ³

Table 2. Mix codes

Mix codes	Explanation
K	Witness concrete without PVC additive
PVC(1)	1 kg/m ³ PVC added concrete
PVC(3)	3 kg/m ³ PVC added concrete
PVC(5)	5 kg/m ³ PVC added concrete

3.RESULTS AND DISCUSSION

Slump in fresh concrete, compressive strength in hardened concrete, split-tensile strength and modulus of elasticity were investigated. In hardened concrete, each test was performed on three specimens. The test results were averaged. Also; compressive strength and split-tensile strength tests were carried out on three different samples that were tested for modulus of elasticity.

3.1. Slump test

The slump value of concrete without PVC additive is 190 mm. With the PVC additive, the slump value of the concrete decreased by 40 mm (Table 3). PVC additive reduced the workability of fresh concrete. But, no segregation was observed in fresh concrete.

Table 3. Slump values

Mix codes	Slump values (mm)
K	190
PVC(1)	150
PVC(3)	160
PVC(5)	150



Figure 2. Before and after curing

3.2. Modulus of elasticity

E module is calculated according to DIN 1048-5 standard. The maximum stress value on the sample was approximately 10 MPa, and the smallest stress value was approximately 0.8 MPa, and 3 times were loaded. The modulus of elasticity was calculated according to the unit deformation at the end of the third loading (Figure 3). The modulus of elasticity of concrete without PVC additive is 34.36 GPa. The modulus of elasticity values in PVC added samples vary between 33.79 GPa and 35.72 GPa. The modulus of elasticity increased in PVC(1) and PVC(2) samples. It decreased slightly in the PVC(3) sample (Figure 4).

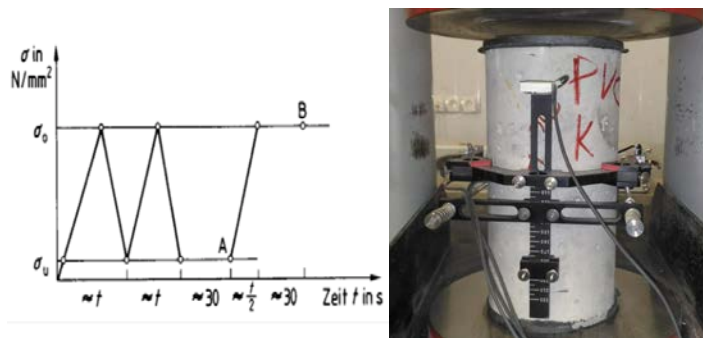


Figure 3. Modulus of elasticity test

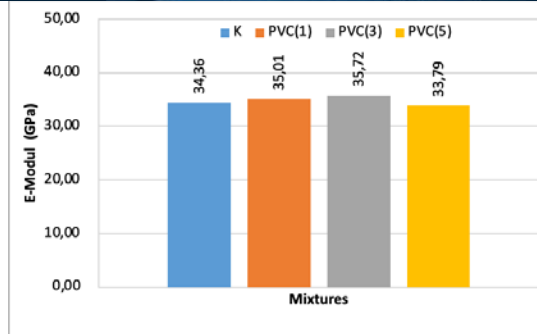


Figure 4. Modulus of elasticity values

3.3. Compressive strength

The witness sample (K) has a compressive strength of 55.08 MPa. As the PVC addition in the mixture increased, the compressive strength decreased. The compressive strengths of PVC reinforced concrete are between 48.94 MPa and 54.64 MPa. After the modulus of elasticity test, the compressive strength of the samples was measured. In the elasticity test, the compressive strength of the samples exposed to repeated loads decreased. more than 3 levels of headings should be used. (Figure 5).

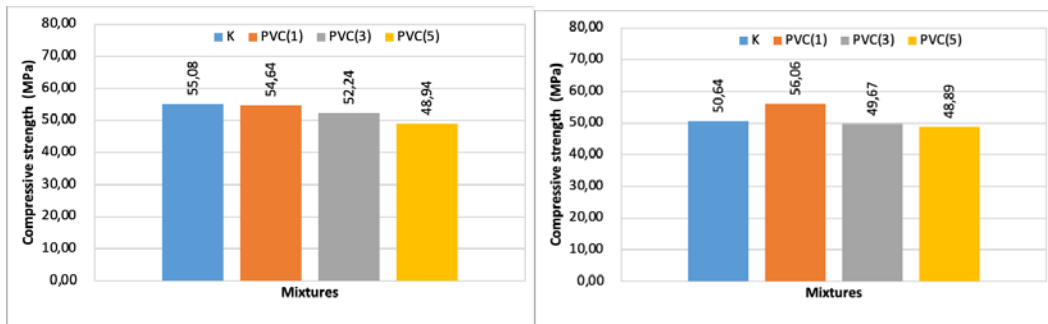


Figure 5. Compressive strength and compressive strength after E-modul

3.4. Tensile splitting strength

The splitting-tensile strength of the witness sample (K) is 4.32 MPa. splitting-tensile strength of PVC added concretes are between 4.17 MPa and 4.56 MPa. splitting-tensile strength increased in PVC(3) mixture. It was decreased in other mixtures. The PVC additive had no effect on the splitting-tensile strength of the concrete. After the modulus of elasticity test, the splitting-tensile strength decreased compared to the blank sample. Splitting-tensile strengths after modulus of elasticity range from 4.47 MPa to 4.72 MPa (Figure 6).

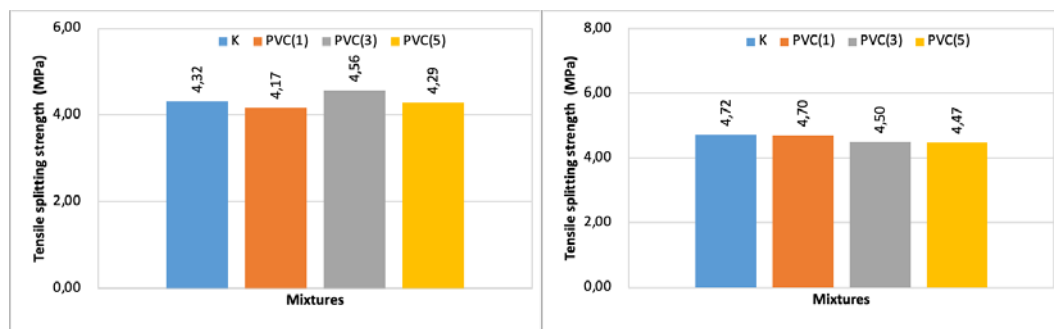


Figure 6. Splitting-tensile strength and Splitting-tensile strength after E-modul

CONCLUSIONS

Workability of fresh concrete decreased with PVC additive. The slump value was reduced by maximum of 40 mm with the PVC additive. Compressive strength decreased by 10% at 5 kg PVC additive. Splitting-tensile strength increased by 5,5% at 3 kg of PVC additive. It was observed that the PVC additive did not have much effect on the E-modulus of the concrete. The result of compressive and splitting-tensile strength on the same sample after E-modulus is less than other samples. This can be explained by the fatigue of concrete in the E-modulus test. The poor adherence between PVC particles and cement phase caused a decrease in compressive strength. The fibrous particles entering the concrete generally increase the tensile strength of the concrete. However, since PVC wastes were used very thinly, it had no effect on the tensile strength of the concrete. However, it was concluded that PVC additive can be evaluated in concrete production.

REFERENCES

- [1]. I. Janerjeh, M. Alshrah and S. Zamzam, Mechanical recycling of PVC plastic waste streams from cable industry: A Case Study, *Sustainable Cities and Society*, 18:13-20, 2015.
- [2]. S.C. Kou, G. Lee, C.S. Poon and W.L. Lai, Properties of lightweight aggregate concrete prepared with PVC granules derived from scraped PVC pipes, *Waste Management*, 29:621-628, 2009.
- [3]. M.S. Shojai and G-R. Bakhshandeh, Recycling of PVC wastes, *Polymer Degradation and Stability*, 96: 404-415, 2011.
- [4]. S.K. Kaliyavaradhan and T.C. Ling, Performance of concrete with PVC fibers, *Woodhead Publishing Series in Civil and Structural Engineering*, 369-385, 2019.
- [5]. S. Tsuyoshi, I. Takayuki, H. Yusaku, K. Yangsun and S. Maito, Analysis of the efficacy and feasibility of recycling PVC waste in Japan, *Resources, Conservation & Recycling*, 131:41-53, 2018.
- [6]. C. Jaklsland, E. Rasmussen and T. Rohde, A new technology for treatment of PVC waste, *Waste Management*, 20: 463-467, 2000.
- [7]. B. Ambika, S. Grish and K. Gajenda, A Sustainable approach: Utilization of waste PVC in asphaltting of roads, *Construction and Building Materials* 54:113-117, 2014.
- [8]. A.A. Mohammed, Mechanical strength of concrete with PVC aggregates, *Woodhead Publishing Series in Civil and Structural Engineering*, 115-135, 2019.
- [9]. G.N. Gopu, R.R. Thummala, Ed., A review on mechanical properties of self-compacting concrete incorporated with various types of plastic waste aggregates, *Materials Today: Proceedings* 64, 976-982, 2022.
- [10]. Y. Ghernouti, B. Rabehi, T. Bouziani, H. Ghezraoui, A. Makhloufi, Fresh and hardened properties of self-compacting concrete containing plastic bag waste fibers (WFSCC), *Constr. Build. Mater.* 82 (2015) 89-100, <https://doi.org/10.1016/j.conbuildmat.2015.02.059>.
- [11]. S.M. Hama, N.N. Hilal, Fresh properties of self-compacting concrete with plastic waste as partial replacement of sand, *Int. J. Sustain. Built Environ.* 6 (2), 299-308, 2017. <https://doi.org/10.1016/j.ijbe.2017.01.001>.
- [12]. A.I. Al-Hadithi, A. Tareq, W. Khairi, Mechanical properties and impact behavior of PET fiber reinforced self-compacting concrete (SCC), *Compos. Struct.*, vol. 224, p. 111021, 2019.
- [13]. R.H. Faraj, A. Far, H. Sherwani, A. Daraei, Mechanical, fracture and durability properties of self-compacting high strength concrete containing recycled polypropylene plastic particles, *J. Build. Eng.* vol. 25, 2019. <https://doi.org/10.1016/j.jobbe.2019.100808>
- [14]. A. Karimipour, M. Ghalehnovi, J. De Brito, M. Attari, The effect of polypropylene fibres on the compressive strength, impact and heat resistance of self-compacting concrete, *Structures*, vol. 25, pp. 72-87, 2020.
- [15]. S. Vivek, P. Hari Krishna, T.D. and Gunneswara Rao, A study on the mechanical behavior of concrete made with partial replacement of fine aggregate with waste plastic (LDPE), *Materials Today: Proceedings*.
- [16]. T. Liu, Ed., Comparative study of mechanical properties between irradiated and regular plastic waste as a replacement of cement and fine aggregate for manufacturing of green concrete, *Ain Shams Engineering Journal* 13, 101563, 2022.
- [17]. P. Janardhan, H. Narayana, N. Darshan, Compressive strength studies of concrete with partial replacement of cement and fine aggregate with incinerated solid waste and recycled plastic waste, *Materials Today: Proceedings*.
- [18]. A. A. Ibrahim, Ed., Experimental investigation of flexural and shear behaviors of reinforced concrete beam containing fine plastic waste aggregates, *Structures* 43, 834-846, 2022.
- [19]. M. Gopinath, P. Abimaniu, C. Dharsan Rishi, K. Pravinkumar, P.G. Tejeshwar, Experimental investigation on waste plastic fibre concrete with partial replacement of coarse aggregate by recycled coarse aggregate, *Materials Today: Proceedings*.
- [20]. M. Harihanandh, P. Karthik, Feasibility study of recycled plastic waste as fine aggregates in concrete, *Materials Today: Proceedings* 52, 1807-1811, 2022.

Biography:

Hasan BAYLAVLI works in Hitit University Construction Technology and Building Audit Programs, in Çorum, Turkey as Research Assistant. Completed associate degree program in 1997 in Gazi University Çorum Vocational School Construction Program. Graduated from Pamukkale University, Faculty of Engineering, Department of Civil Engineering in 2000. Did Master's degree in Eskişehir Osmangazi University, Faculty of Engineering, Department of Civil Engineering Building Materials. Still does doctorate in University, Faculty of Engineering, Department of Civil Engineering Building Materials. Works in these subjects: self-compacting concretes, fiber-reinforced concretes and recycling. Furthermore, has studies in the fields of university campus planning, green campus and energy-efficiency in buildings.

Determining the Structural Performance of the Concrete Ventilation Shaft of a Historic Waterway

Ozlem Ustundag¹, Baris Gunes², Baris Sayin³

Abstract

This study presents a seismic performance evaluation of a ventilation shaft belonging to a historical waterway constructed in 1583. The research involved modeling the current state of the ventilation shaft and conducting performance analyses based on survey data and soil properties related to the examined waterway. Initially, seismic performance analyses were conducted, considering static effects such as soil loads, surcharge loads, and groundwater-induced loads. Subsequently, the structural loads and ground-induced earthquake effects were calculated and applied to the structure. The earthquake effects were categorized into three groups according to the structure mass, soil and surcharge effects, and global ground relative displacement. The analyses revealed that the ventilation shaft satisfies the axial strength requirements under static effects, complying with the local regulations. However, the structure only achieves a "Controlled Damage" performance level for the DD-3 earthquake level and does not meet the same level of performance for the DD-2 earthquake level. The presented study is expected to make a valuable contribution to the literature presenting a methodology to determine the seismic performance of chimney-like structures.

Keywords: Structure, Chimney structure, Seismic performance, Soil study

1. INTRODUCTION

The waterways and their associated structures serve as vital technical systems that supply water to the city. They not only fulfill their functional purpose but also reflect -albeit partially- the architectural and artistic styles of the respective periods. These structures are an integral part of social life and hold architectural significance, representing the evolving social dynamics of their era. The construction of the first waterway in Istanbul, known as the Fatih Waterway, began in 1453 and was later expanded. As the water demand grew, additional waterways such as Kırkçeşme and Taksim waterways were built. The final waterway, called the Hamidiye Waterway, was constructed between 1899 and 1902 during the reign of Sultan II. Abdülhamid. Some of the monumental superstructures of these waterways have survived to this day, serving as historical remnants. The waterways played a fundamental role in Ottoman society by efficiently transporting clean and usable water from its source to the city with minimal loss. Before implementing new settlement programs or establishing Islamic foundation complexes, priority was given to locating clean water sources and ensuring their efficient distribution to the region [1].

Istanbul, being the capital and largest city of the Ottoman Empire, holds the finest examples of waterway systems and structures. The first waterway of the Ottoman era in Istanbul was the Fatih waterway, which served as a water resource for the area between Halkalı Village and Cebeciköy, located west of the city walls. Construction of this waterway began in 1453, and it underwent expansions as new Islamic complexes were established in Istanbul. The final expansion took place in 1755, completing a waterway system consisting of 16 independent waterways [2]. Waterways had the primary function of transporting water from its source to

¹ Istanbul University-Cerrahpasa, Department of Civil Engineering, Construction Materials Division, 34320, İstanbul, Türkiye. ozlem.ustundag@iuc.edu.tr

² Istanbul University-Cerrahpasa, Department of Civil Engineering, Structural Engineering Division, 34320, İstanbul, Türkiye. bgunes@iuc.edu.tr

³ Corresponding author: Istanbul University-Cerrahpasa, Department of Civil Engineering, Structural Engineering Division, 34320, İstanbul, Türkiye. barsayin@iuc.edu.tr

the city. However, these structures were susceptible to destruction due to negligence and natural causes. Moreover, as the city developed, they were sometimes demolished or concealed beneath new structures, making it nearly impossible to trace their exact locations. The only remaining visible remnants of these waterways are certain parts of their monumental surface connection structures. These endangered waterway structures provide valuable insights into the societal characteristics, engineering, architecture, and art history of the period.

During seismic events, chimney-like structures, including ventilation shafts of waterways, are exposed to dynamic forces that can potentially result in structural damage and failure. Therefore, conducting a comprehensive seismic analysis and evaluation of these structures is crucial to ensure their safety and resilience. This literature review provides an overview of key findings and methodologies employed in the seismic analysis of ventilation shafts as chimney-like structures. One important aspect of seismic analysis is determining the dynamic characteristics of the structure, such as natural frequencies and mode shapes. Johnson et al. [3] utilized the finite elements method to obtain the modal properties of chimneys, highlighting the significance of considering higher modes for accurate seismic response predictions. Gupta and Dhawan [4] employed a numerical approach based on the mode superposition method to evaluate the dynamic response of chimneys, emphasizing the influence of earth-structure interaction on their behavior. Various analysis methods have been utilized to investigate the seismic performance of chimney-like structures.

Therefore, the current study presents a seismic performance assessment of the chimney-like ventilation shaft section of a waterway utilizing Midas Gen software [5].

2. THE EXAMINED STRUCTURE

The examined chimney-like ventilation shaft structure is surrounded by various elements such as manholes, trees, walls, and buildings. The ventilation shaft begins at an elevation of -9.35 and extends up to +0.00. It is constructed with reinforced concrete and has a diameter of 117 cm, with a wall thickness of 11 cm. Some visual representations of the ventilation shaft are given in Figure 1.

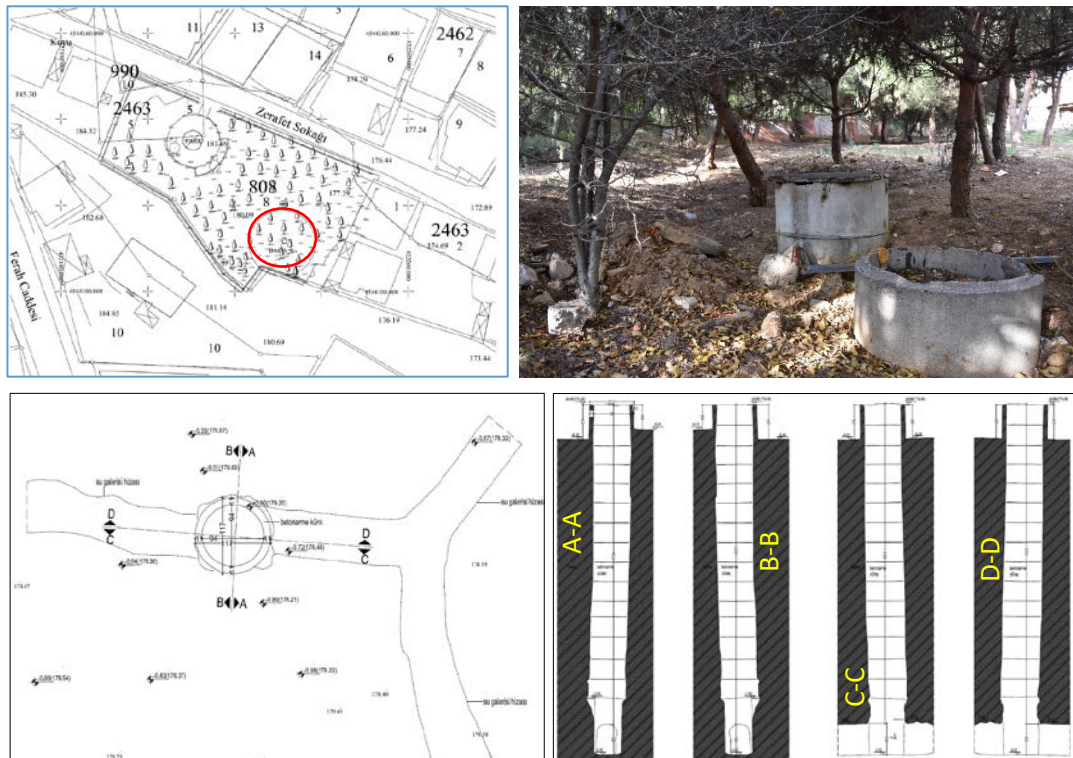


Figure 1. Layout plan, cross-section, a photograph of the current condition

The distance of the structure to the active fault is approximately 23 km. To conduct the seismic analyses, spectral acceleration coefficients (S_s and S_1) were determined based on the soil type and location of the structure. The soil and earthquake parameters are given in Table 1.

Table 1. Soil and earthquake parameters

Parameter	Value / Class
Average shear wave velocity	800 m/s
Local soil type	ZB
Ground motion level	DD-3, DD-2
Spectral acceleration coefficients (Earthquake map) (g)	DD-3, $S_s = 0.337$, $S_1 = 0.096$ DD-2, $S_s = 0.839$, $S_1 = 0.234$
Peak ground acceleration (g)	DD-3, $PGA = 0.145$ DD-2, $PGA = 0.345$
Local soil factors	DD-3, $F_s = 0.900$, $F_1 = 0.800$ DD-2, $F_s = 0.900$, $F_1 = 0.800$
Spectral acceleration coefficients	DD-3, $S_{DS} = 0.303$, $S_{D1} = 0.077$ DD-2, $S_{DS} = 0.755$, $S_{D1} = 0.187$

3. ANALYSIS CRITERIA AND MODELING

To assess the seismic performance of the structure, a finite element analysis was conducted. Since the examined shaft is a historic structure, SMRGHS 2017 was considered for determining performance targets and design approach [6]. Additionally, since the ventilation shaft is an underground structure, TTDY 2020 [7] and TBEC 2018 [8] regulations were also utilized. The determined analysis parameters and assessment method are given in Table 2. According to Section 16.11.1 of TBEC 2018, the structure was subjected to distributed earth pressure. Loadings vary according to the unit volume weight of the soil, the saturated unit weight, the additional surcharge load, and the water surface height. Detailed calculations for the ventilation shafts are provided in the calculations section. Considering the typical load-bearing behavior of ventilation shafts, the “Carrier System Behavior Factor” (R) and “Building Importance Factor” (I) were both set to 1. According to Section 6.1 of TTDY 2020, Type A calculation (free-field ground motion in the transverse direction) was used in the calculations.

Table 2. Performance-based analysis parameters and method

Parameter	Value / Class
Purpose of the structures	Ventilation shaft of waterways
TYDRYK-2017 Importance Factor	Local
Ground motion level	DD-2 DD-3
Performance Target	Controlled Damage, CD
Evaluation/Design Approach	Strength-Based Design, DGT
Analysis/ Design Method for Global Ground Motion According to TTDY 2020	Type A

- Soil parameters were determined using the soil data. The variation of earth pressures for active and passive states by depth are shown in Figure 2a.

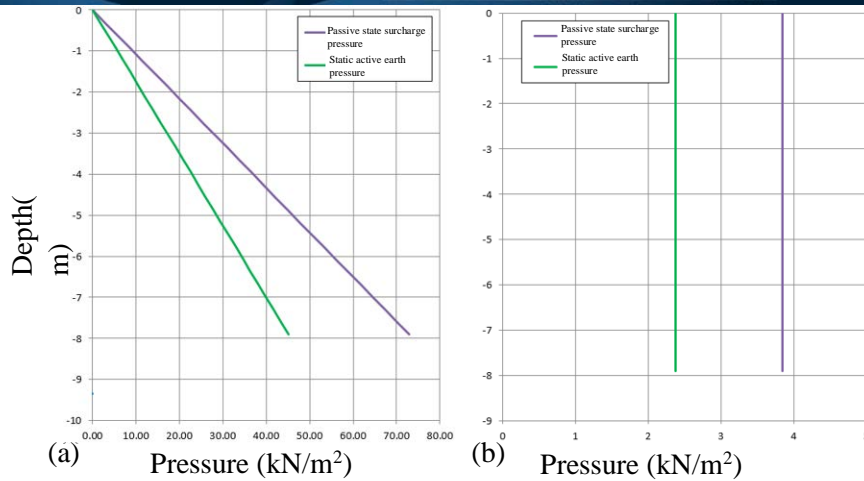


Figure 2. (a) Lateral soil pressure for active and passive states, (b) Surcharge pressure for active and passive states

- Earthquake effects include ground motions-induced loads acting on the structure. TBEC-2018 and TTDY-2020 were utilized to calculate these loads. The seismic behavior of the ventilation shaft was examined for DD-2 and DD-3 ground motion levels. The results obtained from calculations were presented separately for DD-2 and DD-3, respectively. The behavior spectrum and spectral accelerations for DD-2 and DD-3 ground motion levels are given in Figure 3.

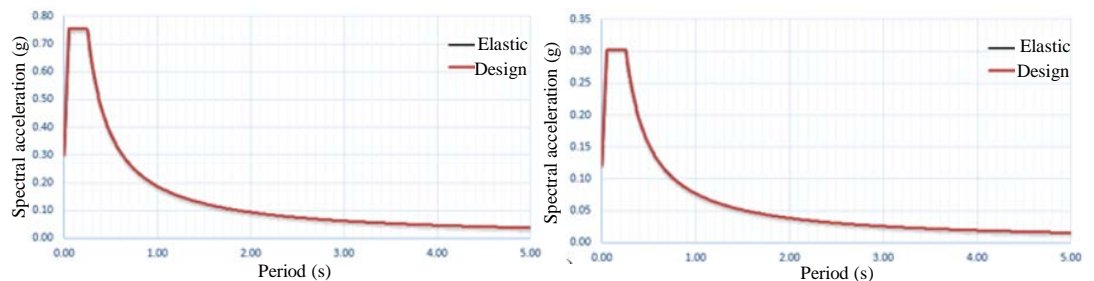


Figure 3. Behavior spectrum and spectral accelerations (a) DD-2, (b) DD-3

- According to TBEC-2018, calculations can be performed using the equation $k_h = 0.4S_{DS}$ with static equivalent earthquake coefficient and static equivalent earthquake loads. Accordingly, lateral earthquake loads corresponding to the masses were applied to the node points of the structure. These loadings were applied using the “Nodal Body Force” loading option in the finite element model.
- Earthquake coefficient = $k_h = 0.4S_{DS} = 0.4 \times 0.755 = 0.302$ (DD-2)
- Earthquake coefficient = $k_h = 0.4S_{DS} = 0.4 \times 0.303 = 0.121$ (DD-3)
- Soil parameters were determined using the soil data. The variation of lateral earth pressures induced by soil load by depth are shown in Figure 4. The variation of surcharge pressures by depth are shown in Figure 5.

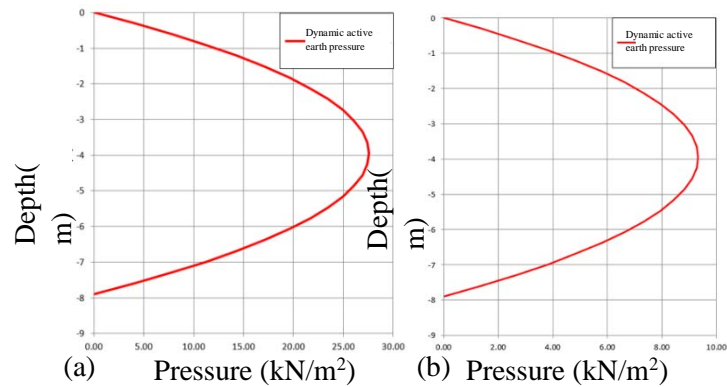


Figure 4. Lateral earth pressures induced by soil load (a) DD-2, (b) DD-3

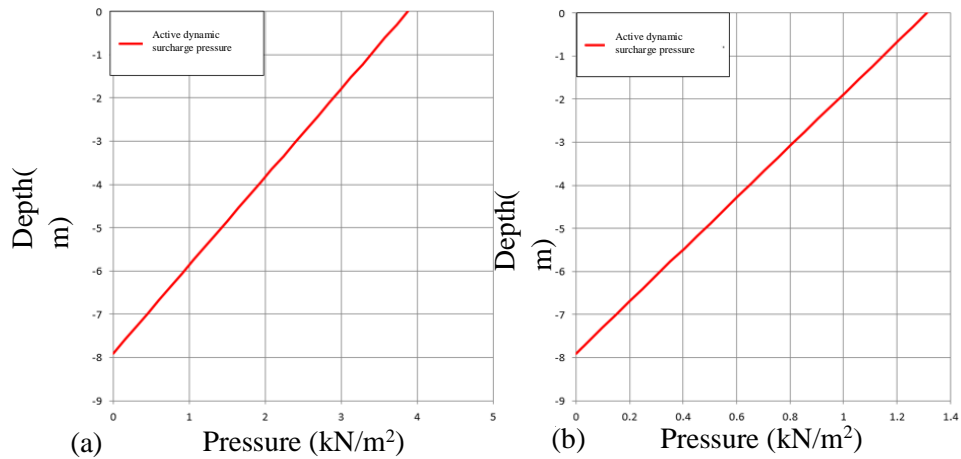


Figure 5. Surcharge pressures induced by soil load (a) DD-2, (b) DD-3

- Cross-sectional details and soil stresses were determined considering the historic documents and previously calculated loads. Seismic effect-induced displacements in the transverse direction were calculated according to TTDY-2020.
- The examined structure was modeled paying attention that the model closely represents its current condition. The 3-D finite elements model of the structure was created using “plate/wall” elements and is given in Figure 2. To represent the interaction between the chimney structure and earth, lateral nonlinear p-y springs were defined in the model. The ground was modeled as p-y springs that can only transmit pressure in the perpendicular direction from each node to the shaft surface (Figure 6).
-

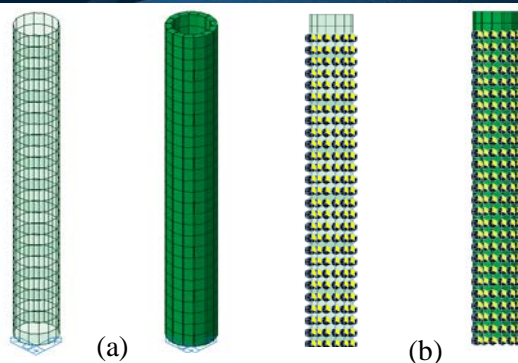


Figure 6. (a) 3-D finite elements model, (b) Spring elements used to model ground

Mechanical properties of concrete were determined by on-site observations as well as SMRGHS 2017 and TBEC 2018. The determined properties are given in Table 3. These mechanical properties were used in the analyses. The type of concrete and its application was determined using the obtained information/documents. The masonry unit type of the load-bearing members of the examined structure were found to comply with the applicable code. No laboratory examination was conducted for the concrete pipe. The uncoated concrete compressive strength of the structural members was taken as approximately 10 MPa.

Table 3. Mechanical properties of concrete pipes

Definition	Value
Masonry unit type	Concrete
Unit Volume Weight, kN/m^3	25
Shaft: characteristic compressive strength, f_k , (MPa)	10
Shaft: initial shear strength, f_{vko} (MPa)	0.7
Shaft: modulus of elasticity, E_{wall} (MPa)	15811

4. ANALYSIS RESULTS

The displacements of the existing structure under vertical loads and the axial forces in the shafts are shown in Figures 7a and 7b. The compressive stresses in the masonry walls resulting from these forces were compared with the allowable stresses for the corresponding masonry wall type, and accordingly, it was checked whether the observed compressive stresses exceed the limit stresses. For a DD-3 ground motion with a 50% probability for exceedance in 50 years, lateral displacements in the current structure induced by vertical loads and earthquakes in the x and y directions are shown in Figures 7c and 7d. Figure 8 shows shear forces observed on the current structure generated by vertical loads and earthquakes in the x and y directions. The analysis results for the current structure and performance evaluations for the DD-3 ground motion are given in Table 4.

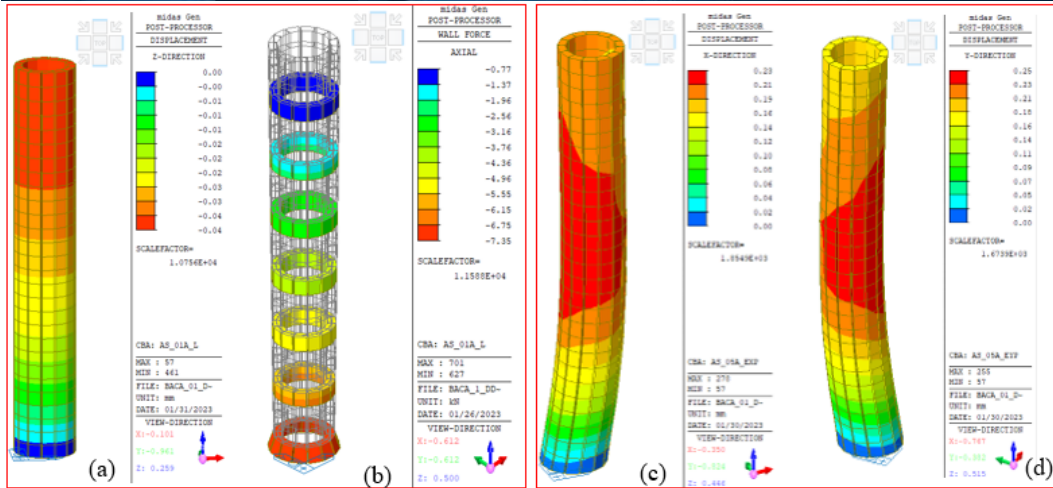


Figure 7. (a, b) Axial forces and displacements in the shafts under vertical loads, (c,d) Lateral displacements induced by earthquake effects in the x and y directions

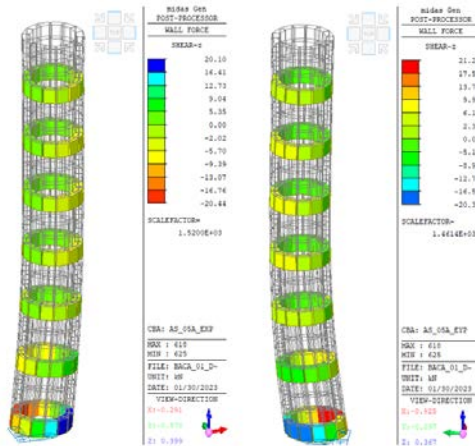


Figure 8. Shear forces generated by earthquake effects in the x and y directions

For a DD-2 ground motion with a 10% probability for exceedance in 50 years, lateral displacements in the current structure induced by vertical loads and earthquakes in the x and y directions are shown in Figure 9a. Shear forces generated by vertical loads and earthquakes in the x and y directions are shown in Figure 9b. The analysis results for the current condition of the structure and performance evaluations for DD-3 and DD-2 ground motions are presented in Table 4.

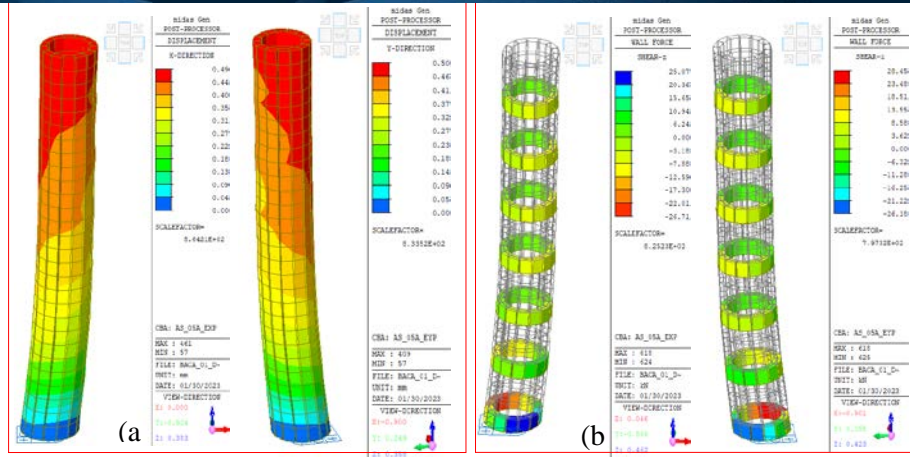


Figure 9. (a) Displacements induced by earthquake effects in the x and y directions, (b) Shear forces generated by earthquake effects in the x and y directions

Table 4. Performance analysis results

Level	Vertical Load-Bearing Elements					Target Performance Level* (CD)	
	(Walls)						
	Ratio of Members Failed in Shear (%)		Total Ratio of Members Failed in Shear (%)		Limit (%)		
	Masonry TBEC (2018) Article 15.8.8						
DD-3	DD-2	DD-3	DD-2		DD-3	DD-2	
01F	13.09	64.27	13.09	64.27	40	✓	✗
02F-07F	0		0		40	✓	

* The performance level of the structure was determined in accordance with SMRGHS 2017.

* The ratios represent the most unwanted direction among the four earthquake directions for each story.

* The structure was modeled by dividing at certain height intervals. So, the stories were hypothetical representations.

5. CONCLUSIONS

This paper presents static calculations and an assessment of a chimney-like ventilation shaft structure. A finite element model of the structure was prepared and performance analyses were conducted on this model. For the current status of the examined structure, axial forces observed on the vertical load-bearing members under static effects (dead loads, lateral earth loads, surcharge loads) were found to be lower than the axial capacity of these members. Therefore, axial strength requirements envisaged in chimney-like structures in the applicable codes were met. It was determined that the examined shaft structure meets the “Controlled Damage” performance for a DD-3 ground motion with a 50% probability for exceedance in 50 years (72-year return period), whereas, failed to meet the “Controlled Damage” performance for a DD-2 ground motion with a 10% probability for exceedance in 50 years (475-year return period).

REFERENCES

- [1]. Ş. Sönmezer, S. Şahin, and İ.A. Kolay, İstanbul'daki Osmanlı su yolu Yapıları, Turkish Studies, Social Sciences, 13-18, 1191-1226, 2018.
- [2]. K. Çeçen, "Osmanlı Suyollarında Künkler, Debi Ölçme Tertibatı ve Su Terazileri", Osmanlı İmparatorluğunun Doruğu 16. Yüzyıl Teknolojisi, İSKİ Yayınları, İstanbul, 55-73, 1999.
- [3]. A.B. Johnson, et al. Modal Analysis of Tall Chimneys Using Finite Element Method. Proceedings of the International Conference on Structural Engineering, Construction and Management, 274-279, 2018.
- [4]. Z. Xiaoyu, S. Qiang, L. Zhuoqiu and W. Yingjun, Dynamic analysis of tall slender structures. Conference on Measuring Technology and Mechatronics Automation (ICMTMA), 2011.
- [5]. Midas Gen (2018) Integrated solution system for building and general structures. MIDAS Information Technology Co.
- [6]. SRMGHS (2017) Seismic risks management guide for historical structures, General Directorate of Foundations, Ankara, Türkiye (in Turkish)
- [7]. TTDY (2020). Principles for the Design of Highway and Railway Tunnels and Other Ground Structures under the Impact of Earthquakes.
- [8]. TBEC (2018) Türkiye Building Seismic Code: Rules for design of buildings under earthquake effect, Official Gazette, Decision no 30364 dated 18.03.2018 (in Turkish)

BIOGRAPHY

Dr. Baris Sayin is currently studying as a Professor in the Department of Civil Engineering at Istanbul University-Cerrahpasa. Dr. Sayin received his BS, MS, and PhD degrees in Civil Engineering from Istanbul University. During the graduate education, he served as a Research Assistant in the Department of Civil Engineering. Between 2009 to 2015, Dr. Sayin worked as a structural engineer in the Department of Construction and Technical Affairs at Istanbul University. In September 2012, Dr. Sayin collaborated with Professor Hamid Saadatmanesh as a Visiting Scholar at the Department of Civil Engineering and Engineering Mechanics, University of Arizona, for a duration of 12 months. Their collaboration focused on insulated FRP-strengthened RC structures and FRP sandwich panels. Dr. Sayin's research interests encompass historical masonry structures, RC buildings, fiber composites, and industrial wastes. He has authored over one hundred articles in the fields of civil engineering and architecture.

Analyzing Seismic Performance of a Timber Structure: Modeling and Analysis Considerations

Ozlem Ustundag¹, Baris Gunes², Baris Sayin³

Abstract

Seismic performance analysis plays a crucial role in assessing the safety and stability of timber structures when subjected to earthquake loads. This study aims to provide an overview of the essential steps and considerations involved in conducting a seismic performance analysis for timber structures. The analysis was carried out utilizing the three-dimensional finite element method, allowing for a comprehensive evaluation of the structural response, including displacement, acceleration, and stress, when subjected to seismic loads. The performance of the building in terms of its ability to withstand seismic forces without sustaining excessive damage or experiencing collapse. The study highlights the importance of understanding the material properties of wood, accurate structural modeling, appropriate seismic load selection, and using appropriate analysis methods. The findings from the seismic performance analysis can provide valuable insights for designing and retrofitting timber structures, enhancing their seismic resilience, and minimizing earthquake-induced damage.

Keywords: Timber structures, Seismic performance analysis, Member checking

1. INTRODUCTION

Timber structures have a long history of widespread use due to their abundance, renewable nature, and aesthetic appeal. However, in seismic-prone regions, understanding the behavior of timber structures under earthquake loads is crucial to ensure their structural integrity and the safety of occupants. Seismic analysis of timber structures involves the assessment of their response to seismic forces, including ground motion, inertial forces, and dynamic effects. By assessing the seismic behavior of timber structures, engineers can develop effective strategies to enhance their seismic resilience and contribute to the development of building codes and standards for timber structures in earthquake-prone regions. Seismic analysis of timber structures has gained significant attention in recent years as there is a growing interest in understanding their behavior and performance under earthquake loads. This section provides a review of studies and research that contribute to the understanding and advancement of seismic analysis techniques for timber structures.

Blaber and Fragiacommo (2011) conducted a comprehensive study on the seismic design of timber buildings in New Zealand, highlighting the importance of considering local ground conditions, building typologies, and design strategies. Their work emphasized the need for appropriate timber connections and the importance of precise detailing to enhance seismic resistance. Frangi and Fontana (2015) presented a thorough examination of seismic design principles for timber structures. Their work discussed the key parameters affecting the seismic behavior of timber buildings, such as the mechanical properties of wood, connection types, and structural configurations. The authors also reviewed various analysis methods, including linear and nonlinear approaches, for assessing the seismic response of timber structures. Kilar and Ceccotti (2018) focused on the seismic performance of tall timber buildings. They investigated the behavior of multi-story timber structures under seismic loads and compared different design strategies and innovative connection systems. Their findings highlighted the need for robust and efficient lateral load-resisting systems to ensure the safety and stability of tall timber structures during earthquakes. Lignos and Fragiacommo (2013) provided a comprehensive review of

¹ Istanbul University-Cerrahpasa, Department of Civil Engineering, Construction Materials Division, 34320, İstanbul, Türkiye. ozlem.ustundag@iuc.edu.tr

² Istanbul University-Cerrahpasa, Department of Civil Engineering, Structural Engineering Division, 34320, İstanbul, Türkiye. bgunes@iuc.edu.tr

³ Corresponding author: Istanbul University-Cerrahpasa, Department of Civil Engineering, Structural Engineering Division, 34320, İstanbul, Türkiye. barsayin@iuc.edu.tr

the seismic design of timber buildings, discussing both traditional and innovative timber construction systems. The authors highlighted the importance of incorporating the dynamic behavior of timber structures and the damping, stiffness, and energy dissipation mechanisms in seismic analysis. They also discussed the challenges associated with modeling and analysis, such as the inclusion of nonlinear behavior and the interaction between timber elements.

In addition to these studies, significant progress has been made in computational modeling techniques for seismic analysis of timber structures. Several researchers have explored the application of finite element analysis (FEA) and numerical simulations to reveal the complex behavior of timber components under seismic loads. These modeling approaches take into account material nonlinearity, connection behavior, and the dynamic response of timber structures, thereby providing valuable insights into their seismic performance. Experimental investigations have also played a significant role in enhancing our understanding of the seismic behavior of timber structures. Researchers have conducted full-scale shaking table tests and laboratory experiments to assess the dynamic response and failure modes of timber elements and connections under various seismic loading scenarios. These experimental studies provide valuable data for developing design guidelines and validating numerical models for seismic analysis of timber structures. In conclusion, the literature review demonstrates the ongoing efforts to enhance the seismic analysis of timber structures. The studies discussed provide valuable insights into the behavior of timber structures under seismic loads, address modeling challenges, and highlight the need for robust design strategies and innovative connection systems to improve the seismic performance of timber structures.

Accordingly, the current paper presents a seismic performance assessment of an existing timber building through on-site observations, laboratory tests, and numeric analysis. Various aspects of the building's seismic response including deformation shapes, base shear forces, relative story drifts, basement shear calculations, slab calculations, and foundation design were examined. Furthermore, checks are conducted on wall cladding members, deflection, and bearing capacity.

2. THE TIMBER STRUCTURE

The properties of the materials used in the examined structure are provided in Table 1. Dead loads were the own weights of the members. Accordingly, the unit weights of the reinforced concrete and C24 timber were considered as 25 kN/m³ and 3.5 kN/m, respectively. Live loads on slabs were estimated to be 2 kN/m². The live load participation factor was accepted as 0.3. The structure falls under the category of “wooden buildings with high ductility level where all the earthquake effects are mitigated by nailed or screwed Oriented Strand Board or plywood wall panels”. Therefore, the load bearing system behavior factor was assumed to be R=4.0 in both directions and the excess strength factor was taken as D=2.0. In accordance with TBEC (2018), the ground motion level was considered DD-2. The behavior spectrum obtained based on these factors is given in Fig. 1.

Table 1. Material properties of the members

Material	Value	Standard
Concrete	C25/30	TS-EN 206 [5]
Steel rebar	S420a	TS708 [6]
Joint plates	S235JR	TS-EN10025-1 [7]
Anchorage	Grade 8.8	TS-EN1993-1-8 [8]
Bolts	Grade 8.8	TS-EN1993-1-8 [8]
Timber	C24	EN-14080 [9]
Timber	Characteristic flexural strength	24 MPa
	Characteristic tensile strength	14 MPa
	Characteristic compressive strength	21 MPa
	Characteristic shear strength	2.5 MPa
	Young modulus (5%)	7400 MPa
Wall panel	Density	610-660 MPa
	Bending strength	120-144 MPa
	MOE bending	13300-16200 MPa
	Shear strength	11.8-14.2 MPa
	Compressive strength	49-60 MPa

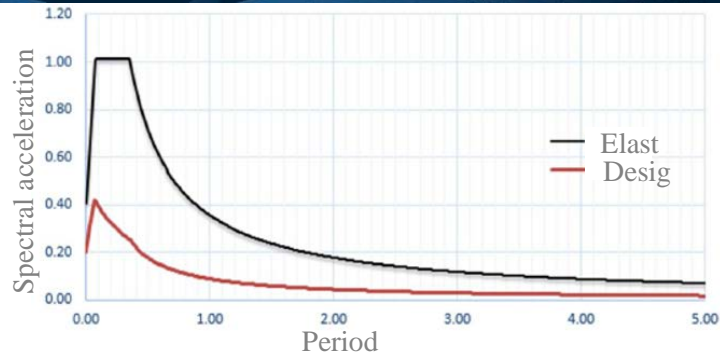


Figure 1. Response spectrum curve

Loading combinations were determined according to Eurocode-1 [10]. In the analysis, 11 strength load combinations and serviceability load combinations were used. The soil parameters were determined based on available documentation and are presented in Table 2. Furthermore, the vertical subgrade reaction coefficient and ground bearing capacity were obtained as $k_v = 14000 \text{ kN/m}^3$ and $q_t = 250 \text{ kPa}$, respectively.

Table 2. Soil parameters

Parameter	Value / Class
Local soil class	ZC
Design earthquake	DD-2
Peak ground acceleration (PGA)	0.347
Peak ground velocity (PGV)	21.62
Short period local ground impact coefficient (S_s)	0.843
1-second period local ground impact coefficient (S_1)	0.237
Short period design spectral acceleration coefficient (S_{DS})	1.012
1-second period design spectral acceleration coefficient (S_{D1})	0.356
Corner period lateral elastic design acceleration spectrum (T_A)	0.07
Corner period lateral elastic design acceleration spectrum (T_B)	0.35
Transition period (T_L)	6 sec
Corner period vertical elastic design acceleration spectrum (T_{AD})	0.02
Corner period vertical elastic design acceleration spectrum (T_{BD})	0.11
Transition period to the constant displacement region for the vertical elastic spectrum	3 sec

3. NUMERICAL ANALYSES

The examined building was a 4-story building including a basement, a ground story, and two normal stories. Structural calculations and checks are presented in this section. The structural analysis was conducted utilizing the 3-D finite elements method (Figure 2). With the data obtained from the structural analysis, the strength and serviceability checks of the structural components as well as the joint checks were made. Structural calculations were performed using Midas GEN [11] software. All columns and beams were modeled as rod elements. On the other hand, shell elements were used to model the shear wall, foundation, and plywood components. The material and geometry were assumed to be linear in the analyses. The timber column material was C24 and the cross sections were rectangular with dimensions of 10×10 , 10×12 , 10×16 , and 5×10 cm. The RC shear materials were C25/30 and S420 with a thickness of 25 cm.

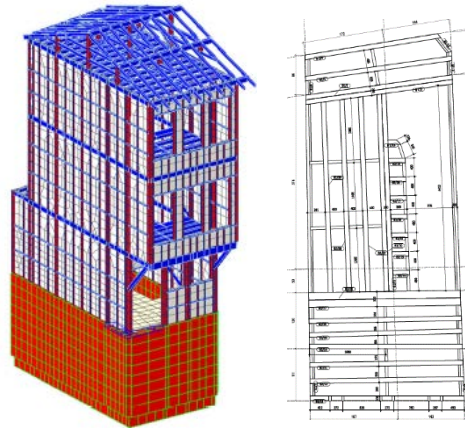


Figure 2. 3D model and plan view of the building

D1 loading represents the weight of members and was automatically calculated by the program. D2 loading represents cladding loads. Accordingly, an OSB cladding load of approximately 0.2 kN/m^2 with a unit volume weight of 6.8 kN/m^3 and a thickness of 2 cm, was considered. A tile roof load of 0.7 kN/m^2 was considered as the coating on the roof surface. A live load of 2.0 kN/m^2 was applied to each story, and the maximum values of these loading effects were considered in the impact calculation. Examples of the loading are shown in Figure 3. The snow load on the roof was taken as 0.75 kN/m^2 . Earthquake analyses were performed using the mode combining method. The earthquake forces obtained were compared with the equivalent base shear forces according to Section 4.8.4 of TBEC 2018 [12]. The load increment coefficient β was set at 0.90. The calculations revealed that an increment of 1.34 in the x direction and 1.36 in the y direction was required. The calculations of these parameters are given below.

4. ANALYSIS RESULTS

The deformation shapes of the building under these loadings are shown in Figure 3. Mode shapes were obtained by modal analysis. The deformation shapes of the building in the dominant modes are given in Figure 4. Accordingly, the rule envisaged in Section 4.8.1.2 of TBEC 2018, “The sum of the effective modal masses corresponding to the base shear force calculated for each mode should not be less than 95% of the total building mass” was satisfied.

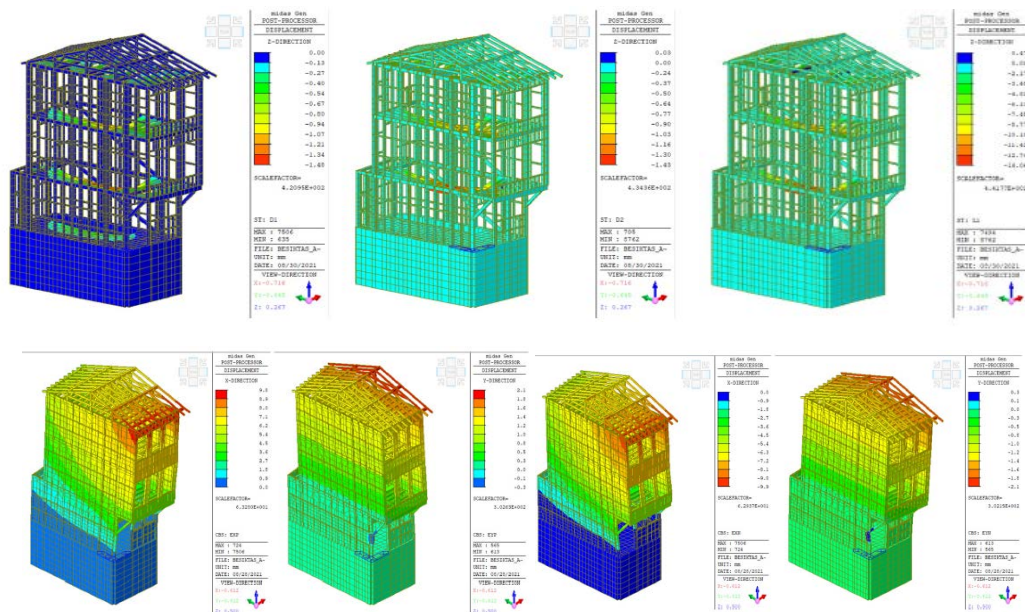


Figure 3. Deformations under D1, D2, L1, Exp, Eyp, Exn, and Eyn Loadings (m)



Figure 4. Deformation shapes in the dominant modes

The timber member checks were carried out according to EN-1995-1 [13] regulation. The characteristic material strengths were determined in accordance with EN-14080 [9] standard. The design strengths were calculated using Equation 2.2.3.2 in EN-1995-1 [13] as below:

$$f_d = k_{mod} \frac{f_k}{\gamma_m} \quad (1)$$

k_{mode} and γ_m values were calculated using Table 3.1.7 in EN-1995-1. The design of the elements under axial tension and moment effects was made according to article 5.1.9 of the applicable code. Similarly, the design of the elements under axial pressure and moment effects was made according to article 5.1.10 of the same code. ACI318 [14] standard was considered in the design of the RC members.

Deflection checks were carried out according to Eurocode 5 [15] criteria. Eurocode 5 allows deflections between $L/150$ and $L/300$ for long-term deflection, depending on the intended use. Accordingly, the checks were conducted for different beam sections. The beams and check results are illustrated in Figure 5.

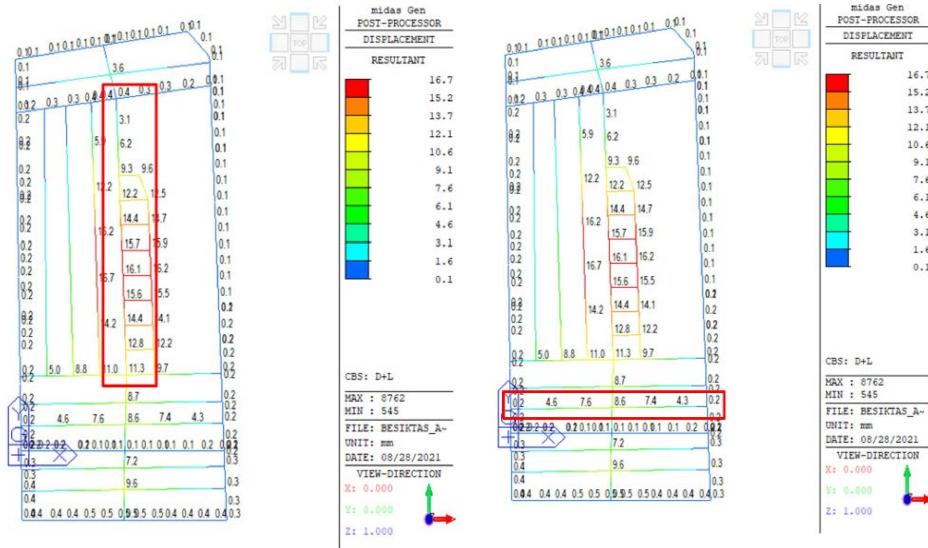


Figure 5. Deformations observed on the main and secondary beams selected for deflection checks (m)

The largest deflection observed was $\delta = 15.7 - 0.4 = 15.3$ mm. The beam length was 4.88 m and the deflection limit for this beam was $4880/300 = 16$ mm. Therefore, the deflection criterion was satisfied. Shear stress examinations were made on the vertical cladding elements of the building. The obtained shear stresses are shown in Figure 6. Accordingly, the highest shear stress observed on the wall claddings was 7.83 MPa, which is lower than the material's shear strength of 11.8 MPa. Displacements under earthquake effects were also assessed. Accordingly, the building was found to comply with the inter-story drift limits.

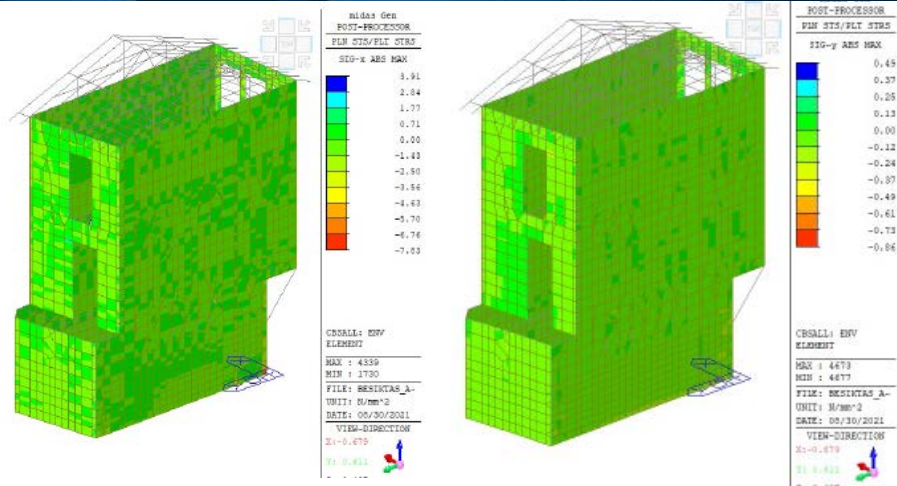


Figure 6. In-plane (left) and out-of-plane (right) shear stresses on wall claddings

The basement of the building has a reinforced concrete shear wall with a thickness of 25. This shear wall includes Ø14 vertical rebars placed at 15 cm intervals and Ø12 lateral rebars placed at 10 cm intervals. The impact capacity ratios for the basement shear wall are shown in Figure 7.

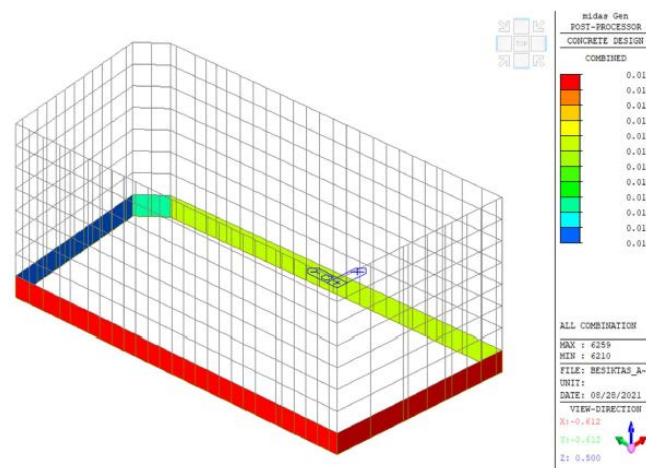


Figure 7. Impact capacity ratios for the basement shear wall

In the RC slabs, a 15-cm-thick continuous foundation was used. For slab rebars, Ø10/200 rebar was used both in the top and bottom sides. The bending impact capacities of the foundation members with this rebar configuration are given in Figure 8.

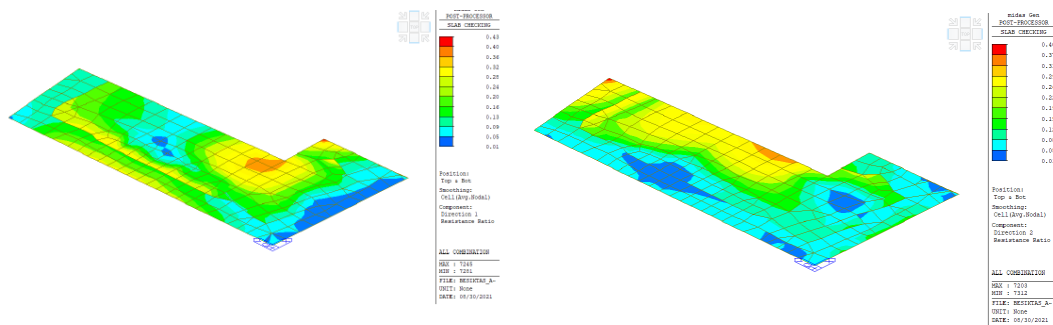


Figure 8. Impact capacity ratios for slab checks: x (left) and y (right) direction

The foundation system of the building consists of a continuous foundation with a thickness of 40 cm. Ø16/150 rebars were utilized for the reinforcement of the foundation, both in the top and bottom sides. The bending

impact capacities of the foundation members with this rebar configuration are shown in Figure 9. The maximum ground pressures observed during the bearing capacity checks are shown in Figure 10. Accordingly, q_0 and q_t were found to be 250 and 118 kPa, respectively. Since $q_0 < q_t$, the ground bearing capacity limit was not exceeded.

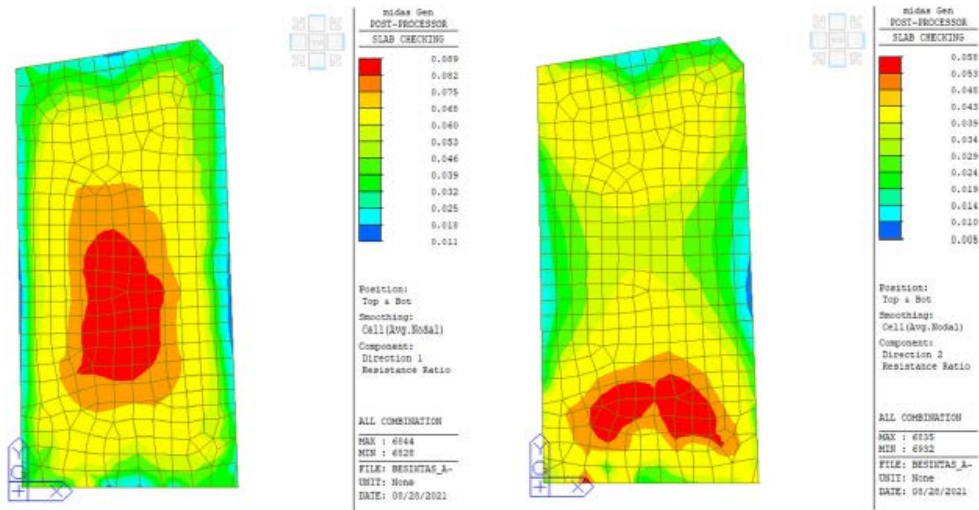


Figure 9. Bending impact capacities of the foundation for the top and bottom sides in the x (left) and y (right) directions

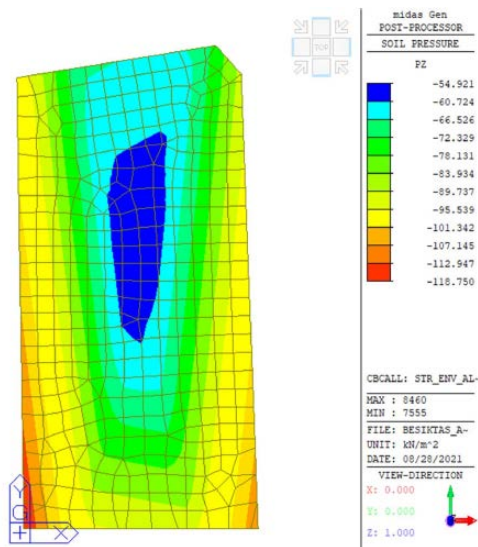


Figure 10. Maximum ground pressures on the foundation (kPa)

CONCLUSIONS

This study presents the modeling of a timber building using a finite elements program and analyses based on the criteria outlined in the local seismic code TBEC 2018. The earthquake performance of the building was evaluated, considering various factors such as deformation shapes, base shear forces, and inter-story drifts. Design calculations were performed for basement shear, slab, and foundation components. Additionally, checks were conducted for deflection, wall cladding elements, and bearing capacity. The analysis results and checks indicated that the building demonstrated sufficient strength in accordance with the provisions of TBEC 2018.

The study provides valuable insights into the seismic analysis of timber structures and establishes a basis for future investigations in this area. However, more advanced analysis methods are still needed to determine the complex behavior of timber structures under seismic loads more accurately. This research aims to address this gap by utilizing advanced computational models and experimental studies to enhance our understanding of the seismic behavior of timber structures and develop effective analysis techniques.

REFERENCES

- [1]. J. Blaber, and M. Fragiaco, "Seismic Design of Timber Buildings in New Zealand," *Bulletin of the New Zealand Society for Earthquake Engineering*, 44(4), 308-326, 2011.
- [2]. A. Frangi, and M. Fontana, "Seismic Design of Timber Structures," *Boca Raton, FL: CRC Press*, 2015.
- [3]. V. Kilar, and A. Ceccotti, "Seismic Performance of Tall Timber Buildings," *Wood Design Focus*, 28(1), 1-6, 2018.
- [4]. D.G. Lignos, and M. Fragiaco, "Seismic Design of Timber Structures: Buildings," In W. E. Baker and C. T. Kelley (Eds.), *Structural Seismic Design Optimization and Earthquake Engineering: Formulations and Applications* (pp. 583-610). Chichester, UK: Wiley, 2013.
- [5]. TS-EN-206, 2014, Concrete - Specification, performance, production and conformity, Turkish Standard Institute, Ankara.
- [6]. TS708, 2010 Steel for the reinforcement of concrete - Reinforcing steel, Turkish Standard Institute, Ankara.
- [7]. TS-EN10025-1, 2006, Hot rolled products of structural steels - Part 1: General technical delivery conditions, Turkish Standard Institute, Ankara.
- [8]. TS-EN-1993-1-8, 2005, Eurocode 3: Design of steel structures - Part 1-8: General rules – Design of connections, Turkish Standard Institute, Ankara.
- [9]. EN-14080, 2014, Timber Structures. Glued Laminated Timber and Solid timber.
- [10]. EN 1991-1-1:2002 Actions on structures- Part 1-1: General actions-Densities, self weight, imposed loads for buildings
- [11]. Midas Gen (2018) Integrated solution system for building and general structures. MIDAS Information Technology Co.
- [12]. TBEC (2018) Türkiye Building Seismic Code: Rules for design of buildings under earthquake effect, Official Gazzette, Decision no 30364 dated 18.03.2018 (in Turkish)
- [13]. EN-1995-1, 2004, Design of Timber Structures, European Committee for Standardization, Brussels.
- [14]. ACI318, 2011, Building Code Requirements for Structural Concrete, American Concrete Institute, MI.
- [15]. EN 1995-1-1: 2004+A1 Design of timber structures. Part 1-1: General-Common rules and rules for buildings

BIOGRAPHY

Dr. Baris Sayin is currently studying as a Professor in the Department of Civil Engineering at Istanbul University-Cerrahpasa. Dr. Sayin received his BS, MS, and PhD degrees in Civil Engineering from Istanbul University. During the graduate education, he served as a Research Assistant in the Department of Civil Engineering. Between 2009 to 2015, Dr. Sayin worked as a structural engineer in the Department of Construction and Technical Affairs at Istanbul University. In September 2012, Dr. Sayin collaborated with Professor Hamid Saadatmanesh as a Visiting Scholar at the Department of Civil Engineering and Engineering Mechanics, University of Arizona, for a duration of 12 months. Their collaboration focused on insulated FRP-strengthened RC structures and FRP sandwich panels. Dr. Sayin's research interests encompass historical masonry structures, RC buildings, fiber composites, and industrial wastes. He has authored over one hundred articles in the fields of civil engineering and architecture.

Seismic Performance Assessment of a Masonry Building with Timber and Reinforced Concrete Slab

Ozlem Ustundag¹, Baris Gunes², Savas Erdem³ Baris Sayin⁴

Abstract

The assessment of the seismic performance of masonry buildings with timber and RC slabs is crucial in determining their structural integrity and resilience to earthquakes. This study employs a methodology that combines laboratory tests and linear performance analysis to evaluate the seismic behavior of a masonry building. The laboratory tests involve cement content assessment and X-ray diffraction (XRD) analyses to understand the material properties. To simulate the seismic behavior, a finite element analysis (FEA) was utilized as part of the linear performance analysis. The FEA model incorporates realistic material properties and geometric details of the masonry components, as well as the timber and reinforced concrete slabs based on the findings from the laboratory tests. The masonry building model was then subjected to seismic loading in accordance with relevant design codes and spectra. Through the linear performance analysis, valuable insights into the behavior and performance of the masonry building under seismic conditions were obtained. The findings help assessing the building's vulnerability to earthquakes and identifying potential retrofitting strategies. The combined approach of laboratory tests and linear performance analysis provides a comprehensive assessment of the seismic behavior of existing masonry buildings. The findings of this study can be applied in seismic performance assessment of similar buildings.

Keywords: Masonry structure, Seismic performance analysis, XRD analysis, Material characterization

1. INTRODUCTION

A significant portion of the existing building stock was constructed using masonry techniques. However, these structures are susceptible to loss of durability and strength over time due to environmental and human factors. In addition, since these structures were built using the construction techniques prevalent during their periods, they may not meet current seismic standards. The reason for this in such structures is the insufficient strength of the carrier system consisting of walls and floors, especially against out-of-plane effects. Supporting the slabs to the walls is one of the most important reasons for this situation. This causes the failure of diaphragm behavior under dynamic effects. In order to eliminate this limitation and to achieve sufficient structural strength, the seismic demand of these structures is reduced or the seismic capacity of the structural elements is increased. The type and level of these interventions can only be determined through seismic analyses.

There are many studies in the literature on seismic analyzes for retrofitting in masonry structures. In these studies, different approaches were utilized in seismic analysis. Akan et al. [1] examined the seismic strength of a mosque. They presented a retrofitting proposal based on the material characteristics and conducted seismic analysis considering three different target earthquakes. They employed different approaches namely, linear, pushover, and kinematic limit analysis. They obtained compressive and tensile stresses as well as story drift ratios with the analyses and compared them with the limit values provided in the applicable codes. Thus, the researchers determined the seismic performance level of the examined structure. In another study, Akcay et al. [2] examined the seismic strength of a 3-story masonry building. The analysis results revealed that the shear

¹ Istanbul University-Cerrahpasa, Department of Civil Engineering, Construction Materials Division, 34320, İstanbul, Türkiye. ozlem.ustundag@iuc.edu.tr

² Istanbul University-Cerrahpasa, Department of Civil Engineering, Structural Engineering Division, 34320, İstanbul, Türkiye. bgunes@iuc.edu.tr

³ Istanbul University-Cerrahpasa, Department of Civil Engineering, Mechanics Division, 34320, İstanbul, Türkiye, savas.erdem@iuc.edu.tr

⁴ Corresponding author: Istanbul University-Cerrahpasa, Department of Civil Engineering, Structural Engineering Division, 34320, İstanbul, Türkiye, barsayin@iuc.edu.tr

stresses exceed the limit values given in the code. Therefore, they proposed strengthening practices for walls and slabs aiming to increase, especially out-of-plane strength of the building. Gunes et al. [3, 4] assessed the seismic performances of a vaulted ruin and a masonry building constructed over this structure using modal, pushover, nonlinear, and kinematic limit analysis methods. They presented a strengthening proposal including a steel system inside the structure and wall jacketing. Sayin et al. [5] proposed a retrofitting practice including conventional and nonconventional techniques to strengthen walls and slabs of a masonry building which was determined to have insufficient strength with linear seismic analysis. Guneş et al. [6] presented a revival proposal for a ruined mosque. They conducted separate analyses for the main section and minaret of the mosque. They conducted analyses considering three different target earthquakes using linear, pushover, and kinematic limit approaches and compared the obtained results with the limit values given in the code. Shariq et al. [7] assessed the seismic performance level of a masonry building. The authors preferred the linear time history method for analysis. They compared the maximum principal stresses with the corresponding values envisaged in the code. Milani [8] examined failure mechanisms and failure loads of a masonry building with kinematic limit analysis. Thus, the researchers determined the in-plane and out-of-plane collapse capacities of the building. Betti and Galano [9] utilized the pushover method and assessed the seismic behavior of a masonry structure. They compared the obtained results with those obtained by the kinematic limit analysis approach.

In the current study, the seismic performance of an existing masonry building was assessed through field studies, laboratory tests, and numerical analysis. Static and kinematic limit analyses of the building were performed using MIDAS [10] software.

2. FIELD SURVEY AND IN-SITU TESTS

The facade views and plan of the examined building are shown in Figure 1. The building consists of a basement, a ground, and 2 normal stories. The vertical load bearing system of the building is composed of masonry structural members. The load-bearing system of the building was supported by reinforced concrete (RC) lateral peripheral ties on the ground floor. The slabs consisted of timber and RC materials. The building's floor area was approximately 73 m² (ground floor).



Figure 1. Facade and plan views of the examined building

On-site inspections revealed the presence of cracks in certain load-bearing walls with moisture and dampness on the wall surfaces. Furthermore, some collapses were observed on the timber slab system, and some of the slabs were broken. Spills caused by extensive corrosion were observed on the covers of RC slabs. Some of the damages observed on the building are shown in Figure 2.



Figure 2. Current damages on the building

The type and application method of the load-bearing masonry members were determined either by removing the plaster layer on the load-bearing walls or through visual examinations. The mechanical properties of the masonry members were also determined by visual inspections in accordance with the guidelines outlined in the relevant codes. Some images related to the examinations conducted on the masonry members are shown in Figure 3.



Figure 3. Masonry load bearing members

The mechanical properties of the masonry walls determined following the guidelines of “In-situ Material Tests”, “SMRGHS 2017 [11], and TBEC 2018 [12] are shown in Table 1. These mechanical properties were used in the seismic analyses. It was found that the masonry unit type of the load-bearing masonry members in the examined structure complied with the relevant regulation.

Table 1. Mechanical properties of masonry walls

Definition	Value / Class
Masonry unit type	Stone & Solid Brick
Masonry unit group	Group I
Unit Volume Weight, kN/m ³	21
Characteristic compressive strength of the walls, MPa	2.8
Initial shear strength of the walls, MPa	0.1
Tensile strength of the walls, MPa	0.15
Modulus of elasticity of the walls, MPa	2000
Shear modulus of the walls, MPa	330

3. NUMERICAL ANALYSES

The examined structure currently has a load bearing system comprised of masonry + RC (lateral peripheral tie) with mostly masonry members. The seismic performance of the structural system has been examined through linear performance analysis in accordance with SMRGHS 2017. The analysis results and evaluations are presented below. Considering the "Earthquake Design Class" and Article E22 of the TBEC-2018, the Building

Height Class (BYS) should be 8. Based on the Building Height Class and Earthquake Design Class, the allowed building height should be $H_N \leq 7$ m. However, this condition is not required for existing buildings. The parameters provided in this section were not used in the performance analysis and are given for informational purposes only, in accordance with the TBEC-2018.

3.1 Linear analysis

In this section, the static analysis model developed for the linear analysis of the building is explained. Also, the target performance according to TYDRYK-2017 and analysis results are presented. The examined building was modeled to represent its current condition approximately. The 3-D finite element model of the building is shown in Figure 4. The finite element model was created using the “beam/column” and “plate/wall” elements. Displacements on the building and axial forces on the walls induced by vertical loads (dead and live loads) were illustrated in Figure 5. The compressive stresses on masonry walls generated by these forces were compared with the allowed limit values. Thus, it was checked whether the compressive stresses exceed the limit stresses. For the seismic assessment of historic buildings, SRMGHS 2017 is used. This code envisages different performance criteria based on the importance level of the building. The performance analysis parameters used for the examined building are presented in Table 3.

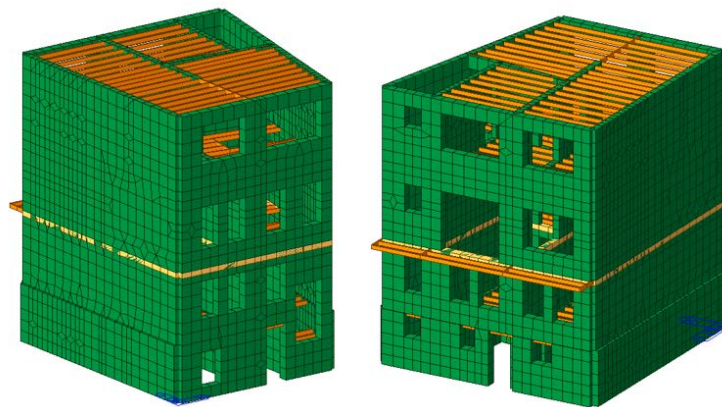


Figure 4. The 3-D finite elements model of the building

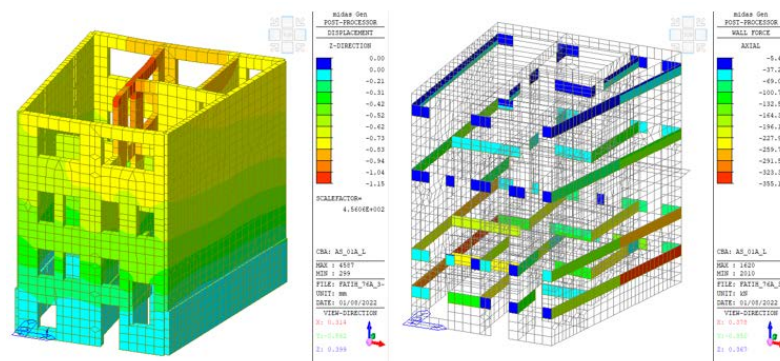


Figure 5. Displacements on the building and axial forces on the walls induced by vertical loads

Table 3. Performance analysis parameters

Parameters	Value / Class
The ground motion level and corresponding target performance	DD-2 and Controlled Damage
Performance analysis method	Linear
Inter story drift limit	0.7% for Controlled Damage
Building Information Level and Factor	Limited, 0.75
Reduction factor for earthquake load, Ra	Ra=3 for DD-2

Lateral displacements on the building under vertical loads and earthquake effects in the x and y directions for an earthquake with a 10-percent probability of exceedance in 50 years (DD-2 ground motion level) are illustrated in Figure 6. The comparison of the inter-story drifts with the target performance limits is shown in Table 4. Based on the obtained results, the inter-story drift ratios of the building meet the "Controlled Damage" performance criteria for a DD-2 ground motion level.

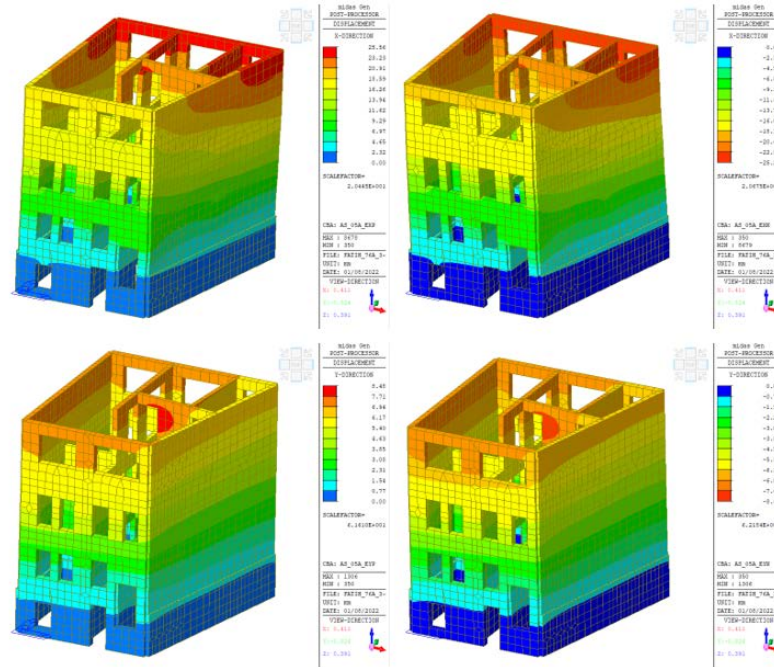


Figure 6. Lateral displacement under earthquake loads for x and y directions

Table 4. The checking of relative story drift ratios

Story	Displacement ΔD , (mm)		Story drift ratio, $\Delta D/H$		Limit value	Result
	x	y	%	%		
Basement	2.95	1.25	0.14	0.06	0.70 (CD)	✓
Ground	8.59	2.76	0.32	0.10	0.70 (CD)	✓
First	9.19	2.92	0.31	0.10	0.70 (CD)	✓
Second	5.66	2.93	0.21	0.11	0.70 (CD)	✓

Figure 7 displays the shear forces acting on the building under vertical loads and earthquake effects in the x and y directions, specifically for an earthquake with a 10-percent probability of exceedance in 50 years (DD-2 ground motion level). The ratios of the shear forces on the structural elements that failed in shear to the total shear force on the corresponding story are given in Table 5. According to the data presented in this table, the building did not satisfy the "Controlled Damage" performance level in terms of shear forces for a DD-2 earthquake.

Table 5. Results of performance analysis

Story	The ratio of the shear forces on the structural elements that failed in shear to the total shear force, %			Target Performance* (CD)
	Masonry	RC	Total	
Basement	86.52	-	86.52	×
Ground	93.38	-	93.38	×
First	94.89	-	94.89	×
Second	78.38	-	78.38	×

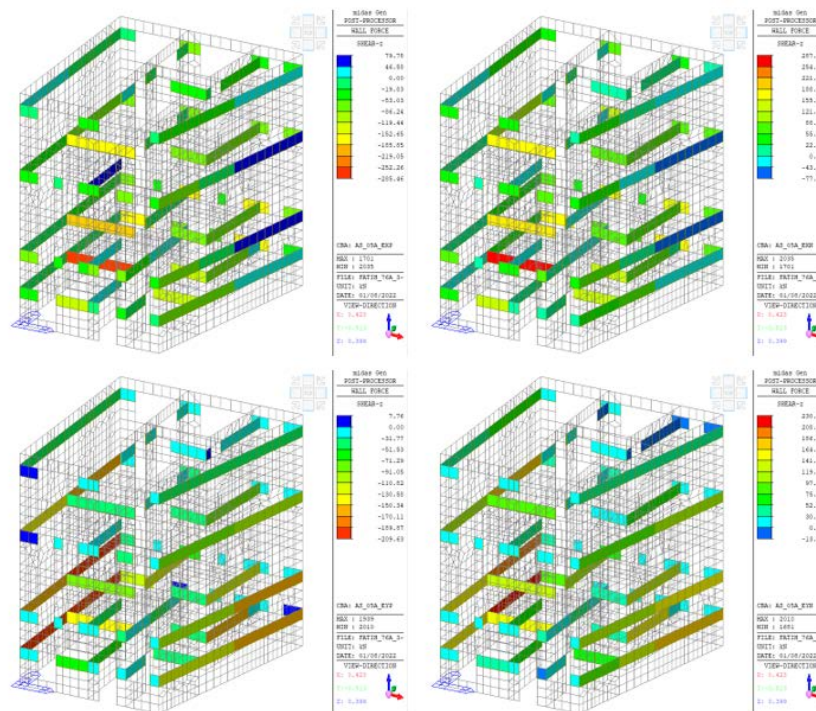


Figure 7. Shear forces on the building under earthquake effects in the x and y direction

3.2 Material analyses

To conduct material analyses, samples were collected from three distinct locations within the building. These samples consisted of mortar and facade decorations. The mortar samples were extracted from the stair hall, ground floor masonry mortar, and layers of plaster on the walls within the same area. On the other hand, the facade decoration samples were obtained from the exterior facade. To determine the presence and dosage of cement in the mortar samples, the maleic acid extraction method described in the TS 2518 standard [13] was employed. Initially, the mortar samples were carefully sieved through a 4.75 mm mesh sieve. Subsequently, the materials were thoroughly mixed to obtain a homogeneous mixture. Approximately 450 g of sample was obtained using the quartering method. The samples were then further processed by grinding, sieving through a 1.18 mm sieve, and subsequently dried in an oven until their mass stabilized.

To determine the chemically bound water fraction (L_c , %), approximately 10 g of the dried sample was placed in an oven set at 520 ± 5 °C for approximately 3 hours. After this period, the sample was weighed and the chemically bound water fraction was calculated. After this procedure, the percentage of insoluble residue (R , %) was determined by subjecting a 20 g sieved sample to a 15% maleic acid solution. The resulting insoluble residue was measured to determine the percentage. To calculate the percentage of cement (C_m , %), the values

of the chemically bound water fraction and insoluble residue were subtracted from 100. Oven-dry density of the mortar samples (D_{dry} , kg/m^3) was determined for cement dosage assessment and calculations were made using Eq. 1. The obtained results indicated that the mortar samples collected from different locations were cement based, with an approximate cement dosage of $117 kg/m^3$.

$$\text{Cement dosage} = (C_m \times D_{dry}) / 100 \quad (1)$$

Table 6. Cement dosages in the masonry and plaster mortar samples

Sample	Chemically bound water (L_c , %)	Insoluble residue (R , %)	Cement amount (C_m , %)	Oven-dry density (D_{dry} , kg/m^3)	Cement dosage (kg/m^3)
1	3.70	88.40	7.90	1790.8	141
2	4.10	89.20	6.70	1794.6	120
3	3.70	91.30	5.00	1820.3	91
4	4.40	89.30	6.30	1802.8	114
Average	3.98	89.55	6.48	1802.1	117

X-ray diffraction analysis (XRD) is one of the most effective advanced characterization methods for materials with crystalline phases. During this analysis, each atom produces a distinctive diffraction pattern when exposed to radiation. Rietveld determined the intensity of each element at any point along the XRD curve using the least squares method (Figure 8). The intensities of these elements are calculated using the Bragg Equation (Eq. 2).

$$2d\sin\theta = n\lambda \quad (2)$$

Accordingly, mortar samples collected from the exterior decorations were pulverized and sieved through a 75-micron sieve. Around 10 mg of the sample was taken from the fraction that pass-through sieve and XRD analysis was carried out with a Bruker diffractometer.

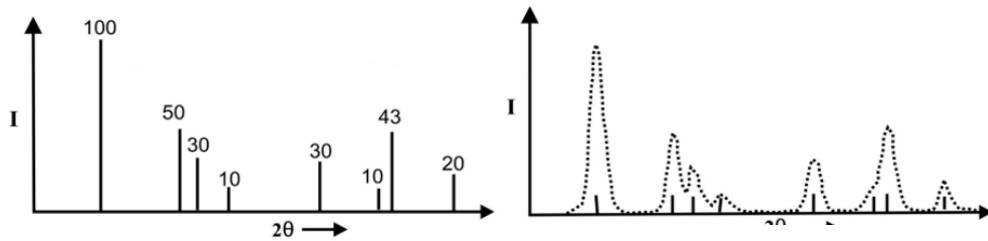


Figure 8. Rietveld XRD Data

The peaks on the XRD curve of the exterior decoration samples were examined using the Match program (Figure 9). The presence of Ca, Al, and Fe-containing compounds as well as quartz particles suggested a binder composition including cement. Furthermore, small bumps observed in the XRD plot indicate the presence of amorphous silica in the samples.

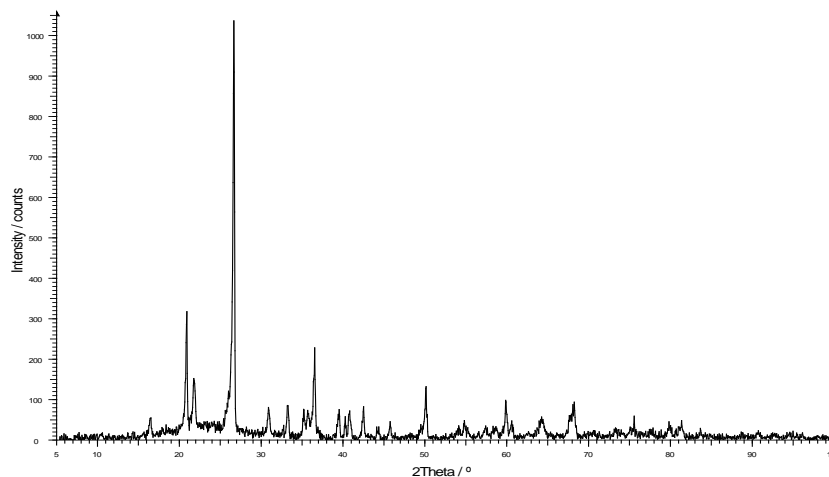


Figure 9. XRD curve of the exterior decoration sample

CONCLUSIONS

In this study, a seismic performance assessment of a masonry building with timber and reinforced concrete slabs was presented. Additionally, structural and non-structural material compositions were examined. The key findings of the study can be summarized as follows:

Considering a target performance level of “Controlled Damage” for a DD-2 ground motion in accordance with the local code, SMRGHS 2017;

- The axial forces on the masonry load bearing members under vertical loads were observed to exceed their axial capacity.
- The ratios of the shear forces on the structural elements that failed in shear to the total shear force on the corresponding story were found to exceed the limit values.
- Inter-story drift ratios of the building were found to meet the limit values. In other words, the drift ratios did not exceed 0.7% at any story which is the limit value corresponding to the “Controlled Damage” performance level.

It was therefore concluded that the examined building does not meet the requirements of the “Controlled Damage” performance level for an earthquake with a 10-percent probability of exceedance in 50 years (DD-2 ground motion level).

The key findings of the material analysis conducted on the samples collected from various parts of the building are listed below.

- The results of the tests conducted using the maleic acid extraction method on masonry and plaster mortar samples collected from the ground floor and stair hall revealed that the mortar samples were cement based. The average cement dosage in masonry mortars was lower compared to plaster mortars. Additionally, the average cement dosage for all samples was calculated to be 117 kg/m³.
- Visual examinations and XRD analysis performed on the exterior decoration samples showed that these decorations were made on a cement-based plaster material. The presence of Ca, Al, and Fe in the material composition also suggested that these decorations were composite materials including cement. Advanced chemical analyses such as petrographic and FT-IR spectrum to be performed on thin-section elements can provide more precise and detailed results.

Based on the test and chemical analysis results conducted on the samples, it was determined that both the masonry and plaster mortar of the examined building were predominantly cement-based. Moreover, the analysis confirmed that the exterior elements were decoration materials composed of cement-based plaster.

REFERENCES

- [1]. A.E. Akan, G.Ç. Başok, A. Er, H.T. Örmecioglu, S.Z. Koçak, T. Cosgun, O. Uzdil and B. Sayin, “Seismic evaluation of a renovated wooden hypostyle structure: A case study on a mosque designed with the combination of Asian and Byzantine styles in the Seljuk era (14th century AD)”, *Journal of Building Engineering*, 2021.
- [2]. C. Akcay, T.S. Bozkurt, B. Sayin and B. Yildizlar, “Seismic retrofitting of the historical masonry structures using numerical approach,” *Construction and Building Materials* 113, 752–763, 2016.
- [3]. B. Gunes, T. Cosgun, B. Sayin, O. Ceylan “Structural rehabilitation of a Middle Byzantine ruin and the masonry building constructed above the ruin. Part I: The ruin”. *Engineering Failure Analysis* 105, 503–517, 2019.
- [4]. B. Gunes, T. Cosgun, B. Sayin and O. Ceylan “Structural rehabilitation of a Middle Byzantine ruin and the masonry building constructed above the ruin. Part II: The building. *Engineering Failure Analysis* 105, 527-544, 2019.
- [5]. B. Sayin, B. Yildizlar, C. Akcay, and B. Gunes, “The retrofitting of historical masonry buildings with insufficient seismic resistance using conventional and non-conventional techniques” *Engineering Failure Analysis*, 97, 454-463, 2019.
- [6]. B. Gunes, T. Cosgun, B. Sayin, O. Ceylan, A. Mangir, G. Gumusdag “Seismic assessment of a reconstructed historic masonry structure: A case study on the ruins of Bigali castle mosque built in the early 1800s”. *Journal of Building Engineering* 39, 2021.
- [7]. M. Shariq, S. Haseeb, M. Arif, “Analysis of existing masonry heritage building subjected to earthquake loading,” *Procedia Engineering* 173 (2017) 1833–1840.
- [8]. G. Milani, P.B. Lourenco, A. Tralli, “3D homogenised limit analysis of masonry buildings under horizontal loads,” *Engineering Structures*. 29, 3134–3148, 2007.
- [9]. M. Betti, L. Galano, “Seismic analysis of historic masonry buildings: the vicarious palace in Pescia (Italy),” *Buildings* 2 (2012) (2012) 63–82.
- [10]. Midas Gen (2018) Integrated solution system for building and general structures. MIDAS Information Technology Co.
- [11]. SRMGHS (2017) Seismic risks management guide for historical structures, General Directorate of Foundations, Ankara, Türkiye (in Turkish)
- [12]. TBEC (2018) Türkiye Building Seismic Code: Rules for design of buildings under earthquake effect, Official Gazette, Decision no 30364 dated 18.03.2018 (in Turkish)



[13]. TS 2518 Turkish Standard, Ankara, Turkey.

BIOGRAPHY

Dr. Baris Sayin is currently studying as a Professor in the Department of Civil Engineering at Istanbul University-Cerrahpasa. Dr. Sayin received his BS, MS, and PhD degrees in Civil Engineering from Istanbul University. During the graduate education, he served as a Research Assistant in the Department of Civil Engineering. Between 2009 to 2015, Dr. Sayin worked as a structural engineer in the Department of Construction and Technical Affairs at Istanbul University. In September 2012, Dr. Sayin collaborated with Professor Hamid Saadatmanesh as a Visiting Scholar at the Department of Civil Engineering and Engineering Mechanics, University of Arizona, for a duration of 12 months. Their collaboration focused on insulated FRP-strengthened RC structures and FRP sandwich panels. Dr. Sayin's research interests encompass historical masonry structures, RC buildings, fiber composites, and industrial wastes. He has authored over one hundred articles in the fields of civil engineering and architecture.

Nonlinear FEA Analysis for Seismic Performance Assessment of an RC Shear Wall-Frame Building

Ozlem Ustundag¹, Baris Gunes², Baris Sayin³

Abstract

Nonlinear performance analysis using finite element analysis (FEA) is an essential tool for assessing the seismic performance of existing reinforced concrete buildings with both frame and shear wall systems. This study aims to conduct a comprehensive nonlinear performance analysis to evaluate the seismic behavior of an existing RC building. A FEA model was developed based on the original building's as-built drawings and specifications, incorporating realistic material properties and geometric details. Nonlinear material models are employed to accurately simulate the behavior of RC elements under seismic loading, taking concrete cracking, steel yielding, and degradation of material properties into account. The building model was subjected to seismic loading in accordance with the relevant design codes and spectra. The performance of the building was assessed using various seismic response parameters, including inter-story drift, plastic hinge formation, and global structural behavior. The nonlinear performance analysis provides valuable information about the structural behavior and performance of the building under different seismic demands. The results of the analysis can be used to assess the seismic vulnerability of existing RC buildings, identify potential weaknesses or deficiencies in the structural system, and develop appropriate retrofitting strategies. The findings are believed to contribute to the development of guidelines for seismic retrofitting of similar buildings, leading to improved seismic resilience and safety in high seismic-prone regions. In conclusion, the nonlinear performance analysis through FEA is a powerful tool for seismic performance assessment of RC shear wall-frame buildings.

Keywords: RC building, Seismic performance analysis, Nonlinear analysis

1. INTRODUCTION

Reinforced concrete structures are often favored due to their advantages in terms of construction time and ease of construction compared to other building systems. However, it is important to assess the existing structural safety of these buildings due to several factors including concrete strength degradation over time, reduction in strength and durability due to rebar corrosion, or revisions in seismic codes. To accurately determine the seismic behavior of a structure, it is crucial to accurately identify its existing characteristics. This involves determining the material parameters and locating the load-bearing members of the building precisely. To develop an accurate structural model, building characteristics should be defined as closely to reality as possible. Hence, the behavior of the structure under earthquake effects can be determined reliably and a retrofitting strategy can be developed that the structure needs.

In the relevant literature, several studies were reported to assess the seismic performance of reinforced concrete structures. Chaulagain et al. [1] conducted a study on the seismic behavior of an RC structure. The building underwent static pushover analysis using various load patterns. Additionally, the authors conducted adaptive pushover analysis and non-linear dynamic time history analysis. Mosleh et al. [2] introduced a methodology for assessing the seismic performance of structures. The study focused on the analysis of two old structures using pushover and time history analyses in both longitudinal and transverse directions. Various earthquakes with different return periods were considered in the seismic analyses, and the resulting seismic demands were compared to the limits specified in the seismic codes. Halder and Paul [3] assessed the seismic performance of

¹ Istanbul University-Cerrahpasa, Department of Civil Engineering, Construction Materials Division, 34320, İstanbul, Türkiye. ozlem.ustundag@iuc.edu.tr

² Istanbul University-Cerrahpasa, Department of Civil Engineering, Structural Engineering Division, 34320, İstanbul, Türkiye. bgunes@iuc.edu.tr

³ Corresponding author: Istanbul University-Cerrahpasa, Department of Civil Engineering, Structural Engineering Division, 34320, İstanbul, Türkiye. barsayin@iuc.edu.tr

a low-rise RC structure. The study involved conducting nonlinear static analysis to derive the capacity curve of the structures. The findings revealed that the building experienced varying degrees of damage, ranging from moderate to severe when exposed to seismic effects. Melani et al. [4] conducted a study on the seismic assessment of low-rise RC structures. Their examinations focused on applying capacity design approaches that to assess shear and flexural capacities. Sobaih and Nazif [5] examined the seismic performance of existing reinforced concrete structures. They proposed an approach that is intended to have a notable impact on the seismic behavior of such structures. Ghojarah et al. [6] performed nonlinear static and dynamic analyses on reinforced concrete frames. They employed a probabilistic methodology, which involved using a substantial number of artificially generated ground motion records as input motion for the structure. Yakut [7] introduced a methodology for assessing the seismic performance of existing RC structures. The method categorizes the structures into two groups namely; safe, suggesting that the building is unlikely to experience significant damage, and unsafe, suggesting that the building may not meet the required life safety performance level. El-Betar [8] examined the seismic vulnerability of buildings and proposed an approach to assess the seismic behavior of existing RC buildings. They employed pushover analysis to assess the structural performance of the building. Hosseini et al. [9] investigated the achievement of life safety performance in RC buildings. The results indicate that the performance of the buildings either surpasses the required life safety level or reaches a state of collapse under certain earthquake events.

In this study, the seismic performance of an existing RC building was determined through field studies, lab tests, and numerical simulation. Firstly, fieldwork and laboratory tests were conducted to identify the concrete strength and rebar layout. Secondly, nonlinear static analyses of the 3D finite element model of the examined building were performed using Midas Gen [10] software, based on the results of the field studies and material tests.

2. THE EXAMINED BUILDING

The examined building consists of a basement, ground, and three normal stories (Figure 1). The floor area of the building is approximately 226 m² (ground floor). The story heights are 2.58 m on the basement and ground floors and 2.53 m on the normal floors. The main carrier system of the building is a reinforced concrete frame-shear system.



Figure 1. Facade and bird's eye view of the building

The foundation system of the building consists of continuous foundations with transverse beams in the x and y directions. There are continuous foundation beams of various sizes in the building. Continuous foundation beams are fixed to each other with 30×40 cm transverse beams. Continuous foundation beams include Ø12, Ø16, and Ø22 rebars as well as Ø10 and Ø12 stirrups at 14~22 cm intervals. There are RC shear walls in the facades of the basement floor.

During on-site examinations, swelling, plaster spills, and cracks were observed on some RC columns, shear walls, and beams due to moisture and humidity. In addition, covers were peeled off on certain structural elements, and corrosion damage was detected on their rebars. Particularly in the basement, extensive damages indicative of corrosion were identified. Figure 2 displays some of these damages.



Figure 2. Current damages in the building

In order to determine the concrete compressive strength and reinforcement bars, laboratory tests were conducted in accordance with the guidelines specified in the local seismic code, TBEC 2018 [11]. For this purpose, the concrete compressive strengths were determined by taking core samples from a total of 24 vertical load-bearing elements and subjecting them to testing. Two different methods were employed to determine the reinforcement bars in the structural members. The first method utilized non-destructive rebar detection, while the second method involved observational rebar detection by scraping the concrete cover. Accordingly, non-destructive rebar detection was carried out on a total of 26 vertical load-bearing members from all floors. Additionally, the observational rebar detection method, involving scraping the concrete cover, was performed on 24 vertical load-bearing members from all floors. By scraping the concrete cover, $\varnothing 14$ and $\varnothing 16$ vertical rebars, as well as $\varnothing 6$ and $\varnothing 8$ stirrups at intervals of 18 to 36 cm were identified in the columns. In the shear walls, $\varnothing 10$, $\varnothing 12$, $\varnothing 14$, and $\varnothing 16$ vertical rebars, along with $\varnothing 6$ and $\varnothing 8$ lateral rebars at intervals of 18 to 57 cm, were determined.

Using both destructive and non-destructive rebar detection methods, it was determined that the vertical rebars and stirrups were plain (flat) bars of type S220. Additionally, it was observed that deformed rebars were used in some of the vertical load-bearing members, while plain bars were used in others. Due to the lack of regular distribution, it was assumed that the vertical rebars in the columns were plain (S220).

3. ANALYSIS MODEL

The examined building was modeled using finite elements software and seismic performance analysis was conducted on this model. The 3D statical analysis model of the building and floor plans are given in Figures 3 and 4, respectively.

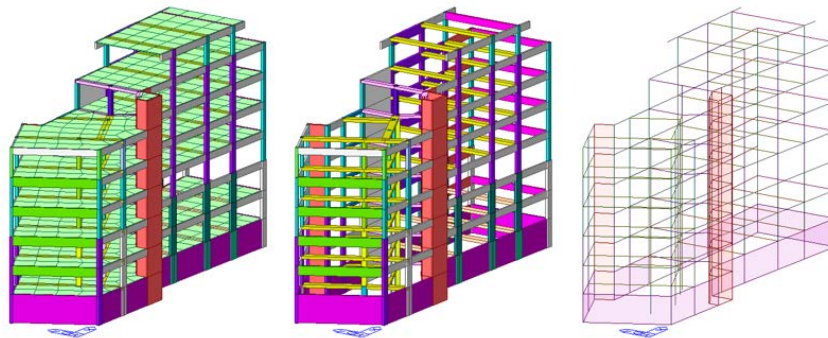


Figure 3. 3D finite element model of the building

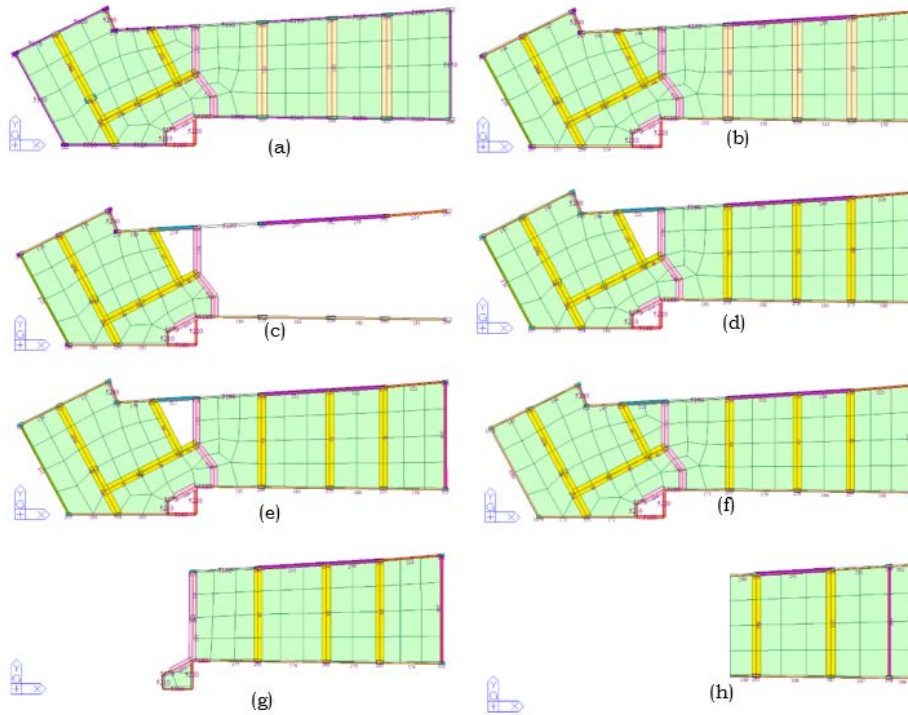


Figure 4. Floor plans in the analysis model (a) Basement, (b) Lower Ground Floor, (c) Upper Ground Floor, (d) Entresol, (e) First, (f) Second, (g) Third, (h) Penthouse

ANALYSIS RESULTS

Base shear–peak displacement and demand spectrum–capacity diagrams of the building when exposed to an earthquake with a 10% chance of exceedance in 50 years (DD-2 ground motion) are given in Figure 5.

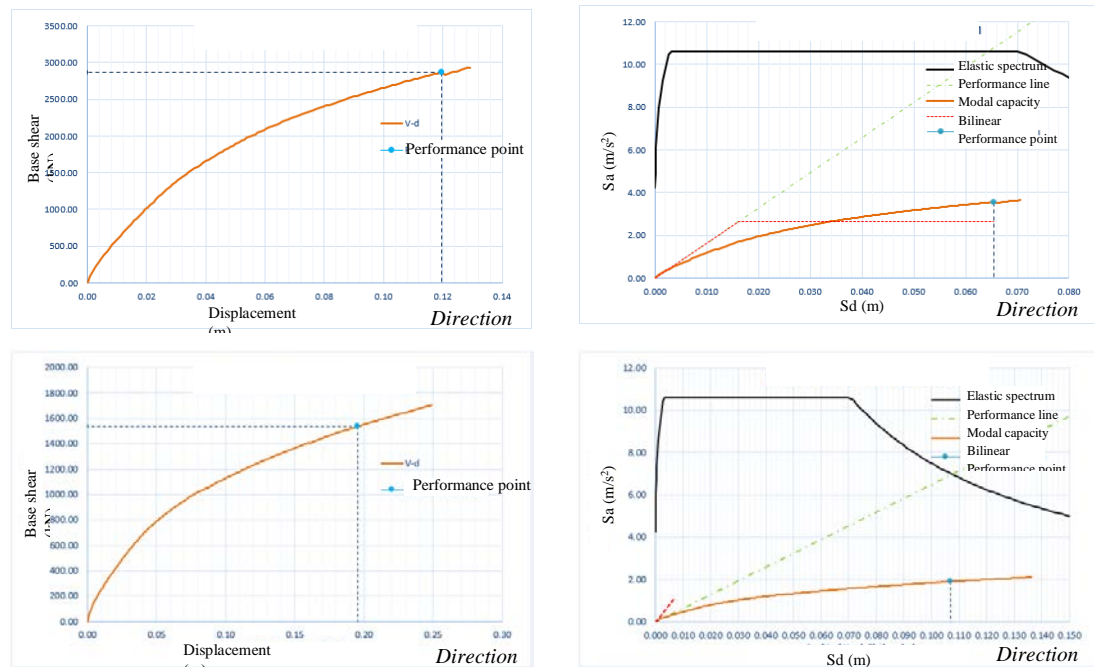


Figure 5. Base shear–peak displacement and demand–capacity diagrams

Lateral displacements on the building under earthquake effects are illustrated in Figure 6. Analysis results and performance assessment of all stories for vertical and lateral load bearing members are presented in Tables 1 and 2, respectively.

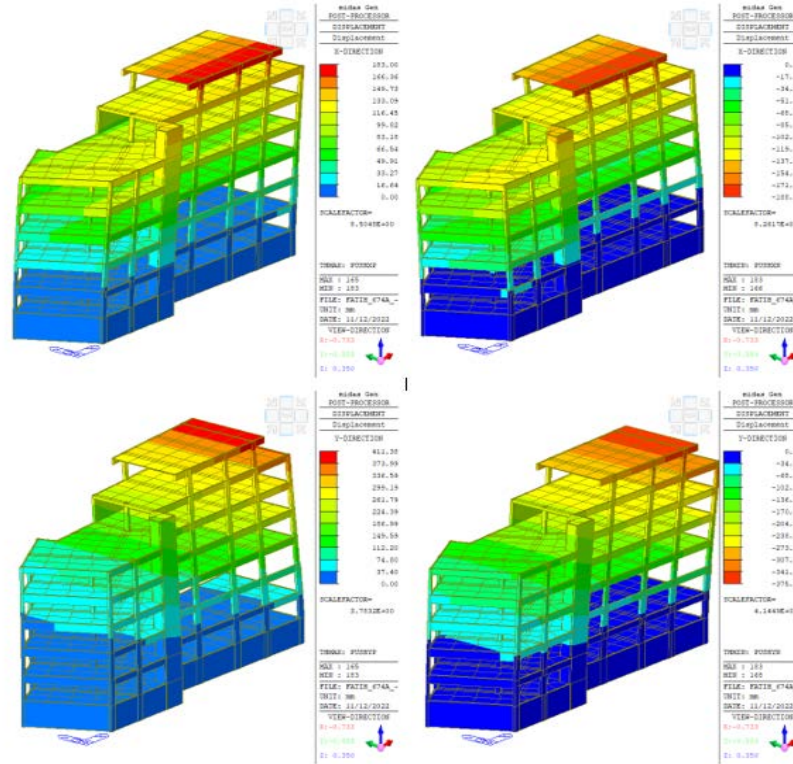


Figure 6. Lateral displacements on the building under earthquake effects in the x (up) and y (down) directions.

Table 1. Performance analysis results for vertical load bearing members

Story	Vertical Load Bearing Members (Columns)			Target Performance Level (CD)
	Article 15.8.4 (b) Strain Check	Article 15.8.4 (c) Strain Check	Article 15.8.4 Brittleness Check	
	RC	RC	RC	
BF	✓	✓	✓	✓
LGF	✗	✓	✗	✗
UGF	✗	✓	✗	✗
Entr.	✗	✓	✗	✗
1	✗	✓	✗	✗
2	✗	✓	✗	✗
3	✗	✓	✓	✗
Penth.	✗	✗	✓	✗

Table 2. Performance analysis results for lateral load bearing members

Story	Lateral Load Bearing Members (Beams)		Target Performance Level (CD)
	Article 15.8.4 (a) Strain Check	Article 15.8.4 Brittleness Check	
	RC	RC	
BF	√	√	√
LGF	×	√	×
UGF	×	×	×
Entresol	×	√	×
1	×	√	×
2	×	√	×
3	×	√	×
Penthouse	√	√	√

CONCLUSIONS

In this study, a building consisting of a basement, ground, and three normal stories was modeled with the finite elements software and analyzed in accordance with the criteria given in the local code TBEC 2018. Therefore, the seismic performance of the building was assessed.

On-site examinations revealed that the vertical load bearing members, particularly those on the basement floor were corroded. Additionally, it was observed that lateral rebars (stirrups) were sparsely implemented, with intervals of up to 60 cm. It was, therefore, determined that the rebar diameters and spacings specified in the building project were generally not followed during the construction process.

Key findings of the seismic analysis conducted for the “Controlled Damage” performance level are summarized below:

- Except for the secondary beams (those not included in the vertical load bearing system), primary RC beams were found to be in the “Limited Damage”, “Significant Damage”, “Excessive Damage”, or “Failure” regions. The percentage of the primary RC beams in the “Excessive Damage” region was observed to be below the limit value. However, some primary RC beams were in the “Failure” region.
- The vertical load bearing members of the building were determined to be in the “Limited Damage”, “Significant Damage”, “Excessive Damage”, or “Failure” regions. In specific stories, the ratio of the vertical load bearing members in the “Excessive Damage” region to all vertical load bearing members in the same story was found to exceed the limit value. Additionally, certain RC vertical load bearing members were identified to be in the “Failure” region.
- In certain stories of the building, it was observed that some RC vertical load-bearing members exhibited damage above the “Significant Damage Limit” in both the lower and upper sections. Additionally, the ratio of the shear force carried by these members to the total shear force in the same story was found to exceed the limit value.
- Some RC members of the building exhibited “Brittle” damage.

In conclusion, it was determined that the current state of the building failed to meet the “Controlled Damage” performance level envisaged in the “Turkish Building Seismic Code 2018” for an earthquake with a 10% chance of exceedance in 50 years (recurrence period of 475 years; DD-2 ground motion). Overall, the building was deemed suitable for retrofitting. Therefore, it is recommended to strengthen the building to enhance the seismic performance of the members that exhibit poor performance, ensuring they meet the desired target performance.

REFERENCES

- [1]. H. Chaulagain, H. Rodrigues, J. Jara, E. Spacone and H. Varum, “Seismic response of current RC buildings in Nepal: A comparative analysis of different design/construction” *Engineering Structures*, 49,284-94, 2013.
- [2]. A. Mosleh, H. Rodrigues, H. Varum, A. Costa and A. Arede, “Seismic behavior of RC building structures designed according to current codes,” *Structures*, 7, 1-13, 2016.
- [3]. L. Halder and S. Paul, “Seismic damage evaluation of gravity load designed low rise RC building using nonlinear static method,” *Procedia Engineering*, 144, 1373-80, 2016.
- [4]. A. Melani, R. K. Khare, R. P. Dhakal and J. B. Mander, “Seismic risk assessment of low rise RC frame structure,” *Structures*, 5, 13-22, 2016.
- [5]. M. E. Sobaih and M. A. Nazif, “A proposed methodology for seismic risk evaluation of existing reinforced school buildings,” *HBRC Journal*, 8, 3, 204-11, 2012.
- [6]. A. Ghobarah, N.M. Aly, and M. El-Attar, “Seismic reliability assessment of existing reinforced concrete buildings,” *Journal of Earthquake Engineering*, 2 (4), 569-92, 1998.
- [7]. A. Yakut, “Preliminary seismic performance assessment procedure for existing RC buildings,” *Engineering Structures*, 26, 1467-81, 2004.
- [8]. S.A. El-Betar, “Seismic vulnerability evaluation of existing R.C. buildings,” *HBRC Journal*, 2016.
- [9]. M. Hosseini, B. Hashemi, and Z. Safi, “Seismic design evaluation of reinforced concrete buildings for near-source earthquakes by using nonlinear time history analyses,” *Procedia Engineering*, 199, 176-81, 2017.
- [10]. Midas Gen (2018) Integrated solution system for building and general structures. MIDAS Information Technology Co.
- [11]. TBEC (2018) Türkiye Building Seismic Code: Rules for design of buildings under earthquake effect, Official Gazzette, Decision no 30364 dated 18.03.2018 (in Turkish)

BIOGRAPHY

Dr. Baris Sayin is currently studying as a Professor in the Department of Civil Engineering at Istanbul University-Cerrahpasa. Dr. Sayin received his BS, MS, and PhD degrees in Civil Engineering from Istanbul University. During the graduate education, he served as a Research Assistant in the Department of Civil Engineering. Between 2009 to 2015, Dr. Sayin worked as a structural engineer in the Department of Construction and Technical Affairs at Istanbul University. In September 2012, Dr. Sayin collaborated with Professor Hamid Saadatmanesh as a Visiting Scholar at the Department of Civil Engineering and Engineering Mechanics, University of Arizona, for a duration of 12 months. Their collaboration focused on insulated FRP-strengthened RC structures and FRP sandwich panels. Dr. Sayin's research interests encompass historical masonry structures, RC buildings, fiber composites, and industrial wastes. He has authored over one hundred articles in the fields of civil engineering and architecture.

Evaluating the Effectiveness of Jacketing and CFRP Strengthening for an RC building through Seismic Performance Analysis

Ozlem Ustundag¹, Baris Gunes², Baris Sayin³

Abstract

Seismic performance analysis plays a crucial role in assessing the effectiveness of proposed strengthening techniques for enhancing the seismic resilience of structures. This study investigates the effectiveness of jacketing and CFRP (carbon fiber reinforced polymer) strengthening techniques through seismic performance analysis. The proposed technique involves the application of a jacketing system and CFRP plates on RC members. Finite element analysis (FEA) is utilized to simulate the seismic response of the examined building following the implementation of the strengthening practices. The performance of the structure is evaluated based on certain parameters such as lateral displacement, inter-story drift, and base shear. The results of the seismic performance analysis indicate that the proposed strengthening technique effectively enhances the seismic resilience of the structure by leading to a significant reduction in lateral displacement and inter-story drift, as well as an increase in the overall stiffness and strength of the structure. In conclusion, the findings of this study reveal the effectiveness of the proposed jacketing and CFRP strengthening technique for improving the seismic performance of structures. The results can serve as a valuable reference for engineers and researchers involved in seismic retrofitting of structures and contribute to the advancement of seismic strengthening strategies.

Keywords: RC building, Seismic performance analysis, Retrofitting proposal

1. INTRODUCTION

Seismic codes consider a range of parameters to assess the seismic performance of newly constructed reinforced concrete (RC) structures when subjected to earthquake effects. On the contrary, different parameters are taken into account when evaluating the seismic performance of existing old RC buildings. Based on the analyses carried out considering these factors, one of the following three results is obtained for the examined building: i. The seismic strength of the building is sufficient; ii. Strengthening is necessary to achieve adequate structural strength; iii. The building must be demolished. In earthquake codes, the assessment of seismic performance for existing buildings involves evaluating their response to earthquake forces based on four different damage scenarios. Linear or nonlinear analysis methods are employed to determine the seismic performance level by examining the damage levels of certain structural elements. Performance targets are established considering the probability of earthquake exceedance and the intended use of the building. The analysis results are then compared with these targets to determine the corresponding performance level.

The seismic performance of a building can be deemed inadequate for various reasons, including updates in seismic codes and standards, environmental factors, changes in the building's intended use, or deviations from the original design project during construction. To assess this situation, seismic performance analyses are conducted on existing structures. Based on the analysis results, buildings that are determined to have insufficient seismic performance can be demolished and rebuilt. Or retrofitting practices can be implemented in the building to increase its seismic performance to the desired level.

The literature contains many studies focusing on the strengthening of existing structures. These studies investigated various techniques and methods to enhance the structural performance of RC buildings. Common

¹ Istanbul University-Cerrahpasa, Department of Civil Engineering, Construction Materials Division, 34320, İstanbul, Türkiye. ozlem.ustundag@iuc.edu.tr

² Istanbul University-Cerrahpasa, Department of Civil Engineering, Structural Engineering Division, 34320, İstanbul, Türkiye. bgunes@iuc.edu.tr

³ Corresponding author: Istanbul University-Cerrahpasa, Department of Civil Engineering, Structural Engineering Division, 34320, İstanbul, Türkiye. barsayin@iuc.edu.tr



strengthening approaches include the addition of RC shear walls, steel bracing, and section enlargement methods. When deciding to strengthen an existing structure, two main methods are often employed namely, element-scale strengthening by enlarging columns and beams or building-scale strengthening by adding RC shear walls to the building. Increasing the cross-sectional size of the member enhances its bending capacity. On the other hand, adding reinforced concrete shear walls is one of the most preferred methods because it effectively reduces the story drifts in the direction in which they are added. Reinforced concrete shear walls are added within or adjacent to the frame system. In some cases, strengthening is also made by adding external steel bracing, apart from RC shears [1-14]. Steel jacketing is used to strengthen columns by increasing shear and compressive strengths. This method is only used for rectangular columns and is implemented by placing vertical brackets on the four corners of the columns as well as lateral flat bars to prevent buckling. Strengthening the columns by wrapping them with fiber polymer materials is also a preferred method since it offers ease of application and increases compressive strength. Fiber polymer materials are also used in strengthening beams to increase the shear strength and ductility of beams. Additionally, to increase the shear strength, exterior stirrups can be added to the beams [17, 18].

In the current study, the seismic performance of an existing RC building was examined through on-site examinations, laboratory tests, and numerical analysis. In the first stage of the study, the building's concrete, rebar, and soil characteristics were evaluated. In the second stage, a 3D finite element model of the building was created using MIDAS software [19] based on the data obtained by on-site examinations and laboratory tests. Numerical analysis was conducted on this model and the seismic performance of the building was assessed.

2. STRENGTHENING PROPOSAL

The building consists of a basement, ground, and three normal stories. The building has a floor area of approximately 226 m² (ground floor). The story heights are 4.30 m in the basement, 3.20 m in the ground story, and 2.80 m in the normal stories. A strengthening proposal was presented for this building. As strengthening members, C25 class structural concrete and S420 class rebar were selected. Figure 1 shows the foundation strengthening plan. As seen in the foundation plan, continuous foundation beams, with widths of 120 cm and 150 cm and a height of 60 cm, were added to the existing foundation system. In the foundation beams, Ø18 and Ø20 rebars were used in the upper and lower sections with 10~20 cm intervals. Furthermore, additional Ø18 rebars at 10~20 cm intervals were used.

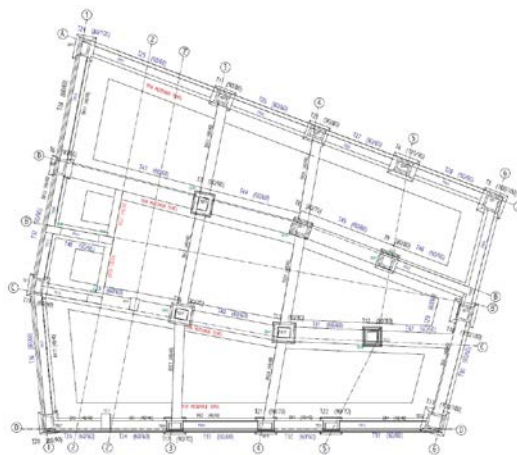


Figure 1. The foundation strengthening plan

Moreover, 30 cm-thick shear walls in both directions were added to the basement and ground stories. Ø12 and Ø14 vertical rebars as well as Ø10 and Ø12 lateral rebars at a 15 cm interval were added to these shear walls. Furthermore, additional reinforced concrete (RC) columns with various dimensions of 60x30 cm, 40x60 cm, and 35x50 as well as RC beams with dimensions of 25x60 cm were added. In the columns, Ø16 vertical rebars and Ø10 stirrups at 10~20 cm intervals were used. In this story, double-sided and four-sided 15-cm thick RC jacketing was performed on some columns. In the jacketing, Ø14 vertical rebars and Ø8 stirrups at 10~20 cm intervals were used. In this story, some of the 40x60 cm RC beams were wrapped with CFRP plates and 3-layer CFRP textile for strengthening. The strengthening plan for the basement story is shown in Figure 2.

In the strengthened 1st, 2nd, and 3rd stories, 30 cm thick shear walls were added in both directions. In these shear walls, Ø12 and Ø14 vertical rebars as well as Ø10 and Ø12 lateral rebars at 15 cm intervals were used.



Furthermore, additional reinforced concrete (RC) columns with various dimensions of 60x30 cm, 40x40 cm, 40x60 cm, and 35x50, as well as RC beams with dimensions of 25x60 cm and 25x50 cm, were placed. In the columns, Ø16 vertical rebars and Ø10 stirrups at 10~20 cm intervals were used. In these stories, double-sided and four-sided 15-cm thick RC jacketing was performed on some columns. In the jacketing, Ø14 vertical rebars and Ø8 stirrups at 10~20 cm intervals were used. In these stories, some of the 25x60 and 40x60 cm RC beams were wrapped with CFRP plates and 3-layer CFRP textile for strengthening. The strengthening plan for the 1st story is shown in Figure 2.

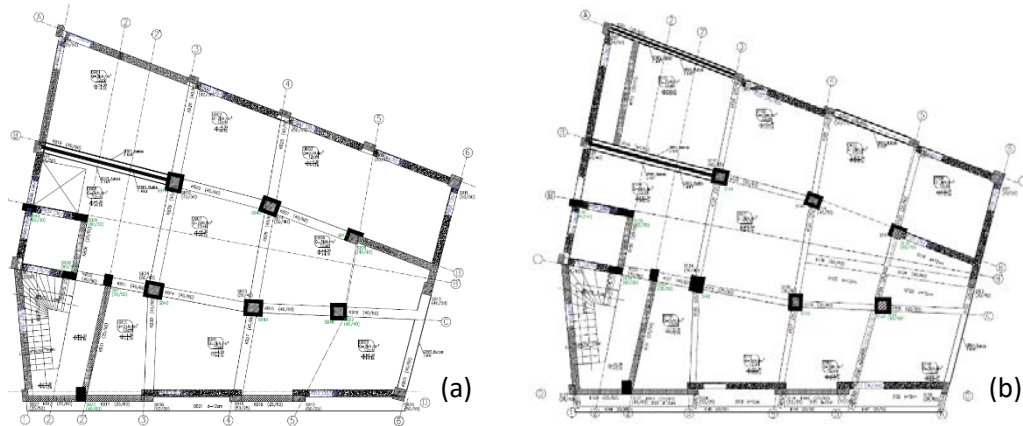


Figure 2. Strengthening plan (a) Basement and ground floors, (b) 1st, 2nd, and 3rd floors

3. LABORATORY

To identify the compressive strength of the concrete and reinforcing bars in the concrete, laboratory tests were performed following the standards given in the local seismic code, TBEC 2018 [20]. Accordingly, core samples were collected from a total of 15 vertical load-bearing elements -3 from each story- and tested to determine concrete compressive strengths. Two approaches were utilized to identify the rebars in the structural components. The initial approach employed non-destructive techniques for rebar detection, whereas the second approach was visual inspection through concrete cover scraping. Accordingly, a total of 20 vertical load-bearing members -4 from each story- underwent non-destructive rebar detection. Furthermore, concrete covers of certain columns were scraped for rebar inspection. These scraping practices were performed on a total of 5 vertical load-bearing members from the basement, ground, and 1-3 normal stories -1 from each story. By scraping the concrete cover, Ø14 and Ø16 vertical rebars, as well as Ø6 and Ø8 stirrups were determined. The stirrups were used at ~27-38 cm intervals. In the beams, Ø12, Ø14, and Ø16 vertical rebars, as well as Ø8 stirrups, were determined. The stirrups were used at ~20-35 cm intervals.

Regarding soil parameters, the local soil class was found to be ZC, the bearing capacity of the soil was 6 kg/cm², and the subgrade reaction coefficient was found to be 7348 t/m³. The soil and earthquake parameters used in the numerical analysis were defined in accordance with the criteria given in TBEC 2018.

4. NUMERICAL ANALYSES

The examined building was modeled with the finite element program and seismic performance analysis was conducted considering the strengthened state of the building. The 3D numerical model of the strengthened building and floor plan is shown in Figure 3.

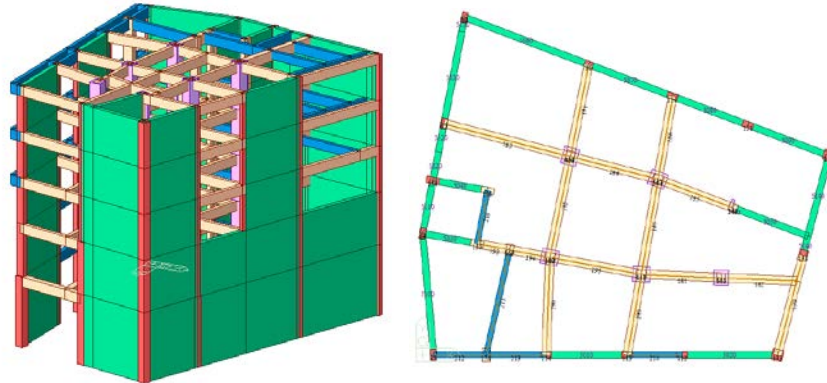


Figure 3. 3D static analysis model and floor plan of the building

TBEC 2018 was considered in the concrete compressive strength calculations and unwrapped cylinder concrete compressive strength was found to be 6.65 MPa. Characteristics of the strengthening materials are listed in Table 1.

Table 1. CFRP material characteristics

Material	Wrap	Plate
Elasticity modulus (N/mm ²)	245000	160000
Tensile strength (N/mm ²)	4900	2400
Breaking elongation (%)	2	1.5
Thickness (mm)	0.168	1.2
Width (mm)	-	100

A seismic performance analysis of the building was performed following the criteria given in TBEC 2018. The information level of the building was considered limited and accordingly, the Information Level was taken as 0.75. To assess the seismic performance level, a nonlinear static pushover analysis was conducted. In accordance with the selected analysis method, no earthquake load reduction [Ra(T)] was applied in the acceleration spectrum. Additionally, the response coefficient and ductility coefficient (refers to the excess of yield strength relative to the design strength) of the load-bearing system (R and D) were not used since a nonlinear analysis method was utilized. In the analysis, plastic hinges (fiber) were defined for column-beam joints. The purpose of the strengthening was to ensure that the building meets the "Controlled Damage" performance level for an earthquake with a 10% probability of exceedance in 50 years (DD-2 Ground Motion with a recurrence period of 475 years). "Assessment/Design according to Strain" was selected as the assessment method. Damage inspections were performed on the structural members to evaluate whether the controlled damage performance criteria were met.

The sectional damage regions defined in the seismic code for the "Assessment/Design according to Strain" approach, are illustrated in Figure 4. Three damage states and limit damages are defined for ductile elements namely, Limited Damage (LD), Controlled Damage (CD), and Collapse Prevention (CP). Limited Damage (LD) refers to a limited level of inelastic behavior in the section. Controlled Damage (CD) indicates inelastic behavior but sectional strength can still be safely achieved. Prevention of Collapse Damage signifies significant inelastic behavior in the section. Critical sections below LD are categorized as being in the Limited Damage (LD) Region. Sections between LD and CD are considered to be in the Significant Damage (SD) region. Sections between CD and CP are categorized as being in the Excessive Damage (ED) region. Elements with damage above CP are considered in the Failure Region (FR).

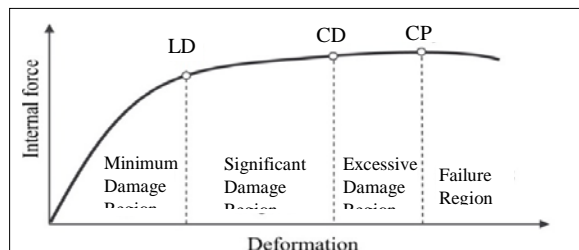


Figure 4. Sectional damaged areas

NUMERICAL ANALYSES

Base shear–peak displacement and demand spectrum–capacity diagrams obtained by the numerical analysis for an earthquake with a 10% chance of exceedance in 50 years (DD-2 ground motion) are given in Figure 5

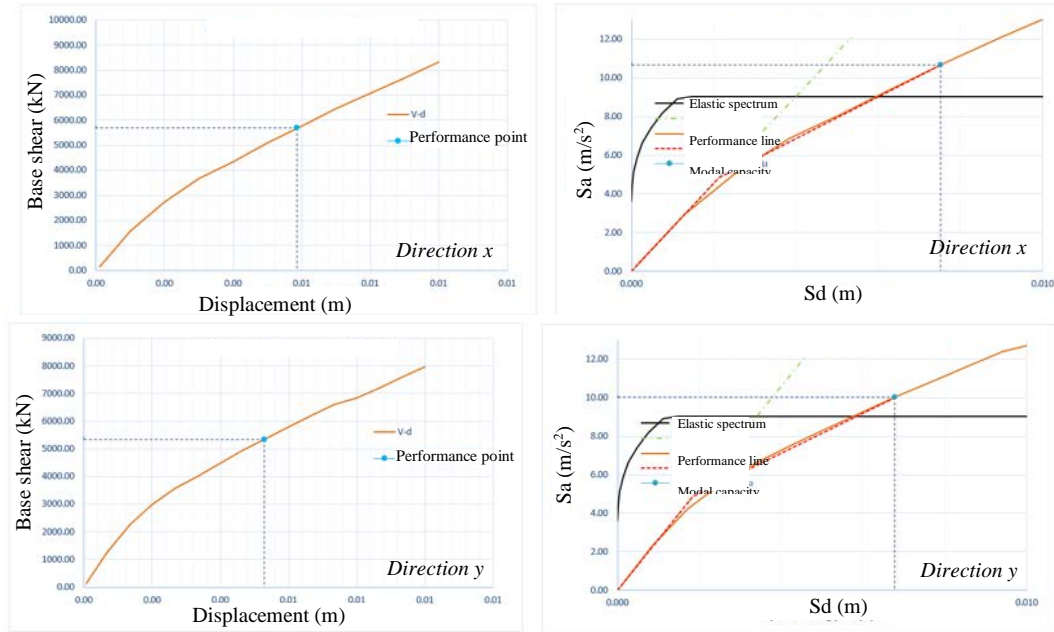


Figure 5. Base shear–peak displacement and demand–capacity diagrams in the x (up) and y (down) directions

Lateral displacements observed under earthquake effects are shown in Figure 6. The results of the analysis and seismic performance evaluations for vertical and lateral load-bearing members in all stories are given in Tables 1 and 2, respectively.

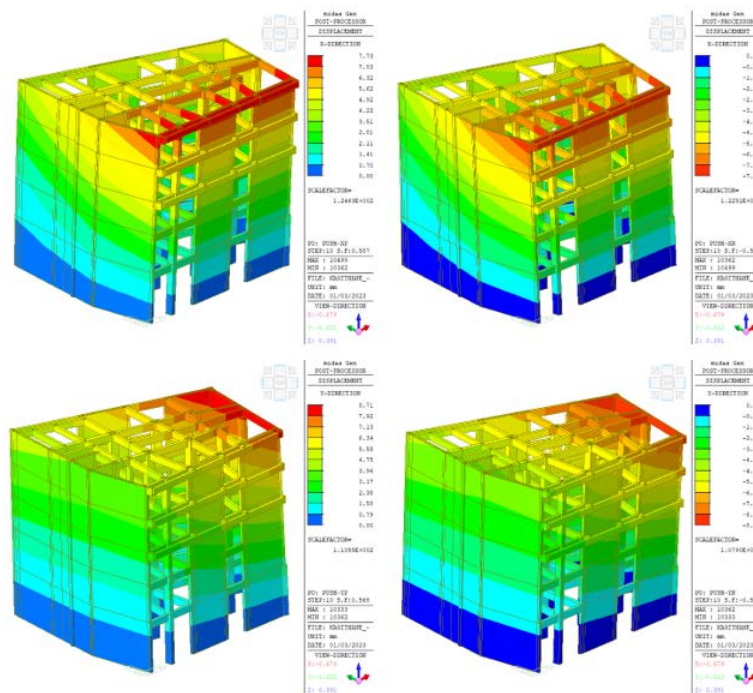


Figure 6. Lateral displacements observed under earthquake effects in the x (up) and y (down) directions

Table 2. Performance analysis of vertical load-bearing members

Story	Vertical Load Bearing Members (Columns and Shear Walls)			Target Performance Level (CD)
	Article 15.8.4 (b) Strain Check	Article 15.8.4 (c) Strain Check	Article 15.8.4 Brittleness Check	
	Reinforced Concrete	Reinforced Concrete	Reinforced Concrete	
BF	✓	✓	✓	✓
GF	✓	✓	✓	✓
1	✓	✓	✓	✓
2	✓	✓	✓	✓
3	✓	✓	✓	✓

Table 3. Performance analysis of lateral load-bearing members

Story	Lateral Load Bearing Members (Beams)		Target Performance Level (CD)
	Article 15.8.4 (a) Strain Check	Article 15.8.4 Brittleness Check	
	Reinforced Concrete	Reinforced Concrete	
BF	✓	✓	✓
GF	✓	✓	✓
1	✓	✓	✓
2	✓	✓	✓
3	✓	✓	✓

The strengthened state of the foundation was modeled and analyzed using the finite elements software. The images of the analysis model are illustrated in Figure 7. Envelope moment curves of the foundation are given in Figure 8. Vertical displacement diagrams that show the foundation's response under loading combinations with and without earthquake are provided in Figure 9. The foundation had a thickness of 60 cm with primary Ø18 and Ø20 rebars in the x and y directions at 10~20 cm intervals. The examinations carried out considering the moment distributions in the foundation revealed that the foundation rebars were sufficient.

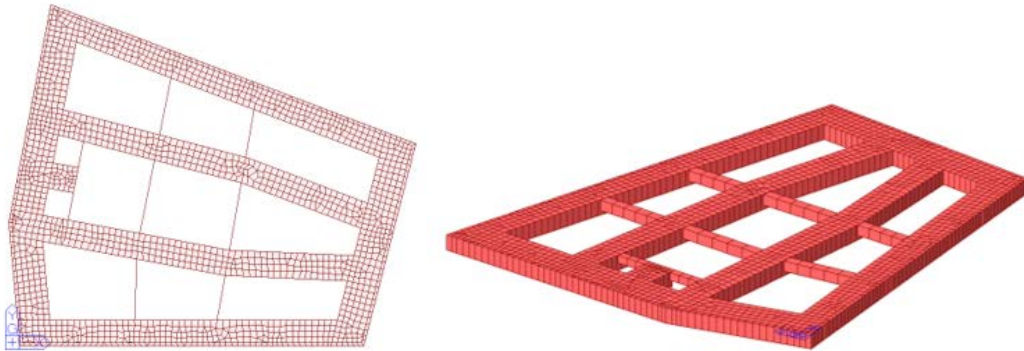


Figure 7. The static analysis model of the foundation

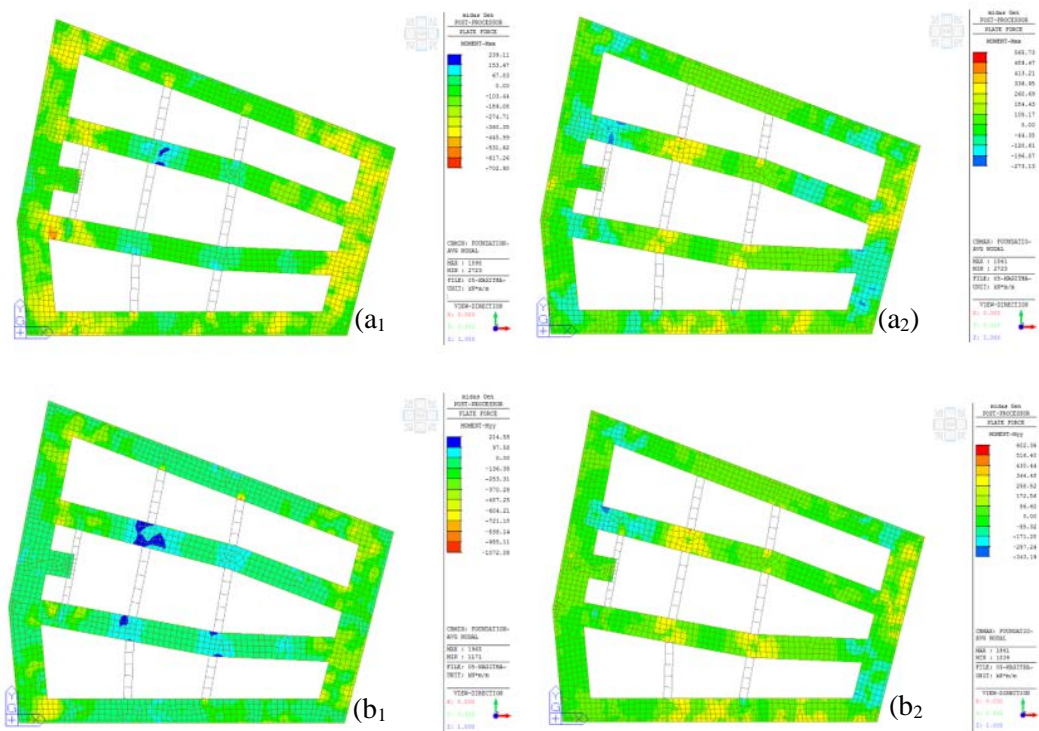


Figure 8. The moment changes in the foundation (a1) $M_{xx_{min}}$, (a2) $M_{xx_{max}}$, (b1) $M_{yy_{min}}$, (b2) $M_{yy_{max}}$

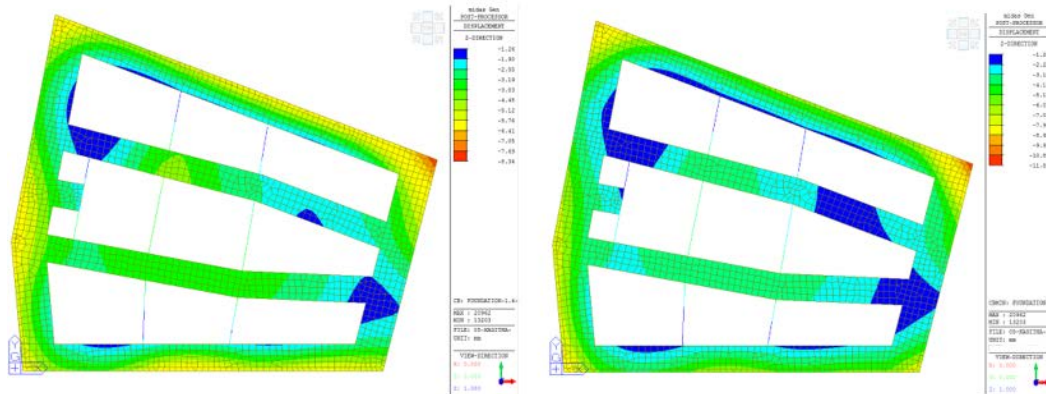


Figure 9. Vertical displacement diagrams for the foundation under loading combinations without (left) and with (right) earthquake

CONCLUSIONS

In this study, a building comprising a basement, ground, and 3 normal stories was modeled using finite element software based on the strengthening proposal. The model was then analyzed in accordance with the criteria given in TBEC 2018 and the seismic performance of the building was assessed.

According to the seismic analysis of the strengthened building for the "Controlled Damage" performance level, all the reinforced concrete (RC) primary beams, except for the secondary beams that are not part of the lateral load-bearing system, were found to be in the "Limited Damage" region. No primary beams were classified in the "Significant Damage," "Excessive Damage," or "Failure" regions. Furthermore, all vertical load-bearing members were also found to be in the "Limited Damage" region. No vertical load-bearing members were classified in the "Significant Damage," "Excessive Damage," or "Failure" regions. Moreover, no RC vertical load-bearing member in the building exceeded the "Significant Damage" level in both the upper and lower sections. Additionally, the analysis results revealed that no RC member exhibited "Brittle" damage. Poor bending and shear strengths of some beams were eliminated by strengthening with CFRP plate and textile. In conclusion, the strengthened state of the building was deemed to satisfy the "Controlled Damage" performance criteria for an earthquake with a 10% chance of exceedance in 50 years (DD-2 ground motion with a recurrence period of 475 years).

REFERENCES

- [1]. P.D. Gkournelos, T.C. Triantafyllou, D.A. Bournas, "Seismic upgrading of existing reinforced concrete buildings: A state-of-the-art review", *Engineering Structures* 240, 112273, 2021
- [2]. J. Yüzbaşı and H.R. Yerli, "Performance Analysis and Strengthening of Reinforced Concrete Structures under Earthquake Impact, Çukurova University," *Journal of the Faculty of Engineering and Architecture*, 33(2), 273-286, 2018.
- [3]. A.H. Mutlu "Criteria Considered for Strengthening or Destroying Existing Buildings, 3rd Turkish Conference on Earthquake Engineering and Seismology", October 14-16, 2015 İzmir.
- [4]. Ö. Keleşoğlu, H. Çakar, A. Polat, "Determination of the Performance of an Existing Reinforced Concrete Structure According to the 2007 Earthquake Regulations and Strengthening Proposal," *International Journal of Pure and Applied Sciences*, 3(2), 58-67, 2017.
- [5]. A. Ergün, G. Kürklü and V. Başaran "A Hospital Case Study in Afyonkarahisar for Evaluating Seismic Safety and Strengthening Work on Existing Reinforced Concrete Buildings," *Afyon Kocatepe University, Journal of Sciences*, 12(2), 1-11, 2012.
- [6]. K. Arı, H. Elcuman, E. Uncuoğlu, B. Somuncu, F. Altun, H.B. Kara and T. Haktanır, "Earthquake Damages in Structures and Retrofitting Work for a Reinforced-Concrete Structure Damaged in Afyon Earthquake," *Afyon Kocatepe University, Journal of Sciences*, 6(1), 81-96, 2006.
- [7]. M. Olbak and S. Naimi, "Examination of Strengthening Results with Non-Linear Analysis Methods Using Experimental Data of Two 5-Storey Building Samples with Urban Transformation," *Journal of Istanbul Aydın University*, 8(3), 145-166, 2016.
- [8]. S.Ö. Değertekin and H. Şik, "Comparison of Different Retrofitting Proposals for a Reinforced Concrete Building with Inefficient Earthquake Safety," *Dicle University Journal of Engineering Faculty*, 6(2), 121-130, 2015.
- [9]. H. Chalugain, H. Rodrigues, E. Spacone and H. Varum (2015) "Assessment of Seismic Strengthening Solutions for Existing Low-Rise RC Buildings in Nepal," *Earthquakes and Structures*, 8(3), 511-539
- [10]. H. Yalciner and A.A. Hedayat, "Repairing and Strengthening of An Existing Reinforced Concrete Building: A North Cyprus Perspective," *American Journal of Engineering and Applied Sciences*, 3(1), 109-116, 2010.

- [11]. M.A. Ismaeil, A. Hassaballa, M.Y. Laissy, I.E. Kamal and F. Adam, "Evaluation and Strengthening of An Eight-Storey Existing Reinforced Concrete Building in Abha City KSA," *Advancements in Civil Engineering & Technology*, 2(5), 1-18, 2019.
- [12]. M.A. Ismaeil, M.E. Sobaih and A.E. Hassaballa, "Assessment of Seismic Performance and Strengthening of RC Existing Residual Buildings in the Sudan," *Journal of Advanced Science and Engineering Research*, 3(3), 209-225, 2013.
- [13]. M.B.D. Hueste and J.W. Bai, "Seismic Retrofit of a Reinforced Concrete Flat-Slab Structure: Part I Seismic Performance Evaluation," *Engineering Structures*, 29(6), 1165-1177, 2007.
- [14]. A. Ghobarah, M. El-Attar and N.M. Aly, "Evaluation of Retrofit Strategies for Reinforced Concrete Columns: A Case Study," *Engineering Structures*, 22(5), 490-501, 2000.
- [15]. A. Bal and A.M. Kılıç, "Comparison of CFRP and Steel Jacketing Methods Applications for Retrofitting an Existing Concrete Industrial Structure in Earthquake Effect," VI. International Earthquake Symposium Kocaeli 2019, September 25-27, 2019 Kocaeli
- [16]. P. Rocha, P. Delgado, A. Costa and R. Delgado, "Seismic Retrofit of RC Frames," *Computers & Structures*, 82(17-19), 1523-1534, 2004.
- [17]. N. Çetinkaya, H. Kaplan, Ş.M. Şenel, "Repair and Strengthening of Reinforced Concrete Beams using Fibre Reinforced Polymer (FRP) Materials," *Pamukkale University, Journal of Engineering Sciences*, 10(3), 291-298, 2004.
- [18]. Z.F. Alemdar and N. İnkaya, "Modeling and analysis of strengthened reinforced concrete beams with CFRP by finite element method," *Journal of Dicle University Engineering Faculty*, 10(3), 1073-1085, 2019.
- [19]. Midas Gen (2018) Integrated solution system for building and general structures. MIDAS Information Technology Co.
- [20]. TBEC (2018) Türkiye Building Seismic Code: Rules for design of buildings under earthquake effect, Official Gazzette, Decision no 30364 dated 18.03.2018 (in Turkish)

BIOGRAPHY

Dr. Baris Sayin is currently studying as a Professor in the Department of Civil Engineering at Istanbul University-Cerrahpasa. Dr. Sayin received his BS, MS, and PhD degrees in Civil Engineering from Istanbul University. During the graduate education, he served as a Research Assistant in the Department of Civil Engineering. Between 2009 to 2015, Dr. Sayin worked as a structural engineer in the Department of Construction and Technical Affairs at Istanbul University. In September 2012, Dr. Sayin collaborated with Professor Hamid Saadatmanesh as a Visiting Scholar at the Department of Civil Engineering and Engineering Mechanics, University of Arizona, for a duration of 12 months. Their collaboration focused on insulated FRP-strengthened RC structures and FRP sandwich panels. Dr. Sayin's research interests encompass historical masonry structures, RC buildings, fiber composites, and industrial wastes. He has authored over one hundred articles in the fields of civil engineering and architecture.

Seismic Performance of a Masonry Building through Finite Element Analysis and Kinematic Limit Analysis

Ozlem Ustundag¹, Baris Gunes², Baris Sayin³

Abstract

This study offers a comprehensive analysis of an existing masonry building through finite element analysis (FEA) and kinematic limit analysis. The building is located in a region prone to seismic activity. The FEA is performed to examine the structural response of the building under various loading conditions, including dead loads, live loads, and seismic loads. The masonry material properties, boundary conditions, and loading patterns are considered in the FEA model. The results from the FEA revealed the stress and deformation distribution within the building, identifying potential areas of concern. Furthermore, a kinematic limit analysis was performed to assess the local collapse mechanisms of the building under seismic loads. The kinematic limit analysis was based on the upper bound theorem of plasticity, which is commonly used to determine the ultimate load-carrying capacity of buildings. The critical collapse mechanism and the corresponding load-carrying capacity were identified through the kinematic limit analysis. The findings from this study have significant implications for the evaluation of the structural performance of masonry buildings and provide valuable information for retrofitting or strengthening practices. The results can also contribute to the advancement of knowledge in the field of seismic analysis of masonry structures and the development of guidelines for the seismic assessment and retrofitting of historical masonry buildings.

Keywords: Masonry structure, Seismic performance analysis, In-situ test

1. INTRODUCTION

Unlike reinforced concrete structures, inadequacies in slab-wall connections of masonry buildings create uncertainties about the behavior of such buildings under earthquake effects. For these reasons, a general evaluation is made with a step-by-step analysis about the behavior of such structures under earthquake effects. As a linear analysis method, modal analysis gives information about the behavior of the structure in the absence of seismic effects. On the other hand, response spectrum analysis provides information about displacements of the walls under seismic effects and the shear forces acting on these walls. Linear analyses are based on the assumption of materials exhibit linear elastic behavior, whereas, plastic materials are defined in nonlinear analysis allowing determining displacement and stress distributions of the walls. Local wall behaviors, which cannot be observed by linear and nonlinear analyses, can be determined by kinematic analysis. Thus, by employing kinematic analysis, a structure can be evaluated holistically, including displacements, shear forces, and local behaviors.

In linear analysis, the macro-modeling method is used in which masonry units and mortar are defined as composite materials. Because composite materials include uncertainties about the determination of material properties in masonry buildings. The macro-modeling method is preferred due to several reasons including variation of masonry material even on different walls. The advantage macro-modeling method is the minimal number of parameters leading to a lower margin of error. Mechanical parameters used for defining masonry walls are listed in Table 1. Kinematic analysis is very important to identify the mechanisms of masonry walls.

¹ Istanbul University-Cerrahpasa, Department of Civil Engineering, Construction Materials Division, 34320, İstanbul, Türkiye. ozlem.ustundag@iuc.edu.tr

² Istanbul University-Cerrahpasa, Department of Civil Engineering, Structural Engineering Division, 34320, İstanbul, Türkiye. bgunes@iuc.edu.tr

³ Corresponding author: Istanbul University-Cerrahpasa, Department of Civil Engineering, Structural Engineering Division, 34320, İstanbul, Türkiye, barsayin@iuc.edu.tr

Various collapse mechanisms were observed in masonry walls due to past earthquakes. Therefore, typical mechanisms of such structures should be examined.

Several studies have been conducted to evaluate the seismic capacity of masonry buildings using various methods, including limit analysis, kinematic analysis, and pushover analysis. Shariq et al. [1] utilized the Finite Element method to investigate the seismic performance of a masonry building. Casapulla and Argiento [2] focused on examining the out-of-plane failure mechanisms of load-bearing walls. Milani et al. [3] examined masonry structures under seismic effects by employing kinematic limit analysis, considering both in-plane and out-of-plane collapse states. Palazzi et al. [4] conducted a kinematic limit analysis to assess the seismic performance of a church. Yildizlar [5] presented the seismic vulnerability assessment for a masonry building utilizing various numerical methods. Akcay et al. [6] determined the seismic performance of a masonry building and found that shear stress values exceeded the limit values. Özen [7] examined a masonry building using the finite element method and compared the results of linear and nonlinear analyses. Roca et al. [8] discussed the applicability of different analysis techniques, such as limit analysis, simplified methods, finite element methods, macro or micro modeling, and discrete element methods. Sayin et al. [9] performed linear analysis to evaluate the seismic level of a masonry structure and presented strengthening practices based on the analysis results.

This study aims to evaluate the seismic performance of an existing masonry building through a comprehensive approach involving field studies, laboratory tests, and numerical analysis. The building is subjected to static and kinematic limit analyses using MIDAS [10] and PRO_CINem [11] software, respectively.

2. FIELD SURVEY AND IN-SITU TESTS

External facade views of the examined building are given in Figure 1. The building consists of two stories, a ground and a normal story. The on-site observations revealed breakings and collapse on the timber slabs within both floors, as well as on the exterior timber walls of the first floor. The vertical load-bearing system of the buildings consisted of stone and masonry structural members on the exterior facade of the ground floor. The dimensions of the buildings are 10.7 in the x direction and 9.3 and 9.2 m (ground floor) in the y direction. The building has a flooring area of 108 m² (ground floor). The plan view of the ground story is shown in Figure 2.



Figure 1. The examined building

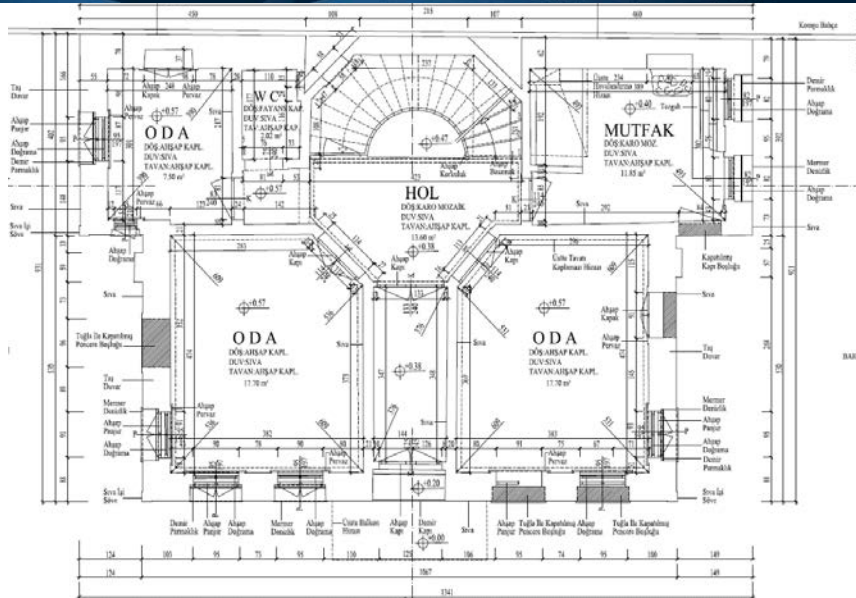


Figure 2. Plan view of ground story

On the ground floor, breaking and collapses were observed on the timber slabs, as well as on the interior and exterior timber walls. Additionally, the exterior stone and masonry walls also exhibited signs of breakage and collapse. The vertical load-bearing system of the building consisted of irregular-pattern stone and solid brick masonry walls, with timber walls in some parts. No vertical or lateral RC peripheral tie was observed in the building. Some window and door openings were later filled with solid brick masonry elements. The slab systems in both the ground and normal stories comprised timber slabs; however, certain slabs were found to be broken. Significant cracks and damages were observed on the load-bearing masonry walls. The wall surfaces showed signs of decay caused by moisture and humidity. A large portion of the load-bearing timber walls had collapsed, and the remaining timber walls that hadn't collapsed suffered from extensive damage. Timber slabs were used in the ground and normal stories; however, collapses and excessive damages were observed on these slabs. On one side of the building, there is a neighboring building on the adjacent parcel that is still in use. Due to the examined building's risk of partial and complete collapse, it poses a danger to the adjacent building in terms of life and property safety. The type and application technique of the stone and masonry elements were determined either by scraping the plaster layer of the masonry walls or visual examinations.

The mechanical properties of the masonry walls were determined through a shear strength index, compressive strength, and flat-jack modulus of elasticity tests. These tests were carried out based on the applicable code requirements and previous studies. In-situ shear tests were conducted on load-bearing masonry walls following the ASTM C 1531 [12] standard Method B and the shear strength index of the masonry unit-mortar joint were obtained. The shear test setup is shown in Figure 3a. In situ test results revealed that the shear strength index of the ground floor was 0.25 MPa.

Solid brick samples were collected from the masonry walls. Uniaxial compression tests were conducted on these samples in the laboratory and the compressive strength was determined to be 4.6 MPa. To measure strains in the masonry walls under loading, flat-jack elements were used in accordance with ASTM C 1197 [13] standard. Two flat-jacks were placed on pre-drilled 4 mm holes in the walls, and the loading on the wall was gradually increased using a hydraulic unit. Strains in the walls were instantly measured using LVDTs (Linear Variable Differential Transformers) with a sensitivity of 1/1,000 mm, and the data were recorded by a data logger. Vertical stress-strain curves of the walls were plotted, and the modulus of elasticity of the wall was determined. Semicircular flat jacks were employed in these tests. The test setup is shown in Figure 3b. The modulus of elasticity was found to be 1285 MPa.

As shown in Table 1, the mechanical properties of the masonry walls were determined by "In-Situ Materials Tests", Seismic risks management guide for historical structures (SRMGHS) 2017 [15], and Türkiye Building Seismic Code (TBEK) 2018 [16]. These parameters were used in the analysis.



Figure 3. (a) The shear strength index test setup, (b) In-situ flat-jack experiment [14]

Table 1. Mechanical properties of masonry walls

Definition	Value / Class
Masonry unit type	Stone-Solid Brick
Masonry unit group	Group I
Unit Volume Weight, kN/m ³	20
Characteristic compressive strength of the walls, MPa	2.8
Initial shear strength of the walls, MPa	0.12
Tensile strength of the walls, MPa	0.18
Modulus of elasticity of the walls, MPa	1285
Shear modulus of the walls, MPa	330

3. NUMERICAL ANALYSES

To evaluate the seismic performance of the masonry building under vertical and earthquake loads, compression and shear stress checks were conducted on the masonry walls using a 3D analysis model. In the 3D finite element model, critical sections around the door and window openings of each story were identified and walls in these sections were modeled using plate elements. Compression and shear stresses were calculated based on the axial and shear forces on these critical walls. The calculated compression and shear stresses on the masonry walls were then compared with the limit stresses of the corresponding masonry wall type. Accordingly, it was determined whether the compression and shear stresses exceeded the limit stress values. The local soil class was determined as "ZC". The distance of the building to the active fault is approximately 18 km. The spectral acceleration coefficients (S_s and S_1) used in the analyses were determined using the Interactive Earthquake Risk Map [17] based on the local soil class and location of the building. These parameters are given in Table 2.

Table 2. Soil and earthquake parameters

Parameters	Value / Class
Average shear-wave velocity	-
Local soil class	ZC
Ground motion level	DD-3, DD-2, DD-1
Spectral acceleration coefficients, Earthquake Map (g)	DD-3, $S_s = 0.489$, $S_1 = 0.125$ DD-2, $S_s = 1.321$, $S_1 = 0.357$ DD-1, $S_s = 2.300$, $S_1 = 0.643$
Peak ground acceleration (g)	DD-3, PGA = 0.209 DD-2, PGA = 0.543 DD-1, PGA = 0.903
Local ground impact coefficients	DD-3, $F_s = 1.300$, $F_1 = 1.500$ DD-2, $F_s = 1.200$, $F_1 = 1.500$ DD-1, $F_s = 1.200$, $F_1 = 1.400$
Spectral acceleration coefficients	DD-3, $S_{DS} = 0.636$, $S_{D1} = 0.188$ DD-2, $S_{DS} = 1.585$, $S_{D1} = 0.535$ DD-1, $S_{DS} = 2.760$, $S_{D1} = 0.900$

3.1 Linear analysis

In this section, the 3D finite element model that was created for the linear analysis of the building is described. Also, the performance target was determined according to SRMGHS 2017 and the analysis results are presented. The building was modeled using “plate/wall” elements to approximately represent its current condition. The finite element model of the building is given in Figure 5.

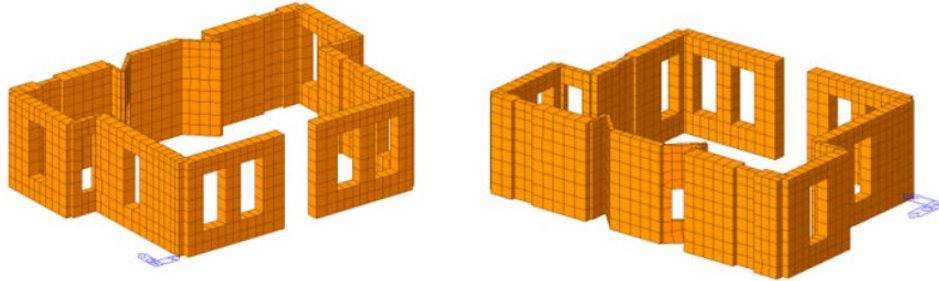


Figure 4. The 3D finite element model of the building

In Figure 5, the displacements and axial forces on the walls under vertical loads, including dead loads and live loads, are illustrated. The compression stresses on the walls induced by these forces were compared with the allowable limit stresses for the corresponding masonry wall type to determine if the stresses on the walls exceeded the limit values.

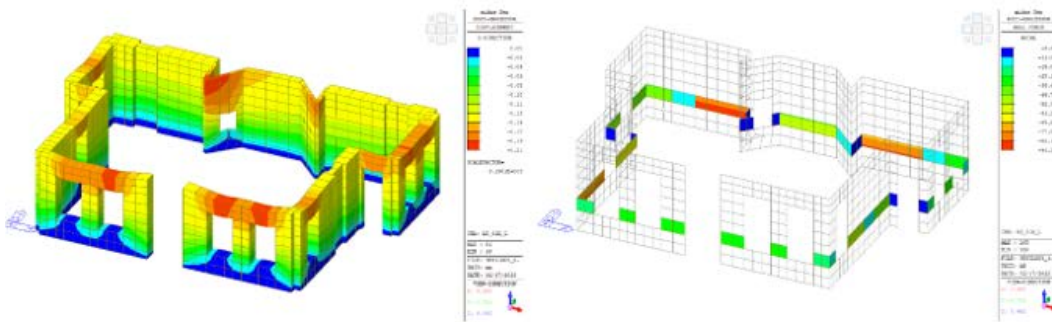


Figure 5. Displacement and axial forces on the walls under vertical loads

In the local code SRMGHS 2017, different performance targets are envisaged for historic buildings according to their importance level. The performance analysis parameters for the current building are given in Table 3.

Table 3. Performance analysis parameters

Parameters	Existing state
	Value / Class
The ground motion level and corresponding target performance	Controlled Damage for DD-2
Performance analysis method	Linear
Inter story drift limit	0.7% for DD2
Building Information Level and Factor	Limited, 0.75
Reduction factor for earthquake load, Ra	Ra=3 for DD-2

In Figure 6, lateral displacement under vertical loads, as well as the seismic effects in the x and y directions generated by an earthquake with a 10% probability of exceedance in 50 years (DD-2 ground motion level) are shown. The comparison of the inter-story drift ratios with the limit values is given in Table 4. As seen in the obtained results, the building failed to meet the performance target of "Controlled Damage" for a DD-2 ground motion level considering inter-story drifts.

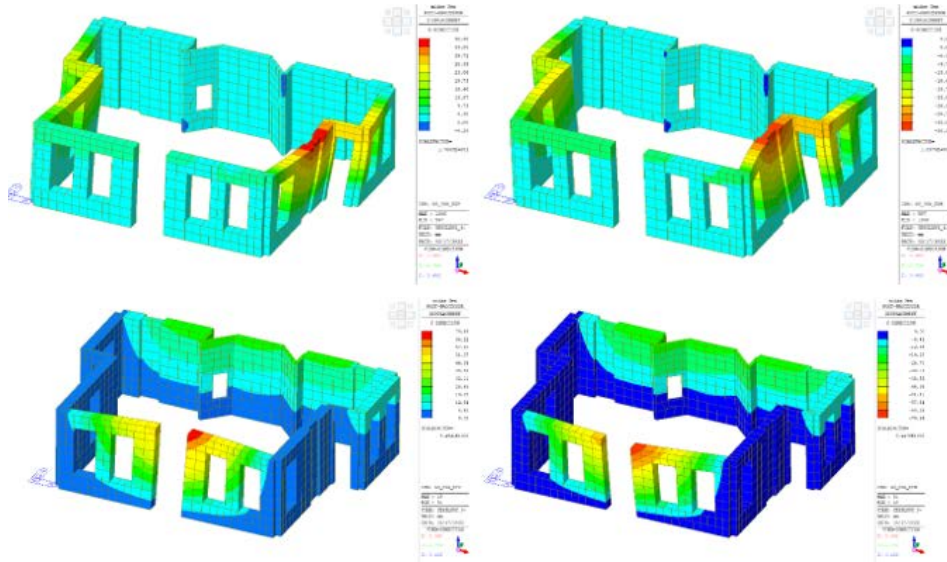


Figure 6. Lateral displacement observed under earthquake loads in the x and y directions

Table 4. Inter story drift ratio examination

Story	Displacement ΔD , (mm)		Story drift ratio, $\Delta D/H$		Limit value	Result
	x	y	%	%		
Ground	38.38	70.69	1.04	1.91	0.70 (CD)	✗

In Figure 7, shear forces observed on the building under both vertical loads and seismic effects in the x and y directions generated by an earthquake with a 10% probability of exceedance in 50 years (DD-2 ground motion level) are shown. The ratios of the shear forces on the structural elements that failed in shear under earthquake effects in the x and y directions to the total shear force on the corresponding story are given in Table 5. Based on these results, it was concluded that the building satisfies the “Controlled Damage” performance level for a DD-2 ground motion level in terms of shear forces. This is an expected result given that the building does not have an upper floor resulting in a relatively lower earthquake load. However, it should be noted that stress is not the only parameter to evaluate such buildings, overbending (kinematic analysis) and displacements are more significant factors in determining seismic performance.

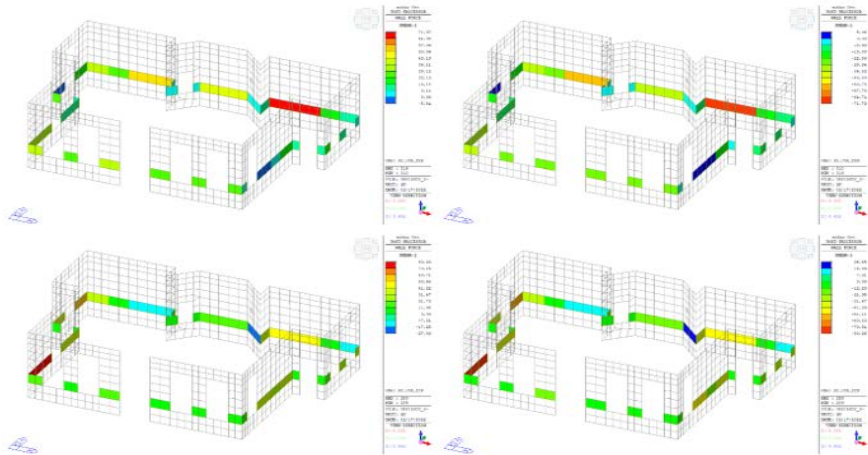


Figure 7. Shear forces observed under earthquake effects in the x and y directions

Table 5. Results of performance analysis

Story	The ratio of the shear forces on the structural elements that failed in shear to the total shear force, %			Target Performance* (CD)
	Masonry	RC	Total	
Ground	20.79	-	20.79	√

3.2 Kinematic limit analysis

Kinematic limit analysis is a significant method for assessing the seismic safety of masonry buildings. It involves the following key steps: (i) determining the lateral force required to trigger potential collapse mechanisms and the corresponding lateral seismic acceleration needed to generate this force (ii) evaluating the demand for lateral acceleration and comparing it with the capacity of the structure, (iii) identifying collapse mechanisms that occur under the examined seismic loads [15]. Historic masonry structures are more vulnerable to lateral effects, especially under tensile forces, due to the absence of horizontal diaphragms and insufficient material strength. Consequently, most collapse mechanisms in these structures occur due to out-of-plane behaviors when subjected to seismic load [18]. The use of kinematic limit analysis in masonry buildings was first introduced by Heyman [19]. This method is based on the assumptions of zero tensile strength, infinite compressive strength, and collapse mechanisms being unrelated to shear forces [20].

To ensure the safety of a masonry building under both vertical and lateral loads, it is necessary to examine multiple failure mechanisms. In this process, a specific collapse mechanism is selected, and the expected vertical and lateral loads are defined. The corresponding virtual displacement associated with the selected mechanism is considered, and the lateral force is calculated using the principle of virtual work. By evaluating the inertial forces related to the examined mechanisms and considering their effects on the joints, the collapse situation can be determined. The identification of collapse mechanisms is based on two key assumptions: (i) wall and wall components exhibit rigid block behavior and (ii) masonry wall elements do not have tensile strength. In addition to the vertical loads directly applied to the walls, loads transferred from the slabs and roof to the walls are also considered. For each mechanism evaluated, the lateral force is divided by the weight of the wall to calculate the lateral impact factor (lateral load/weight). And this lateral impact factor is considered to determine whether the examined failure mechanism occurs.

The collapse mechanisms of different walls of the building were assessed through the kinematic analysis based on the stress distribution and estimated response determined by the static analysis. The analysis results revealed that the overturning point is the bottom point of the walls. Only the overturning mechanism was examined for the walls. Behavior coefficients were taken as $R_a=1$ and $R_a=2$ for DD-3 and DD-2 earthquakes, respectively. Table 6 presents the acceleration values required to trigger the examined mechanism, as well as the accelerations affecting the rigid overturning block of the walls for various earthquake levels. As seen in the results, the overturning mechanism occurs on the wall under the target earthquake level of DD-2.

Table 6. Linear mechanism examinations (50 cm-thick walls)

Mechanism	Ground level	α_o	a_o (g)	a_c (g)	a_c/a_o	Result (a_c/a_o)
Overturning	DD-3	0.129	0.135	0.127	0.94	OK
	DD-2	0.129	0.135	0.317	2.34	Fail

4. CONCLUSIONS

This study presents the static performance assessment of a masonry building in accordance with the criteria specified in the local seismic code SMRGHS 2017. On-site examinations revealed that significant cracks and damages were present on the load-bearing masonry walls. Additionally, there were decays due to moisture and humidity on the wall surfaces. A substantial portion of the load-bearing timber had already collapsed, while the remaining timber walls exhibited excessive damage. The slab system in both the ground and normal stories of the building consisted of timber slabs with collapses and excessive damages. On-site tests conducted on the masonry walls indicated that the load-bearing capacity of the walls was very low. Next to the examined building, there is a neighboring building that is still in use. Due to the identified risk of partial or complete collapse, it was considered that the examined building poses a significant threat to the adjacent building in terms of the safety of occupants and property.

The axial forces observed on the vertical load-bearing members under vertical loads were found to be below the capacity of these members. Furthermore, the ratio of the shear forces on the structural elements that failed in shear under earthquake effects and vertical loads to the total shear force on the corresponding story was found to be below the limit value. However, the building failed to meet the inter-story drift demands. The inter-story drift ratio in the ground floor exceeded the limit value of 0.7% for the “Controlled Damage” performance level. Furthermore, the kinematic limit analysis results revealed that the walls of the building would overturn when exposed to a DD-2 earthquake and therefore, did not meet the statical demand for the target earthquake.

In conclusion, it was determined that the building failed to satisfy the “Controlled Damage” performance level envisaged in SMRGHS 2017 for an earthquake with a 10% probability of exceedance in 50 years (DD-2 ground motion level). Additionally, it was considered that the potential collapse of the examined building poses a danger to the entrance and stair section of the adjacent building in terms of life and property safety.

REFERENCES

- [1]. M. Shariq, S. Haseeb, and M. Arif, “Analysis of existing masonry heritage building subjected to earthquake loading,” *Procedia Engineering*, 173, 1833-1840, 2017.
- [2]. C. Casapulla, and L.U. Argiento, “Non-linear kinematic analysis of masonry walls outof-plane loaded. The comparative role of friction between interlocked walls,” *OMPdYN 2017: 6th ECCOMAS Thematic Conference on Computational Methods in Structural Dynamics and Earthquake Engineering*, Rhodes Island, Greece, 2017.
- [3]. G. Milani, P.B. Lourenco, and A. Tralli, “3D homogenized limit analysis of masonry buildings under horizontal loads,” *Engineering Structures*, 29, 3134–3148, 2007.
- [4]. N.C. Palazzi, L. Rovero, U. Tonietti, J.C. De la Llera, “Kinematic limit analysis of basilica del Salvador, a significant example of neo-gothic architecture in Santiago, Chile,” *16th European Conference on Earthquake Engineering*, Thessaloniki, Greece, 2018.
- [5]. B. Yildizlar, “Seismic performance analysis and rehabilitation applications for a historical masonry building through field works and experimental investigations,” *Structures*, 34, 1811-1833, 2021.
- [6]. C. Akcay, T.S. Bozkurt, B. Sayin, and B. Yildizlar, “Seismic retrofitting of the historical masonry structures using numerical approach,” *Construction and Building Materials* 113, 752–763, 2016.
- [7]. G.Ö. Özen, “Comparison of Elastic and Inelastic Behavior of Historic Masonry Structures at The Low Load Levels,” Master of Science Thesis, Middle East Technical University, Institute of Science and Technology ,2006.
- [8]. P. Roca, M. Cervera, G. Gariup, and L. Pela, “Structural analysis of masonry historical constructions. Classical and advanced approaches,” *Archives of Computational Methods in Engineering*, 17(3), 299–325, 2010.
- [9]. B. Sayin, B. Yildizlar, C. Akcay, and B. Gunes, “The retrofitting of historical masonry buildings with insufficient seismic resistance using conventional and non-conventional techniques,” *Engineering Failure Analysis*, 97, 454-463, 2019.
- [10]. Midas Gen (2018) Integrated solution system for building and general structures. MIDAS Information Technology Co.
- [11]. PRO_CINem, Analysis of Local Mechanisms through Linear and Nonlinear Kinematic Analysis Software, 2Si Software e servizi Per L'ingegneria, Italy, 2019.
- [12] ASTM C 1531 Standard Test Methods for In Situ Measurement of Masonry Joint Shear Strength Index
- [13] ASTM C 1197 [13] (Standard Test Methods for In Situ Measurement of Masonry Deformability Properties Using Flatjack Method)
- [14]. Laboratory tests, Number R.22.265.0009, Ticem Co., 2019
- [15]. SRMGHS (2017) Seismic risks management guide for historical structures, General Directorate of Foundations, Ankara, Türkiye (in Turkish)
- [16]. TBEC (2018) Türkiye Building Seismic Code: Rules for design of buildings under earthquake effect, Official Gazzette, Decision no 30364 dated 18.03.2018 (in Turkish)
- [17]. AFAD (2019) Türkiye Earthquake Risk Map Interactive Web Application. Available at: tdth.afad.gov.tr/TDTH/main.xhtml
- [18] A. Giuffre, *Lecture sulla meccanica delle murature storiche*, Kappa, Roma, 1991.
- [19] J. Heyman, The safety of masonry arches, *International Journal of Mechanical Science*, 11, 363-385, 1969
- [20] J. Heyman The stone skeleton, *International Journal of Solids Structures*, 2, 249-279, 1966.

BIOGRAPHY

Dr. Baris Sayin is currently studying as a Professor in the Department of Civil Engineering at Istanbul University-Cerrahpasa. Dr. Sayin received his BS, MS, and PhD degrees in Civil Engineering from Istanbul University. During the graduate education, he served as a Research Assistant in the Department of Civil Engineering. Between 2009 to 2015, Dr. Sayin worked as a structural engineer in the Department of Construction and Technical Affairs at Istanbul University. In September 2012, Dr. Sayin collaborated with Professor Hamid Saadatmanesh as a Visiting Scholar at the Department of Civil Engineering and Engineering Mechanics, University of Arizona, for a duration of 12 months. Their collaboration focused on insulated FRP-strengthened RC structures and FRP sandwich panels. Dr. Sayin's research interests encompass historical masonry structures, RC buildings, fiber composites, and industrial wastes. He has authored over one hundred articles in the fields of civil engineering and architecture.

ICENS

9TH INTERNATIONAL CONFERENCE ON
ENGINEERING AND NATURAL
SCIENCES

